



Tailoring Conical Diffraction Vector Beams in Linear and Nonlinear Regime

Muhammad Waqar Iqbal

► To cite this version:

Muhammad Waqar Iqbal. Tailoring Conical Diffraction Vector Beams in Linear and Nonlinear Regime. Physics [physics]. Université de Lorraine, 2023. English. NNT : 2023LORR0315 . tel-04708380

HAL Id: tel-04708380

<https://hal.univ-lorraine.fr/tel-04708380v1>

Submitted on 24 Sep 2024

HAL is a multi-disciplinary open access archive for the deposit and dissemination of scientific research documents, whether they are published or not. The documents may come from teaching and research institutions in France or abroad, or from public or private research centers.

L'archive ouverte pluridisciplinaire **HAL**, est destinée au dépôt et à la diffusion de documents scientifiques de niveau recherche, publiés ou non, émanant des établissements d'enseignement et de recherche français ou étrangers, des laboratoires publics ou privés.



**UNIVERSITÉ
DE LORRAINE**

**BIBLIOTHÈQUES
UNIVERSITAIRES**

AVERTISSEMENT

Ce document est le fruit d'un long travail approuvé par le jury de soutenance et mis à disposition de l'ensemble de la communauté universitaire élargie.

Il est soumis à la propriété intellectuelle de l'auteur. Ceci implique une obligation de citation et de référencement lors de l'utilisation de ce document.

D'autre part, toute contrefaçon, plagiat, reproduction illicite encourt une poursuite pénale.

Contact bibliothèque : ddoc-theses-contact@univ-lorraine.fr
(Cette adresse ne permet pas de contacter les auteurs)

LIENS

Code de la Propriété Intellectuelle. articles L 122. 4

Code de la Propriété Intellectuelle. articles L 335.2- L 335.10

http://www.cfcopies.com/V2/leg/leg_droi.php

<http://www.culture.gouv.fr/culture/infos-pratiques/droits/protection.htm>

THÈSE

Présentée et soutenue publiquement pour l'obtention du titre de

DOCTEUR de L'UNIVERSITÉ DE LORRAINE

Spécialité: *Physique. Optics and Photonics*

Présentée par

Muhammad Waqar IQBAL

Tailoring Conical Diffraction Vector Beams in Linear and Nonlinear Regime

Thèse soutenue le **10 Novembre 2023** devant le jury composé de:

Sylvain LECLER	Président	Professeur, INSA Strasbourg, France
Patricia SEGONDS	Rapporteur	Professeure, Université Grenoble Alpes, France
Eugenio FAZIO	Rapporteur	Professeur, Sapienza Università di Roma, Italy
Miguel ALONSO	Examineur	Professeur, Centrale Méditerranée, France and University of Rochester, USA
Virginie CODA	Examineur	Maître de conférences, Université de Lorraine, France
Germano MONTEMEZZANI	Directeur de thèse	Professeur, Université de Lorraine, France
Nicolas MARSAL	Co-directeur de thèse	Maître de conférences, CentraleSupélec, France

UNIVERSITÉ DE LORRAINE

Ecole doctorale : Chimie – Mécanique – Matériaux – Physique (C2MP)
LMOPS – Laboratoire Matériaux Optiques, Photonique et Systèmes – UR 4423
CentraleSupélec – 57070 Metz, FRANCE

CONTENTS

Table of Contents	i
Acknowledgements	iii
List of Abbreviations	vi
Abstract	vii
Résumé	viii
Introduction	1
1 Tailored light	5
1.1 Singular optics: amplitude, phase and polarization singularities	5
1.1.1 Phase singularities: orbital angular momentum	7
1.1.2 Polarization singularities	11
1.2 Vector beams	16
1.3 Perspectives for applications of structured light	20
2 Optically anisotropic materials	21
2.1 Preliminaries of electrodynamics	22
2.2 Dielectric tensor of an anisotropic medium	23
2.3 Plane-wave propagation in anisotropic medium	24
2.4 Optical indicatrix	27
2.5 Classification of anisotropic crystals	28
2.6 Double refraction	30
2.7 Light propagation through uniaxial crystal	31
2.8 Light propagation through biaxial crystal	32
2.8.1 Conical refraction/diffraction	33
2.9 Optical Activity	35
2.10 Nonlinear photorefractive crystals	36
2.10.1 Refractive index modulation via electro-optic effect	37
2.10.2 Holographic recording	38
2.10.3 Two-wave mixing	41
2.10.4 Four-wave mixing	41
3 Conical diffraction: theory and fundamental aspects	43
3.1 History of conical diffraction phenomenon	43
3.2 Principle of conical diffraction	44
3.3 Theoretical model	45
3.3.1 Conical diffraction in a single biaxial crystal	45
3.3.2 Conical diffraction in a cascade	48
3.4 Recent developments and applications	52
3.4.1 Review of fundamental progress in conical diffraction	52
3.4.2 Some applications of conical diffraction	53

4	Tailored conical diffraction beams	55
4.1	Basic concepts and conjugate cascade design	56
4.2	Theoretical model	58
4.3	Structure parameters and general pattern shape	60
4.4	Intensity and polarization distribution	63
4.4.1	Local polarization	63
4.4.2	Variation of crystal orientation angles	68
4.4.3	Non-commutation of the conjugate cascade	69
4.4.4	Possibility to select individual structures	70
4.4.5	Polarization filtering at different stages	71
4.4.6	Evolution of non-circular CD patterns beyond $\zeta = 0$ plane	74
4.5	Conclusion	75
5	Fractional charged OAM beams	77
5.1	Experimental methods for measuring OAM	78
5.2	Examples of OAM determination	82
5.3	OAM of non-circular CD beams	85
5.4	Conclusion	88
6	In-situ holographic recording and two-wave mixing of CD beams	89
6.1	Introduction	89
6.2	Crystal sample and experimental approach	90
6.3	Experiments	92
6.4	Background theory	96
6.5	Discussion and conclusion	100
7	Conclusion and Perspectives	103
A	Conical diffraction inside a double pass semi-cavity	109
B	Fibonacci and degenerate cascades of conical diffraction	117
	Synthèse de la thèse	123
	Bibliography	131
	List of Publications	145

Acknowledgements

First of all, I would like to express my deep gratitude and sincere kindness to Prof. Germano Montemezzani (Directeur de thèse) and Dr. Nicolas Marsal (Co-directeur de thèse), for giving me the opportunity to work on this rich topic in terms of fundamental physics but also historically relevant. Our regular meetings with plenty of lively discussions increased much further the curiosity in our investigations. I specially thank both of you for giving me the freedom in exploring the thesis topic and allowing me to discuss all those ideas without hesitation. All of your valuable suggestions and consistent guidance kept me highly motivated during these three years.

I am also thankful to Prof. Alexander A. Grabar, Yulija Shiposh and Anton Kohutych from Uzhhorod National University, Ukraine, for growing and providing the SPS crystal. Investigations on the nonlinear part of this thesis could not have been done without their support. Despite the difficult times that they are facing as a nation, I found them extremely courageous and brave. I am specially thankful to Prof. Grabar and Yulija for their kind visit to Metz and for the insightful discussions and experiments that we performed during those visits.

I would also like to thank undergraduate students, who showed interest in this research topic and worked under my guidance for their master and bachelor thesis. The names of these brilliant students are Ziad Rustom (M2 thesis), Antonin Gâteau (CentraleSupélec master student), Lisa Muller (L3 PFA), Mayssoune Mina (M1 thesis) and Thibault Rosier (CentraleSupélec master student).

I would like to thank Dr. Mouhamad Al-Mahmoud for his kind behaviour and all those jolly discussions about cultures and other stuff, during the short time when we shared the same lab. During the course of this thesis, I have been lucky enough to find a lot of supportive colleagues including former and present PhD students, who were extremely kind and gave a lot of encouragement. It is difficult to mention all of them and I apologize if I miss someone. Firstly, the former successfully graduated PhD students Dr. Mouhmaed Al-mahmoud, Dr. Rim Alrifai, Dr. Yaya Doumbia, Dr. Sourav Bose, Dr. Christelle Habis, Dr. Carmen Moya Lopez Pelaez and Dr. Nawal Ferdi. The current PhD students deserves a special thanks for re-igniting the spirit of organizing special parties, which were almost forgotten because of covid restrictions, so a special thanks to Rodolph Iskandar, Lucas Oliverio, Wafae El Berjali, Clara Ethuin, Aurélie Grégori, Jules Mercadier, Ning Yang, Xin Wang, Yue Chai, Krishna Lone. Also, a special thanks to my country-mate Sadaqat Ali for all the irrelevant political discussions but also for welcoming me upon my arrival in Metz, France.

Some other colleagues and good friends for their kind support and encouragement, Dr. Luis Antonio García Gutiérrez, David Rincón, Dr. Mohammad Ikhtiham Bin Taher, Dr. Mohammed El Ismaili and Dr. Montassar Billeh Bouzourâa.

Finally, I am extremely thankful to my beloved wife “Rabia Shaheen” for the exceptional support in all matters of my life. I am truly blessed to have you as my partner. Indeed it was a tough time as we both tried very hard in our respective PhD research work but this made me realized that the greatest wealth a man can have is an understanding wife. I am also grateful to my parents and siblings for their unwavering support throughout my academic

career. In the end, I am thankful to ALLAH almighty, the most beneficent and the most merciful for his countless blessings and specially for giving me the good health to complete successfully this thesis research work.

Muhammad Waqar Iqbal

Dedicated to
my beloved wife
Rabia Shaheen
and to
my parents

List of abbreviations

BC	Biaxial Crystal
CB	Conduction Band
CD	Conical Diffraction
CCD	Charge-Coupled Device
CGLEs	Complex Ginzburg–Landau Equations
CL	Cylindrical Lens
DFWM	Degenerate Four Wave Mixing
FIP	Focal Image Plane
FT	Fourier Transform
H-pol	Horizontal Polarization
HyGG	Hypergeometric-Gaussian beams
IL	Imaging Lens
KGW	Potassium Gadolinium Tungstate
LCP	Left Circular Polarization
LG	Laguerre-Gaussian Beam
ND	Neutral Density Filter
OAM	Orbital Angular Momentum
OFDH	Off-Axis Digital Holography
PR	Photorefractive
QWP	Quarter Wave Plate
RCP	Right Circular Polarization
SAM	Spin Angular Momentum
SL	Spherical Lens
SLM	Spatial Light Modulator
SPS	Tin Thiohypodiphosphate
TWM	Two-wave Mixing
V-pol	Vertical Polarization
VB	Valence Band

Abstract

A specific type of vector beams can be created naturally via the conical diffraction (also known as conical refraction) phenomenon, which occurs as a tightly focused beam is incident along one of the optic axis of a biaxial crystal. In the case of a homogeneously polarized input wave, conical diffraction (CD) gives rise to double circular rings, where every two diametrically opposite points on the rings possess orthogonal linear polarization. In this thesis research work, we perform fundamental new investigations on the tailoring of CD vector waves in linear and nonlinear biaxial crystals (BC). The properties being affected are shape, intensity, polarization and orbital angular momentum (OAM). Complex beam shaping is obtained in conjugate cascades of BCs. This breaks the usual circular symmetry characteristics typical of CD and leads to complex non-circular CD patterns with peculiar properties. The conjugate cascade involves at least two BCs with aligned optic axis and two crossed cylindrical lenses between adjacent BCs to perform intermediate wave-vector space manipulation. A modified paraxial diffraction theory of CD, which incorporates the effects of this manipulation reproduces well the experimentally observed features. Besides the exact theoretical treatment, specific rules of thumb established via newly introduced structure parameters help to predict the shape and polarization distribution of the non-circular CD beams. In strong contrast to conventional cascades, which result in generating multiple concentric rings with uniform intensity and homogeneously varying polarization, the conjugate cascades results in the creation of patterns that consist of non-circular individual structures possessing convex or concave curvatures, with non-homogeneously varying intensity and polarization distribution. Extended conjugate cascade of three or more biaxial crystals results in patterns, where individual structures can cross each other or merge locally to give interference. While for conventional cascades the polarization on the rings keeps being linear, in our case elliptical or circular polarizations can be observed locally at structure crossing or merging regions. By looking at the azimuthal phase of the non-circular CD beams, it turns out that they possess single charged vortices and phase discontinuity lines. Their fractional OAM values can be scaled by adapting the conjugate cascade parameters. All in all, the non-circular CD beams lead to an increased vector pattern richness and versatility as compared to the circular rings of conventional CD.

In this thesis we also combine for the first time the linear optical CD effect with the nonlinear recording of dynamic holograms in a photorefractive (PR) biaxial crystal, with all processes taking place within the same medium. Even though the hologram recording is driven by the intensity distribution as in conventional holography, it is observed that efficient recording of CD object beams can be achieved with any combination of the input polarizations of the object and reference waves, including the case of orthogonal linear or circular polarizations. Similarly for a two-wave mixing (TWM) experiments, it is observed that different regions of CD object beam can be amplified by varying the polarization of the pump beam. A simplified theoretical model that considers the physics of the CD phenomenon as well as of the photorefractive grating recording and read-out (in a complex oblique orientation inside the crystal) verifies qualitatively the experimental observations. These investigations might open interesting perspectives for CD holography and TWM to be utilized for multichannel polarization multiplexing of vector beams and for intensity reshaping and equalization within the vector beam.

Résumé

Un type spécifique de faisceaux vectoriels peut être créé naturellement via le phénomène de diffraction conique (également connu sous le nom de réfraction conique), se produisant lorsqu'un faisceau focalisé se propage le long de l'un des axes optiques d'un cristal dit bi-axe (BC). Dans le cas d'une onde initialement polarisée, la diffraction conique (CD) donne naissance à des anneaux circulaires doubles, où deux points diamétralement opposés possèdent des polarisations linéaires orthogonales. Dans ce travail, nous effectuons de nouvelles recherches sur le moyen de contrôler linéairement ou non linéairement ces faisceaux issus de la CD. Lesdits contrôles auront lieu sur : la forme, l'intensité, la polarisation ou bien encore le moment cinétique orbital (OAM) des faisceaux. En ce qui concerne la forme, des faisceaux vectoriels de formes complexes peuvent être obtenues grâce à des cascades conjuguées de BC, ce qui brise la symétrie circulaire usuelle de la CD. Ces cascades conjuguées impliquent au moins deux BC avec un axe optique aligné ainsi que deux lentilles cylindriques croisées placées entre les BC pour effectuer une manipulation spatiale des vecteurs d'onde. Contrairement aux cascades conventionnelles, qui aboutissent à la génération de plusieurs anneaux concentriques avec une intensité uniforme et une polarisation variable de manière homogène, les cascades conjuguées aboutissent à la création de motifs constitués de structures individuelles non circulaires possédant des courbures convexes ou concaves, avec des variations non homogènes de l'intensité, phase et polarisation. Une cascade conjuguée étendue à trois cristaux biaxiaux ou plus donne lieu à des motifs dans lesquels des structures individuelles peuvent se croiser ou fusionner localement pour produire des interférences. Alors que pour les cascades conventionnelles, la polarisation sur les anneaux reste linéaire, dans notre cas, des polarisations elliptiques ou circulaires peuvent être observées localement au niveau des régions de croisement ou de fusion des structures. En examinant la phase azimutale des faisceaux CD non circulaires, ces derniers possèdent des vortex de charge unique et des lignes de discontinuité de phase indiquant la présence d'OAM fractionnaires pouvant être mis à l'échelle en adaptant les paramètres des cascades conjuguées. Nous avons également développé une théorie paraxiale de cette nouvelle CD en cascade, intégrant les effets de manipulation des lentilles dans l'espace des vecteurs d'onde. Nos résultats reproduisent bien les observations expérimentales. Outre le traitement théorique exact, nous proposons deux règles empiriques établies via des valeurs spécifiques des paramètres de structure pour aider à prédire la forme et la distribution de polarisation.

Enfin, pour la première fois, l'effet optique issu de la CD linéaire est combiné à l'enregistrement non linéaire d'hologrammes dynamiques dans un cristal biaxe photoréfractif (PR) : tous les processus (linéaire et nonlinéaire) se déroulant dans le même milieu. Même si l'enregistrement de l'hologramme est piloté par la distribution d'intensité comme dans l'holographie conventionnelle, il est observé qu'un enregistrement efficace des faisceaux objets issu de la CD peut être obtenu avec n'importe quelle combinaison des polarisations d'entrées des ondes objet et référence, y compris le cas d'ondes ayant des polarisations orthogonales. De même, pour les expériences de mélange à deux ondes (TWM), on observe que différentes régions du faisceau objet issu de la CD peuvent être amplifiées en faisant varier la polarisation du faisceau de pompe. Un modèle théorique simplifié prenant en compte la physique du phénomène de CD ainsi que l'enregistrement et la lecture du réseau photoréfractif vérifie qualitativement les observations expérimentales.

INTRODUCTION

Structured or tailored light refers to the tailoring of light beams in one or several degrees of freedom. It may be in time and frequency to create ultrafast tailored time pulses or, more commonly, in controlling the spatial degrees of freedom of light, such as amplitude, phase and polarization. This tailoring of light beams is gaining wider attention from the scientific community, as the technological advancement and fundamental knowledge of beam shaping has evolved enormously in the last decades. Techniques and methods to generate such tailored beams are fuelling this progress faster than ever before [1–6].

Structured laser beams possessing phase singularities and a point of null intensity at the center are termed as optical vortices. Optical vortex beams have helical phase fronts and possess an orbital angular momentum (OAM) of $l\hbar$. Here l is an integer and represents the topological charge of the phase singularity. Tailoring the laser beams polarization has captivated a lot of interest in the research community. In this regard other special unconventional beams are “vector beams”, which have a spatially varying polarization distribution. Vector beams are quite intriguing, as the polarization singularities in their fields makes them interesting candidates for investigating fundamental optics phenomenon from classical to quantum domain. Vector beams have been utilized in many prospective technological applications ranging from free-space optical communication to super-resolution imaging of biological samples [7–9]. Also beams with such singularities (phase and polarization) fall into a well known field of singular optics. Singular beams with such optical singularities have been implemented for optical manipulation or tweezing [10–12], free space optical communication [13], quantum information processing [14, 15], super-resolution imaging [16] and several others key enabling technologies [1].

Among vector beams, the most familiar beams are the radial and azimuthal modes of a Laguerre-Gaussian (LG) beam. This beam possesses both a radial and azimuthal distribution of linear polarization [17]. A specific type of vector beam can be generated naturally from conical diffraction phenomena occurring in a biaxial crystal. The vector beam generated from conical diffraction phenomena possess a unique spatial distribution of linear polarization, which is much different from the familiar radial and azimuthal LG modes.

Vector beams generated naturally via conical diffraction (CD) have intrigued the scientific community owing to their unique properties and their application potential. Despite for a nearly 200 years long history, the interest in CD has been renewed in the last 2 decades, primarily because of the development of adequate diffraction theory and demonstration of novel CD applications [18]. The CD phenomenon is observed when a sufficiently tightly focused beam is incident on an optically biaxial crystal (BC) with its wave-vector \mathbf{k} parallel to one of the optical axes of the crystal. For this singular \mathbf{k} -direction, the Poynting vector directions are degenerate and lie on the surface of a slanted cone with circular base inside the crystal. The section of this cone can be easily visualized in the plane of tighter focusing of the incident wave (focal image plane, FIP), where one observes two closely spaced circularly shaped bright rings (double rings) separated by a dark ring (called Pogendorff ring). Two diametrically opposite points always possess orthogonal linear polarizations, leading to the vector beam character [18–20]. An elegant geometrical explanation on how

the Poynting vector directions on the cone depend on the local electric (\mathbf{E}) and electric displacement vectors (\mathbf{D}) of the wave is given in Born and Wolf's book [21]. This peculiar CD phenomenon was predicted by W. R. Hamilton in 1832 and experimentally observed by H. Lloyd in 1833.

At present a thoroughly investigated configuration considers conical diffraction from a cascade of N biaxial crystals. CD from a cascade of N biaxial crystals gives rise to 2^{N-1} rings (or double rings) [22]. Thus if two biaxial crystals are placed in a series, it leads to two concentric rings (or double rings) in the focal image plane. A simple modification by inserting a spherical lens between the two biaxial crystals (variable cascaded configuration) [23] provides additional versatility to modify the radii of the CD rings by modifying the magnification of the spherical lens. For any two biaxial crystals, a value of magnification can be chosen for which the inner rings would collapse to give a central spot (degeneracy). This variable cascade approach proves very useful for obtaining different patterns out of crystals with fixed length [23]. Modified cascaded configurations with a polarization scrambling element such as a half-wave plate or quarter-wave plate placed between the two biaxial crystals has also been reported earlier [24]. A polarization scrambling element between two biaxial crystals leads to complexly shaped vector beams that break the homogeneous azimuthal intensity. Also, the acquired complex vector beams with this configuration are governed by parameters (crystal strength parameter and its orientation), which allow one to acquire specific patterns with unique localization of azimuthal intensity distribution.

Another interesting aspect of CD beams is that, the conical diffraction from a single biaxial crystal results in a beam possessing fractional OAM of exactly $\pm\hbar/2$ per photon, the sign depends on the handedness of the incident circular polarization (i-e + for left and – for right) [25]. This is evident from the fact that a conical diffraction beam is considered as a composition of two beams that may be labelled B_0 and B_1 ¹. The phase and electric field distributions in these components depends on the input polarization such that a left circularly polarized Gaussian incident beam would result in B_0 component with $J_{orb} = 0$; $J_{spin} = +1\hbar$ and B_1 component with $J_{orb} = +1\hbar$; $J_{spin} = -1\hbar$. Thus the total angular momentum of conical diffraction beam has spin part equals to zero ($S = 0$) while the orbital part is equal to $+\hbar/2$ per photon [26–29]. It has already been shown in various studies that the fractional OAM of CD beams can be scaled in an all optical means by separating and isolating either the B_0 or B_1 [26, 30–32]. For instance in a cascade of two biaxial crystals, one can separate B_0 or B_1 components. This is done by a combination of a quarter wave plate and a linear polarizer. After separation of the desired component, one can vary the polarization state of the highest OAM state generated in a first CD pass to obtain a maximum increment of OAM for the second CD pass in the other BC [27, 33]. Interestingly the fractional OAM property of CD beams has also been investigated with nonlinear effects such as second harmonic generation and sum-frequency generation [31, 34].

In addition to the above mentioned ongoing fundamental investigations, CD from a single BC or a cascade of 2 BC's has been reported as robust means for optical trapping [35], beam shaping [24, 36], free-space multiplexing [37], polarimetric applications [38], Conical diffraction lasers [39], super-resolution imaging [40] and several other potential ap-

¹This naming is connected to the Belskii-khapalyuk integrals introduced in Chapter 3. These integrals contain the zeroth and first order Bessel function of the first kind, respectively.

plications are currently under investigations [18]. This thesis research work is devoted to fundamental investigation of new methods for tailoring various properties of the conical diffraction beams generated in anisotropic biaxial crystals. In this regard, the conical diffraction phenomena is investigated in a linear centro-symmetric potassium gadolinium tungstate (KGW) biaxial crystal as well as in a nonlinear non-centrosymmetric tin thiohy-podiphosphate (SPS) biaxial crystal. The chapters of the thesis are organized as follows

In chapter 1, a brief introduction to the newly emerging field of structured/tailored light is presented. This includes discussion on the fundamental physics regarding amplitude, phase and polarization singularities in optical fields. A short overview of singular optics is presented along with a more detailed discussion on vector beams. The chapter concludes with a brief overview of the current trends and ongoing investigations for applications of structured light.

Chapter 2 introduces crystal optics, after some preliminaries of electrodynamics. We discuss briefly plane wave propagation in anisotropic medium. The various optical phenomenon such as double refraction, optical activity are discussed in this context. The last section of this chapter discusses nonlinear photo-refractive crystals useful for dynamic hologram recording, as this feature has been explored for CD beams in this thesis.

Chapter 3 discusses the phenomenon and primary features of conical diffraction in details. The theoretical treatment developed so far is also presented rigorously. This is followed by few examples of CD patterns obtained from single biaxial crystal and from a conventional CD cascade. The chapter concludes with the review on the recent developments and examples of some demonstrations of CD applications.

Chapter 4 is focused on our novel configurations (known as "conjugate cascade"), which results in the generation of non-circular CD beams with highly peculiar properties. These new patterns are composed of individual structures with non-homogeneous distribution of intensity and polarization around them. It is analyzed in detail that the general shape and polarization distribution of these individual structures correlate with the structure parameters, which depend on the conical diffraction cone aperture angle, on the crystal lengths, and on the magnification values due to x - and y -oriented cylindrical lenses placed between the crystals and coupling common conjugate planes. The way in which the obtained patterns depend on the orientation of individual crystal samples around the common optical axis and on an eventual polarization filtering at various stages of the cascade is discussed as well. Additionally, certain other aspects arising from this conjugate cascade such as non-commutation of CLs, longitudinal evolution of non-circular CD beams and possibility to select individual structures are discussed. In short, this chapter treats in detail the principle concept, theoretical model and obtained non-circular CD patterns via conjugate cascade. Both experimental and theoretical results are presented.

Chapter 5 concerns the fractional orbital angular momentum (OAM) of the non-circular CD beams generated via conjugate cascade configuration. Due to the difficulty involved for a direct measurement of fractional OAM, a brief explanation of the various qualitative and quantitative techniques used to determine the OAM is presented first. This is followed by few illustrative examples showing the robustness of the techniques employed for OAM determination. Finally, the results on the spatial phase distribution and fractional OAM

values of our non-circular CD beams are presented, which show the presence of spatially distributed single charge vortices in the beam cross-section and the possibility to tune the fractional OAM values.

Chapter 6 discusses investigations on combining the linear CD optical effect with the nonlinear recording of dynamic holograms in a photorefractive (PR) material, with all processes taking place within the same medium. Our results demonstrate polarization-sensitive holography and two-wave mixing amplification of the conical diffraction (CD) vector beams. A simplified theoretical model that verifies qualitatively the experimental observations, by considering the physics of the conical diffraction effect as well as the one of the nonlinear photorefractive effect is elucidated.

The final chapter concludes and presents some perspectives of our work. Few preliminaries investigations that were performed during the course of this thesis in parallel to the main investigations are presented in appendices. Appendix A discuss CD patterns obtained from a semi-cavity, involving a single BC with double pass conical diffraction in a counter-propagating feedback architecture. The understanding of such a situation is a prerequisite to address the case where the CD cascade is associated to a ring cavity. Appendix B describes the generation of CD patterns via Fibonacci and degenerate cascades. It is shown with few examples that these special type of cascades can help to generate CD double rings with elliptical polarization, the latter showing a variation along the azimuth direction.

TAILORED LIGHT

Structured or tailored light refers to light beams, whose spatial and temporal degrees of freedom are tailored in some sense. This tailoring of light beams has quite recently opened new avenues for fundamental and applied research. Currently, there is an explosion of research into this emerging field dealing with structured light [1, 2]. Structuring light is like synthesizing or customizing light beams for specific purposes. In the next section, optical singularities naturally present in a wave field are discussed in the first place. Connections with more complex hybrid singularities are also briefly elucidated. The methods to generate or detect various types of optical singularities are also presented. In the last section of this chapter, an overview of the current state-of-the-art applications and fundamental prospects of structured light are presented.

1.1 Singular optics: amplitude, phase and polarization singularities

Optical singularities of amplitude, phase and polarization have always intrigued researchers to understand the underneath fundamental laws of physics. Singular optics deals with the investigations of the topology of light in the presence of optical singularities [41]. It was recognized in 1970s that light focusing by nature underpins a systematic behaviour, this understanding comes from the mathematical work of “catastrophe theory” reported by R. Thom in France [42–44] and further developed by V. I Arnold in Russia [45–47]. The application of catastrophe theory to wave optics started soon after with the 1974 article by J. F. Nye and M. V. Berry treating “Dislocations in wave trains” [48]. Thus investigations of the systematic focusing of light by nature with catastrophe theory started to develop in the next decades [49]. Here it is pertinent to mention that unnatural focusing of light is the artificial focusing of light by carefully engineered materials/instruments such as lenses to focus light onto a spot for image formation. On the other hand, a general refracting medium naturally focuses light rays of a point source placed far away onto a bright caustic surface. The optical caustics resulting from such natural focusing possess fine structural details with characteristic diffraction patterns [50]. A closer look at these diffraction pat-

terns reveals that they are built around zero intensity lines or dark lines inside wave-fields. They are also termed as wave dislocations. These dark lines or threads exist in most wave-fields and they are spatial positions of phase singularities i.e. phase is undefined on these threads [48]. If the wave-field is polarized then a characteristic arrangement of polarization around these threads is observed [51]. Thus, the optical caustics resulting from natural focusing of a general refracting medium invoke intriguing singularities of amplitude, phase and polarization in them [49, 52, 53].

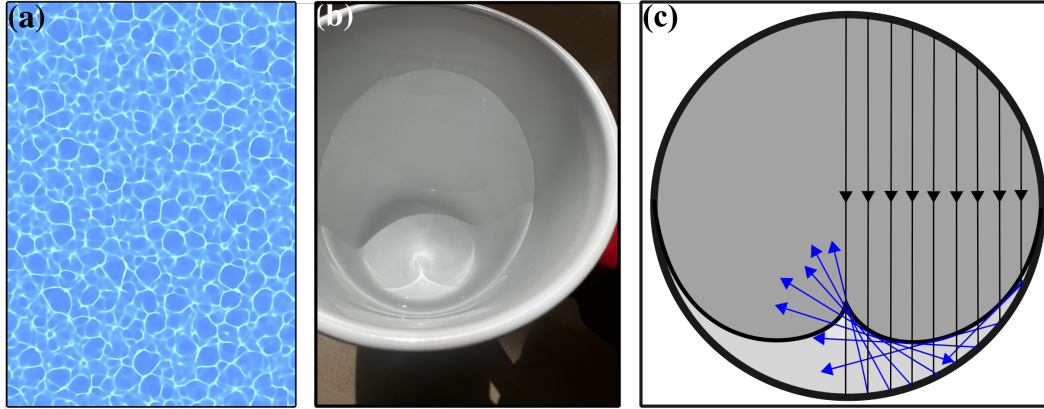


Figure 1.1 – (a) Optical caustics observed as bright lines dancing on the floor of a swimming pool, (b) a coffee cup caustic consisting of cusp and fold caustics observed with the sunlight (here coffee cup filled with water shows a bright caustic line) and (c) shows the construction of bright caustic line from geometrical optics point of view. It is observed that the region below the caustic is brighter than the region above it [49].

The optical caustics are commonly observed on the floor of a swimming pool (see Fig. 1.1(a)), on the bottom of a tea cup (see Fig. 1.1(b,c)) and in many other natural places [49]. Optical caustics are characterized as generic and structurally stable. The genericity of caustics implies that they appear in the wavefields without any necessary conditions i.e. they are typical feature of the system, while the structure stability implies that the caustics are stable upon perturbation in the system. These two features are well observed in optical caustics, for instance the bright lines at the bottom of the swimming pool move about but they survive the small perturbations of the water surface. The above two features also implies that caustics are independent of the particular geometrical shape or symmetry in the system and thus similar caustics forms are expected from different identical systems. In Fig. 1.1(b) optical caustic formed in a coffee cup placed in sunlight are shown. This bright line caustic at the bottom of the coffee cup can be explained via geometrical optics as illustrated in Fig. 1.1(c). By treating Sun as a point source of light, the parallel rays reflect from the cup inner curved surface in such a fashion that the envelope of these rays in three dimensions makes a caustics surface. The bright line is observed due to the intersection of the caustic surface with the coffee surface. This caustic has two features a cusp point (sharp point) and fold caustics. If the rays make small angles with the axis (i.e. paraxial rays), then only cusp will be observed, which implies that fold caustics are only observed due to the presence of rays making large angle with the axis. Finally, the two main characteristics of optical caustics of being generic and structurally stable apply very well to the coffee cup caustic. Firstly, if the coffee cup is deformed then the bright line with a cusp

would merely spatially move from its position but not disappear thus implying structure stability, secondly the coffee cup need not be an exact cylinder, as any curved reflecting surface would in general generate a caustic. Hence the generated caustic is generic [49]. Optical caustics are observed at scales much larger than wavelength, while the phase and polarization singularities are observed at sub-wavelength scales. The next two subsections take a closer look at the phase and polarization singularities in tailored wave-fields.

1.1.1 Phase singularities: orbital angular momentum

In optical wavefields, phase singularity refers to the position where the phase of the field is undefined and thus the amplitude vanishes. There are two types of phase singularities namely shear and vortices. In the former case, the phase changes by π owing to the sign change of the field amplitude on those positions. While in the latter case, the phase is undefined on the particular position and it spans a range of 2π (or a multiple of 2π) in a closed path around that position. Another classification is related to the way in which the phase singularities extends into the three dimensions. This can be screw dislocations, edge dislocations or mixed edge-screw dislocations. A solution to paraxial wave equation in cylindrical coordinates results in a family of beams known as “Laguerre-Gaussian beams”. Laguerre-Gaussian (LG) beams possess a phase singularity at its center, which is termed as optical vortex as this is a spatial position of zero intensity and undefined phase. LG beams forms a complete set of solutions and their optical field can be expressed as $LG_{pl}(r, \phi, z) = u_0^{pl}(r, z)\exp(il\phi)$, where the amplitude u_0 is given by

$$u_0^{pl}(r, z) = \sqrt{\frac{2p!}{\pi(p+|l|)!}} \frac{1}{w(z)} \left[\frac{r\sqrt{2}}{w(z)} \right]^{|l|} \exp\left[\frac{-r^2}{w^2(z)}\right] L_p^{|l|}\left(\frac{2r^2}{w^2(z)}\right) \exp\left(\frac{ik_0 r^2 z}{2(z^2 + z_R^2)}\right) \exp\left[-i(2p + |l| + 1) \tan^{-1}\left(\frac{z}{z_R}\right)\right], \quad (1.1)$$

here $w(z) = w_0 \sqrt{\frac{z^2 + z_R^2}{z_R^2}}$ represents fundamental Gaussian beam with w_0 beam waist, z_R the Rayleigh range and Gouy phase is equal to $(2p + |l| + 1) \tan^{-1}\left(\frac{z}{z_R}\right)$. $L_p^{|l|}(x)$ represents familiar associated Laguerre polynomials determined via $L_p^{|l|}(x) = (-1)^{|l|} \frac{d^{|l|}}{dx^{|l|}} L_{p+|l|}(x)$. l and p denote the azimuthal and radial index respectively. At the beam waist position with $z = 0$, the phase of the Laguerre-Gaussian (LG) beams is simply described by $l\phi$, which implies that the phase of the beam varies with the angular coordinate ϕ . There are two consequences for taking $l \neq 0$, firstly the intensity at the center vanishes due to the term involving l -th power of r , secondly the term $\exp(il\phi)$ dictate that the phase would change by $2\pi l$ in anti-clockwise direction (clockwise for negative l value) around the origin in a constant z -plane. Thus the phase fronts are inclined in the azimuth direction such that they have the shape of l intertwined helical surfaces with handedness that depends on the sign of l . LG beams with $l > 0$ consist of $p + 1$ series of concentric rings of intensity distributions. Figure 1.2 shows the intensity distributions, phase distributions and a plane wave interference (collinear and non-collinear) of few LG modes. It can be observed that for beams with azimuthal index $l > 0$, the number of concentric rings is equal to $p + 1$.

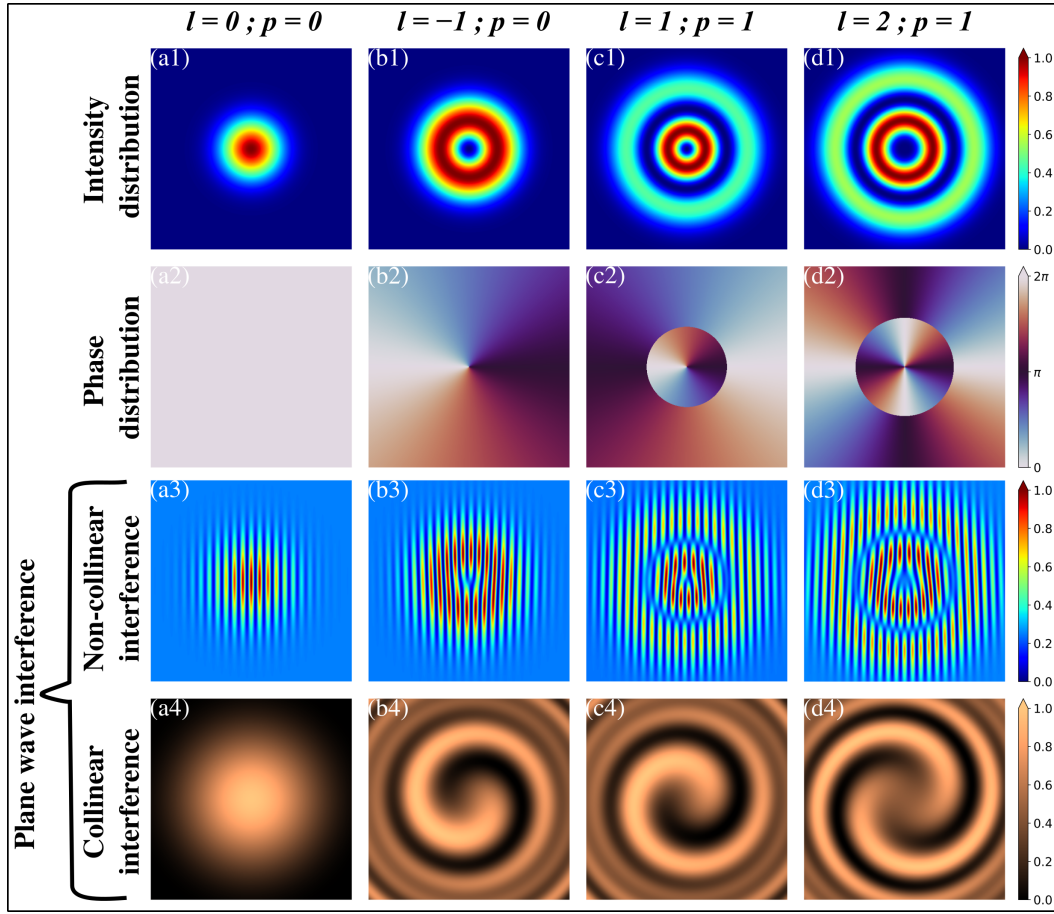


Figure 1.2 – LG Beams with different values of radial (p) and azimuthal (l) index. Intensity distribution (first row), phase distribution (second row), plane wave interference in a non-collinear manner (third row) and collinear manner (fourth row). LG modes with $l = 0; p = 0$ (first column), $l = -1; p = 0$ (second column), $l = 1; p = 1$ (third column), and $l = 2; p = 1$ (fourth column).

Also, the phase distribution reveals that the phase varies by 2π (b(2),c(2)) or by 4π (d(2)) and this value of phase change by multiples of 2π corresponds to the l value of the mode. An interference of the LG mode with a plane wave results in either fringes (non-collinear interference) or spirals (collinear interference), where in the earlier case the l value is equal to the times of the fork minus one, while in the latter case the l value is determined from the number of spirals that appear in the interference pattern. Also, for a positive l value the fork points downward and spiral go anti-clockwise and vice versa for a negative l value. Besides LG beams, there also exists other beams possessing helical phase structures in their field such as Bessel beams, Mathieu beams and Hypergeometric-Gaussian beams [54–57]. All beams with helical or spiral phase fronts possess an orbital angular momentum (OAM) of about $l\hbar$ per photon irrespective of the beams radial distribution.

The quantization of OAM in units of \hbar could simply be understood from a geometrical argument. At any radial distance r from the origin, the phase front inclination or Poynting vector direction (defined as perpendicular to phase fronts surface) with respect to the beam axis could simply be written as $\alpha = l\lambda/2\pi r$ [58]. A photon linear momentum $\mathbf{p} = \hbar\mathbf{k}$ can be resolved into its azimuthal and axial components, and it is the azimuthal compo-

nent (equal to $\hbar k \alpha$ [59]) what is responsible for angular momentum along the beam axis. Thus multiplying the azimuthal component by r^1 and inserting $k = 2\pi/\lambda$, one obtains orbital angular momentum (OAM) of about $l\hbar$ per photon around the axis of the beam [60]. For paraxial light beams, the angular momentum separation into orbital and spin part is well developed [61–63]. Also by deriving the orbital and spin angular momentum from Maxwell’s equations without assuming them as quantized, one can obtain ratios of angular momentum to energy equal to l/ω and σ/ω for a helically phased beam and circularly polarized beam respectively [62], where $\sigma = \pm 1$ indicates right and left circularly polarized wave. Now by multiplying the numerator and denominator of the above two ratios by \hbar and assuming each photon energy is equal to $\hbar\omega$, one obtains the expected values of orbital angular momentum (OAM) equal to $l\hbar$ and spin angular momentum (SAM) equal to $\sigma\hbar$ [56]. SAM has only two states i.e. spin-up or spin-down as SAM arises from the circular polarization with $\sigma = +1$ or -1 . On the other hand, one can generate orthogonal states of OAM corresponding to any l -value as OAM arises from the consequence of beams having inclined phase fronts. The fact that each photon carries an integer OAM explicitly implies that it is a quantum property. Also as OAM is a consequence of the azimuthal phase structure $e^{il\phi}$ of the beams, the presence of OAM properties at the single photon level is expected. The OAM properties have been utilized in many advanced applications such as in optical tweezers [64–66], optical communication [13, 67, 68], quantum entanglement [14, 15, 69, 70], nonlinear optics [71, 72], nanotechnology [73–75], bio-medicine [66, 76], metrology [77–79], astronomy [80] and with recent progress in nanophotonics enabling the generation and detection of OAM beams, novel application prospects are arising in many other disciplinary and interdisciplinary fields [1, 3, 81, 82].

As mentioned above, the OAM of any beam corresponds to the azimuthal component of linear momentum acting at a radius vector from the axis of the beam. Now if the value of OAM depends on the choice of the beam axis then it is called extrinsic OAM, such is the case for Laguerre-Gaussian beam. However it has been shown by Berry that for particular scenarios, it is also possible for beams to have intrinsic OAM i.e. the value of OAM is independent of the choice of the beam axis [83, 84]. Beams possessing helical phase fronts with a certain OAM value are also termed as optical vortices, as there is a phase singularity at the center with an integer topological charge value. For instance, the azimuthal index l in LG beams also represents the topological charge of the central vortex. Optical vortex in LG beams is longitudinally a line singularity exactly on the beam axis. The concept of optical vortices was introduced in 1989 by Coulet and his colleagues [85]. They drew inspiration from hydrodynamical vortices and determined vortex solutions of the Maxwell-Bloch equations. Even before their proposal of optical vortices, the analogies between laser physics and fluids was already reported in some work, where the laser equations were reduced to complex Ginzburg–Landau equations (CGLEs). The CGLEs consists of universal models that describe pattern formations in Bose-Einstein condensate and other peculiar phenomenons. These investigations instigated researchers to study chaos, multistability and turbulence in optical wave-fields [86–89]. Similar to fluid vortex possessing flow singularity in the center, optical vortex soliton has phase singularity at a point of zero intensity with a certain value of topological charge [90]. For a phase distribution ϕ around a singularity, the topological

¹Remember that the angular momentum of a particle is defined as the cross product of its radius vector (equal to its radial position from the origin) with the linear momentum i.e. $\mathbf{L} = \mathbf{r} \times \mathbf{p}$.

charge is defined as below

$$l = \frac{1}{2\pi} \oint_C \nabla \phi(\mathbf{r}) d\mathbf{r}, \quad (1.2)$$

here C represents a closed loop around a singularity. Optical beams with helical phase fronts and an OAM of $l\hbar$ possess a topological charge of l for their phase singularity. It is pertinent to mention that optical vortices with non-integer topological charge have already been investigated [91]. It is possible for beams to have non-integer or fractional charged OAM value. The OAM value of the beams investigated in this thesis are also fractional. It has been shown theoretically and experimentally that non-integer vortices do not exist [91, 92]. Also interestingly vortices in a fractional charged OAM beam have been investigated at the quantum level as well [81].

Numerous experimental method exists for generating beams with optical vortices such as with spiral phase plates, forked gratings and many others, including the most convenient one by using a spatial light modulator (SLM) ². One simple method involves recording a hologram of an interference pattern between a beam of desired structure and plane wave on a photographic film, this film upon illumination by a plane wave generates the beam with desired phase and amplitude in it's first diffraction order. Alternatively, a calculated interference pattern is displayed on SLM and the Gaussian beam or plane wave impinging the display of SLM is easily converted into desired beams of exotic structures in phase and amplitude. The displayed interference pattern on the SLM can be updated electronically and hence SLM provides an extra ability of tunability. SLM have been widely used for applications such as in generating optical tweezers [66], optical vortex links and knots [93], in adaptive optics [94] and others [81].

As discussed earlier for LG beams, the azimuthal phase variations in any beam of light can be observed experimentally by interference experiments. In these experiments, a fundamental beam mode (or plane wave) is interfered with beam of helical phase fronts, which results in either spiral like pattern (collinear interference) representing constant phase difference positions or a fringe pattern (non-collinear interference) with forks representing the location of phase singularity. Such interference patterns for few LG beams has been shown in the third and fourth row of Fig. 1.2 for non-collinear and collinear interference of those LG modes. A forked grating with particular value of l_{dif} could also be utilized to determine the individual photons l -component amplitude in a superposition of OAM eigenstates. In this method, a single mode optical fiber is used to detect the diffracted mode with $l = 0$. Since $l_{dif} = l_{inc} + ml_{fork}$, thus this implies that the unknown incident mode is $l_{inc} = -ml_{fork}$ [15].

Optical vortices exist in nonlinear media as optical solitons and they are also wavelength dependent. Thus investigations with white light as well as with ultrashort pulses is also an interesting regime for them [95–102]. It has been shown that it is possible to generate vortex free beams with well defined but unquantized OAM as here [103]. By superposition of various eigenmodes of OAM, beams with composite vortices can be generated, in which the location and number of new vortices is based on the nature of superposed OAM eigenmodes. Also, it is possible to generate beams where the phase variation around the vortex

²There are different type of spatial light modulators (SLM) but the most common are pixelated liquid crystal device on which the required interference pattern can simply be displayed.

is nonlinear with the azimuth angle [104].

An object placed in the cross-section of beam possessing OAM experiences an optical tweezing force. It is possible to tailor beams possessing composite vortices with non-uniform variation of phase along the cross-section, the object inside such a field would experience kicks rather than uniform push or rotational force. The potential for beams with tailored vortices inside their cross-section is huge as these could be utilized for classical communication purposes or for quantum information purposes [104]. It is pertinent to mention here that optical vortices of charge higher than one usually splits into single charge vortices upon perturbation in the field. Overall, the OAM vortices are resilient to propagation and the topological charge is always conserved [1, 104, 105]. Optical vortices exist in three dimensions and in recent decades lots of investigations have been made on the vortices that are wrapped around the beam axis in transverse direction. They are known as torus loops. Also, there are axial vortices, which are present in the beam axis itself and can make connections with the loops forming the so called “vertex knots” [17, 93, 106].

1.1.2 Polarization singularities

In this subsection, the concept of polarization in electromagnetic wave is briefly presented. For a monochromatic electromagnetic wave, it can be shown that the electric field vector traces out an elliptical or closed path within a transverse plane of that field [17]. This elliptical path is referred to as the polarization ellipse. A polarization ellipse for a general elliptically polarized field for an observer looking into the field (observer direction matters³) is shown in Fig. 1.3. The rectangular box around the polarization ellipse in Fig. 1.3(a) with side lengths equal to twice the amplitudes of the two orthogonal components of the field (E_x and E_y), gives the information about the share of the field provided by each component. This share is quantified by the diagonal angle (α) of this rectangular box with sides lengths $2E_{x0}$ and $2E_{y0}$. In order to retrieve information about a polarization state, one requires knowledge of the length of the semi-major and semi-minor axis (a_M and a_m respectively) as well as the orientation of the polarization ellipse Ψ , which is defined as the rotation of the semi-major axis with respect to the E_x axis. The orientation angle Ψ varies between $+\pi/2$ and $-\pi/2$. For the case, where $E_{x0} = E_{y0}$ the orientation angle $\Psi = \pm\pi/4$. From the information of the axis length of the polarization ellipse, the ellipticity χ can be determined, as it is the arc-tangent of the ratio of the length of the semi-minor axis to semi-major axis i.e. $\chi = \arctan[\mp a_m/a_M]$. As the light field propagates, the tip of its electric field vector can rotate either clockwise or anti-clockwise. This sense of rotation is termed as the handedness or light helicity. It can be determined by acquiring the values of \mathbf{E} at time $t = 0$ and $t = T/4$, then by taking $\mathbf{E}_{t=0} \times \mathbf{E}_{t=T/4}$ if one obtains a vector pointing in the field propagation direction, then the sense of rotation is anti-clockwise (left handed) otherwise it is clockwise (right handed). Also the \mp sign in front of the ellipticity indicates the path taken by the electric field vector around the polarization ellipse, thus a positive value of the ellipticity represents right handedness while negative ellipticity represents left

³The perspective of polarization ellipse is different for an observer looking into the field with respect to the observer looking from the opposite direction.

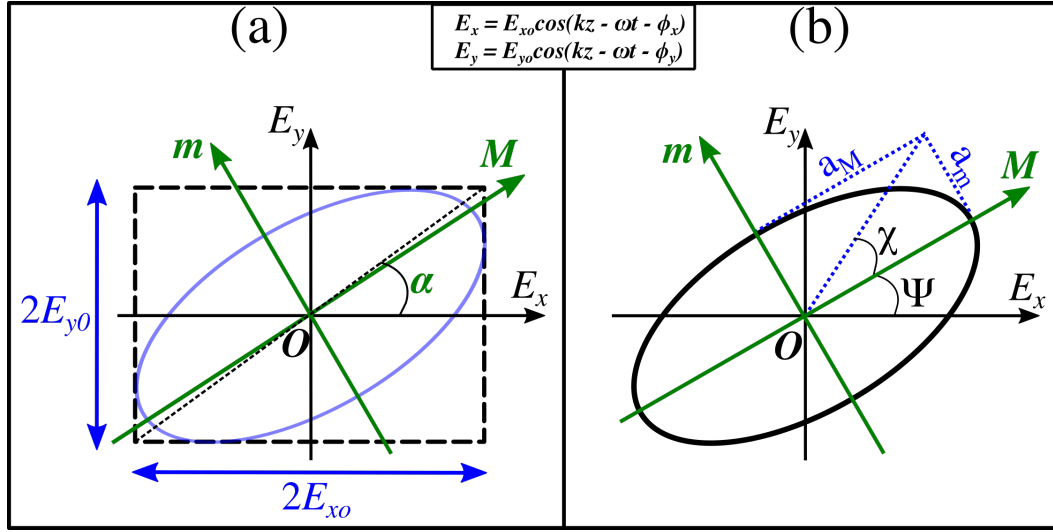


Figure 1.3 – Polarization ellipse is depicted in terms of its field properties (a) and geometric properties (b).

handedness⁴.

Linear and circular polarization represent two special cases of the polarization ellipse. For linearly polarized state, the polarization ellipse geometric parameters define a straight line equation, whose handedness is undefined. Similarly for circularly polarized light, the geometric parameters of the polarization ellipse would define the equation of a circle, whose orientation is undefined [107]. In order to have a specific information about the polarization state, the phase difference ($\Delta\phi = \phi_y - \phi_x$) between the two components of \mathbf{E} -field must be considered as well. All the geometric parameters of the polarization ellipse (a_M , a_m , Ψ) can easily be related with the amplitude (E_{x0} , E_{y0}) and phase difference ($\Delta\phi = \phi_y - \phi_x$) of the field [17]. However both of these two descriptions for polarization states i.e field parameters and geometric parameters are not directly measurable experimentally⁵. G. G. Stokes (in 1852) described a set of four parameters, which were experimentally measurable. These four parameter in terms of the field parameters are,

$$S_0 = E_{x0}^2 + E_{y0}^2, \quad (1.3)$$

$$S_1 = E_{x0}^2 - E_{y0}^2, \quad (1.4)$$

$$S_2 = 2E_{x0}E_{y0} \cos \Delta\phi \quad (1.5)$$

$$S_3 = 2E_{x0}E_{y0} \sin \Delta\phi \quad (1.6)$$

It can be shown that the above four Stokes parameters obey, $S_0^2 = S_1^2 + S_2^2 + S_3^2$. Which implies that they are not independent. With the aid of a polarizer and quarter-wave plate, one can determine cycle average intensity of six experimental measurements to find out the three field parameters. S_0 is the total intensity and it has no connection with the orientation or ellipticity of the polarization ellipse. For such reasons, generally a set of normalized stoke

⁴Since the ratio $0 \leq |a_m/a_M| \leq 1$ gives the values of ellipticity χ ranging from $-\pi/4$ to $\pi/4$.

⁵In the optical domain, the oscillation of the field is too rapid for any such measurement.

parameters are introduced as below

$$s_1 = S_1/S_0 \quad (1.7)$$

$$s_2 = S_2/S_0 \quad (1.8)$$

$$s_3 = S_3/S_0 \quad (1.9)$$

which also satisfy the relation of fully polarized light; $s_1^2 + s_2^2 + s_3^2 = 1$. The field parameters, geometric parameters and Stokes parameters can be collectively used to characterize any polarization state of the field. The above three set of parameters can be elegantly related to each other in a geometrical construction known as "Poincaré Sphere" ⁶. Figure 1.4 shows a Poincaré sphere, which illustrates that each point on the sphere gives information about the Stokes parameters as well as the geometric parameters of the polarization ellipse, which ultimately can be used to determine field parameters. It can be shown that the positions on the Poincaré sphere and normalized Stokes parameters are related by the expressions below [17],

$$s_1 = \cos(2\chi) \cos(2\Psi) \quad (1.10)$$

$$s_2 = \cos(2\chi) \sin(2\Psi) \quad (1.11)$$

$$s_3 = \sin(2\chi). \quad (1.12)$$

In the above expressions (Eqs. (1.10) - (1.12)), Ψ and χ represent the orientation and ellipticity of the polarization ellipse. While the surface of the Poincaré sphere is connected to fully polarized waves, points inside the sphere indicate partially polarized light. Any point on the surface or within the Poincaré sphere is specified by a radius, azimuth and ellipticity. The radius for any coordinate point tells the degree of polarization and its values ranges from 0 to 1. The degree of polarization is defined as the ratio of the polarized light intensity to total light intensity. This implies that the points within the Poincaré sphere represent partially polarized light, thus a point with radius equal to 1 represent fully polarized light. The azimuth (longitude) and ellipticity (latitude) angles on the sphere are expressed by 2Ψ and 2χ (see Fig. 1.4) and their values are obtained from the polarization ellipse. The azimuth angle (also known as orientation angle) is measured from the S_1 -axis of the Poincaré sphere and it has a value ranging between $-\pi/2$ and $+\pi/2$. While the ellipticity (χ) is also measured in angular values from the equator of the sphere and it has values ranging between $-\pi/4$ to $\pi/4$.

For a linearly polarized light, the phase difference $\Delta\phi = 0$ or $p\pi$, with $p = 0, \pm 1, \pm 2, \dots$. This explicitly results to all the points on the equator line of the Poincaré sphere. Figure 1.4 shows four blue circles on the equator line for linear polarized states of 0° (horizontal polarization), 45° , 90° (vertical polarization) and 135° . Similarly, circular polarization requires field amplitudes to be $E_{x_0} = E_{y_0} = E_0$ and phase difference to be $\Delta\phi = (2p + 1)\pi/2$, with $p = 0, \pm 1, \pm 2, \dots$. By inserting these values in Eqs. (1.10) - (1.12), one finds that circular polarization is represented by the points on the poles (North and South). Right and left handed circularly polarized states are depicted by green circles (top and bottom respectively) on the Poincaré sphere in Fig. 1.4. All the rest of the points on the sphere represent

⁶The Poincaré sphere of optical polarization has a direct equivalence with the Bloch sphere used in quantum mechanics.

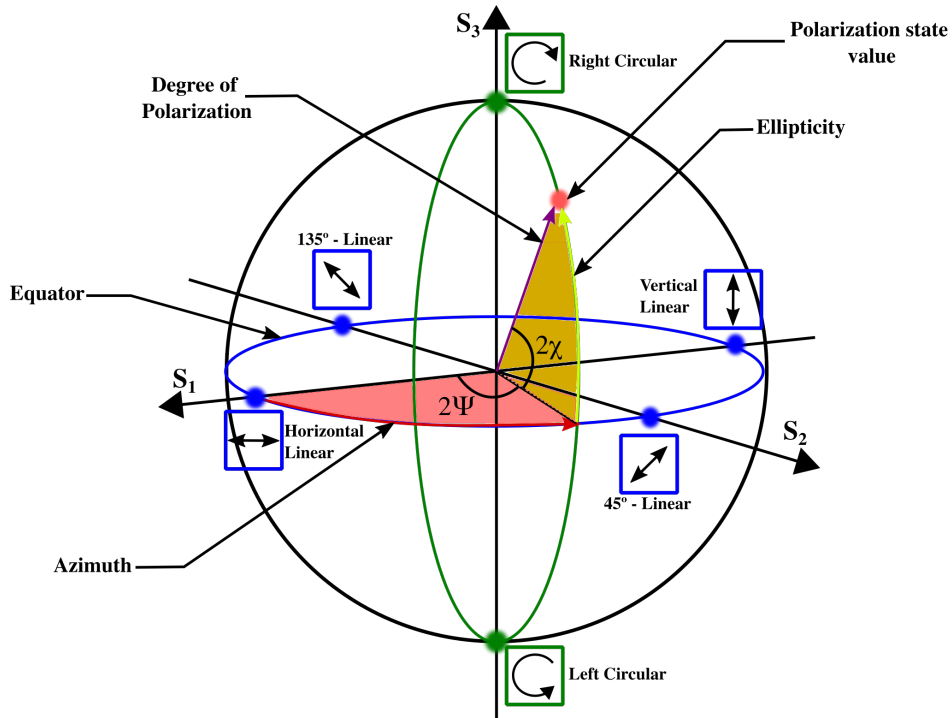


Figure 1.4 – Poincaré sphere illustrating the relationship between Stokes parameters and geometric parameters of the polarization ellipse. Linearly polarized states are represented by the equator line (blue line). Horizontal, vertical and two oblique linear states of $+45^\circ$ and $+135^\circ$ are depicted by blue dots on this line. Right and left circularly polarized states occupy the two poles (depicted by two green dots) on the Poincaré sphere. All other positions on the surface of the Poincaré sphere are occupied by elliptically polarized states.

elliptical polarizations with right and left handed elliptical polarization above and below the equator respectively. A certain polarization state such as the red circle in the Fig.1.4 possess a unique azimuth and ellipticity values. An arc can connect this polarization state to any other state on the surface of the Poincaré sphere and thus the difference in the azimuth and ellipticity of the two polarization states could be calculated via spherical trigonometry. Thus it is possible to predict the transformation of a polarized state after interaction with a polarizing element and also how to achieve a desired polarization state by setting the polarizing element for that specific transformation [17, 107–109].

From the above discussion, it follows that in a transverse plane for a monochromatic wave with general state of polarization being elliptical, there are two polarization singularities that are defined: C-points and L-lines. The C-points refer to the states of circular polarization, which are represented by two points on the poles of Poincaré sphere. Importantly, the polarization ellipse orientation (Ψ) is undefined at these points. Thus the C-points (left and right handed) are regarded as singularity of direction. Similarly, the linear polarization states represented by the equator line on the Poincaré sphere, divide the sphere into northern (right handed) and southern (left handed) hemispheres. Thus in a transverse plane, they are represented by lines which are closed or stretched off to infinity separating the corresponding regions of the plane into right and left handed polarization. The handedness of the polarization on these lines is undefined and is flipped across them,

thus these are known as L-lines of singularity resulting from the singularity of handedness. These two polarization singularities are generic singularities of the optical fields and it has already been well established that the polarization singularities possess distinct features and unique topological properties. The singularity of orientation (C-points) and handedness (L-points) were initially discussed and presented by Nye [110]. The theoretical aspect of these singularities were discussed further in [51, 111] and treated experimentally first in [112].

The field structure in the neighbourhood of polarization singularity is non-trivial and possess few standard generic features. By looking at the distribution of polarization ellipses around a C-point singularity (shown with red circles in Fig. 1.5) in a transverse plane (fixed z), it can be observed that there are only three possible distinct distributions. These three distinct distributions known as star, monstar and lemon are depicted in Fig.1.5. These three distributions are constructed by considering stream of lines that join the major axis of the polarization ellipses around the singularity. A closed path in the clockwise direction around the origin (C-point singularity), it can be observed that the polarization ellipses rotates anticlockwise for the star case (see distribution in Fig.1.5(a)), while a similar closed path in clockwise direction for the monstar and lemon shows that polarization ellipse rotate clockwise (see the distributions in Fig.1.5(b) and Fig.1.5(c)). Since, they rotate by a half revolution, thus it is deduced that the singularity index (or topological index) is $-1/2$ for star (Fig.1.5(a)) while it is $+1/2$ for monstar (Fig.1.5(b)) and lemon (Fig.1.5(c)). This rotation of polarization ellipse orientation implies that it is discontinuous around a singularity. It is pertinent to mention here that there are three straight lines joining the major axis of the polarization ellipses for a star and monstar patterns, while there is only one straight line for the lemon case. These straight lines are also known as separatrix and are shown by blue lines in Fig. 1.5 [17, 49].

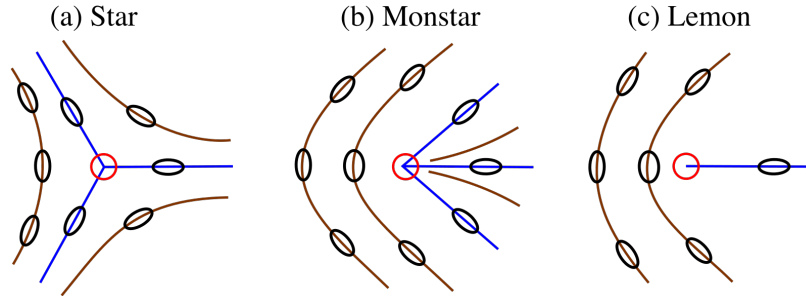


Figure 1.5 – Polarization ellipse field topology around a C-point singularity in a transverse plane with fixed z . (a) star ; index = $-1/2$ (b) monstar ; index = $+1/2$ (c) lemon; index = $+1/2$.

An overlap of these fundamental polarization singularities would result in a higher order polarization singularity [17, 113]. The merging of two stars or two lemons would result in a singularity with topological index of -1 and $+1$ respectively. Lastly, it is important to mention here that polarization singularities resulting from the non-uniform polarization distribution are the ones that have turned out to be extremely useful for fundamental and application oriented purposes. Radially and azimuthally polarized beams are the most common vector beams, which possess a distribution of linear polarization across a cross-section. Their topological index is $+1$. Thus, they can be thought of as a superposition of two fundamental polarization singularities (such as lemon) each with topological index of

$+1/2$. One should be careful in the interpretation as radial and azimuthal vector beams have quite unique distribution of polarizations in their transverse plane. This is quite different as compared with general elliptic polarization distribution around the nodes and centers in fundamental polarization singularities. Vector beams including the radial and azimuthally polarized beams are briefly discussed in the next section.

1.2 Vector beams

Polarization is a beautiful manifestation of light that enables it for a myriad of applications ranging from microscopy, spectroscopy, optical trapping of particles, quantum entanglement, optical communication and many more [16, 114–116]. Besides conventional scalar beams, which have uniform distribution of polarization i.e. linear, circular or elliptic polarization, other unconventional beams also exist. Among these unconventional beams, one peculiar type consists of “vector beams”, which possess a spatially varying or non-uniform polarization. Vector beams have aroused a lot of curiosity in the last few decades as the non-uniform polarization in vector beams gives them a special attribute for utilization in several applications for instance for tight focusing [114, 117], high-resolution imaging [118, 119], high-precision sensing [120], high-quality machining [121] and in many other key applications [9, 115].

The advent of lasers also brought plethora of quite complex spatial modes. The most familiar of all are the Hermite-Gauss and Laguerre-Gauss families of beams, which are wave equation solutions in Cartesian and cylindrical coordinates respectively. These two families of beams are the scalar solutions of the paraxial wave equation, thus all the beams generated are scalar beams i.e. with uniform polarization distribution. It has been demonstrated via π mode converters (a pair of afocal cylindrical lens) that Hermite-Gauss and Laguerre-Gauss beams can be converted into each other as both of them form a complete set of functions, thus they can be easily expressed in terms of each other [122–124]. The earliest vector beams demonstrated, which had non-uniform polarization in their field are constructed from a non-separable superposition of spatial and polarization modes. The super-imposing of two spatial modes (from either Hermite-Gauss or Laguerre-Gauss families of beams) with orthogonal polarization results into a vector beam [115]. One can write a general expression representing the super-position of two Laguerre-Gaussian beams as follows:

$$U_{\theta,\chi}(p_1, l_1, p_2, l_2) = (LG_{p_1}^{l_1} e^{i\theta} \hat{e}_R \cos \chi + LG_{p_2}^{l_2} e^{-i\theta} \hat{e}_L \sin \chi), \quad (1.13)$$

here \hat{e}_R and \hat{e}_L denote the right and left circular polarization states. These can be expressed in terms of linear polarization states along x and y axis (\hat{e}_x and \hat{e}_y respectively) as below:

$$\hat{e}_R = \frac{1}{\sqrt{2}}(\hat{e}_x - i\hat{e}_y), \quad (1.14)$$

$$\hat{e}_L = \frac{1}{\sqrt{2}}(\hat{e}_x + i\hat{e}_y). \quad (1.15)$$

For the discussion below, superposition of LG modes with equal amplitudes is considered thus $\chi = \pi/4$. In order to generate first order vector beams such as radial and azimuthal vector beams, one needs to keep $p_1 = p_2 = 0$. A radial vector mode is obtained by keeping

$\theta = 0, \chi = \pi/4$ and $p_1 = 0, l_1 = 1, p_2 = 0, l_2 = -1$. It is shown in Fig. 1.6(a1)-(a3). The radial vector beam has an intensity distribution of a single ring with polarization vectors pointing radially outwards with the azimuthal angle (see Fig. 1.6(a3)). The relative phase difference $\Delta\phi = \phi_y - \phi_x$ i.e the phase difference between the y - and x -components is also shown for this radial vector mode in Fig. 1.6(a2). It can be observed that $\Delta\phi$ only takes values of 0° (gray colour) or 180° (black colour) indicating the presence of only linear polarization. The linear polarization direction relative to the x -axis is defined by an angle θ , which is given as the ratio of the y - and x -components of the field via the relation $\theta = \arctan[(|U_y|/|U_x|) \exp^{i(\phi_y - \phi_x)}]$. The value of angle θ giving the direction of linear polarization matches with the azimuthal angle for the radial vector beam (see Fig. 1.6(a3)). This was the first vector beam that attracted interest among the research community due to its ability of producing a tighter waist [125–127], which could be utilized for optical tweezing. The other aspect was that upon focusing a longitudinal component of the electric field appears, which could be utilized for acceleration of electrons or other charged particles [128]. Azimuthal vector beams with polarization vectors such that they are always tangential to the ring of the mode are obtained by having $\theta = \pi/2, \chi = \pi/4$ and $p_1 = 0, l_1 = 1, p_2 = 0, l_2 = -1$ (see Fig. 1.6(b1)-(b3)). Again it can be observed that $\Delta\phi$ only takes values of 0° (gray colour) or 180° (black colour) indicating the presence of only linear polarization (see Fig. 1.6(b2)). Also, the value of angle θ giving linear polarization direction differs by 90° with the azimuthal angle in a way that each point on the ring has tangential direction of the linear polarization. Radial and azimuthal vector beams are categorized within the cylindrically symmetric vector beams as the polarization distribution in them follows such a symmetry [114, 115]. Radial and azimuthal vector beams are the most

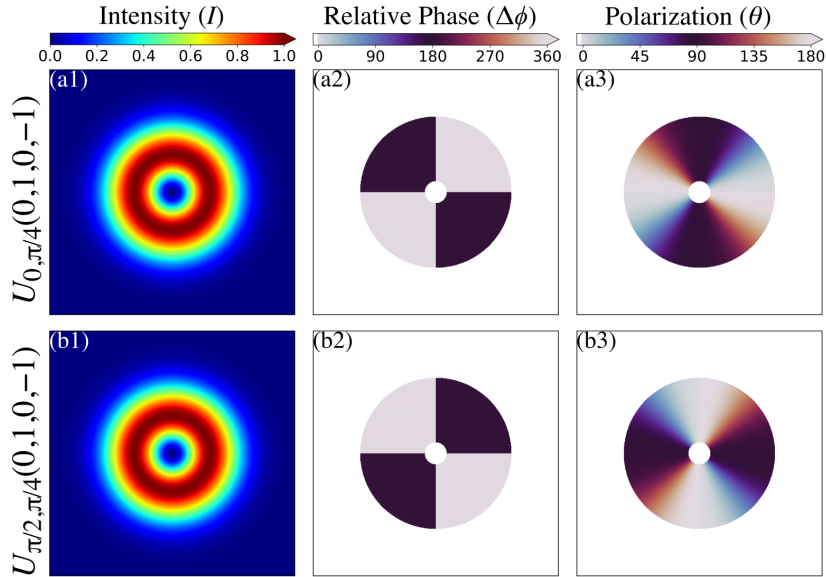


Figure 1.6 – Generation of first order vector beams by superposition of two zero order Laguerre-Gaussian beam according to Eq. (1.13). First row: [(a1)-(a3)] corresponds to the radial polarization mode while second row: [(b2)-(b3)] corresponds to the azimuthal polarization mode. Intensity, relative phase and linear polarization distribution are shown in the first, second and third column respectively.

common and ubiquitously deployed beams. However, one can generate more exotic vector

beams by using higher order spatial modes. Such higher order vector modes constructed from a super-position of two Laguerre-Gaussian modes with polarization states are shown in the Fig. 1.7. By considering $p \neq 0$, as expected one gets a series of $p+1$ concentric rings of alternating opposite absolute phases. The case in Fig. 1.7(a1)-(a3) is a higher order analogue of radial vector beams and similarly the case in Fig. 1.7(b1)-(b3) represents a higher order analogue of azimuthal vector beams. As can be observed that the polarization distribution is the same on both the rings of these higher order modes. The case in Fig. 1.7(c1)-(c3) considers $l_1 = 2, l_2 = -2$ and since phase advances l times in comparison with circular polarization states, the polarization distribution is no longer radial anymore on both rings. Finally, the case in Fig. 1.7(d1)-(d3) considers a fundamental LG mode ($p_1 = 0, l_1 = 0$) superposed with an LG mode having $p_2 = 0, l_2 = 2$. This superposition results in a vector beam where the polarization state varies along the radial coordinate (see Fig. 1.7(d2)-(d3)). There is a certain position along the radial distance, below which fundamental mode has higher amplitude and above which the other has higher amplitude. At exactly this radial distance one gets a linear polarization (black and white colour in Fig. 1.7(d2)), thus if one move inward from this radial position the polarization state become elliptical but this ellipticity increases such that at the center there is left circular polarization state (brown colour in Fig. 1.7(d2)). Similarly, if one moves outwards from that radial position the polarization state changes to elliptical and the ellipticity increases towards circular until the polarization state becomes right circular polarization at $r = \infty$ (blue colour with $\Delta\phi = 90^\circ$ in Fig. 1.7(d2)). Hence this beam contains all the states of polarization and it is termed as “full-Poincaré beam” [129, 130].

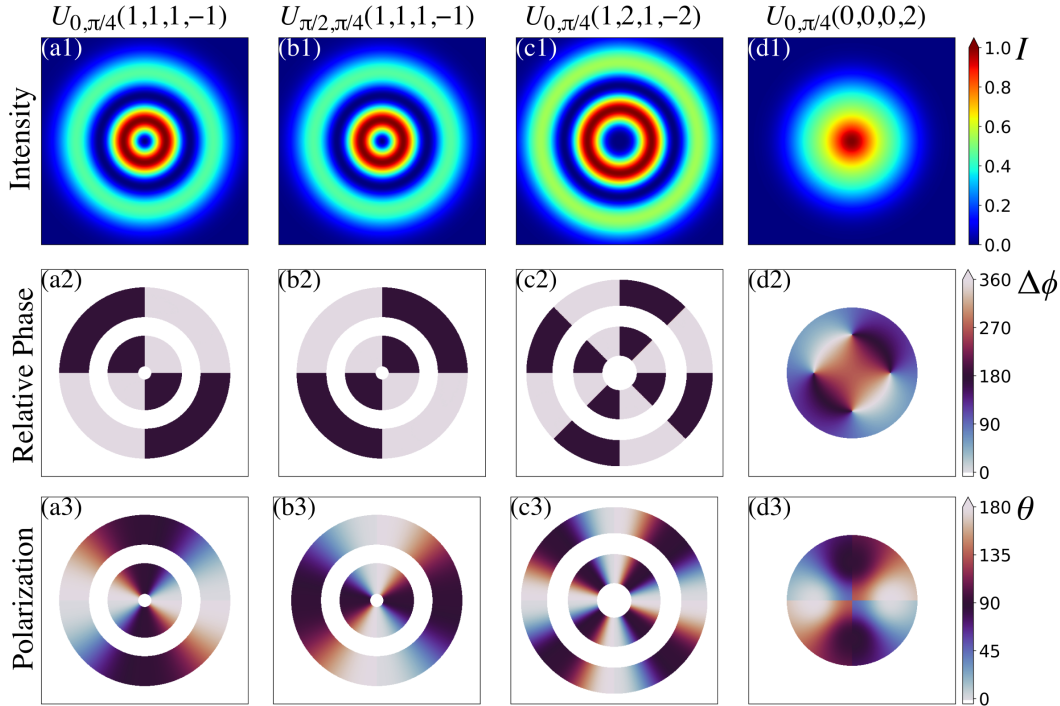


Figure 1.7 – Superposition of Laguerre-Gaussian modes and circular polarization states by keeping relative amplitude χ and phase 2θ respectively. Intensity (first row), relative phase (second row) and polarization distribution (third row) are shown with values of the various parameters mentioned on top of each column.

Numerous experimental methods exist to generate vector beams including but not limited to free-space and optical fiber propagation, inside a laser cavity via utilizing intra-cavity elements, by displaying computer generated holograms on SLMs, naturally via birefringent crystals and plenty of others [6, 9]. Many detailed reviews and textbooks on the generation techniques of vector beams have been written and the interested reader is referred to them [6, 9, 17, 105, 114, 115, 131]. The most common methods in free space include a Mach-Zehnder interferometer, where in both arms an optical element (such as dove prisms or spiral phase plates) is utilized to encode the spatial modes which are then superimposed on the output of the interferometer. There also exist some direct methods for conversion into radially or azimuthally polarized beams. Such direct configurations employ a waveplate divided into four sectors, with each sector converting the linearly polarized input beam into a corresponding radially outward polarization state. In this configuration, commercially available liquid crystal retarders are available as well, which provide a customized rotation of the polarization. Finally, the advent of spatial light modulators (SLMs), which possess the ability to modify the amplitude, phase and polarization of the beams, have opened a whole new dimension to generate all sorts of complex vectorial optical fields. An SLM is based on a translucent or reflective liquid crystal display and their versatility comes from the fact that both spatial modes can be encoded. Thus the required vector modes are adequately collected after diffraction or reflection from the SLM display. The limitation of SLM comes from a fact that the diffraction or reflection efficiencies are dependent on the orientation of the polarization [105, 114]. It is pertinent to mention here that interferometric techniques require a precise phase control. For instance the two situations in Fig. 1.6 and the first two columns of Fig. 1.7 differ only by a $\pi/2$ relative phase shift between the LG beams.

Finally, the vector beams can be generated via the birefringent crystals, which are at the heart of my thesis. It has been shown via two methods [132], that internal conical diffraction (CD) beam can be used to generate a radially polarized beam by passing the CD beam in a certain configuration of an interferometer. Biaxial crystals (BCs) have high optical quality thus the radially polarized beams generated by this method have high fidelity. It has also been demonstrated that uniaxial crystals can also be utilized for spatial engineering of beam shapes and polarization in a mono and polychromatic light beams [133].

The simplest method of detection and identification of vector beams involves the projection of polarization states via an analyser (linear polarizer). The transmitted beam mode possess intensity nodes and the rotation of these intensity nodes with the rotation of analyser can give an idea of the distribution of the polarization inside the mode and hence the mode is easily identified. The polarization of higher order complex modes can be determined via a spatial light modulator. Poincaré sphere is used to represent all the possible polarization states of light beams. In addition to that a higher order Poincaré sphere can be constructed as discussed in [134], to represent higher order states of polarization of vector vortex beams, including the above discussed radially and azimuthally polarized vector beams as well as other exotic vector beams.

1.3 Perspectives for applications of structured light

Recently, a lot of attention is given to the fundamental investigation on structured light as its true potential has been demonstrated in applications as diverse as quantum information processing, metrology, communication, optical trapping, super-resolution imaging, material processing and several others [1, 135, 136]. These application prospects have only come up with the ability to tailor or structure light beyond the two-dimensional transverse fields to four-dimensional structured light or even from the linear regime to include also the nonlinear light matter interactions of structured light [2]. The explosion in research in this field of structured light is partly owned by invention of devices such as liquid crystal spatial light modulators (SLM), digital micro-mirror devices and other elements like geometric phase plates etc. However, the research for generating structured light from conventional approaches have also thrilled to an extent that beams with desired intensity, phase and polarization distributions are generated readily in laboratories for fundamental or applied purposes.

Structured light has already demonstrated a profound impact across various disciplines, as evidenced by the 2014 Nobel Prize in Chemistry [137]. Therefore, when considering the future prospects of structured light, it is evident that there is considerable progress yet to unfold in this captivating field. This progress may manifest in fundamental aspects such as singularities in light fields, interactions between phase or polarization structured light and matter, the application of structured fields for micro-level optical trapping or optical tweezers, holographic shaping of light enabling the generation of intricate light fields applicable from classical to quantum physics, polarization-tailored light leading to strong electric field confinement and intriguing phenomena at the nano-scale, imaging or microscopy employing structured light for broader spectral coverage and enhanced time resolution compared to single-pixel detectors, advancements in metrology facilitating efficient measurements in fluid dynamics, remote sensing, optical activity of chiral molecules, and thin film measurements, the development of atomtronics devices aiming to establish analogous systems of electronic devices in superfluid systems, and the realm of quantum information processing where structured light holds the potential for quantum computations in higher dimensions. Additionally, structured light is poised to contribute to classical optical communication systems by leveraging its unique characteristics. The discussion is limited here for brevity but the new avenues of research for fundamental and application oriented prospects of structured light has just started [1, 3, 104].

OPTICALLY ANISOTROPIC MATERIALS

An optically anisotropic material is a medium whose optical properties are a function of the polarization of light and eventually of the propagation direction. In most cases such materials are crystalline in nature and the branch of optics dealing with them is called “**Crystal Optics**”. Indeed crystals can exhibit interesting optical phenomena upon propagation of electromagnetic waves through them, such as double refraction, conical diffraction (CD), optical activity and so on. The Danish scientist E. Bartholin observed the phenomena of double refraction in 1669 in a crystal of Iceland spar (Calcite), this is considered as the start of the field of crystal optics. There also exists crystals, which are anisotropic as well as nonlinear in their response to the effect of applying electric field, magnetic field, mechanical stress or sound waves, thus giving rise to a whole sub-field of investigations namely electro-optics, magneto-optics, acousto-optics, nonlinear optics, photorefractivity, etc. This rich potential of linear and nonlinear anisotropic crystals has been thoroughly investigated and implemented in the last century for making novel optical devices. This thesis is concerned with one of the peculiar phenomena that happens in anisotropic biaxial crystal. Thus in this chapter I give first a brief introduction to crystal optics, followed by the discussion on the propagation of electromagnetic waves through anisotropic crystals and briefly explain some curious optical effects in anisotropic crystals. I also introduce briefly nonlinear photorefractive effect which is most often encountered in non-centrosymmetric crystals possessing also an optical anisotropy. This is in view of the treatment of the photorefractive holographic recording of CD waves that will be presented in chapter 6.

2.1 Preliminaries of electrodynamics

The Maxwell's equation in their differential form can be written as [138, 139]

$$\nabla \cdot \mathbf{D} = \rho, \quad (2.1)$$

$$\nabla \cdot \mathbf{B} = 0, \quad (2.2)$$

$$\nabla \times \mathbf{E} = -\frac{\partial \mathbf{B}}{\partial t}, \quad (2.3)$$

$$\nabla \times \mathbf{H} = \mathbf{J} + \frac{\partial \mathbf{D}}{\partial t}. \quad (2.4)$$

In these equations, \mathbf{E} and \mathbf{H} represent the electric field vector and magnetic field vector of the wave respectively. The effect of this field on the material requires the introduction of \mathbf{D} and \mathbf{B} , which represent the electric displacement and magnetic induction, respectively. \mathbf{J} and ρ represents the electric current density and electric charge density respectively. The propagation of electromagnetic waves can be fully described with the above four Maxwell's equations. Besides these coupled differential equations, to describe the effect of the field on the material media, there are constitutive equations expressed as

$$\mathbf{D} = \epsilon_0 \mathbf{E} + \mathbf{P} = \epsilon_0 \overleftrightarrow{\epsilon} \cdot \mathbf{E}, \quad (2.5)$$

$$\mathbf{B} = \mu_0 \mathbf{H} + \mu_0 \mathbf{M} = \mu_0 \overleftrightarrow{\mu} \cdot \mathbf{H}, \quad (2.6)$$

$$\mathbf{J} = \overleftrightarrow{\sigma} \cdot \mathbf{E}. \quad (2.7)$$

Again here $\overleftrightarrow{\epsilon}$ and $\overleftrightarrow{\mu}$ are second rank tensors, known as dielectric tensor (or permittivity tensor) and permeability tensor, respectively. While σ represents the conductivity of the medium. \mathbf{P} and \mathbf{M} represent the electric polarization and the magnetization respectively. ϵ_0 and μ_0 represent the permittivity and permeability of the vacuum respectively. By assuming charge free or current free medium (perfect dielectric) leads to $\rho = 0$ and also consideration of non-magnetic medium would imply that $\mu = 1$. In an isotropic medium, $\overleftrightarrow{\epsilon}$ and $\overleftrightarrow{\mu}$ reduce to scalars. Also in most of the cases $\overleftrightarrow{\epsilon}$ and $\overleftrightarrow{\mu}$ are independent of the field strengths but under the presence of strong field strengths their dependence on the field becomes significant. In such cases the induced polarization is written as below,

$$\mathbf{P}(\omega) = \epsilon_0 \overleftrightarrow{\chi}_e^{(1)}(\omega) \cdot \mathbf{E}(\omega) + \epsilon_0 \overleftrightarrow{\chi}_e^{(2)}(\omega) \cdot \mathbf{E}^2(\omega) + \epsilon_0 \overleftrightarrow{\chi}_e^{(3)}(\omega) \cdot \mathbf{E}^3(\omega) + \dots, \quad (2.8)$$

where $\overleftrightarrow{\chi}_e^{(n)}$ are in general tensors of the $n + 1$ rank. The above equation implies that the induced polarization in a material is not proportional to the electric field but it is rather expressed in Taylor series expansion. The first term on the right correspond to the linear response while the rest of the terms correspond to the nonlinear response of the material in response to the electric field. The tensors $\overleftrightarrow{\chi}_e^{(n)}$ in Eq. (2.8) are the n^{th} order optical susceptibilities of the medium. Thus there exists a classification of nonlinear materials based on their relation with higher powers of $\overleftrightarrow{\chi}_e^{(n)}$. The nonlinear response leads to interesting optical effects such as crystals exhibiting a $\overleftrightarrow{\chi}_e^{(2)}$ nonlinearity are utilized for parametric nonlinear frequency conversion and those exhibiting a $\overleftrightarrow{\chi}_e^{(3)}$ nonlinearity are exploited for instance for their optical Kerr effect. Similarly, there are plenty of other optical effects¹

¹For a more profound discussion on nonlinear optical effects, the reader is referred to the textbooks in Refs. [140, 141]

regarding the refractive index changes in the crystal with the intensity of the incident light, such as photorefractive effect [142] and many others. The photorefractive effect is discussed briefly in the last section of this chapter.

2.2 Dielectric tensor of an anisotropic medium

In an isotropic linear medium, the macroscopic relation between induced polarization and the applied electric field involves a scalar quantity i.e. $\mathbf{P} = \epsilon_0 \chi \mathbf{E}$. Here χ is the scalar electric susceptibility and independent of the applied field direction. In contrast for an anisotropic medium, the induced polarization depends on the polarization of the applied electromagnetic wave and the above relation is generalized to

$$\begin{aligned} P_x &= \epsilon_0(\chi_{11}E_x + \chi_{12}E_y + \chi_{13}E_z), \\ P_y &= \epsilon_0(\chi_{21}E_x + \chi_{22}E_y + \chi_{23}E_z), \\ P_z &= \epsilon_0(\chi_{31}E_x + \chi_{32}E_y + \chi_{33}E_z), \end{aligned} \quad (2.9)$$

with $\overleftrightarrow{\chi}$ being a second rank tensor. One can also write the constitutive relation between the electric displacement vector \mathbf{D} and electric field \mathbf{E} guided by the dielectric response of the crystal as below

$$\begin{aligned} D_x &= \epsilon_0(\epsilon_{11}E_x + \epsilon_{12}E_y + \epsilon_{13}E_z) \\ D_y &= \epsilon_0(\epsilon_{21}E_x + \epsilon_{22}E_y + \epsilon_{23}E_z) \\ D_z &= \epsilon_0(\epsilon_{31}E_x + \epsilon_{32}E_y + \epsilon_{33}E_z) \end{aligned} \quad (2.10)$$

since $\mathbf{D} = \epsilon_0 \mathbf{E} + \mathbf{P}$, it follows from Eqs. (2.9) and (2.10) that

$$\epsilon_{ij} = (\delta_{ij} + \chi_{ij}). \quad (2.11)$$

Thus the dielectric response of the material is also expressed by the second rank dielectric tensor $\overleftrightarrow{\epsilon}$ and the values of its coefficients are properties of the medium. The nine (3x3) elements of this second rank tensor depends on the choice of coordinates - x,y & z. In lossless and non optically active materials the dielectric tensor is real and symmetric ($\epsilon_{ij} = \epsilon_{ji}$) and one can always choose a coordinate system aligned such that the off-diagonal elements vanish. Thus Eq. (2.10) becomes in this case

$$\begin{pmatrix} D_x \\ D_y \\ D_z \end{pmatrix} = \epsilon_0 \begin{bmatrix} \epsilon_{11} & 0 & 0 \\ 0 & \epsilon_{22} & 0 \\ 0 & 0 & \epsilon_{33} \end{bmatrix} \begin{pmatrix} E_x \\ E_y \\ E_z \end{pmatrix}. \quad (2.12)$$

The axes directions in such a coordinate system correspond to the principal dielectric axes of the crystal. In tensor notation Eq. (2.10) can be written as

$$D_i = \epsilon_0 \epsilon_{ij} E_j, \quad (2.13)$$

where the Einstein summation rule over equal indices is followed².

²Note that for all lossless media (eventually possessing optical activity), the dielectric tensor is hermitian ($\epsilon_{ij} = \epsilon_{ji}^*$) as a result of conservation of electromagnetic energy. Eventual losses are thus connected to the non-hermitian components of the tensor [143].

For a medium which is non-absorbing and non-optically active, the $\overleftrightarrow{\epsilon}$ tensor is real and symmetric, which also allows the diagonalization as in Eq. (2.12). Even in the case of lossless medium, where the complex dielectric tensor is considered as opposed to a real, it turn out that the dielectric tensor is hermitian i.e. $\epsilon_{ij} = \epsilon_{ij}^*$. In principle, it is the conservation of electromagnetic energy that demands the dielectric tensor to be hermitian [143].

2.3 Plane-wave propagation in anisotropic medium

For an anisotropic crystal, in general there exists two eigenwaves for a particular direction of propagation. Each of the two eigenwaves possess well defined phase velocity and polarization direction. A propagating wave corresponding to an eigenwave polarization will retain its polarization as it propagates through the crystal. The expressions for these eigen-polarizations and eigen-phase velocities are briefly discussed below. Let's consider first the electric and magnetic fields for a monochromatic plane wave of angular frequency ω

$$\mathbf{E} = \mathbf{E}_0 e^{i(\mathbf{k} \cdot \mathbf{r} - \omega t)}, \quad (2.14)$$

$$\mathbf{H} = \mathbf{H}_0 e^{i(\mathbf{k} \cdot \mathbf{r} - \omega t)} \quad (2.15)$$

where $\mathbf{k} = (n\omega/c)\hat{k}$ is the wave-vector, with \hat{k} representing a unit vector in the propagation direction. n represents the refractive indices to be determined. Substituting the above \mathbf{E} and \mathbf{H} into the Maxwell's equations (2.3) and (2.4), and applying the constitutive relations (2.5) and (2.6) results in the following relationships,

$$\mathbf{k} \times \mathbf{E} = -\omega\mu_0\mu\mathbf{H}, \quad \mathbf{k} \times \mathbf{H} = \omega\epsilon_0\overleftrightarrow{\epsilon} \cdot \mathbf{E}.$$

By utilizing relations, $c^2 = \frac{1}{\mu_0\epsilon_0}$ and $n_i^2 = \mu\epsilon_i$ (with $i = x, y, z$) and then substituting the value of \mathbf{H} from the first equation into the second equation results into a wave equation for the \mathbf{E} -field,

$$\mathbf{k} \times (\mathbf{k} \times \mathbf{E}) + \frac{\omega^2}{c^2}n_i^2\mathbf{E} = 0. \quad (2.16)$$

By expanding the first term in (2.16) with a vector triple product identity, it follows

$$(\mathbf{k} \cdot \mathbf{E})\mathbf{k} - (\mathbf{k} \cdot \mathbf{k})\mathbf{E} + \frac{\omega^2}{c^2}n_i^2\mathbf{E} = 0, \quad (2.17)$$

that is

$$\begin{aligned} & (k_x E_x + k_y E_y + k_z E_z)(k_x \hat{x} + k_y \hat{y} + k_z \hat{z}) \\ & - (k_x^2 + k_y^2 + k_z^2)(E_x \hat{x} + E_y \hat{y} + E_z \hat{z}) \\ & + \frac{\omega^2}{c^2}n_i^2(E_x \hat{x} + E_y \hat{y} + E_z \hat{z}) = 0. \end{aligned} \quad (2.18)$$

As each x, y and z component of Eq. (2.18) must be individually equal to zero, this leads to a system of three homogeneous equations. By defining effective refractive index as $n = kc/\omega$, one can re-write the three homogenous equations in matrix notation as below,

$$\begin{bmatrix} n_x^2 - n^2(\hat{k}_y^2 + \hat{k}_z^2) & n^2\hat{k}_x\hat{k}_y & n^2\hat{k}_x\hat{k}_z \\ n^2\hat{k}_y\hat{k}_x & n_y^2 - n^2(\hat{k}_x^2 + \hat{k}_z^2) & n^2\hat{k}_y\hat{k}_z \\ n^2\hat{k}_z\hat{k}_x & n^2\hat{k}_z\hat{k}_y & n_z^2 - n^2(\hat{k}_x^2 + \hat{k}_y^2) \end{bmatrix} \begin{bmatrix} E_x \\ E_y \\ E_z \end{bmatrix} = 0. \quad (2.19)$$

A nontrivial solution (other than $k = \omega = 0$ or other than $\mathbf{E} = 0$) requires that the determinant of the above matrix system should vanish,

$$\det \begin{bmatrix} n_x^2 - n^2(\hat{k}_y^2 + \hat{k}_z^2) & n^2 \hat{k}_x \hat{k}_y & n^2 \hat{k}_x \hat{k}_z \\ n^2 \hat{k}_y \hat{k}_x & n_y^2 - n^2(\hat{k}_x^2 + \hat{k}_z^2) & n^2 \hat{k}_y \hat{k}_z \\ n^2 \hat{k}_z \hat{k}_x & n^2 \hat{k}_z \hat{k}_y & n_z^2 - n^2(\hat{k}_x^2 + \hat{k}_y^2) \end{bmatrix} = 0,$$

which simplifies to the below expression,

$$(n_x^2 - n^2)(n_y^2 - n^2)(n_z^2 - n^2) + n^2[k_x^2(n_y^2 - n^2)(n_z^2 - n^2) + k_y^2(n_x^2 - n^2)(n_z^2 - n^2) + k_z^2(n_x^2 - n^2)(n_y^2 - n^2)] = 0 \quad (2.20)$$

The terms in the 6th power of n in the above equation vanish because $\hat{k}_x^2 + \hat{k}_y^2 + \hat{k}_z^2 = 1$. Equation (2.20) is thus a quadratic equation in n^2 , which explicitly implies that there are two eigen modes for a given propagation direction $\hat{\mathbf{k}}$. Also, this leads to an implicit relation between ω and \mathbf{k} , which represents a three dimensional surface known as “wave normal surface” (or wave surface). This wave normal surface in \mathbf{k} space (momentum space) is shown in the Fig. 2.1. It consists of two sheets of surface or in other words has two shells, which in general can intersect each other at four points. These can be separated into two pairs, with the points of a pair being on opposite sides of the surface. The two lines that pass through the origin and join the two points on opposite side of the surfaces are called the optic axes. A wave with a certain propagation direction would result into two k

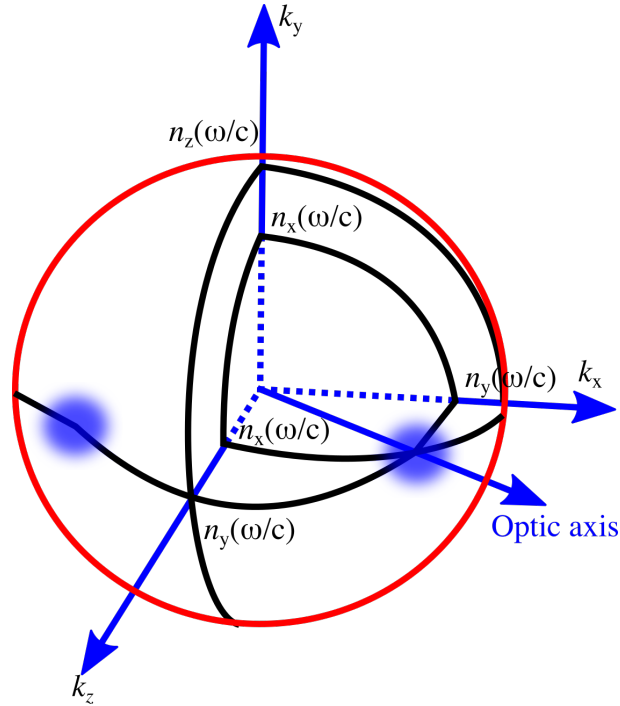


Figure 2.1 – Wave normal surface of a biaxial crystal.

values, which correspond to the intersection points of the propagation direction with the two sheets of the normal surface. Hence, in general for a wave incident on an anisotropic medium along a certain propagation direction, it would result into two waves propagating

with two different phase velocities corresponding to mutually orthogonal polarizations. By considering $n \neq n_i$, one can rewrite Eq. (2.20) in a more familiar form given as,

$$\frac{\hat{k}_x^2}{n^2 - n_x^2} + \frac{\hat{k}_y^2}{n^2 - n_y^2} + \frac{\hat{k}_z^2}{n^2 - n_z^2} = \frac{1}{n^2}, \quad (2.21)$$

or the equivalent homogeneous form [21]

$$\frac{\hat{k}_x^2}{\frac{1}{n^2} - \frac{1}{n_x^2}} + \frac{\hat{k}_y^2}{\frac{1}{n^2} - \frac{1}{n_y^2}} + \frac{\hat{k}_z^2}{\frac{1}{n^2} - \frac{1}{n_z^2}} = 0. \quad (2.22)$$

In the above equations, $\hat{k}_i = \frac{k_i}{|k|}$ and also $\hat{k}_x^2 + \hat{k}_y^2 + \hat{k}_z^2 = 1$. Equation (2.21) and (2.22) are known as Fresnel's equation of wave normals and can be solved for the values of the eigen-phase velocities of the two waves. If \mathbf{E}_1 and \mathbf{E}_2 correspond to the electric field vectors and \mathbf{D}_1 and \mathbf{D}_2 correspond to the electric displacement vectors of the n_1^2 and n_2^2 eigen-waves respectively, then it can be shown from Maxwell equations that $\mathbf{D}_1, \mathbf{D}_2, \hat{k}$ form an orthogonal triad. Maxwell equations also imply the following two relations

$$\mathbf{D} = -\frac{n}{c} \hat{k} \times \mathbf{H} \quad (2.23)$$

$$\mathbf{H} = \frac{n}{\mu c} \hat{k} \times \mathbf{E} \quad (2.24)$$

thus \mathbf{H} is perpendicular to \mathbf{D} , \mathbf{E} , and propagation direction \hat{k} . Which implicitly implies that \mathbf{D} , \mathbf{E} and \hat{k} are co-planar. In addition also the direction of energy flow (Poynting vector $\mathbf{S} = \mathbf{E} \times \mathbf{H}$) in anisotropic medium is non-collinear with propagation direction \hat{k} . The relative orientation of field vectors, wave vector and Poynting vector for an anisotropic medium is shown in the Fig. 2.2. The walk-off angle ρ can be zero for some special prop-

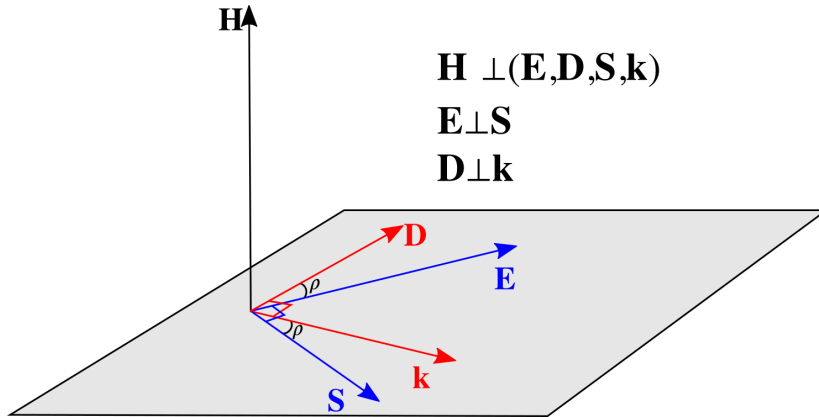


Figure 2.2 – General orientation of vectors in an optically anisotropic medium. The propagation vector \mathbf{k} is co-planar with electric displacement vector (\mathbf{D}), electric field vector (\mathbf{E}) and Poynting vector (\mathbf{S}). Also, $\mathbf{D} \perp \mathbf{k}$ and $\mathbf{E} \perp \mathbf{S}$. ρ denotes the walk off angle between \mathbf{k} and \mathbf{S} as well as between \mathbf{E} and \mathbf{D} .

agation directions in the anisotropic medium. It is also important to mention here that propagation along the principal planes and optic axis results into different scenarios. For

instance, propagation along the optic axis in a biaxial crystal would result into a singular case i.e there is just one phase velocity corresponding to a single value of k . As the normal surfaces are degenerate with conical region surrounding this direction, a beam propagating along this direction would spread out conically. Up to now, we have only established that each direction \hat{k} is associated to two phase velocities (and two values of the refractive index), each corresponding to one of the two surfaces being the solution of Eq. (2.21) and (2.22). Next we discuss the corresponding polarization directions (directions of vector \mathbf{D}) with the help of the geometrical method (optical indicatrix) as introduced in the next section.

2.4 Optical indicatrix

Optical indicatrix (also known as index ellipsoid) is a geometrical construction for determining the direction of vibrations as well as phase velocities and eventually indirectly ray velocities. The components of \mathbf{D} at a particular energy density obey the relation

$$\frac{D_x^2}{\epsilon_x} + \frac{D_y^2}{\epsilon_y} + \frac{D_z^2}{\epsilon_z} = C, \quad (2.25)$$

where $C = 2\epsilon_0 U_e = \epsilon_0 \mathbf{E} \cdot \mathbf{D} = \epsilon_0 E_i \epsilon_{ij} E_j$. Here U_e represents the electric energy density for an anisotropic medium, which is assumed to be homogeneous, non-absorbing and magnetically isotropic. By replacing $\frac{D_x}{\sqrt{C}}, \frac{D_y}{\sqrt{C}}$ and $\frac{D_z}{\sqrt{C}}$ by x, y and z respectively, the above equation becomes an equation of an ellipsoid

$$\frac{x^2}{\epsilon_x} + \frac{y^2}{\epsilon_y} + \frac{z^2}{\epsilon_z} = 1. \quad (2.26)$$

It can be observed that the semiaxes of this ellipsoid are square roots of the principal dielectric constants and are parallel with the principal dielectric axes directions. For any wave-normal direction in a crystal, the optical indicatrix can be used to determine the two vibration directions of \mathbf{D} as well as two indices of refraction corresponding to the two propagating plane waves. This is done by performing the following steps: Finding the plane that is perpendicular to the wave-normal direction \hat{k} . The ellipse that is formed by the intersection curve of the plane with the ellipsoid surface, has principal semiaxes equal in length to the two indices of refraction (n_1 and n_2 values) and the direction of these semiaxes correspond to the two vibration directions ($\mathbf{D}_{1,2}$ directions). For the two eigenwaves, these values of n_1 and n_2 also correspond to the solutions of the Fresnel equation of wave normals for the same \hat{k} direction (Eq. (2.21)). The elliptical curve formed by the intersection of that plane with the ellipsoid is shown in the Fig. 2.3. A rigorous verification of this method can be found in various textbooks as for instance in Born & Wolf [21]. In summary, for a wave propagating in an arbitrary direction \hat{k} , there exist two linearly plane polarized propagating waves with phase velocities $\pm c/n_1$ and $\pm c/n_2$ with n_1 and n_2 being solutions of the Fresnel equation of wave normals. The surface $\omega(\hat{k}) = \text{constant}$ also gives valuable information of phase and group velocities, v_p and v_g , respectively. Both of them can be

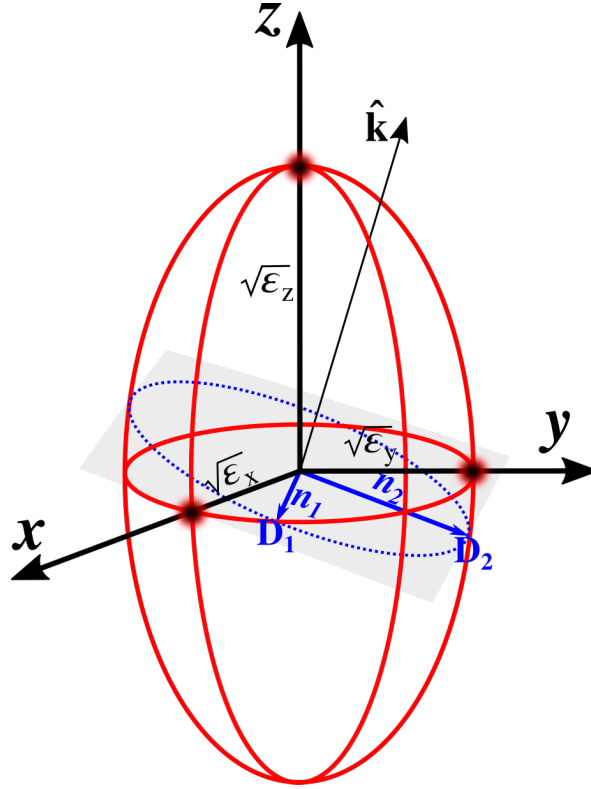


Figure 2.3 – Optical indicatrix and geometrical construction for determining the vibration directions D_1 and D_2 as well as the n_1 and n_2 for the two eigenwaves associated to the propagation direction \hat{k} .

defined as below,

$$v_p = \frac{\omega}{k} \hat{k} \quad (2.27)$$

$$v_g = \nabla_k \omega(k) \quad (2.28)$$

Also, the energy flow is propagated at

$$v_e = \frac{\mathbf{S}}{U_e} \quad (2.29)$$

Here \mathbf{S} and U_e represent the Poynting vector and the electromagnetic energy density, respectively. The above definition of group velocity states that it corresponds to a vector perpendicular to the normal surface. It can be shown that $v_g = v_e$ for a wave-packet in an anisotropic medium and thus it also represents the energy transport in an anisotropic medium [143].

2.5 Classification of anisotropic crystals

In terms of their optical properties all crystalline materials can be classified into three categories i.e. isotropic, uniaxial and biaxial crystals. The wave normal surface is based on

Table 2.1 – A Table showing the relation of optical symmetry with crystal systems and the corresponding diagonal dielectric tensor in the coordinate system of the principle dielectric axes [143].

Optical Symmetry	Crystal System	Point Groups	Dielectric Tensor
Isotropic	Cubic	$\bar{4}3m$ 432 m3 23 m3m	$\epsilon = \begin{bmatrix} n^2 & 0 & 0 \\ 0 & n^2 & 0 \\ 0 & 0 & n^2 \end{bmatrix}$
Uniaxial	Tetragonal	4 $\bar{4}$ 4/m 422 4mm $\bar{4}2m$ 4/mmm	$\epsilon = \begin{bmatrix} n_o^2 & 0 & 0 \\ 0 & n_o^2 & 0 \\ 0 & 0 & n_e^2 \end{bmatrix}$
	Hexagonal	$\bar{6}$ $\bar{6}$ 6/m 622 6mm $\bar{6}m2$ 6/mmm	
	Trigonal	3 $\bar{3}$ 32 3m $\bar{3}m$	
Biaxial	Triclinic	1 $\bar{1}$	$\epsilon = \begin{bmatrix} n_x^2 & 0 & 0 \\ 0 & n_y^2 & 0 \\ 0 & 0 & n_z^2 \end{bmatrix}$
	Monoclinic	2 m 2/m	
	Orthorhombic	222 2mm mmm	

the values of the principal refractive indices. In the case, where all the three principal refractive indices have different values i.e. $n_x \neq n_y \neq n_z$, such a material is called biaxial crystal. The optical indicatrix for a biaxial crystal is an ellipsoid (triaxial) and there exists two planes at the center of the ellipsoid for which the intersection curve of the plane and the ellipsoid results into a circle. The directions corresponding to these planes represent the two singular directions (optic axes) i.e. for any wave propagating in this direction possess same phase velocity for all the polarizations. As discussed earlier, the two sheets of the wave normal surface for a biaxial crystal intersect at four points and two straight lines passing through the center and joining two intersection points located diagonally opposite to each other correspond to the optic axis direction. Fig 2.4(a) shows the cross-section of the wave-normal surface in xz -plane for a biaxial crystal system with the assumption that $n_x < n_y < n_z$.

A biaxial crystal can be either monoclinic, orthorhombic or triclinic. In contrast if two of the principal refractive indices are equal for instance i.e. $n_x = n_y = n_o$ and $n_z = n_e$ ³, it is a uniaxial crystal. In uniaxial crystals, the two refractive indices are termed as ordinary and extraordinary (hence the subscript in n_o and n_e). The optical indicatrix for a uniaxial crystal is an ellipsoid of revolution and the two optic axis merge. The two sheets of wave

³Note that it is not always n_z which is n_e , even if most often so.

normal surface in a uniaxial crystal intersect each other at only two point. For a crystal with n_z as the unique refractive index, these two points will be along the z -axis. Thus the z -axis is the only optic axis for such uniaxial crystals. Fig 2.4 (b)-(c) shows the cross-section of the wave-normal surface in xz -plane for a positive uniaxial and negative uniaxial crystal systems. A uniaxial crystal belongs to either trigonal, tetragonal or hexagonal system. Also, if $n_e > n_o$ the crystal is said to be positive uniaxial otherwise negative uniaxial (for $n_e < n_o$). Finally, if all the principal refractive indices in a crystal are equal i.e. $n_x = n_y = n_z$, the material is optically isotropic. All the diametrical sections of the index ellipsoid are circular and the wave normal surfaces degenerates to a sphere. Crystals belonging to the cubic system show this property. It is apparent from the above discussion that the point group symmetry of a crystal holds the information of its optical symmetry. For instance a crystal belonging to a cubic system possess three physically equivalent axis and thus it is optically isotropic. Table 2.1 relates the optical symmetry with crystal systems.

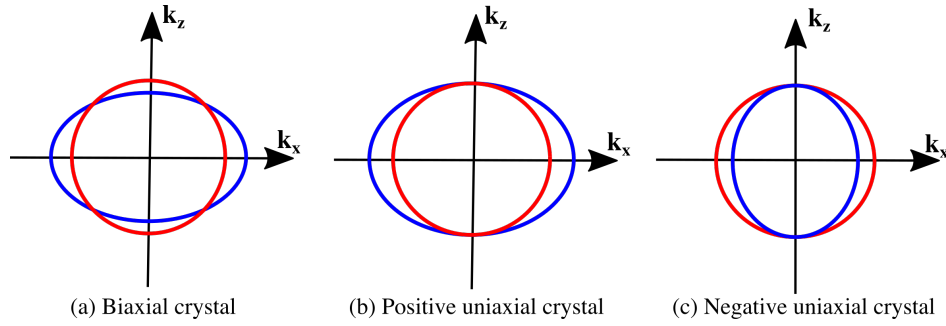


Figure 2.4 – The wave normal surface intersection with the xz -plane for the cases of (a) biaxial crystal (b) positive uniaxial crystal (c) negative uniaxial crystal.

2.6 Double refraction

A basic phenomenon of double refraction that occurs at the interface of an anisotropic medium is a consequence of the existence of the two eigenwaves discussed above. An incident plane wave on an anisotropic medium results into two refracted waves, which propagate with different phase velocities in general and eventually under different directions. For a uniaxial crystal, the refracted waves are composed of an ordinary and an extraordinary wave. Let \mathbf{k}_i be the incident propagating wave vector and \mathbf{k}_1 , \mathbf{k}_2 represents the wave vectors of the refracted waves. The boundary conditions state that all wave vectors must lie in the plane of incidence and the tangential component (k_{\parallel}) of all wave vectors should be identical. These are the properties of \mathbf{k}_i , \mathbf{k}_1 and \mathbf{k}_2 onto the interface. These boundary conditions hold for refracted waves at any interface of an anisotropic medium including the case where one of the two media is isotropic or both media are anisotropic⁴. An example is shown schematically in Fig. 2.5, where the conservation of k_{\parallel} is clearly seen,

$$|\mathbf{k}_i| \sin \theta_i = |\mathbf{k}_1| \sin \theta_o = |\mathbf{k}_2| \sin \theta_e \quad (2.30)$$

⁴Note that the conservation of the tangential component of the wave vector holds also for the reflected wave(s).

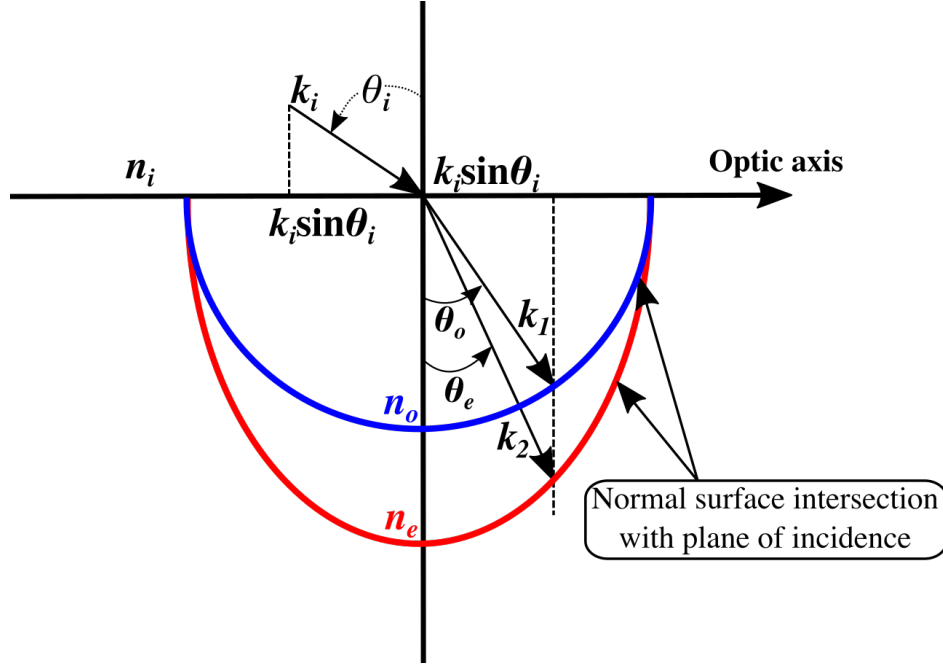


Figure 2.5 – Double refraction at the interface of an anisotropic medium

The algebraic solution for θ_o and θ_e could require solving a quartic equation. Thus a graphical method is always preferred. The Eq. (2.30) is nothing else than a generalized Snell law. Indeed $|\mathbf{k}_1|$ and $|\mathbf{k}_2|$ depend on the direction of incident propagating wave vector \mathbf{k}_i . For a uniaxial crystal, one of the shell of normal surface is a sphere while the other shell is an ellipsoid of revolution. Thus the shell consisting of sphere leads to a constant wave vector \mathbf{k} for all possible propagation directions. This direction independent wave is the ordinary wave and it obeys Snell's law

$$n_i \sin \theta_i = n_o \sin \theta_o \quad (2.31)$$

Here n_i represents incident medium refractive index and n_o represents ordinary refractive index of the uniaxial crystal. The direction dependent wave corresponding to the ellipsoid of revolution shell in the wave normal surface is called the extra-ordinary wave. The expression for the extra-ordinary refractive index (n_e) of a uniaxial crystal is given in the next section. The next two sections discuss light propagation through uniaxial and biaxial crystal.

2.7 Light propagation through uniaxial crystal

Quartz, calcite and lithium niobate are some of the familiar uniaxial crystals that have been investigated thoroughly for utilization in many optical devices. The equation of index ellipsoid reduces for a uniaxial crystal to

$$\frac{x^2}{n_o^2} + \frac{y^2}{n_o^2} + \frac{z^2}{n_e^2} = 1. \quad (2.32)$$

We assume here $n_x = n_y = n_o$ and $n_z = n_e$. By substituting these values into the Eq. (2.20), two factors are obtained as below,

$$(n_o^2 - n^2) \left(\frac{1}{n^2} - \frac{(k_x^2 + k_y^2)}{n_e^2} - \frac{k_z^2}{n_o^2} \right) = 0 \quad (2.33)$$

In the above equation, the first factor corresponds to the sphere of the normal surface (ordinary wave) while the second factor corresponds to the ellipsoid of the normal surface (extraordinary wave). The sphere and ellipsoid have a one common point along z -direction. In conclusion, the light propagating in a uniaxial crystal results into an ordinary and an extraordinary wave travelling with phase velocities c/n_o and c/n_e respectively. The phase velocity for ordinary wave is independent of the propagation direction. The electric displacement vector \mathbf{D}_o and electric field vector \mathbf{E}_o for ordinary wave are always perpendicular to the wave propagation vector \mathbf{k} . For an extraordinary wave, the electric displacement vector \mathbf{D}_e is perpendicular to the propagation direction (\mathbf{k}_e) but in general the electric field vector \mathbf{E}_e is not. Although \mathbf{E}_e lies in the plane formed by the \mathbf{D}_e and \mathbf{k}_e . Both \mathbf{E}_o and \mathbf{E}_e are mutually orthogonal. The refractive index of the extraordinary wave can be deduced as

$$\frac{1}{n^2(\theta)} = \frac{\cos^2 \theta}{n_o^2} + \frac{\sin^2 \theta}{n_e^2}. \quad (2.34)$$

It can easily be seen that the refractive index of the extraordinary wave varies from being $n(\theta) = n_o$ at $\theta = 0^\circ$ to $n(\theta) = n_e$ at $\theta = 90^\circ$.

2.8 Light propagation through biaxial crystal

The wave normal surface for a biaxial crystal is shown in the figure 2.1. The simplest way to investigate this surface is to visualize it's intersection with the three coordinate planes i.e. set $k_x = 0$ for visualizing the $k_y k_z$ plane, set $k_y = 0$ for visualizing $k_x k_z$ plane and set $k_z = 0$ for visualizing $k_x k_y$ plane. These three planes are shown in Fig. 2.6. It can be

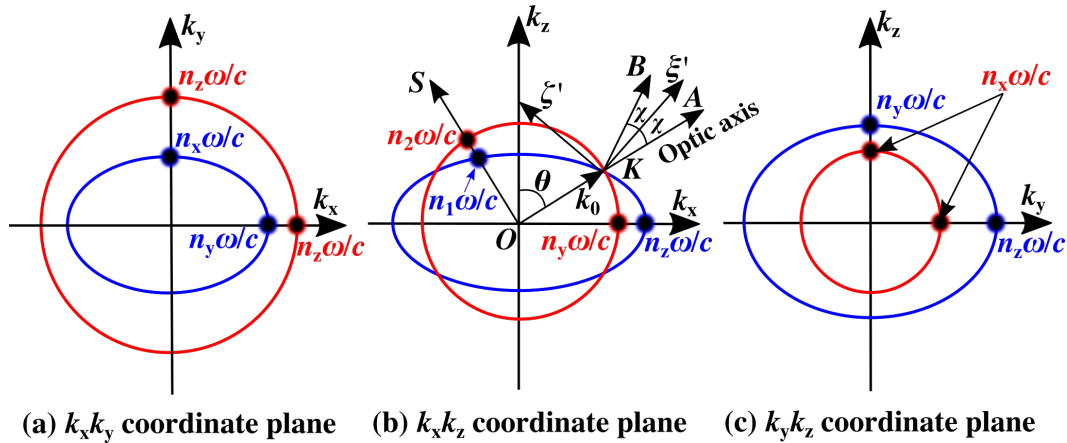


Figure 2.6 – Intersection of biaxial crystal wave normal surface with the three coordinate planes by assuming $n_x < n_y < n_z$. (a) $k_x k_y$ plane, (b) $k_x k_z$ plane, (c) $k_z k_y$ plane.

observed that the intersection of the wave normal surface with the coordinate planes results

in the formation of a circle and an ellipse. The circle has a radius equal to $n_i\omega/c$ with i equal to the coordinate set equal to zero (in the case where $k_x = 0$, $n_i = n_x$) and the ellipse has semi-axes equal to the $n_j\omega/c$ and $n_k\omega/c$, with j and k being the two remaining coordinates (for instance $n_j = n_y$, $n_k = n_z$). The circle and ellipse intersect only (at four points) in the plane $k_x k_z$, that is the plane associated with the intermediate refractive index for the case $n_x < n_y < n_z$. As already mentioned before, the line passing through the origin and joining any of the two points is an optic axis. It can be observed that for a biaxial crystal there are two such directions and hence the name “biaxial”.

Let's consider wave propagating along a line OS in the coordinate plane formed by $k_y = 0$. It can be observed that the line intersects the wave normal surface at two points, thus corresponding to two wave-vectors with lengths equal to the distance between origin and intersection points (see Fig. 2.6(b)). The two modes corresponding to the circle and ellipse are polarized perpendicular and parallel respectively to the coordinate plane $k_y = 0$. Generally, the wave propagation in any other direction or in any other coordinate plane follows the similar behaviour, except the waves propagating along the optic axes directions. It has been shown analytically that when the wave vector coincides with the optic axis there exists infinite number of Poynting vectors dictating the flow of energy in the form of a cone [143]. In this method by considering infinite number of unit normal vectors (as schematically depicted in Fig. 2.6(b)) perpendicular to the wave normal surface $\omega(k)$ in the infinitesimal neighbourhood around singular point, it is possible to show that the wave normal surface is a cone around the singularity. More details on this analytical treatment can be found in [143]. Alternative to this method, we present below a short geometric explanation for a wave propagating along one of the optical axes of the biaxial crystal and leading to the situation of conical diffraction. The interested reader to understand the consequences of wave propagation in a general direction or in the principal planes of a biaxial crystal is referred to [144], where a complete treatment is presented with expressions for the field directions and walk-off angles between the fields.

2.8.1 Conical refraction/diffraction

The wave propagating along the optic axes direction possess a single phase velocity regardless of the state of polarization. In biaxial crystals the two sheets of wave normal surface cross in four points along the two optic axes directions, thus the electromagnetic energy flow represented by group velocity is undefined in this direction. The wave propagating along this direction undergoes a peculiar refraction known as “conical refraction” or “conical diffraction”, the effect at the origin of the investigations in this thesis. Here we give a geometric argumentation that follows closely the one in [21], that explains why the Poynting vectors distribute on a cone surface. We can assume that the optical axis is in the xz -plane⁵. A propagation vector along one of the optic axes has therefore the form $\mathbf{k} = (k_x, 0, k_z)$. Since \mathbf{k} is always perpendicular to \mathbf{D} , one can write

$$\mathbf{k} \cdot \mathbf{D} = 0 \quad \Rightarrow \quad k_x D_x + k_z D_z = 0. \quad (2.35)$$

⁵This corresponds to the case where the middle refractive index is associated to the y -direction of polarization.

Equation (2.35) defines a plane Π , which contains all the possible \mathbf{D} vectors and is perpendicular to the propagation vector \mathbf{k} (see Fig. 2.7). Also $\mathbf{D} = \epsilon_0 \overleftrightarrow{\epsilon} \cdot \mathbf{E}$ thus

$$\begin{aligned} \epsilon_0(\mathbf{k} \cdot \overleftrightarrow{\epsilon} \cdot \mathbf{E}) &= 0 \\ k_x \epsilon_x E_x + k_z \epsilon_z E_z &= 0. \end{aligned} \quad (2.36)$$

Equation (2.36) defines a second plane Λ , which contains all the \mathbf{E} vectors. This plane is perpendicular to the vector $\mathbf{S}_0 = (k_x \epsilon_x, 0, k_z \epsilon_z)$, which points in the direction of a possible Poynting vector \mathbf{S} (the one with the maximum walk-off with \mathbf{k}). We place the origin O of the reference frame on the plane Λ . The lines passing through O and containing the electric field vector \mathbf{E} cross the plane Π in points P lying on the straight line AB (A and B go to infinity) representing the intersection of the planes Π and Λ . As we have discussed in Sect.

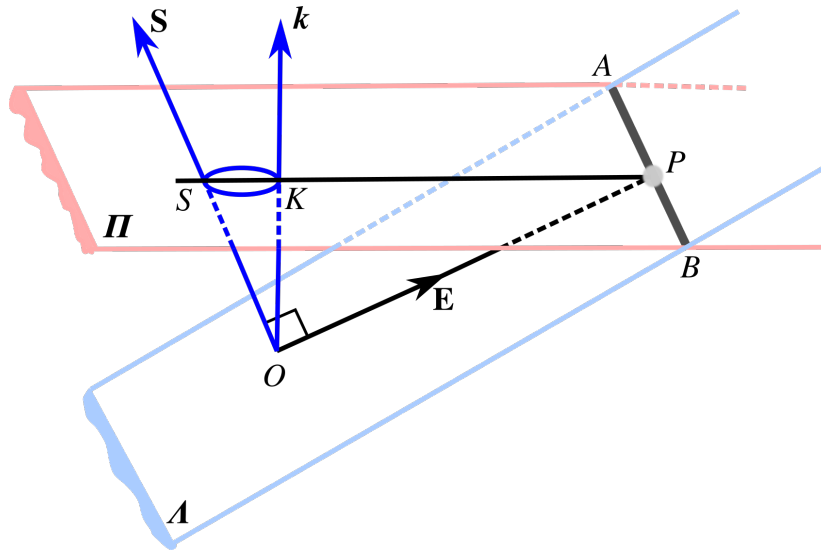


Figure 2.7 – Geometrical origin of conical diffraction phenomena happening in a biaxial crystal. Illustration of field vectors directions as the wave vector propagates along the optic axis of the biaxial crystal.

2.3, the Poynting vector \mathbf{S} is co-planar with \mathbf{k} , \mathbf{D} and \mathbf{E} but also perpendicular to \mathbf{E} . Let's call K the point of intersection of the \mathbf{k} vector direction (starting at O) with the plane Π . For a given direction of \mathbf{E} in Λ the corresponding point of intersection of the vector \mathbf{S} is S . It is easy to see that the triangles OKS and OKP are similar thus

$$\frac{KS}{OK} = \frac{OK}{KP} \Rightarrow KS \cdot KP = \text{constant}. \quad (2.37)$$

As the locus of P is a straight line AB , thus the locus of S is the inverse of AB which means it is a circle containing point K as center of inversion and a circle has tangents in every direction. The conclusion is that there exists an infinite number of Poynting vectors \mathbf{S} (intersecting the plane Π in all points S on the circle in Fig. 2.7). The Poynting vectors are thus on the surface of a cone with circular base that contains the direction of the \mathbf{k} vector. As the foot of the perpendicular from O to the Π plane does not pass through the center of the circle, thus the cone is slanted. By considering \mathbf{S} , \mathbf{k} and \mathbf{E} to be in xz -plane, it is also

possible to determine easily the half-aperture angle of this cone as below [21],

$$\alpha \cong \frac{1}{2n_g n_p} \sqrt{(n_g^2 - n_m^2)(n_m^2 - n_p^2)}. \quad (2.38)$$

Here n_g, n_m and n_p represent the three main refractive indices with $n_g > n_m > n_p$.

2.9 Optical Activity

“Optical Activity” refers to the phenomena by which some crystals rotate the plane of polarization of a linearly polarized light passing through them⁶. It was first observed in Quartz. Fresnel explained in 1825 that circular birefringence (a different refractive index for right and left circular polarized light) gives rise to optical activity. The eigenwaves in this case are right and left circular polarization. The magnitude of rotation is proportional to propagation distance in that medium. Thus, the specific rotatory power is measured as the amount of rotation per unit length. A crystal is called dextrorotatory (right handed) and levorotatory (left handed), if the sense of rotation of the plane of polarization is counter-clockwise and clockwise, respectively. It is important to mention here that optical activity in itself provides an extremely sensitive method of quantitatively determining circular birefringence [109, 143, 145]. The specific rotatory power is expressed as below,

$$\rho = \frac{\pi}{\lambda} (n_l - n_r) \quad (2.39)$$

The above equation implies that if $n_l > n_r$ then the optical rotation is counterclockwise (right handed) otherwise clockwise (left handed) as viewed by an observer facing the approaching light beam. Thus the circularly polarized wave with greater phase velocity dictates the rotation sense of the plane of polarization. Quartz and certain other materials, which possess a helical molecular structure show optical activity. As the origin of this optical activity is the induced dipole moment of the helical molecule resulting via the changing magnetic flux through it. To include the existence of optical activity, the displacement vector \mathbf{D} involves an additional contribution in a direction perpendicular to \mathbf{E} field

$$\mathbf{D} = \epsilon_0 \epsilon \mathbf{E} + i\epsilon_0 \mathbf{G} \times \mathbf{E}. \quad (2.40)$$

Here $\mathbf{G} = (g_{ij} k_i k_j / k_0^2) \hat{k}$ is called the gyration vector and it is parallel to the propagation direction. g_{ij} represent the matrix elements of the gyration tensor and they describe the optical activity of the corresponding crystal. The gyration tensor is symmetric with only six independent components and some of which disappear due to crystal symmetry. Here it is worth to mention that centrosymmetric crystal cannot be optically active. The vector product $\mathbf{G} \times \mathbf{E}$ can be re-written as below,

$$\mathbf{G} \times \mathbf{E} = \begin{bmatrix} 0 & -G_z & G_y \\ G_z & 0 & -G_x \\ -G_y & G_x & 0 \end{bmatrix} \begin{bmatrix} E_x \\ E_y \\ E_z \end{bmatrix} = [\overleftrightarrow{G}] \cdot \mathbf{E}. \quad (2.41)$$

⁶Optical activity is a manifestation of spatial dispersion in the medium.

The $[\vec{G}]$ is an antisymmetric tensor. Now it's convenient to define an effective dielectric tensor as follow,

$$\overleftrightarrow{\epsilon}' = \epsilon_0(\overleftrightarrow{\epsilon} + i[\vec{G}]) \quad (2.42)$$

Thus

$$\mathbf{D} = \overleftrightarrow{\epsilon}' \cdot \mathbf{E} \quad (2.43)$$

Hence, this allows for solving the wave equation for the determination of eigen polarizations of propagation and two $[\vec{G}]$ dependent corresponding refractive indices. It is pertinent to mention here that for directions where the waves experience a linear birefringence, this usually dominates over the optical activity and the eigenwaves are practically always linearly polarized or very weakly elliptical. Only for crystals lacking birefringence or for corresponding specific directions the optical activity is really relevant.

2.10 Nonlinear photorefractive crystals

Photorefractive (PR) crystals are those which possess the properties of being electro-optic and photoconductive at the same time. An electro-optic material shows changes in its refractive indices by the application of an external electric field, a phenomena termed as Pockel's effect, when the change is linear to the applied electric field. Whereas a photoconductive material has the ability to generate mobile charge carriers upon light excitation at certain wavelengths. The movement of these charge carriers could be by diffusion, by a drift under the action of an electric field and in some cases, due to an internal asymmetry associated to a photovoltaic effect. Photorefractive crystals besides being electro-optic and photoconductive are also in most cases anisotropic (either with or without the presence of an externally applied electric field) in addition of being piezo-electric, elasto-optic, and optically active among other interesting properties [142, 146, 147].

Even though photorefraction is a nonlinear effect, we introduce it in this chapter on optically anisotropic materials because most PR crystals are anisotropic. However, some isotropic (but non-centrosymmetric) PR crystals do exist. In a photorefractive material, a spatially modulated intensity of light created by the interference of two coherent beams can excite electrons and/or holes from photoactive centers (donor and acceptor states or localized states inside forbidden energy bandgap) to the conduction band (CB) and/or the valence band (VB), respectively. These charge carriers (electrons and holes) upon reaching the extended states (CB and VB) have the ability to diffuse away due to the presence of diffusion gradient or can also experience an electric drift due to the application of an externally applied electric field. They are then retrapped after drifting an average distance of L_D (via diffusion gradient) or L_E (via external applied electric field). In the following they can eventually be excited again out of the traps. This process of retrapping and excitation continues and leads to the accumulation of charges in the less illuminated region, while the more illuminated region accumulates oppositely charged carriers. This spatial modulation of charges is responsible for creating a space charge field, which in turn spatially modify the refractive index via the electro-optic effect. As the space charge field continues to build-up, it also starts counteracting the diffusion process, until an equilibrium between the space charge field and charges carriers motion is achieved. It is evident from the above

discussion that the space charge field is able to build up thanks to the presence of localized states (or defects) inside the band gap of the photorefractive material. These defects could be intrinsic or extrinsic, which implies that in the former case they appear due to the growing process and in the later case they are created by intentional doping with certain materials [142, 146].

An interference of coherent laser beams can generate modulated sinusoidal intensity patterns with spatial periods of the order of the recording wavelength, thus generating large diffusion gradients and enabling space charge fields of a few kV/cm, which consequently results in the observation of relatively large refractive index changes. It is also pertinent to mention here that the photons in the recording wavelengths should merely be energetic enough to excite charge carriers from the localized states but not from VB to CB⁷. Thus the material stays transparent to the radiation enabling recording in the whole volume of the crystal. Also, the recording beams can be diffracted in real time from the refractive index variations created by themselves. A time constant with dependence on dielectric relaxation time ($\tau \propto 1/\sigma$, here σ represents the conductivity) among other parameters characterizes the charge carrier transport and hence the build-up of space-charge modulation. Since holographic build-up and conductivity are related, it is possible to determine the conductivity of a material by studying the holographic build-up and decay.

It needs to be pointed out here that some samples exhibit behaviour which could be understood by simple models such as the one-center/two-valence/one-charge-carrier model. However, there are other photorefractive materials exhibiting more complex behaviour, such as a coexistence of shallow and deep traps or photochromic effects⁸ and even electron-hole competition. In such cases a quantitative analysis is more complex. Electron and hole participation in this process depends on the applied external electric field, concentration of donor and acceptor states, their corresponding cross-sections for the incident light wavelength as well as their mobilities in the CB and VB, respectively. Here the objective of the discussion is to give a rapid summary of the photorefractive process. Deeper details can be found in references [142, 146].

2.10.1 Refractive index modulation via electro-optic effect

The photorefractive space-charge field modulation generates a refractive index modulation via the linear electro-optic effect. The indicatrix equation (2.26) represents an ellipsoid in the principal coordinate system and its expression can be given in the general form ([149]),

$$B_{ij}x_ix_j = 1 \quad \text{with} \quad B_{ij} = \frac{1}{\epsilon_{ij}}. \quad (2.44)$$

The electro-optic effect describes the (small) changes induced in the refractive index by an electric field and is described by a third-order electro-optic tensor r_{ijk} that modifies the

⁷Interband photorefractive using photons exceeding the bandgap energy is possible and gives rise to PR gratings limited to a thin layer near the material surface but having a much faster response time [148].

⁸Materials exhibiting photochromic effects require two-center model with shallow traps. As they can't be explained by the one-center/two-valence model

tensor B_{ij} according to

$$\Delta B_{ij} = r_{ijk} E_k \quad (2.45)$$

Due to the symmetry of the B_{ij} tensor ($B_{ij} = B_{ji}$), it follows immediately that $r_{ijk} = r_{jik}$. This symmetry is often used to reduce the number of indices in the electro-optic tensor to two $r_{ijk} \Rightarrow r_{mk}$ with $m = 1, 2, \dots, 6$ values relates to the ij indices values

m	1	2	3	4	5	6
ij	11	22	33	23,32	13,31	12,21

This allows to represent the electro-optic relation in the reduced form

$$\begin{bmatrix} \Delta B_1 \\ \Delta B_2 \\ \Delta B_3 \\ \dots \\ \Delta B_6 \end{bmatrix} = \begin{bmatrix} r_{11} & r_{12} & r_{13} \\ r_{21} & r_{22} & r_{23} \\ r_{31} & r_{32} & r_{33} \\ \dots & \dots & \dots \\ r_{61} & r_{62} & r_{63} \end{bmatrix} \begin{bmatrix} E_1 \\ E_2 \\ E_3 \end{bmatrix}. \quad (2.46)$$

Note that the number of non-vanishing elements in r_{ijk} (or r_{mk}) depends on the symmetry (point group) of the crystalline lattice. The higher the symmetry the smaller the number of non-zero independent elements. The above expression describes the electro-optic response for a homogeneous electric field and for a crystal being free to move. The corresponding electro-optic tensor is called the unclamped electro-optic tensor. For photorefraction the use of this tensor represents only an approximation. Indeed, in a photorefractive experiments the space charge electric field is generally periodic in space and the electro-optic response is neither unclamped nor clamped, but partially clamped. In this case this response is significantly more complex and its full description involves the knowledge of the clamped electro-optic coefficients, and of the elastic, elasto-optic and piezo-electric properties of the crystal. The interested reader is referred to the reference [150].

2.10.2 Holographic recording

Photorefractive materials are an excellent choice for holographic recording as they possess good advantages such as reversibility, real-time recording with infinite number of recording and erasure cycles and very high spatial resolution of the recorded holograms. Above all the recording is done for the illuminated light patterns and is independent from the irradiance and total energy. Thus allowing the interesting perspective of recording holograms with low levels of irradiance. A schematic setup used for holographic recording and readout is shown in Fig. 2.8 and is explained briefly in the caption.

The holographic recording and read-out process is qualitatively depicted in Fig. 2.9. Firstly, as described above two interfering beams of wavelength λ inside the crystal generate a pattern of fringes⁹, which enables excitation of electrons (electrons are considered just for the sake of simplicity) from the localized states (photoactive centers) to the CB. These electrons upon reaching CB, diffuse along their diffusion gradient direction with a

⁹The fringe spacing is $\Lambda = \frac{\lambda}{2 \sin \theta}$.

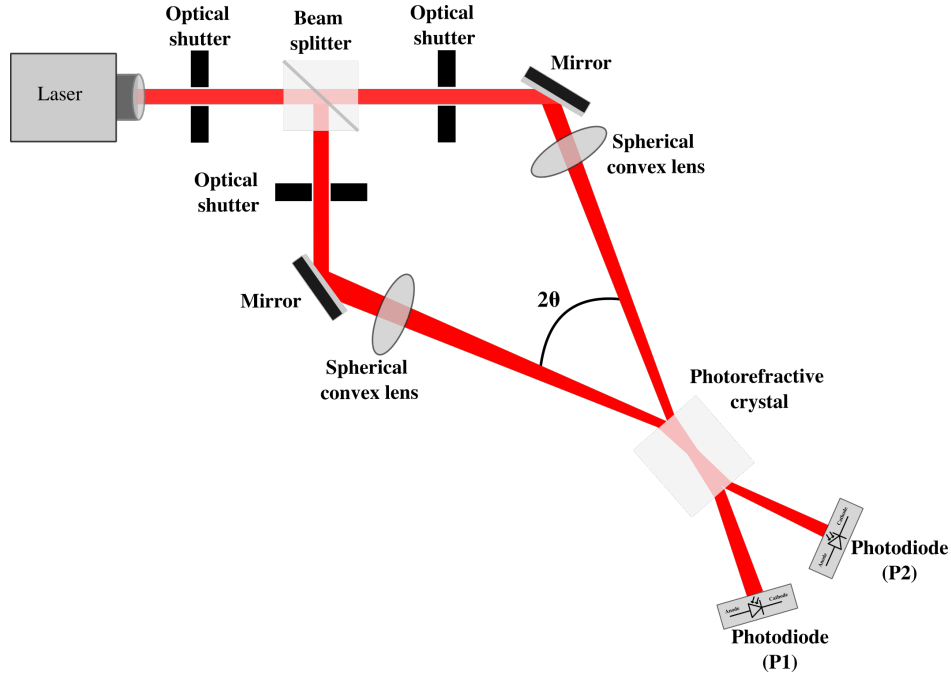


Figure 2.8 – Holographic setup for recording and read-out of phase volume holograms created by the interference of two beams. A laser beam is split into two beams via a beams splitter and both the beams are made to interfere at an angle 2θ generating a sinusoidal intensity pattern in the volume inside the photorefractive crystal. The optical shutters can be placed in both arms to block either of them and read-out from the other. Typically the read-out gives rise to a progressive erasure of the hologram, which can be further accelerated by shining additional spatially homogeneous light on the crystal.

characteristic diffusion length of $L_D = \sqrt{D\tau}$, where D and τ are the diffusion constant¹⁰ and the average excited lifetime of the charge carriers respectively. As already mentioned, the electrons are free and can be re-trapped, re-excited and re-trapped again several times. This leads to a generation of spatially modulated distribution of charges, i.e. the positive charges are accumulated in the brighter region and negative charges in the darker regions of the light fringe pattern. This spatial modulation of charges results in the generation of an associated space-charge field. It is important to mention here that the space-charge field modulation and the charges modulation are generally $\pi/2$ phase shifted with respect to each other due to Poisson's equation that relates charge and electric field. Also, if there is additionally an externally applied electric field there is an electron drift in addition to the diffusion gradient, what has the consequence that the charge modulation is no longer in-phase with the incident light pattern. Finally, a photorefractive material being electro-optic as well helps to produce an in phase index of refraction modulation from the space-charge field modulation. This refractive index modulation representing a hologram or "phase volume grating" is either in phase or in antiphase with the space charge field. In the simplest approximation the diffraction efficiency η of such a volume phase grating can be expressed

¹⁰It refers to the rate of diffusion, which in turn depends on how fast the charge carrier move and on the spatial distance between their scattering events. It is measured in cm^2/s .

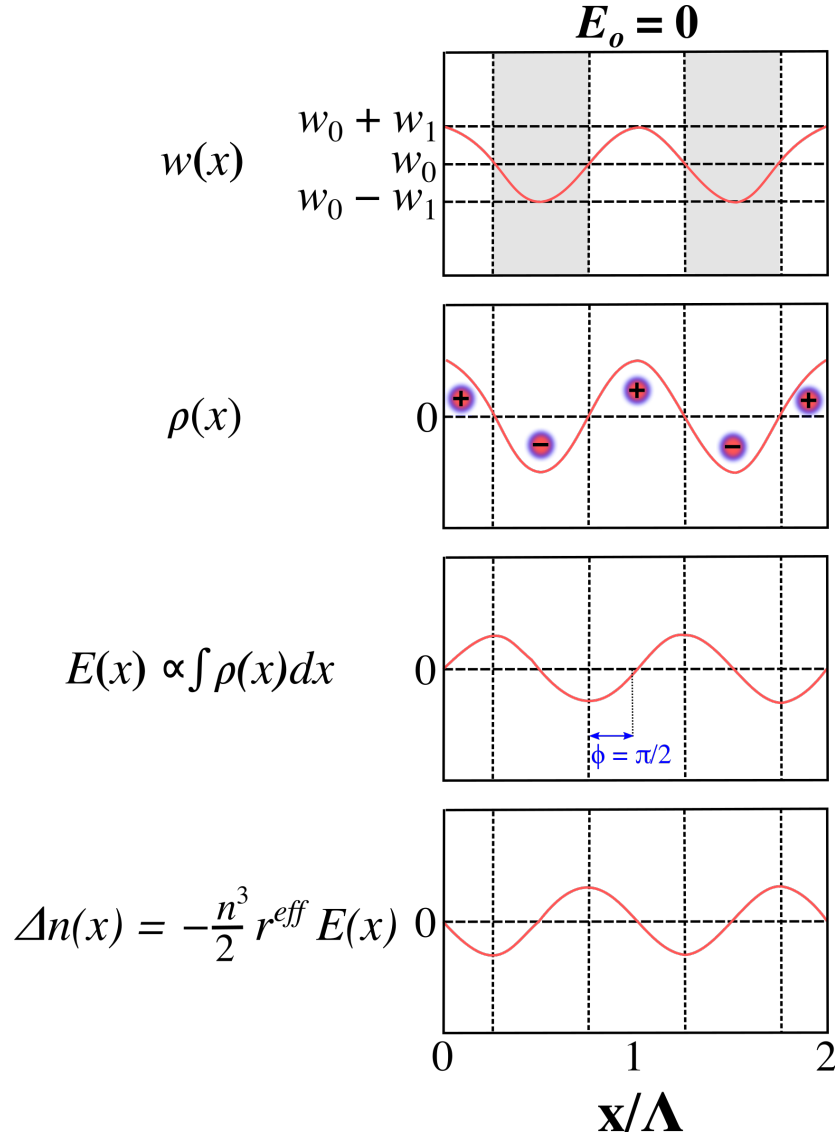


Figure 2.9 – Scheme of holographic recording process in a photorefractive crystal in the absence of any externally applied electric field. Firstly the interference of two coherent beams inside photorefractive crystal creates dark and bright fringes (see $w(x)$). This results in the excitation of electrons (holes) from the illuminated regions to the conduction band (valence band). After some time, due to the diffusion gradient, a spatial charge modulation is created ($\rho(x)$), which results in a modulated space-charge electric field ($E(x)$). The space charge field modulation enables a corresponding refractive index modulation ($\Delta n(x)$) via the electro-optic effect. The resulting phase volume grating can be read-out by either of the interfering beams or by a third beam at another wavelength arriving under the appropriate Bragg angle. The recorded grating is generally gradually erased during the read-out process and after some time only the transmitted beam persists. The whole process can be re-done an infinite number of times.

by Kogelnik's formula [151]

$$\eta = \sin^2 \left[\frac{\pi n_1 d}{\lambda \cos \theta} \right], \quad (2.47)$$

where

$$n_1 = -(n^3/2)r_{eff}E_{sc}. \quad (2.48)$$

Here r_{eff} represents the effective electro-optic coefficient in the given configuration, E_{sc} represents the amplitude of space-charge field modulation, n is the average undisturbed refractive index and d is the interaction distance inside the crystal. Equation (2.47) for calculating diffraction efficiency assumes that the refractive modulation along the sample thickness is uniform. This approximation works well for samples with low diffraction efficiencies and where there is very little energy exchange involved between the interfering beams as they propagate along the sample thickness.

2.10.3 Two-wave mixing

As mentioned above, the refractive index grating is generally out-of-phase with respect to the intensity fringes. The phase shift is $\pi/2$ in the case where diffusion is the dominant charge transport mechanism. Under these conditions coupled wave theory predicts that the two interfering beams will exchange energy as they propagate through the grating they themselves generate. Let's distinguish the two interfering beams as a pump and a signal beam. Importantly, whether the pump amplifies or deamplifies the signal beam depends on the propagation direction of the interfering beams as well as on the crystal orientation and on whether electrons or holes are the dominant moving carrier. The two-wave mixing effect is analogous to an amplifier in electronic circuits. Importantly, two-wave mixing is a relative phenomenon, meaning that the light coupling modifies on its turn the grating recording beams, which modifies again the grating, and so on in a rather complicated feedback process. Two-wave mixing will be discussed together with grating diffraction in Chapter 6, where we will present photorefractive holography of CD beams.

2.10.4 Four-wave mixing

In a two-wave mixing phenomena, due to the presence of feedback mechanism between the interfering beams and the nonlinear material, the phase and amplitude of the interfering beams is coupled and thus it can be modified. In a similar fashion, one can mix four waves of same frequency to perform "degenerate four-wave mixing" (DFWM) (see Fig. 2.10). In DFWM two mutually coherent interfering beams (**S** and **R**) create a real time hologram inside the medium. If a strong pump beam **P** with similar wavefront as **R** but incoherent to **R** is injected in opposite direction, this wave is diffracted by the hologram to create a conjugate **S*** beam travelling in opposite direction to **S**. The wave **S*** reproduces the wavefront **S** as it was travelling back in time and the whole system behaves like a "phase conjugate mirror". This mechanism is schematically shown in Fig. 2.10.

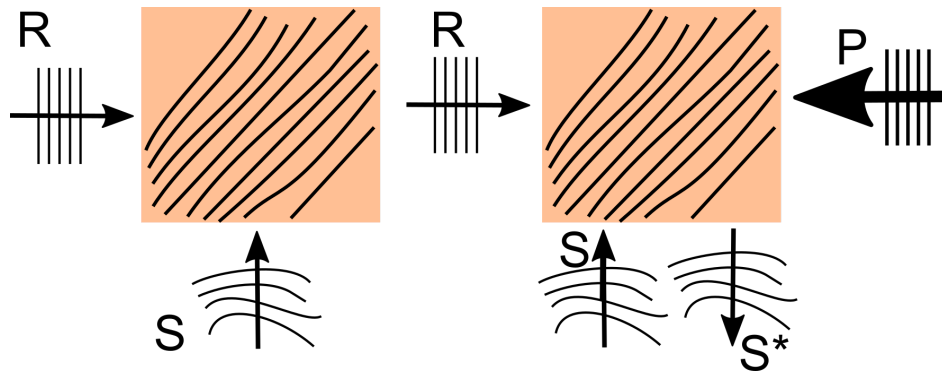


Figure 2.10 – Degenerate four-wave mixing phenomena in photorefractive materials. Two interfering beams S and R are used to generate a phase volume grating inside the material and a high intensity pump beam P travelling in the opposite direction to R diffracts to create a conjugate beam S^* [146].

CONICAL DIFFRACTION: THEORY AND FUNDAMENTAL ASPECTS

In this chapter, the phenomena of conical diffraction (CD) is discussed in detail. Thus, besides a short introductory discussion on the history of the phenomena, a brief review of the diffractive theory of CD in paraxial regime is presented both for a single biaxial crystal and for a cascade of N biaxial crystals. This is followed by a discussion of the main features characterising conical diffraction, which have been observed in recent years [18, 20, 24, 30, 39, 152–155]. The last section is devoted to the overview of the recent developments and applications that have emerged in the investigations of CD.

3.1 History of conical diffraction phenomenon

In this section, the major milestones achieved in the exploration of the conical diffraction phenomenon, since its prediction almost 200 years ago by Hamilton are briefly discussed. Hamilton's prediction dates in 1832 [156] and the first experimental observation came soon after by Lloyd in 1833 [157, 158]. Hamilton realized that the propagation of a bundle of rays along the optic axis direction of an anisotropic biaxial crystal should result in a slanted light cone inside the crystal and emerge as hollow cylinder of light. Hamilton also thought of another solution, in which a light cone propagates as pencil of light inside the crystal and emerges as light cone. These two peculiar singular propagation of waves were termed as “Internal Conical Diffraction” and “External Conical Diffraction” [156], respectively. Hamilton convinced Lloyd to investigate these two phenomena, who successfully observed experimentally both the internal and external conical diffraction phenomena in an aragonite biaxial crystal. The prediction by Hamilton and observation by Lloyd was certainly not the last words on CD phenomena. A few years later in 1839 Poggendorff used fire lamp as a light source and found that there are actually two light rings separated by a dark ring [159], known today as Poggendorff dark ring. At the start of twentieth century, Voigt presented a comprehensive investigations on the theoretical and experimental aspects of conical diffraction, as known at that time [160]. He also tried to explain the origin

of the Poggendorff ring. In 1930 Nobel laureate Raman used Naphthalene for experiments with conical diffraction. Naphthalene had ten times larger birefringence than aragonite. Raman confirmed the presence of the Poggendorff ring and also reported that the conical diffraction beam transverse intensity pattern changes along the propagation direction. The Poggendorff ring is clearly visible in a certain plane, if one moves away from that plane then the rings become broader and at a certain distance the inner ring converts into an axial spot [161, 162]. These observations of Raman could only be explained by the diffractive theory of conical diffraction, which started developing atleast four decades after these observations.

With the advent of lasers, the explosion of research in nonlinear crystals also brought some researchers to investigate the phenomena of conical diffraction in nonlinear crystals. The first attempts to describe the conical diffraction with diffractive formalism was put forward in the seventies by Lalor et al. [163–165] and also by Schell and Bloembergen [166, 167]. However, the full diffractive theory in which the input beam is decomposed into transverse plane waves propagated and finally back Fourier transformed to obtain the field of the wave behind the crystal was presented by Belsky and Khapalyuk in 1978 [168]. This diffractive theory was able to explain most of the phenomenology associated with conical diffraction phenomenon. Further modification of this theory to include gyroscopic crystals was reported by Belsky and Stepanov [169, 170]. The final breakthrough was presented by Sir Michael Berry in 2004, who reformulated the diffractive theory with paraxial optics and deduced analytical formulas for the two bright rings as well as the Raman spot [19]. Later on (in 2010), he also gave analytical expressions for the field transmitted from a cascade of N biaxial crystals with aligned optic axis [22]. The theoretical models proposed by Berry, opened a whole new dimension for investigating fundamental aspects and finding potential applications of conical diffraction beams in modern photonics.

3.2 Principle of conical diffraction

As already mentioned, the CD phenomenon is observed when a sufficiently tightly focused beam is incident on an optically biaxial crystal (BC) with its wave-vector \mathbf{k} parallel to one of the optical axes of the crystal [19]. For this singular \mathbf{k} -direction, the Poynting vector directions are degenerate and lie on the surface of a slanted cone with circular base inside the crystal. The section of this cone can be easily visualized in the plane of tighter focusing of the incident wave (focal image plane, FIP), where as already mentioned, one observes two closely spaced circularly shaped bright rings (double rings) separated by the dark Poggendorff ring. Two diametrically opposite points always possess orthogonal linear polarizations, leading to the vector beam character [18–20]. The CD phenomenon is schematically illustrated in the Fig. 3.1. An elegant geometrical explanation on how the Poynting vector directions on the cone depend on the local electric (\mathbf{E}) and electric displacement vectors (\mathbf{D}) of the wave is given in Born and Wolf's book [21] and was described in Sect. 2.8.1. For a single crystal the radius of the CD double ring corresponds to the product $R_0 = \alpha L$ of the half-angle of aperture α of the CD cone (that depends on the material birefringence according to Eq. (2.38)) and on the crystal length L . A single dimensionless parameter ρ_0 , defined as the ratio of the radius of the ring to the beam width (i.e. $\rho_0 = R_0/w$) is used to

describe all the features of conical diffraction both qualitatively and quantitatively. In order to observe the fine features associated to CD one requires $\rho_0 \gg 1$, otherwise most of the features will be obscured by the beam width.

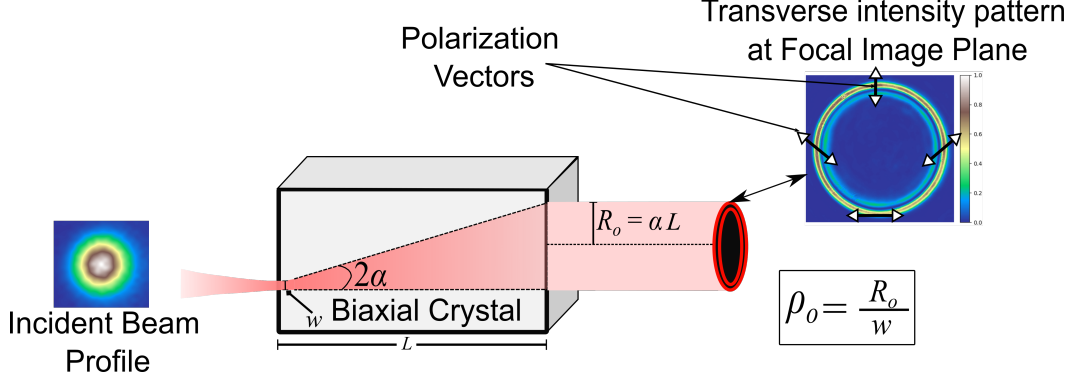


Figure 3.1 – Schematic illustration of the phenomenon of internal conical diffraction in a biaxial crystal.

3.3 Theoretical model

As mentioned in the last section, the primary features of the conical diffraction rings can only be explained with diffraction theory, which was first proposed by Belskii and Khatpaluyk. This theory is later on reformulated by Berry and this reformulation which is based on paraxial optics will be presented briefly in Sect. 3.3.1 [19]. After that, propagation of an incident beam through a cascade of biaxial crystals is considered in Sect. 3.3.2 [22].

3.3.1 Conical diffraction in a single biaxial crystal

Conical diffraction (CD) phenomenon happening in a single biaxial crystal is schematically illustrated in Fig. 3.2. Firstly, the dimensionless variables used in the theoretical model are

$$\boldsymbol{\rho} = \{\xi, \eta\} = \rho \{\cos \varphi, \sin \varphi\} \equiv \frac{1}{w} \{x + R_0, y\}, \quad (3.1)$$

$$\boldsymbol{\kappa} = \{\kappa_x, \kappa_y\} = \kappa \{\cos \phi, \sin \phi\} \equiv w \{k_x, k_y\}, \quad (3.2)$$

$$\rho_0 \equiv \frac{R_0}{w} \equiv \frac{\alpha L}{w}, \quad (3.3)$$

$$\zeta \equiv \frac{L + n_2(z - L)}{n_2 k_0 \omega^2}. \quad (3.4)$$

Here $\boldsymbol{\rho}$ represents the transverse position from the axis of the cylinder, $\boldsymbol{\kappa}$ represents the normalized transverse wavevectors, ρ_0 is the radius of the cylinder and ζ is a measure of the distance from the beam waist position or focal image plane i.e. from $z = L(1 - 1/n_2)$ (see Fig. 3.2). All these four parameters ($\boldsymbol{\rho}$, $\boldsymbol{\kappa}$, ρ_0 , ζ) are measured in units of beam width w . The latter is defined in our case as 1/e intensity radius of the incident beam focused by a spherical lens and measured in its focal plane. The parameter ρ_0 is the most important

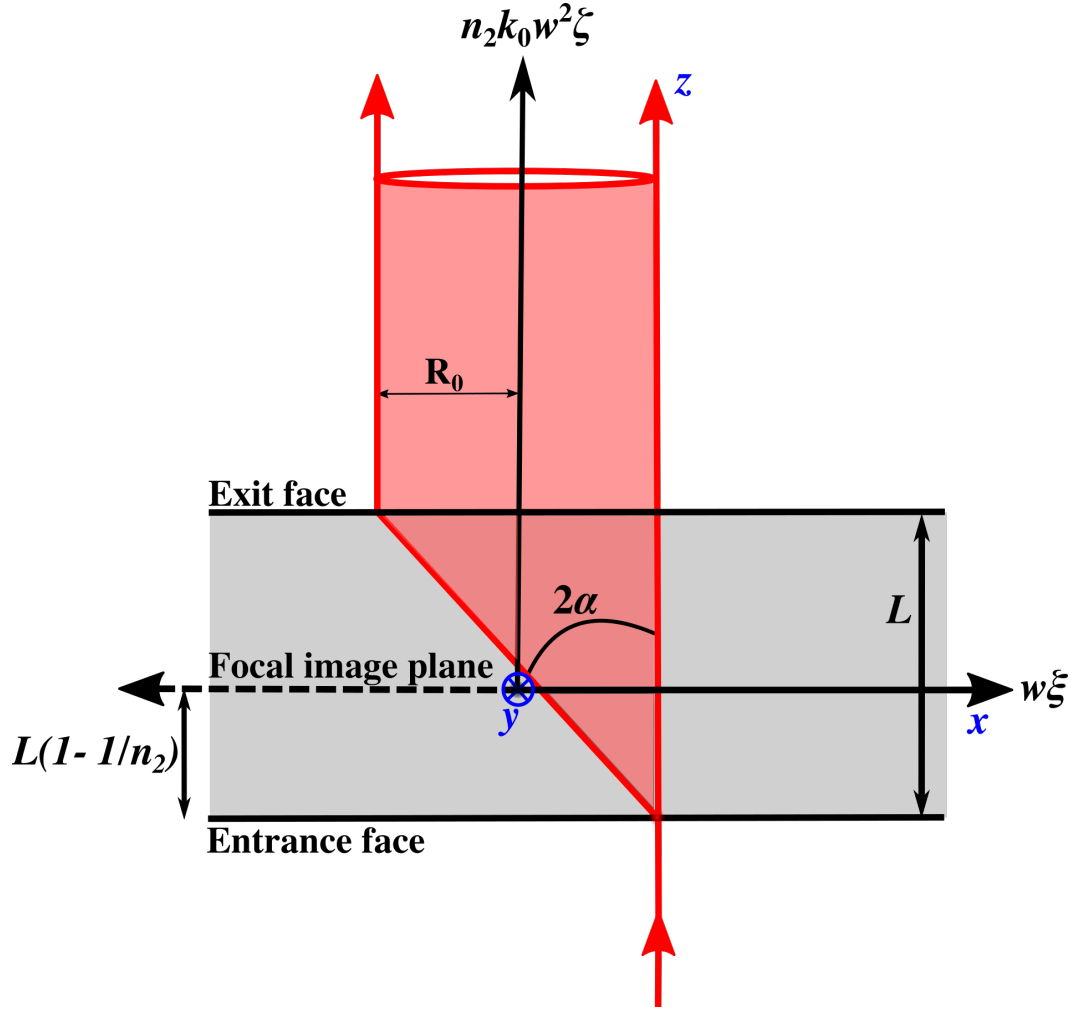


Figure 3.2 – Dimensionless parameters are used to describe the conical diffraction through a single biaxial crystal.

qualitative parameter as it replaces five other parameters i.e. n_1, n_2, n_3, L, w . By considering the superposition of plane waves (each of which is operated by a unitary transformation matrix $\mathbf{U}(\kappa, \phi)$) acting on the initial wavevector amplitude $\mathbf{a}(\kappa)$, one can write the complex $\mathbf{D} = \{D_x, D_y\}$ field beyond the crystal as a double integral as below,

$$\mathbf{D} = \frac{1}{2\pi} \iint e^{i\kappa \cdot \rho} \mathbf{U}(\kappa) \mathbf{a}(\kappa) d\kappa \quad (3.5)$$

Here $\mathbf{U}(\kappa)$ is a 2×2 unitary transformation matrix and its expression for a single crystal CD satisfying certain requirements is [154],

$$\mathbf{U}(\kappa) = \exp \left[-\frac{1}{2} i \kappa^2 \zeta \right] \left(\cos \rho_0 \kappa \mathbf{I} - i \frac{\sin \rho_0 \kappa}{\kappa} [\kappa_x \sigma_3 + \kappa_y \sigma_1] \right). \quad (3.6)$$

Here $\mathbf{I} = \begin{pmatrix} 1 & 0 \\ 0 & 1 \end{pmatrix}$ is the identity matrix, $\sigma_1 = \begin{pmatrix} 0 & 1 \\ 1 & 0 \end{pmatrix}$ and $\sigma_3 = \begin{pmatrix} 1 & 0 \\ 0 & -1 \end{pmatrix}$ being two of the Pauli spin matrices. By the consideration of uniformly polarized and circularly symmetric

incident beam, one can write initial wave-vector amplitude as below,

$$\mathbf{a}(\kappa) = a(\kappa) \begin{pmatrix} d_{0x} \\ d_{0y} \end{pmatrix} = a(\kappa) \mathbf{d}_0, \quad (3.7)$$

here \mathbf{d}_0 is the unit vector of the input polarization. While $a(\kappa)$ is the Fourier transform of the incident beam transverse amplitude and for a circularly polarized Gaussian beam with width (w) defined at the $1/e$ of intensity, it is equal

$$a(\kappa) = \exp\left(-\frac{1}{2}\kappa^2\right). \quad (3.8)$$

It's relation to the transverse profile of the incident beam $D_0(\rho)$ is as follows,

$$\mathbf{D}_0 = \mathbf{d}_0 D_0(\rho) = \mathbf{d}_0 \int_0^\infty \kappa J_0(\kappa\rho) a(\kappa) d\kappa. \quad (3.9)$$

Now after combining Eqs. (3.5),(3.6) and (3.9) and performing some elementary integrations over the azimuthal variable ϕ , one can write the output \mathbf{D} -field as,

$$\mathbf{D}(\rho, \varphi, \zeta; \rho_0) = \begin{pmatrix} B_0 + B_1 \cos \varphi & B_1 \sin \varphi \\ B_1 \sin \varphi & B_0 - B_1 \cos \varphi \end{pmatrix} \begin{pmatrix} d_{0x} \\ d_{0y} \end{pmatrix}. \quad (3.10)$$

Here $B_0(\rho, \zeta; \rho_0)$ and $B_1(\rho, \zeta; \rho_0)$ are the so called Belsky-Khapalyuk integrals [168] expressed as

$$B_0(\rho, \zeta; \rho_0) = \int_0^\infty \kappa a(\kappa) \exp\left\{-\frac{1}{2}i\zeta\kappa^2\right\} J_0(\kappa, \rho) \cos(\kappa\rho_0) d\kappa, \quad (3.11)$$

$$B_1(\rho, \zeta; \rho_0) = \int_0^\infty \kappa a(\kappa) \exp\left\{-\frac{1}{2}i\zeta\kappa^2\right\} J_1(\kappa, \rho) \sin(\kappa\rho_0) d\kappa. \quad (3.12)$$

In the case of circularly polarized light with

$$\mathbf{d}_0 = \frac{1}{\sqrt{2}} \begin{bmatrix} 1 \\ \pm i \end{bmatrix}, \quad (3.13)$$

the intensity distribution from Eq. (3.10) is proportional to

$$I \propto \mathbf{D}^* \cdot \mathbf{D} = |B_0|^2 + |B_1|^2. \quad (3.14)$$

Some of the features of conical diffraction beam emerging from a single biaxial crystal by an incident circularly polarized Gaussian beam are shown in the fig. 3.3. The focal image plane corresponds to $\zeta = 0$ (Fig. 3.3(a)), the rings are sharpest in this plane. By increasing the distance ζ , the rings become wider in width and some weak inner rings start to appear as seen in fig. 3.3(b-c). These weak inner rings or oscillations were first predicted by theoretical calculations in [171] and later observed by many others [18, 154]. By further increasing ζ , the inner ring would collapse into a central spot known as ‘‘Raman spot’’ [161, 162] (see fig. 3.3(d)). This central spot in the far field becomes just the incident Gaussian beam.

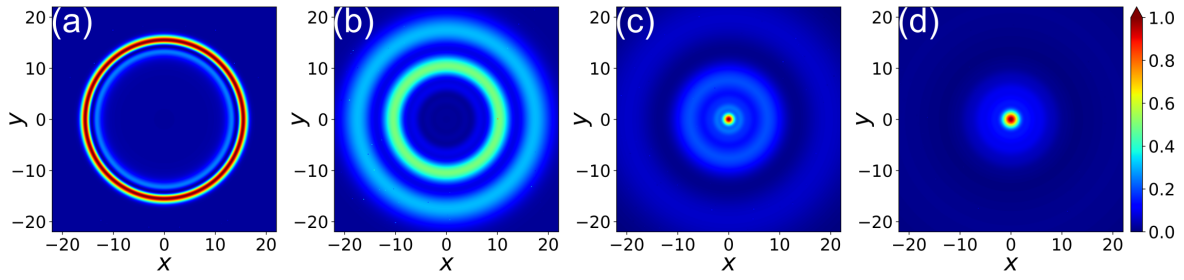


Figure 3.3 – Primary features of conical diffraction with parameters as follows: $\rho_o = 15$ for all the cases with (a) $\zeta = 0$ (b) $\zeta = 4$ (c) $\zeta = 8$ (d) $\zeta = 12$. In the focal plane with $\zeta = 0$, the rings intensity is the sharpest and the rings becomes wider as one looks at planes away from the focal plane. The transverse coordinates are $x = \rho \cos \varphi$, $y = \rho \sin \varphi$.

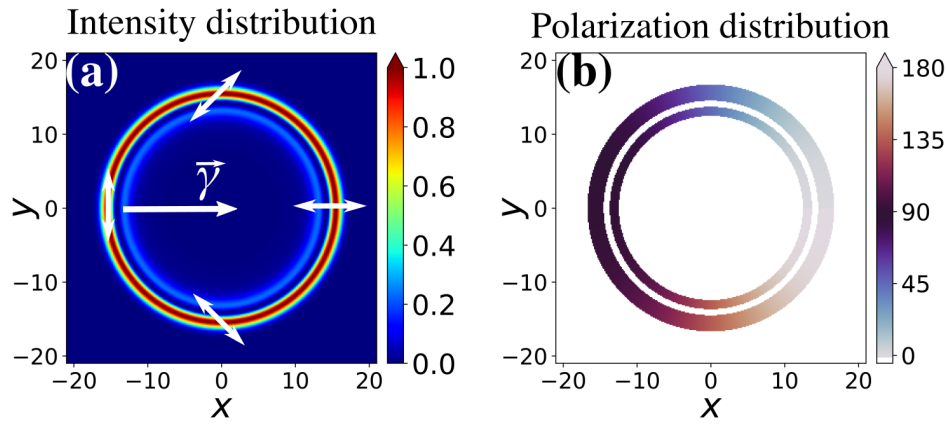


Figure 3.4 – Intensity (a) and polarization (b) distribution for a CD in a single BC with parameters $\rho_o = 15$, $\zeta = 0$ (observation in the focal image plane) and $\gamma = 0^\circ$. The white arrows indicate the orientation of linear polarization at various positions on the ring.

The intensity and polarization distribution for a conical diffraction beam in the focal image plane ($\zeta = 0$) is shown in Fig. 3.4. It can be observed that any two diametrically opposite points on the rings possess orthogonal linear polarization. The position where the polarization is tangent to the ring (vertical linear polarization in the present case) is the one for which the \mathbf{k} and \mathbf{S} vectors overlap. The position where the local polarization is perpendicular to the ring (horizontal polarization in the present case) is the one for which the \mathbf{k} and \mathbf{S} vectors have the maximum walk-off (\mathbf{S}_{max}). One can define a vector γ pointing between these two positions (see Fig. 3.4(a)). The angle γ between this vector and the laboratory x -axis ($\gamma = 0$ here) is an important parameter to characterize the crystal orientations.

3.3.2 Conical diffraction in a cascade

Here we discuss how the above model is extended to the case of a cascade of N aligned biaxial crystals (BC's). This situation was first analyzed theoretically by Berry in [22]. We consider a cascade of N biaxial crystals (represented by $n = 1, 2 \dots N$) with arbitrary lengths

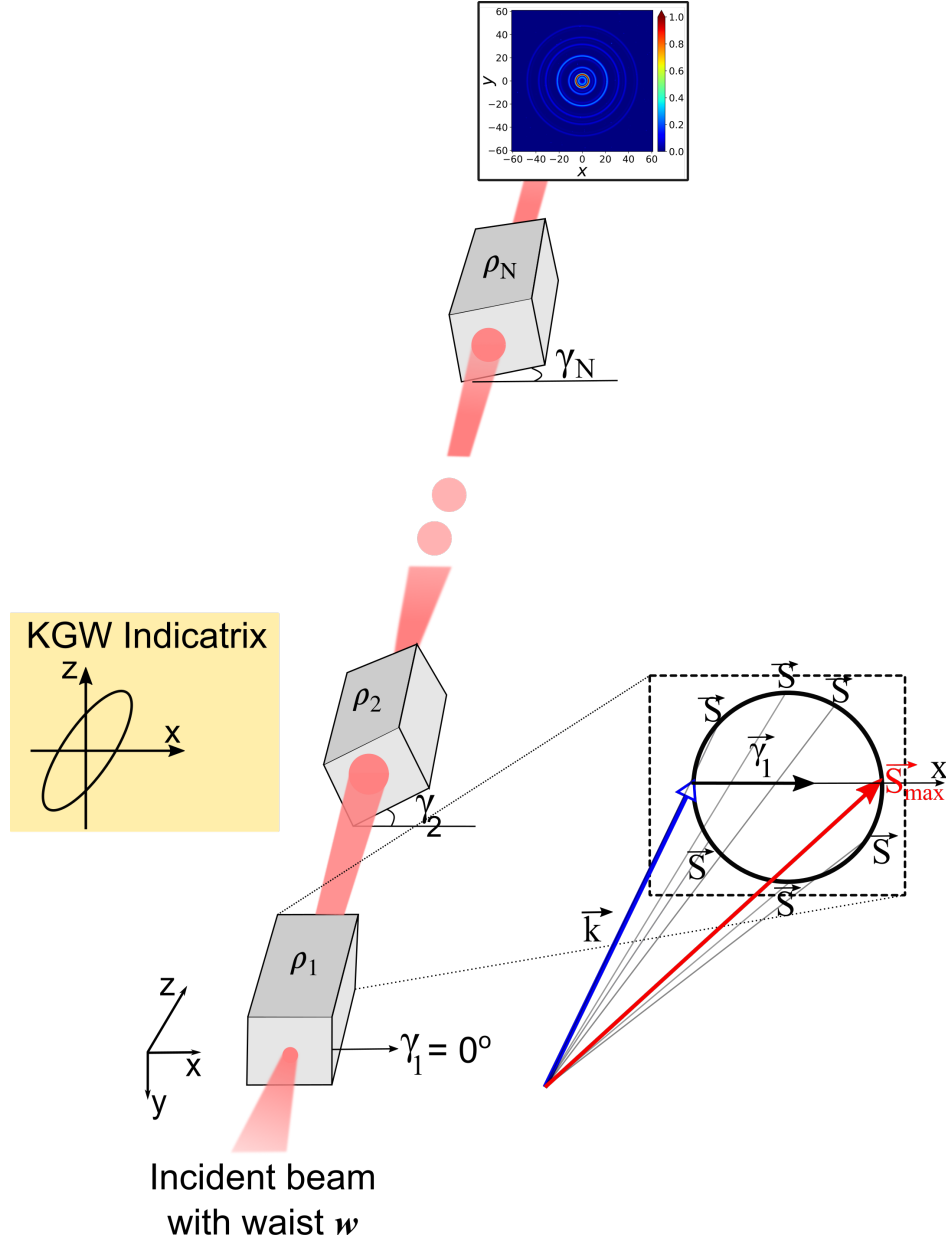


Figure 3.5 – Illustration of an N crystal cascade with arbitrary orientations of the γ_n vector for each crystal.

L_n , possibly different cone semi-angles (α_n) and aligned optic axes in the z -direction. In developing the single crystal CD theoretical model, the orientation of the optic axis plane or the BC rotation around the optic axis defined by γ_n angle was assumed zero (see Fig. 3.4(a)). For a cascade, it is essential to define the γ_n angles as the intensity and polarization in the generated CD pattern depend on the orientation of the BCs in the cascade. This rotation angle γ_n for each crystal in the cascade is defined as the angle between the space fixed x -axis and the direction of the displacement of the cone (expressed by γ_n). This direction of displacement of the cone is explicitly given by $\gamma_n \propto \mathbf{k} \times (\mathbf{S}_{max} \times \mathbf{k})$ where \mathbf{S}_{max} is a unique Poynting vector on the ring, which has a maximum walk-off angle from \mathbf{k} . A schematic illustration of the shifting of the CD cone for the first BC in an extended cascade of BCs is

shown in Fig. 3.5. Here, we consider an extended cascade of BCs for CD with aligned optic axes and arbitrary orientations (γ_n) around the optic axis as in Fig. 3.5. For an incident beam with beam width w (defined as $1/e$ of the intensity), each crystal in the cascade can be characterized by the parameter $\rho_n = \alpha_n L_n / \omega$. As, the radius of the conical diffraction ring is equal to $R = \alpha_n L_n$, thus the parameter ρ_n quantifies ring radius in terms of beam width. The cascade of biaxial crystals transforms a plane wave identified by the transverse normalized wave-number κ with a 2×2 unitary matrix denoted by $U_{tot}(\kappa) = U_{tot}(\kappa, \phi)$. As before all of the parameters are normalized with the beam width. An incident Gaussian beam with Fourier amplitude represented by $\mathbf{D}_0(\kappa, \phi)$ is transformed by the unitary matrix of the cascade and the output electric displacement field $\mathbf{D}_N(\rho, \varphi, \zeta)$ in planes at scaled distances of ζ are obtained by Fourier transformation as below

$$\mathbf{D}_N(\rho, \varphi, \zeta) = \frac{1}{2\pi} \int_0^{2\pi} \int_0^\infty e^{i(\mathbf{k} \cdot \rho - \frac{1}{2}\kappa^2 \zeta)} \mathbf{U}_{tot}(\kappa, \phi) \cdot \mathbf{D}_0(\kappa, \phi) \kappa d\kappa d\phi \quad (3.15)$$

The matrix $\mathbf{U}_{tot}(\kappa, \phi)$ is expressed as the product of the individual unitary matrices associated to each crystal in the cascade.

$$\mathbf{U}_{tot}(\kappa, \phi) = \mathbf{U}_N(\kappa, \phi) \mathbf{U}_{N-1}(\kappa, \phi) \dots \mathbf{U}_2(\kappa, \phi) \mathbf{U}_1(\kappa, \phi), \quad (3.16)$$

whereas each individual unitary matrix of the cascade with its orientation γ_n is given as

$$\begin{aligned} \mathbf{U}_n(\kappa, \phi) &= \exp \left[-i\rho_n \kappa \begin{pmatrix} \cos \phi - \gamma_n & \sin \phi - \gamma_n \\ \sin \phi - \gamma_n & -\cos \phi - \gamma_n \end{pmatrix} \right] \\ &= \begin{bmatrix} \cos(\kappa_n \rho_n) - i \sin(\kappa_n \rho_n) \cos(\phi_n - \gamma_n) & -i \sin(\kappa_n \rho_n) \sin(\phi_n - \gamma_n) \\ -i \sin(\kappa_n \rho_n) \sin(\phi_n - \gamma_n) & \cos(\kappa_n \rho_n) + i \sin(\kappa_n \rho_n) \cos(\phi_n - \gamma_n) \end{bmatrix}. \end{aligned} \quad (3.17)$$

Each of the individual unitary matrix describes the direction dependent dephasing for wave-vectors departing slightly away from the exact optical axis. Thus the final intensity distribution in the plane after the N crystal cascade for a homogeneous and circularly polarized input field (given by Eqs. (3.7),(3.8)) can be obtained as the square of the module of the final \mathbf{D} -vector distribution

$$\mathbf{I}_N(\rho, \varphi, \zeta) \propto \mathbf{D}_N^*(\rho, \varphi, \zeta) \cdot \mathbf{D}_N(\rho, \varphi, \zeta) = |\mathbf{D}|^2. \quad (3.18)$$

From the above formalism, it can be shown that the resulting CD pattern from an N -crystal cascade can be expressed as a coherent superposition of the parameter ρ_n for individual crystals in the cascade

$$|\rho_{tot}| = |\rho_1 \pm \rho_2 \pm \rho_3 \dots \pm \rho_{N-1} \pm \rho_N|. \quad (3.19)$$

By combining all the possible \pm signs, this gives a total of 2^{N-1} values. Hence, there will be 2^{N-1} concentric double rings in the focal image plane for a cascade of N crystals. The amplitudes of these rings would depend on the relative orientations of the successive crystals in the cascade (i.e. on $\Gamma_{mn} = \frac{1}{2}(\gamma_m - \gamma_n)$). An illustrative examples of CD cascades of two, three and four biaxial crystals are shown in Fig. 3.6. All the values of the parameters for the three cascades are given in the caption of the figure.

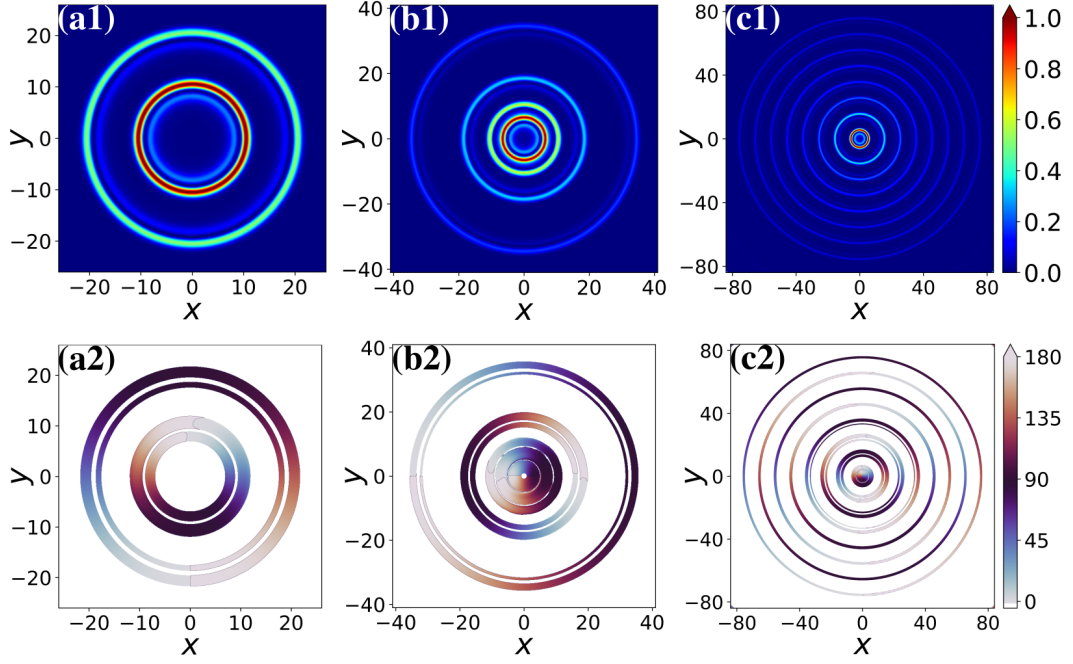


Figure 3.6 – Intensity and polarization distribution in the $\zeta = 0$ plane for a cascade of two [(a1),(a2)], three [(b1),(b2)] and four biaxial [(c1),(c2)] crystals. The parameter are as follows: two crystal cascade ρ values are $\rho_1 = 5$, $\rho_2 = 15$ and γ values are $\gamma_1 = 0$, $\gamma_2 = 90$; three crystal cascade ρ values are $\rho_1 = 8$, $\rho_2 = 12$, $\rho_3 = 14$ and γ values are $\gamma_1 = 0$, $\gamma_2 = 90$, $\gamma_3 = 180$; four crystal cascade ρ values are $\rho_1 = 5$, $\rho_2 = 10$, $\rho_3 = 20$, $\rho_4 = 40$ and γ values are $\gamma_1 = 0$, $\gamma_2 = 90$, $\gamma_3 = 0$, $\gamma_4 = 90$. The number of double rings in each cascade correspond to the 2^{N-1} rule i.e. two, four and eight double rings for the cascade of two, three and four crystals respectively.

In all cases the γ values (crossed crystals configurations) are chosen such that each ring gets equal contribution of energy but this allows for the most internal ring to have more intensity than the external ones as its radius is smaller than others. A choice of crossed crystal configurations also allows all the rings to be observed in the focal images plane and any other choice of γ values could allow to change the corresponding intensities on each ring or even get some rings to disappear. This would be illustrated in detail in the next chapter.

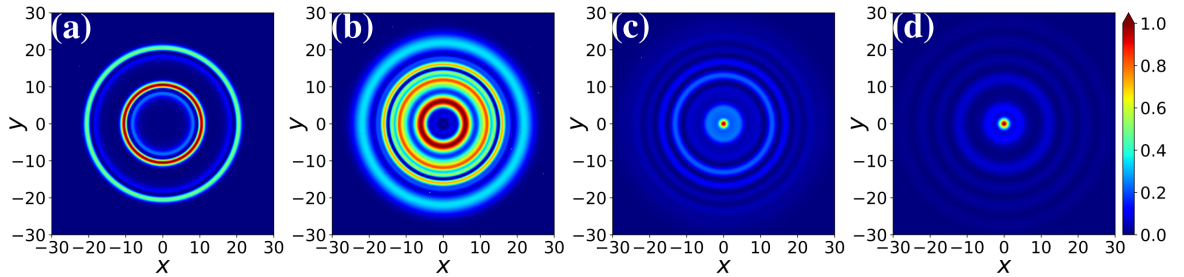


Figure 3.7 – Illustration of the longitudinal evolution of the CD pattern for a cascade of two crystals. The ζ values for the different cases are: (a) $\zeta = 0$, (b) $\zeta = 3$, (c) $\zeta = 6$, and (d) $\zeta = 9$ while the rest of the parameters are same for all cases: $\rho_1 = 5$, $\rho_2 = 15$ and $\gamma_1 = 0^\circ$, $\gamma_2 = 90^\circ$.

The evolution of a CD pattern longitudinally for a cascade of two crystals is shown in Fig. 3.7. It can be observed that at focal image plane ($\zeta = 0$) there are two sharp double rings at radii of $|\rho_1 - \rho_2| = 10$ and $\rho_1 + \rho_2 = 20$. As before for the case of conical diffraction from a single biaxial crystal, as the observation plane is moved away i.e. with increasing ζ values internal rings/oscillations start to appear and also the two double rings increase in their width as they diverge. At $\zeta = 9$ a single spike (central spot) appears and dominates as one moves further away from the focal image plane.

3.4 Recent developments and applications

In the preceding sections, conical diffraction phenomena has been discussed thoroughly with particular focus on the recent developments of the theoretical models for a single as well as a cascade of N biaxial crystals [19, 22]. These theoretical tools have permitted to open a rich and wide range of possibilities for exploring conical diffraction vector beams in fundamental and applied purposes. Below, I give a short overview of the recent progress in conical diffraction phenomena in fundamental aspects as well as application oriented prospects.

3.4.1 Review of fundamental progress in conical diffraction

A major recent development in the field of CD consists in the study of cascaded configurations where two or more crystals are put in series with their optical axes being aligned [22–24, 152, 172–174]. As discussed in the last section, such a cascaded CD leads to a multiplication of the number of observed rings in the FIP, for N crystals one gets 2^{N-1} double rings [22]. Importantly, for two BCs in cascade of the same kind (same α) of lengths L_1 and L_2 the external and internal double rings have a radius $\mathcal{R}_{ext} \propto L_1 + L_2$ and $\mathcal{R}_{int} \propto |L_1 - L_2|$, respectively [22, 174]. Obviously, if the lengths of the two crystals are identical, the internal double-ring will degenerate into a central spot. There is, however, an elegant way introduced recently by Peet [23] to modify these radii by a technique called variable two-crystals cascade. A spherical lens is intercalated between the two cascaded crystals in such a way as to image the FIP near the first crystal into a second FIP near the second BC. It was shown that the magnification factor M of this imaging modifies the relative values of the observed double ring radii according to $\mathcal{R}_{ext} \propto ML_1 + L_2$ and $\mathcal{R}_{int} \propto |ML_1 - L_2|$ [23]. This makes the effect much more versatile and allows the continuous tuning of the actual cascade parameters despite using crystals of fixed lengths.

With respect to the intensity distribution, if the input wave has circular polarization the intensity along the rings is homogeneous. An inhomogeneous azimuthal distribution can be achieved by linearly polarizing the light at the input or output [18] or, more drastically, by scrambling the polarization between two or more BCs in cascade [24], in which case also polarization patterns of increased complexity are obtained. Nevertheless, despite for all the above described developments, the CD patterns obtained before this thesis work possess an intrinsic circular shape. This form is associated to the section of the CD cone with a plane perpendicular to the central light wavevector and the optical axis of the BCs.

Biaxial crystals are inherently capable of spin-orbit coupling, thus besides this vector character of the CD beam, the generated beam has an orbital angular momentum (OAM) which is the half of the total incident momentum. Thus an incident circularly polarized beam would generate CD beam with $\pm \frac{1}{2}$ (sign depending on the incident light being right or left handed circularly polarized) OAM [18, 26–30, 175]. The phase distribution for a non-integer OAM beam is extremely complex and intricate. Recently, several investigations have addressed the continuous scaling of the fractional OAM of CD beams [26–28].

3.4.2 Some applications of conical diffraction

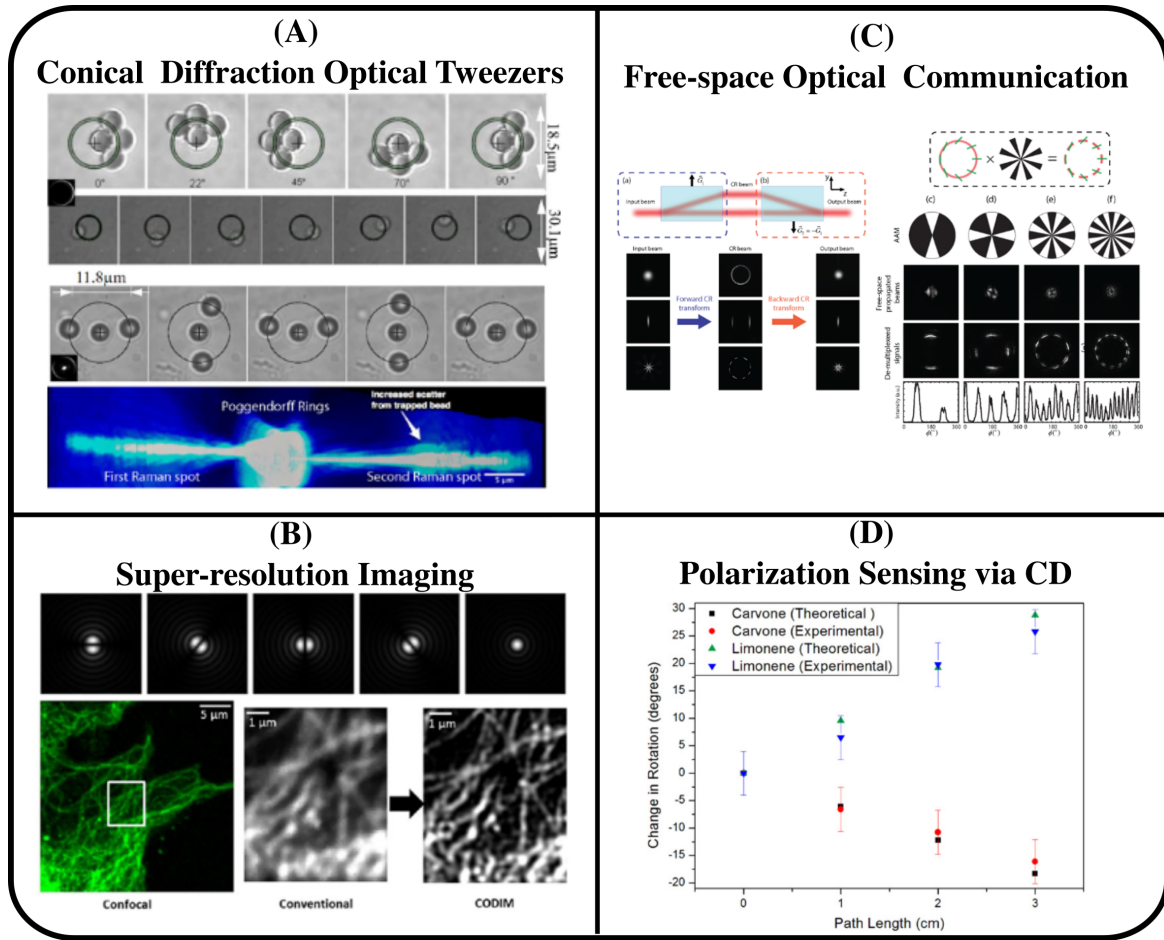


Figure 3.8 – Examples of four applications of conical diffraction demonstrated in the last decade. (A) conical diffraction as optical tweezers [35, 176, 177], (B) super-resolution imaging [40, 178], (C) Free-space optical communication [37] and (D) Polarization sensing via CD [179].

In the last two decades, a renewed interest in conical diffraction has resulted in opening a variety of new regimes for conical diffraction beams such as in optical trapping [35, 180], beam shaping [24, 36], free-space multiplexing for communication [37], polarimetric applications [38, 181], super-resolution imaging [40] or OAM management [26, 27]. Conical diffraction (CD) beams can be used efficiently to rotate or circulate or even levitate micron sized particle [35, 176, 177]. An example for particle control and optical tweezing is shown

in Fig. 3.8(A). The first row shows the anti-clockwise rotation of melamine formaldehyde ($5.3\ \mu\text{m}$) particles, the second row shows the circular motion of red blood cell $8\ \mu\text{m}$ in size, the third row shows the rotation of two particles at diagonally opposite position on the ring while a particle is held in the center and finally, the fourth row show optical levitation of a micron-sized particle near the second Raman spot. In super-resolution imaging, it has been demonstrated that conical diffraction phenomena in a thin biaxial crystal enable acquisitions of super-resolved images of biological samples with very low intensity of light. This avoids the big hurdle of photo-toxicity in those samples due to the high light intensity used in other techniques [40]. An example is shown in Fig. 3.8(B). By utilizing various spatial distributions of conical diffraction patterns as shown in the first row, one can achieve super-resolution images of biological samples in comparison with conventional or confocal microscope. In free-space optical communication, it has been demonstrated that a degenerate cascade of two biaxial crystals (equal lengths and oriented such that the γ vectors are anti-parallel) can be used quite efficiently for multiplexing and de-multiplexing of conical diffraction beams [37]. This example is illustrated in Fig. 3.8(C). The two biaxial crystals are anti-parallel to each other. This implies that an incident Gaussian beam is converted into a CD beam by the first crystal (acts as a multiplexer). Then by the utilization of amplitude masks, one can separate certain polarizations on the rings and eventually propagate them in air or fiber. Finally, the last crystal can be used to convert the CD beam back into the incident Gaussian beam (acts as a de-multiplexer). Finally it has been shown in [179], that unique polarization distribution in CD beams can be utilized to construct a novel optical sensor for detecting the plane of polarization of a linearly polarized light. This CD based polarization sensor determined the amount of rotation of the plane of polarization by the two liquids Carvone and Limonene, which possess the property of being able to rotate the plane of polarization of linearly polarized light passing through them. The obtained results show excellent agreement between theoretical predictions and experimentally obtained values via CD based polarization sensor (see Fig. 3.8(D)).

TAILORED CONICAL DIFFRACTION BEAMS

As described with examples in the last chapter, a cascade of two or more biaxial crystals leads to a multiplication of the number of observed rings in the FIP, i.e. for N crystals one gets 2^{N-1} double rings [22, 172–174]. Despite of all the described developments in the Sect. 3.4 of chapter 3, the CD patterns preserve an intrinsic circular shape. This form is associated to the section of the CD cone with a plane perpendicular to the central light wavevector and the optical axis of the BCs.

In this chapter, it is shown that the circular symmetry can be dramatically broken by a proper manipulation in the wave-vector space between the BCs in a cascade. This leads to CD patterns with highly increased complexity, both in terms of the shapes and of the polarization distribution. The resulting vector beams can be modified in an extremely versatile way by changing the positions of the elements inserted in the cascade that will be described below. What follows gives a detailed analysis of the peculiar non-circular vectorial structures by concentrating on the influence of the cascade parameters, on the structure's general shapes and on their polarization distribution. While the structure forms can be predicted by numerical integration of a properly adapted paraxial diffraction model, simple analytical expressions describing the structure shapes in the last focal image plane cannot be given. However, it is shown that the general shape can be qualitatively predicted with the help of structure parameters (X and Y), which are associated to each individual structure for the horizontal and vertical transverse dimensions, respectively. These structure parameters depend on the birefringence and length of the BCs and on the magnification factors M_x and M_y associated to the imaging between pairs of focal image planes. Also, it is shown that the hierarchy of the structure parameters allows a reliable prediction as whether intersections between structures will occur or not. The structure parameters also influence the polarization distribution on the patterns and its change under variation of experimental parameters, such as the input polarization, an intermediate polarization filtering, or a relative rotation of the BCs around the common optical axis. In single crystal CD and in conventional CD cascades, the local polarization on the rings is linear [18, 22, 24]. This is still true in large extent for the non-circular structures studied in this work. However, we show that some exceptions exist for which elliptical or even circular polarizations can locally occur. It is the case at intersections between structures or when different branches of a

single structure occupy the same spatial position due to degeneracy. The results presented in this chapter correspond in large extent to those contained in Refs. [182] and [152]. The chapter is constructed as follows. Section 4.1 recalls some properties and useful parameters for the description of CD and illustrates the design concept underlying the theoretical and experimental treatment. Section 4.2 gives the theoretical model allowing to calculate the expected patterns numerically, while Sect.4.3 introduces the structure parameters as well as their product parameter and discusses the correlation with the general structure shape with the help of few examples for up to $N = 4$. Finally Sect. 4.4 discusses the output polarization distribution and its change under varying experimental arrangements. This is illustrated theoretically for a three-crystals cascade, as well as theoretically and experimentally for a two-crystals cascade, showing very good agreements. The latter case is simpler because only two structures without intersections can exist. We show that the possible types of patterns as well as their polarization distributions can be classified in three major categories on the basis of the structure parameters. Few other aspects of conjugate cascades such as non-commutation property, possibility to select individual structures and longitudinal evolution of non-circular patterns are also presented.

4.1 Basic concepts and conjugate cascade design

Before describing the specific approach for the conjugate cascade leading to the non-circular patterns we first recall some basic concepts and some formalisms useful to understand CD and the model approach in the theoretical section. Most of these concepts have already been introduced in chapter 3.

A biaxial crystal is characterized by three principal refractive indices, their values determine the cone semi-angle α_n in CD [18, 24], here the index n identifies an individual BC in a cascade. Importantly, for one specific linear polarization the wavevector \mathbf{k} (always aligned to one of the optical axes) and the corresponding Poynting vector \mathbf{S} remains parallel, meaning that the direction of \mathbf{k} lies on the surface of the CD cone formed by all possible \mathbf{S} -vectors. In contrast, for the polarization perpendicular to the previous one, the walk-off angle between \mathbf{k} and $\mathbf{S} \equiv \mathbf{S}_{max}$ is maximum. The angle α_n equals half this maximum walk-off angle. Propagation along an optic axis leaves a free experimental parameter as the whole crystalline sample can be rotated around this axis without preventing the occurrence of the CD effect, but causing a different direction of the slanting of the cone. In the simplest approach the orientation of the BCs can be associated to a vector γ_n , which gives this cone displacement direction and is defined as $\gamma \propto +\mathbf{k} \times (\mathbf{S}_{max} \times \mathbf{k})$ (see Fig. 3.5). Here we take $\mathbf{k} \parallel z$ so that γ_n is in the xy -plane and we define the angle γ_n as the one between γ_n and the laboratory x -axis. Without loss of generality we assume $\gamma_1 = 0$ for the first BC. For standard single crystal CD, the radius of the observable cone ring depends not only on the semi-angle α_n but also on the BC sample length L_n and its sharpness depends on the focusing conditions. It is useful to define a normalized CD strength parameter ρ_n for each crystal given as $\rho_n \equiv \alpha_n L_n / w$, which is the radius of the emerging ring in units of the beam width w . As in [22, 24], w is defined here as the $1/e$ intensity radius of the incident beam focused by a spherical lens and measured in its focal plane. Importantly w corresponds to the incident beam radius in the first focal image plane (FIP1) near the first

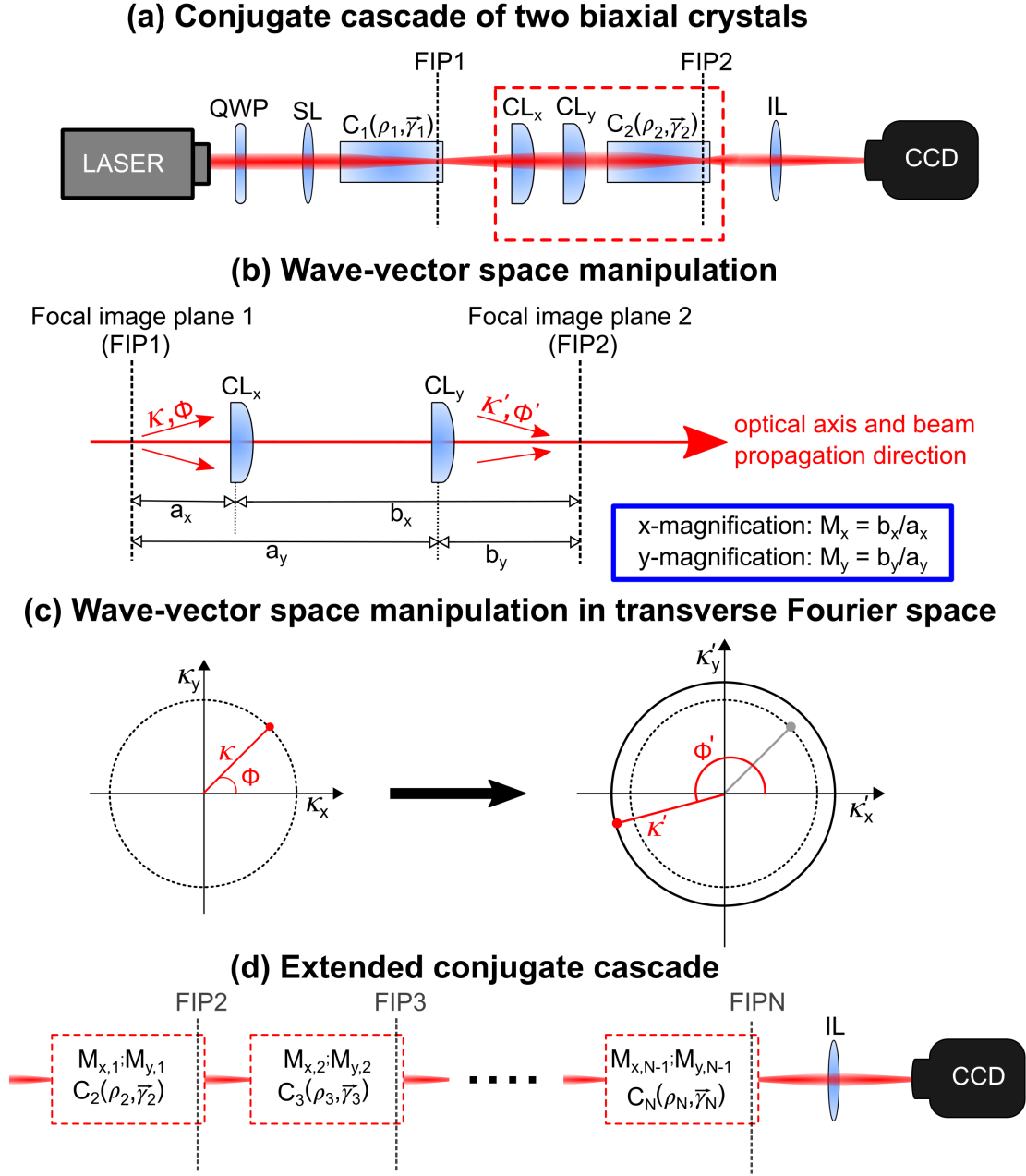


Figure 4.1 – Arrangement and wavevector manipulation in conjugate cascades for generating non-circular CD beams. (a) Schematic set-up for two-crystals cascade. QWP: quarter wave plate, SL: spherical lens, C_1/C_2 : biaxial crystals, CL_x/CL_y : crossed cylindrical lenses, FIP1/FIP2: focal image planes, IL: imaging lens. (b) Wavevector space manipulation and magnifications by the two crossed cylindrical lenses, both imaging the plane FIP1 into FIP2. (c) Wavevector manipulation in transverse Fourier space. (d) Extended conjugate cascade of N crystals with $N - 1$ pairs of cylindrical lenses.

BC in the cascade. All spatial transverse distances are normalized to w . Similarly, the small transverse components of the \mathbf{k} vector (associated to the paraxial beam in Fourier space) are normalized to $1/w$, that is $\kappa = (\kappa_x, \kappa_y) \equiv (k_x w, k_y w)$.

The principle and simplified set-up for generating non-circular CD patterns by conju-

gated cascades via crossed cylindrical lenses is illustrated in Fig. 4.1. Figure 4.1(a) shows schematically the simplest case of a two-crystals cascade. A well collimated laser beam is made circularly polarized and focused by a spherical lens (SL) onto the first focal image plane FIP1 near the first BC (C_1). The two BCs have their optic axes aligned to the propagation direction of the incident beam, however the crystal C_2 may be rotated to an angle $\gamma_2 \neq 0$, most often $\gamma_2 = \pi/2$ in this work. The two crossed cylindrical lenses CL_x and CL_y are arranged in such a way as to make a common image plane FIP2 of the plane FIP1, what is most easily achieved if the focal lengths of the two lenses are different. The principal concept lies in splitting the 2D \mathbf{k} -space into two orthogonal 1D \mathbf{k} -spaces. This allows to independently manipulate the two 1D \mathbf{k} -spaces, as the imaging between FIP1 and FIP2 is associated to independent magnifications, as shown in Fig. 4.1(b). If this imaging would be accomplished by a spherical lens, the module $\kappa \equiv |\kappa|$ of the normalized transverse wavevector would generally change and the sign of each component would be reversed (rotation of the azimuthal polar coordinate angle ϕ by π , $\phi' = \phi + \pi$). In our case (Fig. 4.1(c)), due to the asymmetry in which the x and y components are treated, not only there is a change of κ , but also ϕ is transformed in a more complex way, as discussed in the next section. As illustrated in Fig. 4.1(d), the basic element (dashed box in Fig. 4.1(a)) can be repeated many times to get an extended cascade of N BCs, generally with different magnification pairs $M_{x,i}$ and $M_{y,i}$ between each couple of them. In all cases the pattern observation occurs on the last focal image plane, experimentally (in the case $N = 2$ here) by imaging this plane by a spherical lens (IL) onto a CCD (charge-coupled device) camera.

4.2 Theoretical model

The model presented here builds on Berry's paraxial diffraction theory for a conical diffraction cascade [22]. It is based on a Fourier optics approach and takes into account the asymmetric \mathbf{k} -space manipulations by the CLs as well as the effect of each BC on the phase of the vectorial wave by means of the appropriate transfer function. The latter is a complex matrix in Fourier space. It incorporates the effect of propagation through the corresponding BC with the arguments respecting the \mathbf{k} -space transformation between the crystals. We consider an incident paraxial wave field whose electric displacement vector \mathbf{D} in Fourier space is given by $\mathbf{D}_0(\kappa, \phi)$, with ϕ and κ designating a normalized transverse wavevector in polar coordinates corresponding to a specific plane-wave component (see Fig. 4.1(c)). The emerging \mathbf{D} -field as a result of the cascade is given by the integral;

$$\mathbf{D}(\rho, \varphi) = \frac{1}{2\pi} \int_0^{2\pi} \int_0^\infty e^{i\kappa\rho \cos(\phi-\varphi)} \mathbf{U}_{\text{tot}} \cdot \mathbf{D}_0(\kappa, \phi) \kappa d\kappa d\phi . \quad (4.1)$$

Here ρ is the normalized radial distance and φ is the azimuthal angle in real space. The above real space \mathbf{D} -field is calculated at the plane FIP1 at which the input field \mathbf{D}_0 and the beam width w are defined. The key element in the above integral is the transfer matrix \mathbf{U}_{tot} that contains the effect of the cascade on each plane wave component composing the input beam. This transfer function for a conjugate cascade of N crystals is expressed as

$$\mathbf{U}_{\text{tot}}(\kappa, \phi) = \mathbf{U}_N(\kappa_N, \phi_N, \rho_N, \gamma_N) \cdots \mathbf{U}_2(\kappa_2, \phi_2, \rho_2, \gamma_2) \cdot \mathbf{U}_1(\kappa_1, \phi_1, \rho_1, \gamma_1) , \quad (4.2)$$

where the individual unitary matrices $\mathbf{U}_i(\kappa_i, \phi_i, \rho_i, \gamma_i)$ for $i = 1, 2 \dots N$ are as in Eq. 3.17

$$\mathbf{U}_i = \begin{bmatrix} \cos(\kappa_i \rho_i) - i \sin(\kappa_i \rho_i) \cos(\phi_i - \gamma_i) & -i \sin(\kappa_i \rho_i) \sin(\phi_i - \gamma_i) \\ -i \sin(\kappa_i \rho_i) \sin(\phi_i - \gamma_i) & \cos(\kappa_i \rho_i) + i \sin(\kappa_i \rho_i) \cos(\phi_i - \gamma_i) \end{bmatrix} \quad (4.3)$$

and describe the direction-dependent dephasing of the \mathbf{D} -field x - and y -components for wavevectors slightly departing from the exact optical axis. Equation (4.2) includes the transformations in wavevector space of the arguments from (κ_i, ϕ_i) to $(\kappa_{i+1}, \phi_{i+1})$ between two adjacent matrices, what reflects the action of the crossed CLs. These transformations correspond to the diagram of Fig. 4.1(c) and are a function of the magnifications $M_{x,i}$ and $M_{y,i}$ for the i -th CL pair, i.e.

$$\kappa_{i+1} = \kappa_i \sqrt{\frac{\cos^2 \phi_i}{M_{x,i}^2} + \frac{\sin^2 \phi_i}{M_{y,i}^2}} \quad (4.4)$$

and

$$\phi_{i+1} = \arctan \left[\frac{M_{x,i}}{M_{y,i}} \left(\frac{-\sin \phi_i}{-\cos \phi_i} \right) \right] . \quad (4.5)$$

In Eq. (4.5), special care should be taken to determine the correct quadrant for the arctangent function in accordance with the signs of numerator and denominator. As mentioned above, Eq. (4.1) gives the calculated complex \mathbf{D} -field at FIP1 and would correspond to the observation at FIPN back-imaged to FIP1 through the series of conjugate planes. Thus, in order to compare with experiments one needs to forward-image the calculated results from FIP1 to FIPN. This is better done in cartesian coordinates by taking the calculated field at a position $(x_1, y_1) = (\rho \cos \varphi, \rho \sin \varphi)$ at FIP1 and assigning it to the corresponding imaged position (x_N, y_N) at FIPN, with $x_N = x_1 \prod_{i=1}^{N-1} (-M_{x,i})$ and $y_N = y_1 \prod_{i=1}^{N-1} (-M_{y,i})$. To simplify the notation, these values of x_N and y_N will be simply called x and y in the following theoretically calculated pictures. We remind that imaging by a single lens gives rise to a quadratic phase that depends on the out-of-axis position, on the lens focal length and imaging magnification, and on the light wavelength [183, 184]. For our case with crossed CLs one has independent quadratic phase terms in x - and y -directions for each passage to the next conjugate plane. However, this spatially-varying phase is common to both cartesian components of the \mathbf{D} -field. Therefore it does not influence neither the local polarization, nor the intensity distribution, and it can be safely neglected for the sake of the present investigations.

The theoretical patterns in the following sections are obtained by numerical integration of the two-dimensional complex integral of Eq. (4.1) by considering an incident circularly polarized Gaussian beam with an input electric displacement field;

$$\mathbf{D}_0 = 1/\sqrt{2} \exp(-\kappa^2/2) (1, i)^T. \quad (4.6)$$

The local intensity for any point on FIPN is determined as $I \propto |\mathbf{D}|^2$ after the above described forward imaging. It is important to mention here that the integrals in Eq. 4.1 involve a complex vector quantity (2-dimensional vector) to be integrated over two variables (therefore the equivalent of 4 integrals for each point). For all the obtained theoretical images, a square raster of at least 400×400 integration points have been considered in order to have a sufficient resolution. The integration for such a raster grid could not be performed on a normal computer as it would take upto a week to compute just one raster

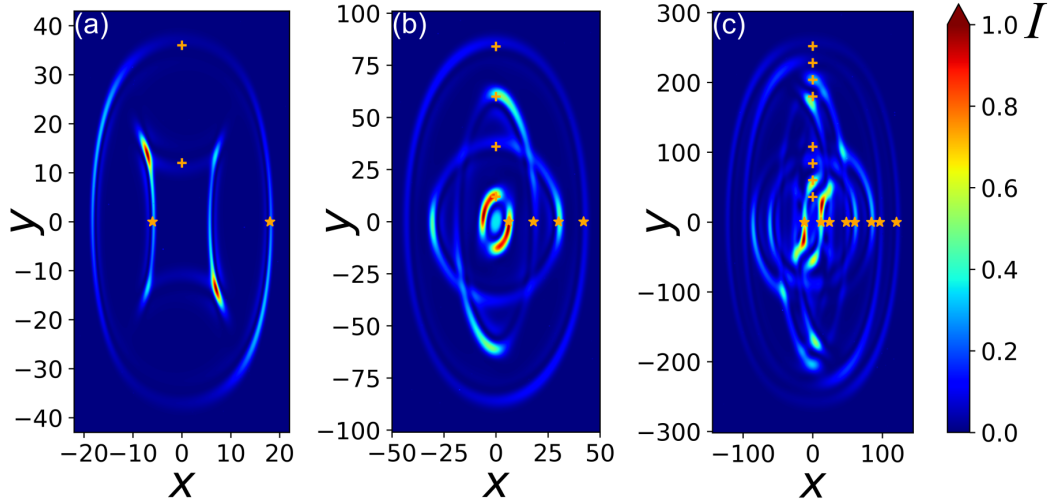


Figure 4.2 – Examples of patterns obtained by conjugate cascades of two (a) three (b) and four (c) biaxial crystals. The CD strength parameters are assumed identical for all BCs, $\rho_1 = \rho_2 = \rho_3 = \rho_4 = 12$. The BC orientation angles are $\gamma_1 = 0$, $\gamma_2 = \pi/2$, $\gamma_3 = \pi$ and $\gamma_4 = 3\pi/2$. The magnification values $M_{x,i}$ and $M_{y,i}$ for each case are given in Table 4.1. The yellow stars and plus signs give the X and Y structure parameters corresponding to the intersection points of the individual structures with the x and y axis, respectively. Their values are also given in Table 4.1. The color scale gives the calculated normalized intensity.

grid for a particular case. Hence integration is performed on a computational cluster and the code for solving this double integral is written in python language involving packages such as SciPy, mpi4py, numba, multiprocessing etc. Gauss- Kronrod quadrature algorithm provided by the QUADPACK library is utilized for numerical computation of the double integral. In order to parallelize the code, MPI (message passing interface) library is utilized, which is pretty standard for parallelizing the computational parts of the code. The computation time is reduced massively by running the codes on the cluster, for instance a raster grid of 400×400 integration points could be calculated in just under 3 hours, by utilizing 25 nodes each with 40 CPU (processors or threads utilized for parallel processing) allowed to calculate 1000 integration points in parallel. Thus decreasing the processing time by atleast 1000 times in comparison with serial computation on a normal computer.

4.3 Structure parameters and general pattern shape

This section aims at understanding qualitatively the various general pattern shapes being observable with our type of CD cascade. This will be done with the help of structure parameters and their hierarchy, which permit to derive some "rules of thumb" for the type of pattern that can be expected. Before entering this discussion, we present in Fig. 4.2 three examples of calculated patterns for a conjugate cascade of two, three and four crystals, respectively. Figure 4.2(a) is for a two-BC cascade. If we place ourselves in the center of the pattern, the external non-elliptical structure is concave, what is also the case for all conventional ring structures obtained by CD in absence of the wavevector manipulation by

the CLs. The internal rectangle-like structure, in contrast, is surprisingly convex and has therefore a reversed curvature. Note that each of the two structures is actually doubled, similarly to the double rings separated by a dark Poggendorf ring observed in conventional CD. Interestingly, the concave external double structure has most of its intensity outside (as in conventional CD [19]), while the internal curvature-reversed convex double structure has most of its intensity on the inside. In Fig. 4.2(b) for $N = 3$ we have four concentric structures, all are concave but two of them intersect each other. Finally, in Fig. 4.2(c) for $N = 4$ we have a total of eight structures with several crossings. In the center region one of the structures is actually convex, even though this is hardly seen due to the local multiple interferences. The complexity obviously increases if one would increase the number N of BCs further. It is worth noting that, in terms of intensity, all patterns of Fig. 4.2 loose a mirror symmetry with respect to the horizontal or vertical axis, but still possess a point symmetry with respect to the central point at $x = y = 0$.

We will now attempt to understand under which conditions one has the appearance of concave or convex structures and in which case one or multiple crossings do occur. To this aim we introduce the so called structure parameters $X_{\pm\pm\ldots\pm}$ and $Y_{\pm\pm\ldots\pm}$ associated to the x - and y -dimensions. These parameters correspond to the intersection points of the structures with the x - and y -axis and are indicated in Fig. 4.2 with yellow stars and plus signs, respectively. The structure parameters depend on the CD strength parameters ρ_i and on the x and y magnifications $M_{x,i}$ and $M_{y,i}$. For a two-crystals cascade they are expressed as

$$X_{\pm} = M_{x,1} \rho_1 \pm \rho_2 \quad ; \quad Y_{\pm} = M_{y,1} \rho_1 \pm \rho_2 . \quad (4.7)$$

The pattern in Fig. 4.2(a) has actually four intersections with each of the axis occurring at $\pm X_-$, $\pm X_+$, $\pm Y_-$ and $\pm Y_+$. Even though the parameters X_- and Y_- in Eq. (4.7) can become negative, this could suggest that only their module would be actually important. This is not true and, as will become clear below, the sign of the structure parameters is a key element for identifying the kind of structure. The corresponding expressions to Eq. (4.7) for the case $N = 3$ are

$$X_{\pm\pm} = M_{x,2}(M_{x,1} \rho_1 \pm \rho_2) \pm \rho_3 \quad ; \quad Y_{\pm\pm} = M_{y,2}(M_{y,1} \rho_1 \pm \rho_2) \pm \rho_3 , \quad (4.8)$$

and for the general case of conjugate cascades of N crystals one has

$$X_{\underbrace{\pm\pm\ldots\pm}_{N-1}} = M_{x,N-1}(M_{x,N-2}(\cdots \pm \rho_{N-1})) \pm \rho_N = M_{x,N-1}(X_{\underbrace{\pm\ldots\pm}_{N-2}}) \pm \rho_N \quad (4.9)$$

and an equivalent relation for $Y_{\pm\pm\ldots\pm}$. Note that in the absence of any lenses (equivalent to the condition where all magnifications M_x and M_y are unity), the absolute values of the above structure parameters give the CD ring radii of the 2^{N-1} concentric rings in a N -crystal cascade [22, 174]. Also, by replacing the crossed CLs by a spherical lens (equivalent to putting $M_{x,i} = M_{y,i}$ for all values of i), the absolute values of the above expressions give the radii of the concentric rings obtained by a so called variable cascade introduced by Peet [23].

A specific structure of a given CD pattern like those shown in Fig. 4.2 is associated to a specific and same combination of "+" and "-" in the X and Y structure parameters among the 2^{N-1} possibilities. For instance, the most external structure in Fig. 4.2(b) is associated to

Table 4.1 – Magnification values $M_{x,i}$ and $M_{y,i}$, structure parameters $X_{\pm\ldots\pm}$ and $Y_{\pm\ldots\pm}$ and signs of product parameters $P_{\pm\ldots\pm}$ for the structures contained in the patterns of Fig. 4.2. The ranks r_x and r_y for the structure parameters are given in the parenthesis.

Number of crystals	Magnification values		X-structure parameter and rank $[X_{\pm\ldots\pm}(r_x)]$		Y-structure parameter and rank $[Y_{\pm\ldots\pm}(r_y)]$		Sign of product parameter $P_{\pm\ldots\pm}$	Obtained pattern
$N = 2$	$M_{x,1}$	0.5	$X_+(1)$	18	$Y_+(1)$	36	pos.	Fig. 2(a)
	$M_{y,1}$	2	$X_-(2)$	-6	$Y_-(2)$	12	neg.	
$N = 3$	$M_{x,1}$	4	$X_{++}(1)$	42	$Y_{++}(1)$	84	pos.	Fig. 2(b)
	$M_{y,1}$	2	$X_{+-}(3)$	18	$Y_{+-}(2)$	60	pos.	
	$M_{x,2}$	0.5	$X_{-+}(2)$	30	$Y_{-+}(3)$	36	pos.	
	$M_{y,2}$	2	$X_{--}(4)$	6	$Y_{--}(4)$	12	pos.	
$N = 4$			$X_{+++}(1)$	120	$Y_{+++}(1)$	252	pos.	Fig. 2(c)
	$M_{x,1}$	3	$X_{++-}(2)$	96	$Y_{++-}(2)$	228	pos.	
	$M_{y,1}$	2	$X_{+-+}(5)$	48	$Y_{+-+}(3)$	204	pos.	
	$M_{x,2}$	0.5	$X_{+--}(6)$	24	$Y_{+--}(4)$	180	pos.	
	$M_{y,2}$	3	$X_{-++}(3)$	84	$Y_{-++}(5)$	108	pos.	
	$M_{x,3}$	3	$X_{-+-}(4)$	60	$Y_{-+-}(6)$	84	pos.	
	$M_{y,3}$	2	$X_{--+}(7)$	12	$Y_{--+}(7)$	60	pos.	
			$X_{---}(7)$	-12	$Y_{---}(8)$	36	neg.	

X_{++} and Y_{++} , while the vertically oriented ellipse-like structure among the two crossing each other is associated to X_{+-} and Y_{+-} . For each structure it is useful to define also a product parameter $P_{\pm\pm\ldots\pm}$ as

$$P_{\pm\pm\ldots\pm} \equiv X_{\pm\pm\ldots\pm} \cdot Y_{\pm\pm\ldots\pm} , \quad (4.10)$$

where again the same combination should be taken in X and Y . Only the sign of the product parameter P will be of importance for our purposes. It is found that a given structure is concave whenever the corresponding value of P is positive, while it is convex if P is negative, meaning that either $X_{\pm\pm\ldots\pm}$ or $Y_{\pm\pm\ldots\pm}$ is negative, but not both. The above conditions can be applied as rules of thumb to determine the general shape of a structure. The case where P is positive can be obtained in two different ways, either both X and Y positive, or both negative. While both cases give a concave structure, the corresponding distribution and behavior of the light polarization is different in the two cases, as it will be illustrated in the next section in the case of a two-crystals conjugate cascade. The values of all structure parameters and the sign of the P -parameter are listed in Table 4.1 for all the structures contained in Fig. 4.2 and confirm the above rules.

It remains to find a rule predicting whether two structures will intersect or not. To this purpose it is useful to assign to each structure parameter also a rank r_x , resp. r_y . The structure parameter $X_{\pm\pm\ldots\pm}$ possessing the largest module will get the rank $r_x = 1$ and the others will get increasing rank with descending value of their module until $r_x = N$. The same procedure is made independently for the ordering of the Y parameters and the assignment of the r_y rank. A given structure is therefore identified not only by the combination of the "+" and "-" indices, but also by the two ranks. For instance, one of the structures in Fig. 4.2(c) corresponds to $X_{+-+}(5)$ and $Y_{+-+}(3)$, meaning that this structure is 5th in rank along x and 3rd in rank along y . Crossing of structures can be avoided only when all the ranks correspond, i.e. $r_x = r_y$ for all pairs of structure parameters.

This is obviously always satisfied for $N = 2$ and crossing are not possible in this case. In contrast, intersections are possible for any $N \geq 3$. Evidently, a given structure can intersect several other ones if the corresponding ranks are very different. The ranks of all structures of Fig. 4.2 are also given in Table 4.1 and confirm the above argumentation. For instance, the crossing observed in Fig. 4.2(b) is explained by the fact that the ranks 2 and 3 are switched for X and Y . Note that the most internal structure parameters X_{--+} and X_{---} have the same rank r_x . This means that the two corresponding structures of Fig. 4.2(c) are degenerate. They occupy the same region of space near the x -axis intersection and interfere in this region. Let us finally remark that changing the orientation angles γ_i of the BCs does not change the general structure shapes and the above rules of thumb remain valid. However, this would change the intensity and polarization distribution, as discussed later.

4.4 Intensity and polarization distribution

In this section we discuss the intensity and polarization distribution of the non-circular patterns generated by the conjugate cascades of Fig. 4.1. This will be done by providing examples for the cases of three BCs and two BCs in the cascade, in the latter case including some experimental comparisons. The polarization is locally linear in most parts of the pattern and the discussion will include the local orientation of this linear polarization (or the main axis orientation of the polarization ellipse), the local phase shift between the y - and x -components of the \mathbf{D} vector, and an eventual elliptical S_3 component of the Stokes vector, where it exists. The impact of a variation of the sample orientation angles γ on the intensity and polarization distribution, as well as the effect of a polarization filtering at various stages in the set-up are also discussed. Few interesting features of conjugate cascades such as non-commutation property, possibility to select individual structures and longitudinal evolution of non-circular patterns are also discussed with illustrative examples.

4.4.1 Local polarization

As discussed earlier, the pattern complexity increases many folds as the number of crystals in the cascade is increased. Due to this reason we limit here our discussion to the cases $N \leq 3$. We start by a three BCs cascade for which two examples are given in Fig. 4.3. The first row gives the relative intensity distribution of the patterns with the position of the stars and plus symbols corresponding to the structure parameters. The argumentations in the last section about the shapes can be applied again. For the pattern in the left column one has two convex internal structures forming together a "Malta cross"-like ensemble. These structures are associated to negative values of P_{+-} and P_{-+} , while the concave structure second in rank is actually associated to negative values of both X_{--} and Y_{--} . The pattern in the right column of Fig. 4.3 is specific with respect to two aspects. First, the central structure is associated to a zero value of Y_{+-} , which results locally on a horizontal straight line in the center ($x = y = 0$). Second, the absolute values of two of the Y structure parameters are degenerate ($Y_{+-} = -Y_{--} = 24$). This means that the corresponding structures have the same rank $r_y = 2$ and interfere near the values $y = \pm 24$, leading to the horizontal nearly

straight lines at these levels.

The second row in Fig. 4.3 gives the color-coded values of the local polarization direction θ on the light pattern observable on FIP3. The angle θ is related to the ratio of the y - and x -components of the \mathbf{D} -field. These components are in general complex, i.e. $D_x = R_x \exp(i\phi_x)$, $D_y = R_y \exp(i\phi_y)$ and θ is defined as $\theta \equiv \arctan [(R_y/R_x)\text{sign}(\cos \Delta\phi)]$, with $\Delta\phi \equiv (\phi_y - \phi_x)$. At most positions the polarization is linear and θ gives simply the polarization direction with respect to the laboratory x -axis. At positions where an elliptical component exists, the angle θ gives the orientation of the polarization ellipse, i.e. the direction of a linear polarizer giving maximum local transmission of the light at the corresponding position on the pattern. Note that, in order to maintain the visibility of the underlying structures, in Fig. 4.3(b) and Fig. 4.3(f) the polarization angle θ is plotted only for positions where the local intensity exceeds a threshold of 0.3% of the maximum one. First, it can be seen that the polarization evolves in the same way in both parts of a single double-structure, this is the case also for the double circular rings in conventional CD. Another common feature with conventional CD is the fact that two opposite points on a given individual structure (connected through a central point reflection) always have orthogonal polarizations. Looking more closely, it can be recognized that here increasing values of θ (from blue to black to brown) are found by moving clockwise on the concave structures and by moving counter clockwise on the convex ones (see Fig. 4.3(b)). This is true also for the more complex pattern in Fig. 4.3(f) that contains only one convex structure, whose intensity for the vertically oriented sections is very faint in Fig. 4.3(e). Interestingly, in the regions of strong degeneracy (on the y -axis near $y = 0$ and $y = \pm 24$), zones with strongly different θ exist in near proximity. It is also important to note that for both patterns the change in the angle θ is not a linear function of the azimuthal polar angle φ , the relationship between these two angles can vary strongly for different structures. In contrast, in the case of circular patterns in conventional CD one has always the linear relationship $\Delta\theta = \Delta\varphi/2$ [18].

The predominantly linear polarization on the patterns can be easily visualized with the help of the relative phase shift $\Delta\phi$ between the phases of the local cartesian y - and x -components of the electric displacement field \mathbf{D} . The light is exactly linearly polarized whenever $\Delta\phi = 0^\circ$ or $\Delta\phi = 180^\circ$. These two values are represented in the third row of Fig. 4.3 as gray and black colors and span most of the pattern's areas. However, relative phase shifts $\Delta\phi$ departing from these two values (bluish or brownish colors), and thus local elliptical polarization, can be observed in regions of interferences where different structures overlap, for instance at intersections. The same conclusions can be drawn by evaluating the elliptical component S_3 of the polarization Stokes vector defined as $S_3 \equiv I_R - I_L$, where I_R (I_L) are the right (left) circularly polarized components of the local intensity (light intensity transmitted through a right (left) circular polarizer). The S_3 components are depicted in the last row (Fig. 4.3(d) and Fig. 4.3(h)). Since the S_3 components are proportional to the local intensity, intense regions gain in importance with respect to the representation based on the phase shift $\Delta\phi$. This is clearly apparent in Fig. 4.3(h) by considering the three intense horizontal zones of Fig. 4.3(e) arising from structure merging due to the above discussed degeneracies along the y -axis.

Next we concentrate on the somewhat simpler case where the cascade is composed of

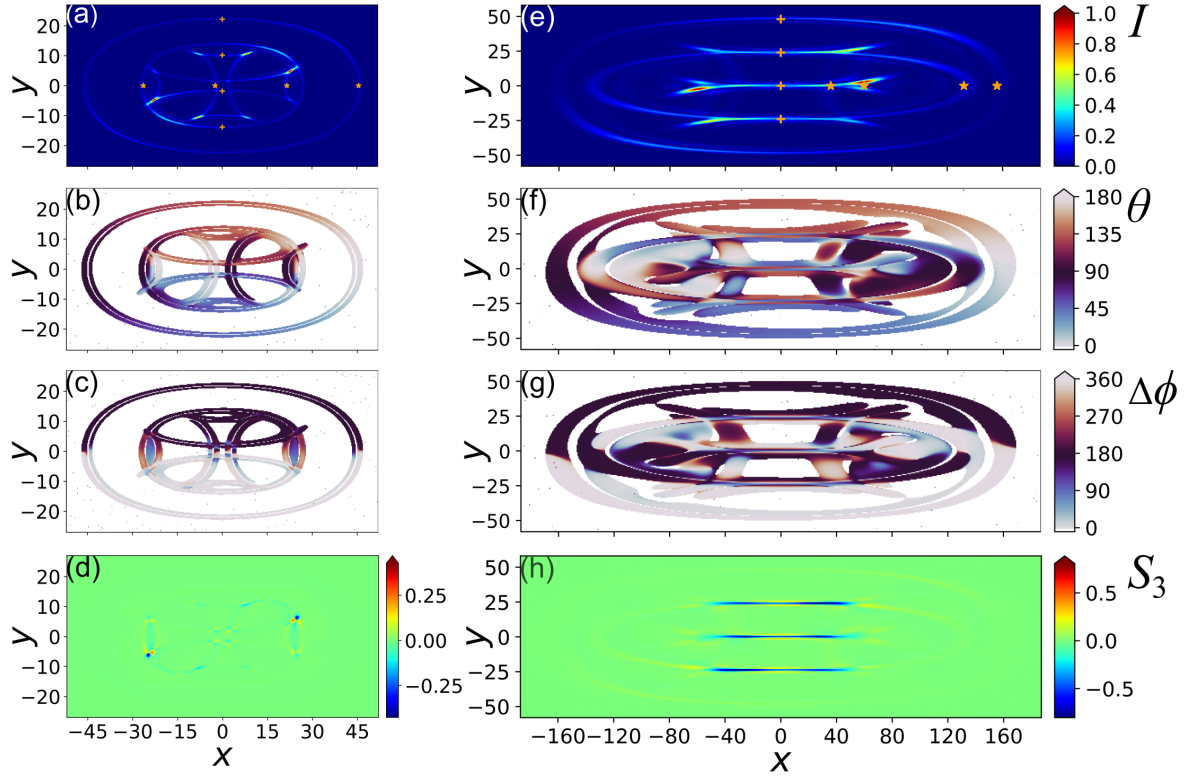


Figure 4.3 – Examples of polarization distributions for two patterns obtained by conjugate cascade of three BCs. Both patterns are for $\rho_1 = \rho_2 = \rho_3 = 12$ and crystal orientation angles $\gamma_1 = 0, \gamma_2 = \pi/2, \gamma_3 = \pi$. For the left column pattern in (a)-(d) the pair of magnification values are $(M_{x,1}; M_{y,1}) = (0.4; 0.7)$ and $(M_{x,2}; M_{y,2}) = (2; 0.5)$. For the right column pattern in (e)-(h): $(M_{x,1}; M_{y,1}) = (2; 0.5)$ and $(M_{x,2}; M_{y,2}) = (4; 2)$. (a) and (e): Distribution of normalized intensity I and calculated positions for the X and Y structure parameters (stars and plus signs). (b) and (f): Angle θ for the orientation of the local polarization ellipse. (c) and (g): Relative phase shift $\Delta\phi$ for the two components of the \mathbf{D} -vector. $\Delta\phi = 0^\circ$ (gray) and $\Delta\phi = 180^\circ$ (black) indicate exact linear polarization. (d) and (h): Local S_3 Stokes vector component for the patterns in (a) and (e). The color scale for each row is given on the right side.

only two BCs, for which structure intersections are absent. Here the CD strength parameters are $\rho_1 = 17.9$ for crystal C_1 and $\rho_2 = 13.9$ for crystal C_2 are chosen to be consistent with our input beam focusing conditions and with the lengths $L_1 = 22.6$ mm and $L_2 = 17.6$ mm of two $\text{KGd}(\text{WO}_4)_2$ ¹ BC samples used for experiments. We choose $\gamma_1 = 0$ and $\gamma_2 = \pi/2$, which implies that the two crystals are oriented in a crossed configuration. The interesting role of the relative orientation angles γ will be discussed in the next subsection. Figure 4.4 illustrates the polarization behavior for three representative patterns corresponding to three distinct cases called respectively case A (left column), case B (central column) and case C (right column). The corresponding calculated and experimentally observed pat-

¹The three main indices for KGW at 633 nm are $n_g = 2.0860$, $n_m = 2.0458$ and $n_p = 2.0135$ and the optical axes lie therefore in the plane containing the indices n_g and n_p . By calculating the direction of the optical axes of KGW, one finds that these axes make an angle of 47.4° with the axis associated to the index n_p and thus an angle of 42.6° with the axis associated to the largest index n_g . The above refractive indices values also allow the calculation of CD cone aperture angle, $\alpha = 19.6$ mrad (via Eq. 2.38).

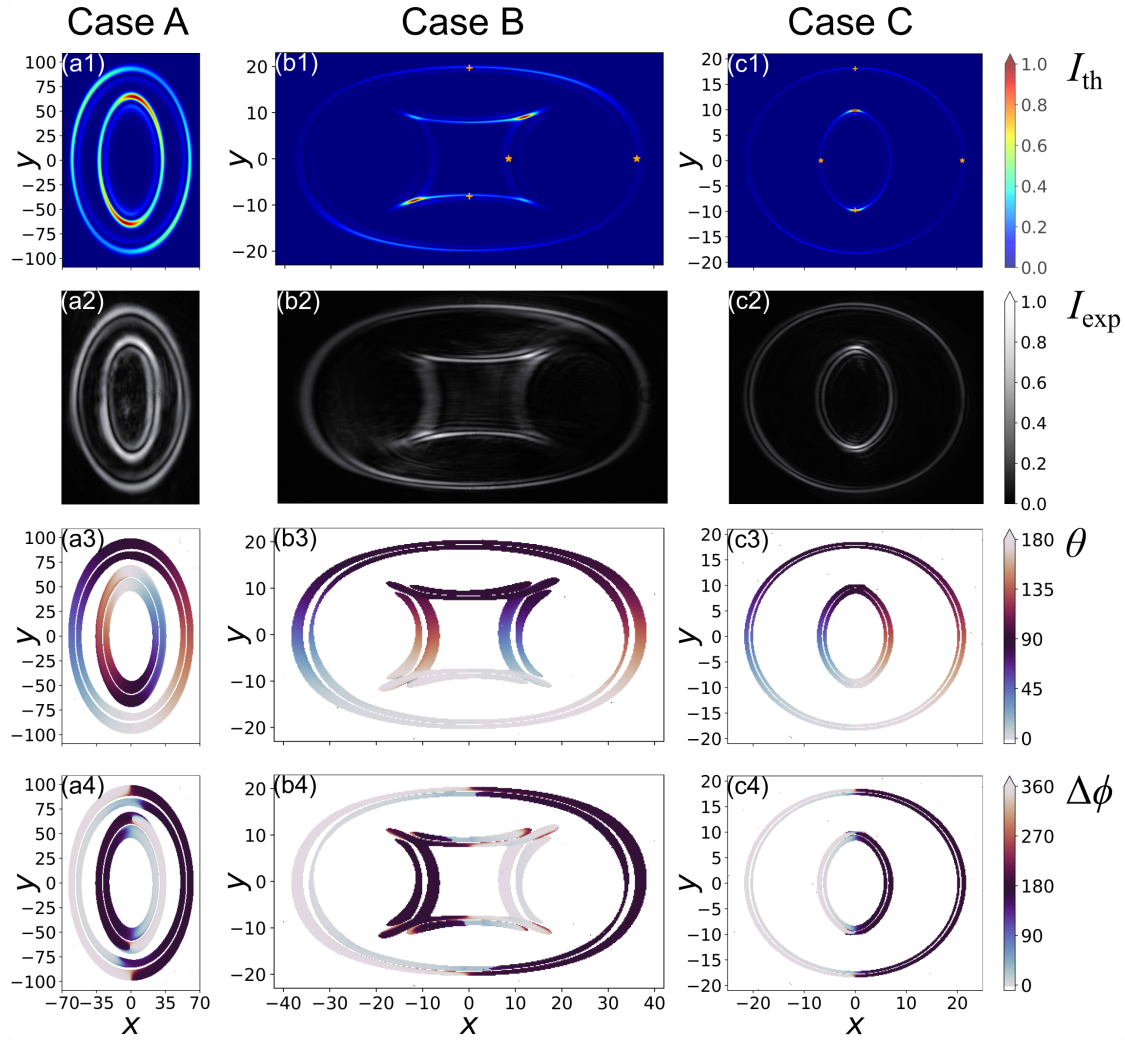


Figure 4.4 – Intensity and polarization distribution for three distinct cases of a two-crystal conjugate cascade. All patterns are for $\rho_1 = 17.9$, $\rho_2 = 13.9$, $\gamma_1 = 0$ and $\gamma_2 = \pi/2$. Case A [left column, (a1)-(a4)] is for magnifications $(M_x; M_y) = (2.5; 4.3)$, case B [central column, (b1)-(b4)] for $(M_x; M_y) = (1.25; 0.325)$ and case C [right column, (c1)-(c4)] for $(M_x; M_y) = (0.4; 0.232)$. First line [(a1)-(c1)]: Calculated normalized intensity I_{th} and positions for the X and Y structure parameters (stars and plus signs). Second line [(a2)-(c2)]: Corresponding experimentally observed intensity patterns (I_{exp}). Third line [(a3)-(c3)]: Orientation angle θ for the local polarization. Fourth line [(a4)-(c4)]: Relative phase shift $\Delta\phi$ for the two components of the \mathbf{D} -vector. The color scale for each row is given on the right side.

terns (upon illumination of the cascade at the wavelength of 633 nm) are given in the first ((a1)-(c1)) and second line ((a2)-(c2)) of Fig. 4.4. In case A both structures are concave and all structure parameters are positive. For case B the internal structure is convex with Y_- being negative. Finally, for case C both structures are again concave. However, this case is distinct from case A because here both internal structure parameters X_- and Y_- are negative. For this specific case one observes strong intensity spots on top and bottom of the internal structure. The local polarization angle θ is shown in the third line (Fig. 4.4(a3)-(c3)). As in the case $N = 3$ discussed above, here increasing values of θ are again observed by turning

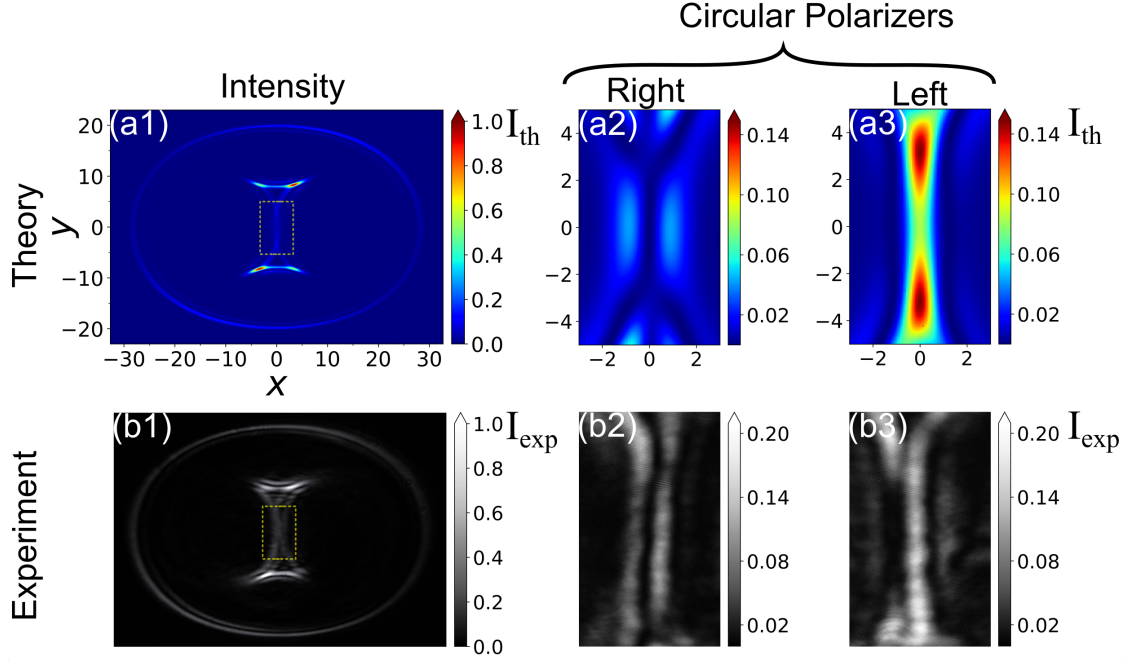


Figure 4.5 – Circular polarization analysis for a two-BC cascade pattern with branches overlap. The pattern is obtained for $(M_x; M_y) = (0.778; 0.323)$ with all remaining parameters as in Fig. 4.4. First line (a1)-(a3): theory. Second line (b1)-(b3): experiments. The four panels on the right show the region of the small rectangles in (a1) and (b1) after filtering with a right ((a2) and (b2)) or a left ((a3) and (b3)) circular polarizer. The center is purely left circularly polarized and the neighboring pair of vertical lines are right circularly polarized.

clockwise for all concave structures and by turning in counter clockwise direction in the internal convex structure of case B. The cases A and C differ by the fact that the positions with a common polarization on the two structures are in phase for case C, while they are in anti-phase for case A. For instance, the vertical polarization ($\theta = 90^\circ$) is on top for both structures in Fig. 4.4(c3), while this polarization is once on top and once on bottom of the two structures in Fig. 4.4(a3). Finally, it is important to note that for these non overlapping structures the local polarization remains linear all over, as in the case of conventional CD. This is easily recognized in the fourth line of Fig. 4.4, where the relative phase shift between the two components of the \mathbf{D} vector assumes only the values $\Delta\phi = 0^\circ$ or $\Delta\phi = 180^\circ$.

The structures in Fig. 4.4 do not cross each other, what prevents the observation of local elliptical components of the polarization. Nevertheless, it is possible to obtain local interferences even for $N = 2$ if different branches of a same structure overlap in the same region of space. This is possible if one of the internal structure parameters (X_- or Y_-) is zero or close to zero, such a case is shown in Fig. 4.5 where $X_- \approx 0.03$. Here one obtains an elongated vertically oriented central structure resembling a letter I, with strong branch overlap in the region identified by the rectangles in Fig. 4.5(a1) (calculated pattern) and Fig. 4.5(b1) (experimental pattern). The four panels on the right side of Fig. 4.5 show the zoomed region of these rectangles after the output light goes through a right or left circular polarizer. Experimentally this is composed of a linear polarizer sandwiched between two quarter-wave plates. It is observed both theoretically (Fig. 4.5(a2)) and experimentally

(Fig. 4.5(b2)) that the right circularly polarized component splits into two vertical sections with a zero intensity node in between. This central region is thus occupied by purely left circularly polarized light, as seen by the central vertical line in Fig. 4.5(a3) and (b3). This spatial separation between the right and left circularly polarized components proves that the output pattern cannot be locally linearly polarized in the corresponding spatial region.

4.4.2 Variation of crystal orientation angles

The relative orientation γ of the various BCs around the common optical axis is a free parameter and influences both, the pattern intensity as well as polarization distribution. This is illustrated in the following with the help of two examples for $N = 2$ (Fig. 4.6(a1)-(b5)) and $N = 3$ (Fig. 4.6(c1)-(d5)), respectively. Each line in Fig. 4.6 shows the intensity and polarization distribution for values of γ_2 increasing from 0 to 180° in steps of 45° , with fixed γ_1 (always) and γ_3 (for $N = 3$). The pattern for $N = 2$ is similar to case B in Fig. 4.4

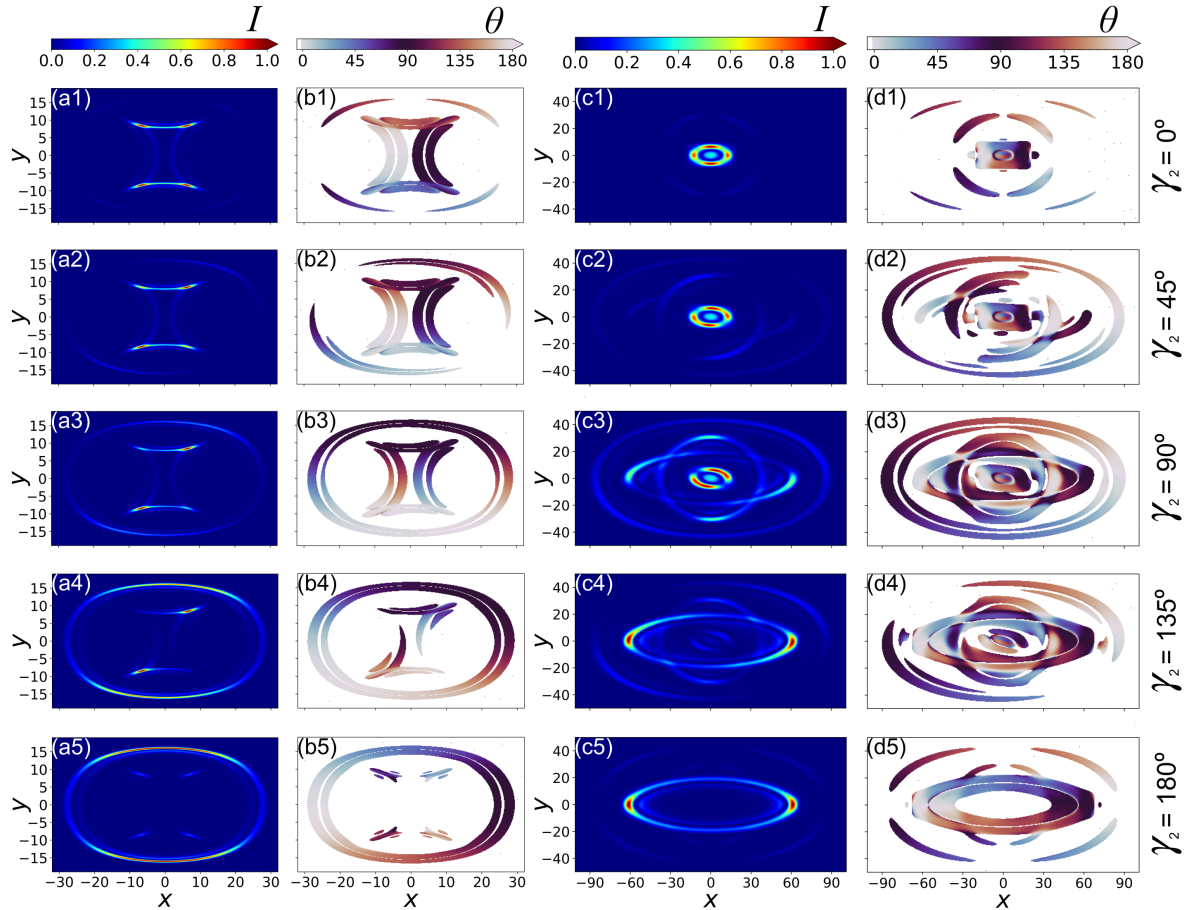


Figure 4.6 – Pattern intensity (1st and 3rd column) and distribution of polarization angle θ (2nd and 4th column) upon variation from 0 to 180° of the orientation angle γ_2 of the second BC in the cascade (given on the right side of each row). The angles $\gamma_1 = 0$ and $\gamma_3 = 180^\circ$ (two right columns) are fixed. (a1)-(b5): $N = 2$ with $(M_x; M_y) = (1.25; 0.325)$. (c1)-(d5): $N = 3$ with $(M_{x,1}; M_{y,1}) = (2; 4)$ and $(M_{x,2}; M_{y,2}) = (2; 0.5)$. All CD strength parameters are assumed equal, $\rho_1 = \rho_2 = \rho_3 = 12$.

and the corresponding relative orientation with crossed crystals ($\gamma_2 = 90^\circ$) is found in Fig. 4.6(a3)+(b3). In contrast, if the two crystals are parallel ($\gamma_1 = \gamma_2 = 0$, Fig. 4.6(a1)+(b1)) the pattern intensity conserves a horizontal and vertical symmetry axis and the individual polarization orientations θ are at azimuthal position rotated by $\pm 90^\circ$ to the previous case. Remarkably, here the internal structure is dominant with only very faint and hardly visible external one (Fig. 4.6(a1)). This feature is exactly opposite to the case of a conventional two-BCs CD cascade, where for parallel crystals only the external ring survives and the internal one completely vanishes [22, 174]. The reason lies in the inversion of the sign of each transverse κ component occurring upon imaging between the FIPs. In the opposite case of anti-parallel BCS ($\gamma_2 = 180^\circ$, Fig. 4.6(a5)) it is the other way round with the external structure dominating and a very faint internal one, again in opposition to the conventional cascade case. For the intermediate angles γ_2 one gets a different balance and intensity distribution in the two structures (left column in Fig. 4.6) and an overall rotation of the positions of individual polarization angles θ by $+\gamma_2$ for the internal structure and by $-\gamma_2$ for the external one (Fig. 4.6(b1)-(b5)), as compared to the case $\gamma_2 = 0$. Note that the situations for angles γ_2 exceeding 180° are not given explicitly because they can be obtained from those depicted here by trivial symmetry operations.

The above argumentation shows that individual structures can be enhanced or "switched off" by a proper choice of the relative angle $\gamma_2 - \gamma_1$. The influence of the γ_i values remains valid for $N \geq 3$, as seen in the two right columns of Fig. 4.6 for a pattern similar to the one in Fig. 4.2(b). Here $\gamma_1 = 0^\circ$ and $\gamma_3 = 180^\circ$ and the four structures are evident for $\gamma_2 = 90^\circ$ (Fig. 4.6(c3)). If the γ_2 value is equal or near to γ_1 the most internal structure is enhanced as compared to all others (Fig. 4.6(c1)). In contrast, if $\gamma_2 \approx \gamma_3$ it is the structure second in rank along x being highly enhanced, as seen in Fig. 4.6(c5). Promoting the two remaining structures is not possible with this combination of the angles γ_1 and γ_3 but would be possible with other choices. For example, the combination $\gamma_1 = 0^\circ$, $\gamma_2 = 180^\circ$ and $\gamma_3 = 0^\circ$ would promote the most external structure. Unlike in the above example for $N = 2$, here the relative orientation of the first and last crystal in the cascade is not changed. As it can be verified in Fig. 4.6(d1)-(d5), this has the interesting consequence that the θ angles for the local polarization are not modified by changing the intermediate angle γ_2 , apart for the regions of structure overlap where the polarization is no longer exactly linear, as we have discussed in Sect. 4.4.1. This is due to the fact that the polarization distribution is largely determined by the last crystal in the cascade. Indeed, the polarization orientation pattern would move drastically if instead of γ_2 one would turn the angle γ_3 .

4.4.3 Non-commutation of the conjugate cascade

Here we discuss a property that is related to the non-commutation of the cylindrical lenses in the conjugate cascades resulting into totally different CD patterns at the focal image plane. Two calculated examples for the case of a cascade of three mutually crossed crystals with wave-vector space manipulation between each pair of them are shown in Fig. 4.7. Figure 4.7 depicts the intensity distribution observable at FIP3. The case of Fig. 4.7(a) shows four structures looking like planetary orbits with two of them intersecting each other is obtained for $M_{x1} = 2.50$, $M_{y1} = 4.30$ and $M_{x2} = 1.25$, $M_{y2} = 0.325$. Remarkably, the

mere permutation of the M_{x1} and M_{y1} values with the M_{x2} and M_{y2} leads to a completely different beam shape. This situation is shown in Fig. 4.7(b), where one observes an internal Maltese cross-like shape formed by the two intersecting convex internal structures, combined with two concave external ones. The above permutation of the magnification values corresponds in practice to exchanging the cylindrical lenses between the first and second BC with those between the second and the third. The fact that this operation leads to fully different patterns is related to the lack of commutation of the matrices within the integral in Eq. (4.1) associated to a generalization of Eq. (4.2). The eight intersection points $\pm X_{\pm\pm}$ and $\pm Y_{\pm\pm}$ of the four structures with the x - and y -axes are found via Eq. 4.8 and the values are listed in Table 4.2. It can be observed that the ordering and the signs of the eight values $X_{++}, X_{+-}, X_{-+}, X_{--}, Y_{++}, Y_{+-}, Y_{-+}$ and Y_{--} give a direct answer that one should expect completely different patterns in these two cases.

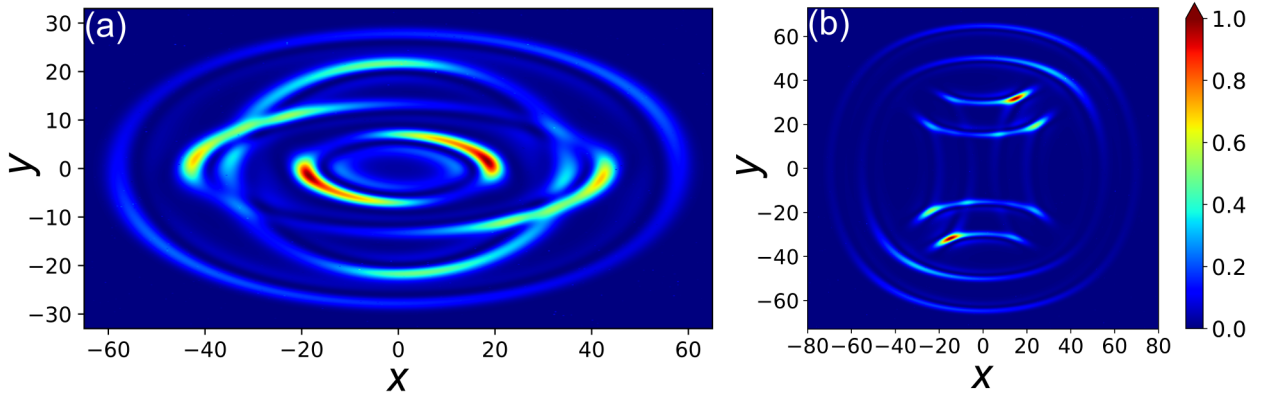


Figure 4.7 – Theoretically calculated intensity distribution of non-circular CD patterns for a cascade of three mutually crossed crystals ($\gamma_1 = 0$, $\gamma_2 = \pi/2$, $\gamma_3 = \pi$) with CD strengths $\rho_1 = 12.0$, $\rho_2 = 9.3$ and $\rho_3 = 7.3$. The magnification factors associated to the k -space manipulations between each pair of BCs are: (a) $M_{x1} = 2.50$, $M_{y1} = 4.30$, $M_{x2} = 1.25$, $M_{y2} = 0.325$; (b) $M_{x1} = 1.25$, $M_{y1} = 0.325$, $M_{x2} = 2.50$, $M_{y2} = 4.30$. Therefore the manipulation in (b) between the second and third BC is the same as the one in (a) between the first and second BC, and vice versa.

For the case in Fig. 4.7(a), we identify from the structure parameter values that the ranks of the second and third structure are different along x -axis and y -axis (see Table 4.2 case (a)), thus these two structures cross each other. However, for the case in Fig. 4.7(b), it is the third and fourth rank structures that are different along x -axis and y -axis (see Table 4.2 case (b)) and hence cross each other. Similarly the sign of the product parameter dictates that all structures in Fig. 4.7(a) possess concave curvature as it is positive for all of them, while the case in Fig. 4.7(b) possess two structures with negative value of the product parameter and thus has two structures with convex curvature (see last column of table 4.2 for product parameter sign).

4.4.4 Possibility to select individual structures

As mentioned above, the intensity on individual structures depends on the given choice of the γ_n angles. Here we discuss briefly how any given structure can be made dominant

Table 4.2 – The values of structure parameters $X_{\pm\dots\pm}$ and $Y_{\pm\dots\pm}$ and signs of product parameters $P_{\pm\dots\pm}$ for the structures contained in the two cases of Fig. 4.7(a) and (b). The ranks r_x and r_y for the structure parameters are given in the parenthesis.

Case	Magnification values		X-structure parameter and rank [$X_{\pm} \dots (r_x)$]		Y-structure parameter and rank [$Y_{\pm} \dots (r_y)$]		Sign of product parameter $P_{\pm\dots\pm}$
(a)	$M_{x,1}$	2.50	$X_{++}(1)$	56	$Y_{++}(1)$	27	pos.
	$M_{y,1}$	4.30	$X_{+-}(2)$	42	$Y_{+-}(3)$	13	pos.
	$M_{x,2}$	1.25	$X_{-+}(3)$	33	$Y_{-+}(2)$	21	pos.
	$M_{y,2}$	0.325	$X_{--}(4)$	19	$Y_{--}(4)$	6	pos.
(b)	$M_{x,1}$	1.25	$X_{++}(1)$	68	$Y_{++}(1)$	64	pos.
	$M_{y,1}$	0.325	$X_{+-}(2)$	54	$Y_{+-}(2)$	50	pos.
	$M_{x,2}$	2.50	$X_{-+}(3)$	22	$Y_{-+}(4)$	-16	neg.
	$M_{y,2}$	4.30	$X_{--}(4)$	7	$Y_{--}(3)$	-31	neg.

over all others. This is done by the same three BCs cascade example as in Fig. 4.6(c1)-(d5). The key is to choose the proper γ_n angles of the BCs in the cascade. In experiment, this situation is achieved by orienting each crystal to a specific orientation (γ angle) required to obtain that corresponding structure. This possibility is illustrated in Fig. 4.8. The choice for the second and third BCs must be either parallel ($\gamma_n = 0^\circ$) or anti-parallel ($\gamma_n = 180^\circ$) to the orientation of the first one (assumed $\gamma_1 = 0^\circ$). There are four possible combinations for the γ_2 and γ_3 angles under these conditions. Each one permits to select one of the four structures as the dominant one, as illustrated in Fig. 4.8.

In the specific case shown here, an interesting non-intuitive observation is that the choice of $\gamma_1 = \gamma_2 = \gamma_3 = 0$ (all BCs parallel) results in selection of the second inner most structure (third in rank along x -axis). Similarly, a choice of $\gamma_1 = \gamma_3 = 0$ and $\gamma_2 = 180$ results in selection of the outermost structure (first rank structure along x -axis and y -axis). It is important to point out that the same kind of approach can be used to select individual structures in a cascade of N BCs by choosing the $\gamma_2\dots\gamma_N$ orientation angles of the last $N - 1$ BCs between the values 0° and 180° .

4.4.5 Polarization filtering at different stages

The patterns given in the preceding sections were obtained with circular polarized input wave and without additional polarizing elements in the cascade. However, the insertion of a linear polarizer at the input, between the BCs or at the output of the cascade modifies the pattern intensity distribution. In this section, we use again the cases A, B and C for a two-crystals conjugate cascade to illustrate this effect in Fig. 4.9, which is associated to the same cascade parameters as Fig. 4.4. There are obviously many possible combinations for the polarizer positions and orientation angles β . For all cases investigated, good agreements between theoretical expectations and experiments have been found, as illustrated below for

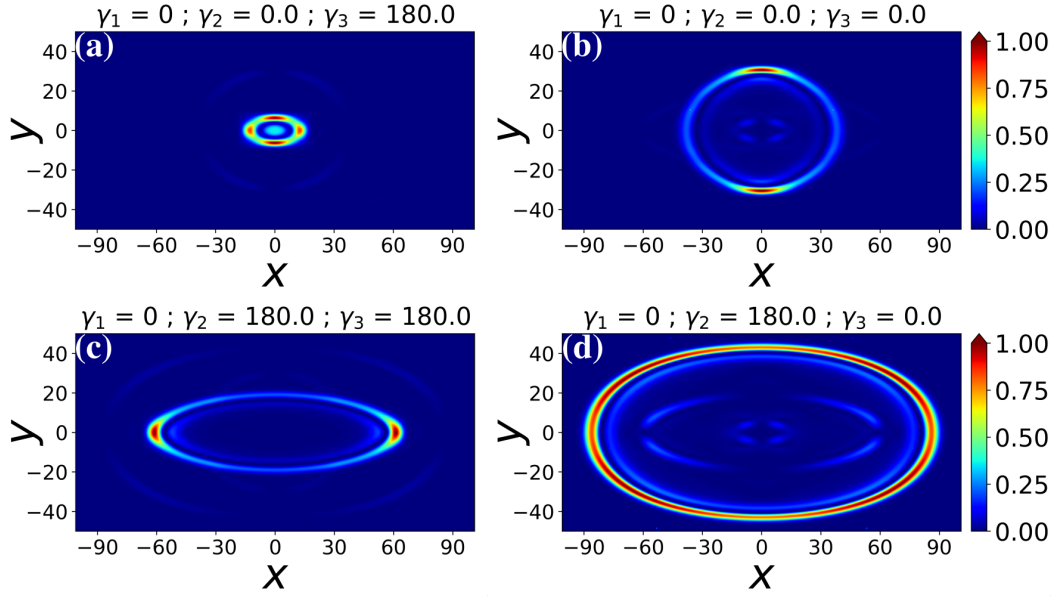


Figure 4.8 – A three crystal cascade with variations in γ angles in order to select individual structures. The values of the γ angles for each crystal in the cascade are mentioned on top of each pattern. Other parameters are as follows: $\rho_1 = \rho_2 = \rho_3 = 12$ and $(M_{x,1}; M_{y,1}) = (2; 4)$ and $(M_{x,2}; M_{y,2}) = (2; 0.5)$.

the case where the polarizer is at the input of the cascade. The effects observed when the polarizer is either in the middle (between the BCs) or at the end (after FIP2) of the cascade are discussed here only by experiments but agree with our simulations.

Let us address first the case where an input linear polarizer is inserted before the cascade, this case is shown in Fig. 4.9(a1)-(c2) for the theory and Fig. 4.9(a3)-(c4) for the experiments. A careful observation shows that for all three cases A, B and C a linearly polarized input leads to a zero intensity node on each of the two structures composing the pattern. These nodes have the same origin as the intensity node on the ring observed in conventional CD with linear, rather than circular, input light polarization [18]. For a polarizer angle $\beta = 0^\circ$ (1st and 3rd rows in Fig. 4.9) the nodes are on the same side for the two structures for cases A and B, while for case C the internal node is on the left side and the external one on the right side. If the input polarizer is rotated by an angle β ($\beta = 45^\circ$ in 2nd and 4th rows of Fig. 4.9), the node positions rotate by $-2\beta = -90^\circ$ for case A and case C. For case B the nodes rotate by $+2\beta$ for the internal structure and by -2β for the external one, leading to nodes on opposite sides in Fig. 4.9(b2) and (b4). These opposite directions for the node positions are associated to the opposite evolution of the polarization angle θ in the two structures of case B, discussed above in connection to Fig. 4.4(b3).

The situation where the polarizer (analyzer) is inserted at the output of the cascade is shown in the 5th and 6th rows (Fig. 4.9(a5)-(c6)) and is easy to understand. Here the transmitted pattern is the output polarization pattern at FIP2 projected onto the output analyzer and weighted with the local light intensity. Each structure exhibits one node at the position where the local polarization is perpendicular to the orientation of the analyzer. For instance, for case C a horizontal analyzer ($\beta = 0^\circ$) leads to attenuation of the top parts of

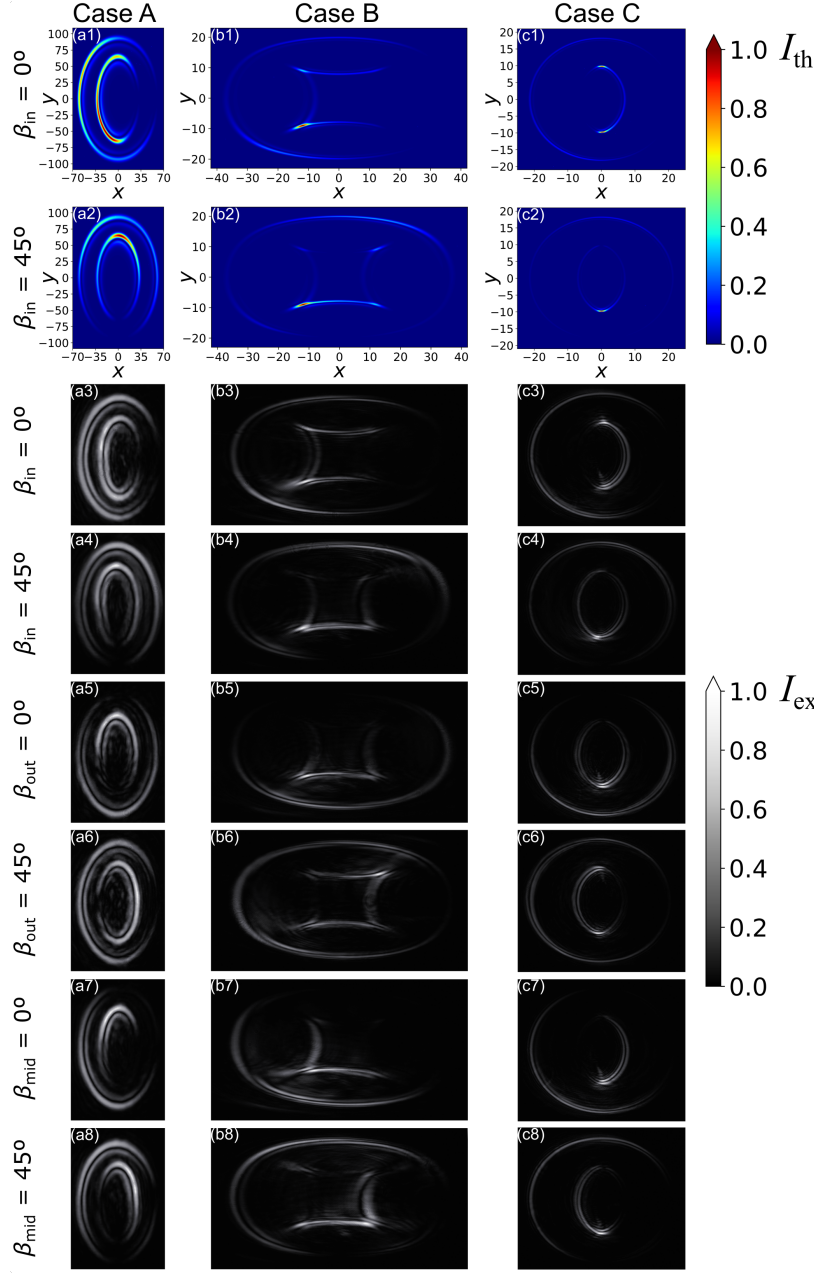


Figure 4.9 – Intensity patterns upon filtering with a linear polarizer at different stages of a two-BC cascade. The first column, (a1)-(a8) is for case A of Fig. 4.4, the second, (b1)-(b8) for case B and the third (c1)-(c8) for case C. First four rows (a1)-(c4): Filtering of the input polarization under the angle $\beta_{in} = 0^\circ$ or $\beta_{in} = 45^\circ$, as given on the left. (a1)-(c2): Theory, (a3)-(c4): Corresponding experiments. (a5)-(c6): Experimental patterns for filtering at the cascade output with a linear analyzer under the angles $\beta_{out} = 0^\circ$ or $\beta_{out} = 45^\circ$. (a7)-(c8): Experimental patterns for intermediate filtering between the two BCs with polarizer angles $\beta_{mid} = 0^\circ$ or $\beta_{mid} = 45^\circ$. All CD strength parameters and magnification values are as in Fig. 4.4.

both structures, with nodes on the top where the polarization is vertical (Fig. 4.9(c5)). If the analyzer is turned to $\beta = 45^\circ$ the left side of both structures is conserved (Fig. 4.9(c6)) while the right side, associated to polarizations near 135° in Fig. 4.4(c3), is strongly attenuated.

Similar conclusions can be drawn for cases A and B.

The last two rows of Fig. 4.9 illustrate the case where a polarization filtering is performed between the two BCs of the conjugate cascade. This situation is somehow more complex and is connected to the intermediate polarization scrambling or filtering that was studied earlier in Ref. [24] for the case of circular CD patterns. For an intermediate polarization transformation being a simple linear polarization filtering like here and for two crossed crystals, it was shown in [24] that each of the two CD rings gets two intensity nodes. It was also found that the external ring nodes are azimuthally shifted with respect to those for the internal ring and that the nodes on a single ring are azimuthally separated by 90° . Such a double node for each of the two structures obtained for $N = 2$ is theoretically predicted also for our non-circular patterns. Nevertheless, since the expected and observed intensity in the structure regions between the two nodes are often very faint, their existence is hardly seen by a mere visual inspection, giving the impression of whole dark quadrants. For the experimental patterns shown in Fig. 4.9 the existence of the double nodes can be recognized better in Fig. 4.9(a7) (case A, internal nodes on bottom and right and external nodes on top and right) and Fig. 4.9(b8) (case B, internal nodes on left and top and external nodes on right and bottom). In all cases the double nodes have the effect that on each structure a given quadrant is dark or nearly dark. Since the relative orientation of these external and internal quadrants is off by 90° , also the high intensity regions on the two structures forming the pattern are shifted by the same amount. This is in contrast to the above discussed cases where the polarization filtering is at the entrance or at the output of the cascade. It is worth noting that, as demonstrated in [24], other types of intermediate polarization manipulations can also be applied, all resulting in complex and eventually reconfigurable azimuthal distributions of the intensity and polarizations on the patterns. This is even more true if the cascade is extended to more than two BCs.

4.4.6 Evolution of non-circular CD patterns beyond $\zeta = 0$ plane

In this section, the evolution of the non-circular CD patterns beyond the focal image plane (i.e. beyond $\zeta = 0$ plane) of the conjugate cascade are presented. The discussion is limited to a cascade of two crystals and only the experimental results are presented here. Three different cases are analysed for the longitudinal evolution of the patterns (see fig. 4.10). It is important to mention here that CD beams from a convectional cascade would result into a Raman spot at a certain plane beyond the focal image plane, which is like the incident Gaussian beam. However a conjugate cascade results into unique evolution of the patterns depending on the rule of thumb parameters and shape of the structures in the conjugate focal image planes.

The three patterns in Fig. 4.10 correspond to the three cases A, B and C as discussed earlier on. The far-field patterns in Fig. 4.10(a) correspond to the case where both of the structures have concave curvature and it can be observed that this pattern keep its shape in the far-field, i.e. diverges symmetrically. However, both the inner and outer structures of the pattern in Fig. 4.10(b) transform into a caustic pattern. Finally, the pattern in Fig. 4.10(c) behaves like the conventional cascade in the sense that the outer structure develops weak internal rings in the far-field, but the internal structure instead of conversion into an axial

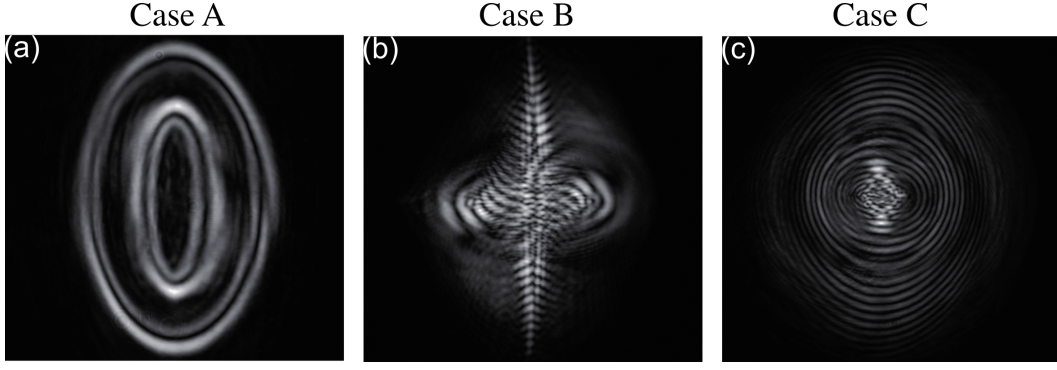


Figure 4.10 – Experimentally obtained far-field images for the conjugate cascade of two biaxial crystals. The parameters for the three cases are as follows: (a) $M_x = 2.5$, $M_y = 4.3$, (b) $M_x = 1.25$, $M_y = 0.325$ and (c) $M_x = 0.4$, $M_y = 0.232$. $\rho_1 = 17.9$ and $\rho_2 = 13.9$ for each of the case.

spike (Raman spot) transforms into a caustic with spun cusps [49]. This is interesting from the point of view that these caustics shapes are polarization dependent. It is worth noting that interest has arisen recently in generating caustics for fundamental and application purposes [185, 186].

4.5 Conclusion

We have analyzed theoretically and experimentally the unusual non-circular vector beam patterns obtained in a conjugate conical diffraction cascade with intermediate manipulation in wave-vector space. It was shown that the intensity and polarization distribution on the concave or convex structures composing the conical diffraction pattern can be successfully predicted by a paraxial model taking into account the asymmetric \mathbf{k} -space transformations. For a N -crystals cascade a total of 2^{N-1} structure parameters $X_{\pm\pm\ldots\pm}$ and $Y_{\pm\pm\ldots\pm}$ in each of the Cartesian directions were introduced. These parameters depend on the conical diffraction strengths of the individual BCs and on all magnification values between adjacent conjugate planes. They allow to find rules of thumb for the general shape of the pattern structures and to predict eventual intersections. It was shown that the local polarization on the non-circular structures is linear with the exception of regions of structure crossings or local overlaps of different branches of a same structure, where elliptical or circular polarizations can be present. The polarization angle evolution is not a linear function of the polar angle on the structure and for the case $N = 2$ three distinct cases for the polarization distribution were identified on the basis of their structure parameters combination. In this latter case the modified patterns expected by a linear polarization filtering at the input, output or at the intermediate position in the cascade were determined and confirmed experimentally. Finally, it was shown that the local polarization angles and local intensities on the individual structures depend on the rotation angles γ_i of the BCs around the common optical axis. The orientation of the last crystal determines the polarization distribution, while the relative orientation of all crystals determines the intensity distribution and the relative importance of individual structures. Another interesting aspect observed was the possibility to isolate a specific structure out of 2^{N-1} for a N BC cascade by a careful choice

of the rotation angles γ_i of the individual BCs in that cascade. It was also shown that non-commutation of the cylindrical lenses in the conjugate cascades leads into totally different CD patterns at the focal image plane and the non-circular patterns evolve in a complex manner longitudinally. The effects discussed here lead to an increased vector pattern richness and versatility as compared to the circular rings of conventional CD cascades.

FRACTIONAL CHARGED OAM BEAMS

As already discussed in Chapter 1, the orbital angular momentum (OAM) arises naturally in beams with azimuthal phase structure of $e^{il\varphi}$, where l is an integer and φ is the azimuthal angle. Light beams with integer OAM consists of a stable optical vortex possessing corresponding topological charge in the center of the beam (on propagation axis). However, the beams with fractional charge OAM in general consists of alternating charge (± 1) vortices around the center of the beam. Another particular feature is that the intensity distribution contains a low intensity line, which corresponds to the branch cut orientation or phase step discontinuity of the generating optical device. The number of optical vortices in the cross-section of a fractional OAM beam are equal to the value of OAM rounded to the nearest integer i.e. $S_\alpha = \text{integer}(l + 1/2)$ but this excludes the exactly half integer or multiples of half integer OAM values, as for them there exists an infinite number of alternating charge vortices along the direction of low intensity line which corresponds to the phase step discontinuity of the spatial phase plate utilized to generate them [56, 91, 187]. This implies that vortices are created and annihilated in beams with fractional OAM. The creation of a vortex happens as the OAM value increases from exact half integer and annihilation of a vortex happens as the OAM value decreases from exact half integer. This has already been thoroughly investigated both theoretically and experimentally. The theoretical and experimental work relating to fractional OAM beams has been performed by generating these sort of beams via spiral phase plate or by a spatial light modulator [91, 187–190]. In contrast, fractional OAM beams of a natural origin such as those generated via the conical diffraction (CD) phenomenon still lack profound investigations.

Standard conical diffraction beam possess fractional OAM of exactly $\pm\hbar/2$ per photon, the sign depends on the handedness of the incident circular polarization (i.e. + for left and – for right circular) [25]. This is evident from the fact that a conical diffraction beam can be considered as a superposition of two beams corresponding to the B_0 and B_1 components in Eqs. (3.10) - (3.12), which are related to the Bessel functions of zero and first order respectively. The phase and electric field distribution in these components depends on the input polarization such that a left circularly polarized Gaussian incident beam would result in B_0 component with $J_{orb} = 0$; $J_{spin} = +1\hbar$ and B_1 component with $J_{orb} = +1\hbar$; $J_{spin} = -1\hbar$. Thus the total angular momentum of conical diffraction beam has spin part equal to

zero ($S = 0$) while the orbital part is equal to $+\hbar/2$ per photon [26–28]. It has already been shown that the fractional OAM of CD beams can be scaled by all optical means by separating either B_0 or B_1 [31–33]. In this chapter, it is demonstrated that the fractional OAM can be scaled in non-circular conical diffraction beams without separating or selecting any one component of the beams. This scaling in addition to the non-circular complex distribution of phase and intensity brings interesting new fundamental aspects into play.

5.1 Experimental methods for measuring OAM

The most familiar method for determining the OAM or observing the vortices in a beam are plane wave interferences, where the OAM beam is interfered in a collinear or noncollinear manner with its mirror image or a plane reference wave. The collinear interference results in spirals in the intensity pattern with the number of spiral equal to the absolute value of the OAM and the handedness of these spirals indicates the \pm charge of OAM. Similarly, a non-collinear interference results in interference fringes with forks appearing at the positions of the vortices, the charge of the vortex is equal to the number of prongs minus one. The fractional OAM beams contains an additional degree of complexity as the single charge vortices in them are displaced across the beam cross-section. Thus, we have resorted to two additional methods for determining the fractional OAM of our non-circular CD beams. Firstly, an off-axis digital holography is used to simultaneously measure the spatial amplitude and phase of the beam and secondly, a quantitative measurement of fractional OAM is performed by utilizing a cylindrical lens. These three methods and the fundamental physics involved are described below.

Plane wave interference

Let's consider an interference of a signal beam \mathbf{E}_s and reference beam \mathbf{E}_r of same frequency and amplitude (mutually coherent) but propagating with an angle of 2α between their wavevectors \mathbf{k}_s and \mathbf{k}_r . Our intention is to take a look at the density of the electromagnetic energy in a plane perpendicular to the sum of the interfering wavevectors $\mathbf{k}_s + \mathbf{k}_r$. The signal and reference beams can be written in the complex notations in paraxial regime as

$$\mathbf{E}_s = \mathbf{E}_0 e^{i(\omega t - \mathbf{k}_s \cdot \mathbf{r})}, \quad (5.1)$$

$$\mathbf{E}_r = \mathbf{E}_0 e^{i(\omega t - \mathbf{k}_r \cdot \mathbf{r})}. \quad (5.2)$$

The free space density of electromagnetic energy can be expressed as

$$w_E = \frac{1}{4} \epsilon_0 \mathbf{E} \cdot \mathbf{E}^* \quad (5.3)$$

where \mathbf{E} is the superposition of the interfering waves i.e.

$$\begin{aligned} \mathbf{E} &= \mathbf{E}_s + \mathbf{E}_r \\ &= \mathbf{E}_0 e^{i\omega t} (e^{-i\mathbf{k}_s \cdot \mathbf{r}} + e^{-i\mathbf{k}_r \cdot \mathbf{r}}) \end{aligned} \quad (5.4)$$

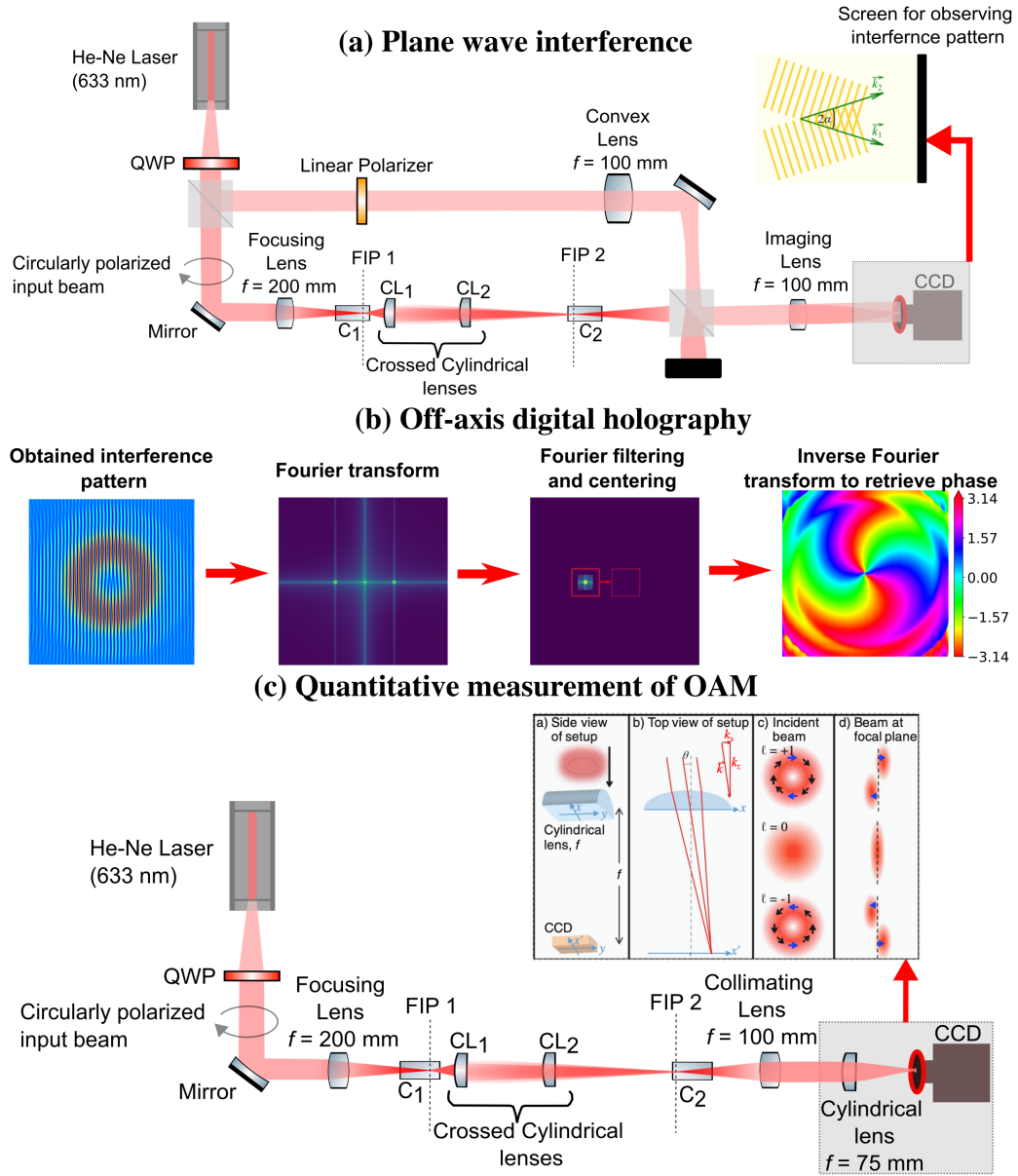


Figure 5.1 – Three experimental techniques are utilized to determine OAM of the non-circular patterns generated in a conjugate cascade of biaxial crystals. (a) shows an optical setup for plane wave interference technique, (b) shows off-axis digital holography and (c) shows quantitative measurement of OAM of non-circular CD beams via a single stationary cylindrical lens, while the inset shows the principle concept of OAM measurement via a cylindrical lens [191].

By calculating the scalar product of the resulting field (i.e. $\mathbf{E} \cdot \mathbf{E}^*$) and utilizing cartesian coordinates, it can be shown that the energy density at the projected screen (plane of observation) can be written as

$$w_E = E_0^2 \epsilon_0 \cos^2(kx \sin \alpha). \quad (5.5)$$

This expression for energy density clearly indicates that the energy density varies only along the coordinate (x -axis) that lies in the plane defined by the signal and reference beams

wavevectors¹. The interference pattern on the screen consists of fringes perpendicular to the x -axis. The corresponding fringe spacing between two minima is

$$\Delta x = \frac{\lambda}{2 \sin \alpha}. \quad (5.6)$$

Thus the fringe spacing in the interference pattern gets sparser with increasing wavelength and denser with increasing angle between the interfering beams wavevectors. This particular behaviour is of high importance for the off-axis digital holography (OFDH) measurements, so it would be discussed later on.

The optical setup for plane-wave interference experiments is shown in Fig. 5.1(a). The incident beam is split into two beams via a beam splitter and then one of the beam (signal beam) passes through the conjugate cascade setup for generating non-circular CD beams while the other beam (reference beam) after traversing approximately identical path length² is combined with the first beam via a second beam splitter. The two beams at a slight angle (non-collinear) with each other are directed via an imaging lens onto the CCD for observing the interference pattern.

Off-axis digital holography

Off-axis digital holography utilizes the hologram (or interference pattern) recorded onto a CCD to determine the amplitude and phase of the signal beam[192]. The term off-axis is used here as the interference pattern is created by two beams that propagate at small angles, and the word digital is used as the interference pattern is recorded into a CCD and later on processed digitally. In our investigations, the plane wave interference patterns recorded via the method described above are used for determining the spatial phase of the beams. The recorded intensity (into the CCD) of the interference pattern generated by the interfering signal and reference beams has four components

$$|\mathbf{E}_s + \mathbf{E}_r|^2 = |\mathbf{E}_s|^2 + |\mathbf{E}_r|^2 + \mathbf{E}_s^* \mathbf{E}_r + \mathbf{E}_s \mathbf{E}_r^*. \quad (5.7)$$

The first two terms on the right-hand side correspond to the intensity of the signal and reference beams respectively and they contain no phase information. The last two terms are basically the signal beam modulated by the reference beam. These last two terms contain the full complex field of the object and reference beams and they are complex conjugate of each other. Actually, it is sufficient to isolate the last term and get rid of the other three terms. In order to separate the term $\mathbf{E}_s \mathbf{E}_r^*$ (i.e. signal beam times the conjugate of reference beam), a Fourier transform is performed and indeed, due to the tilt in the reference beam, it becomes possible to separate off-axis terms in the Fourier domain. As already discussed in the last section, the tilt in the reference beam is responsible for creating a cosine fringe pattern. Such a fringe pattern is composed of straight lines in the background, these lines

¹In other words, energy density becomes only the function of the coordinate that lies in the plane formed by the interfering wavevectors (in the above case $w_E = w_E(x)$) and it is independent from the other coordinates.

²In order to have reasonably resolved fringe patterns, the path difference between the two beams should be within the coherence length/coherence time of the laser source.

can become curved upon interaction with a non-planar signal beam and hence this curving also captures the phase information of the signal beam. Now, one can also write the Fourier transform of the interferogram (interference/fringe pattern) as the super-position of the Fourier transform of each of the four terms above

$$FT(|\mathbf{E}_s + \mathbf{E}_r|^2) = \underbrace{FT(|\mathbf{E}_s|^2)}_{\text{DC component}} + \underbrace{FT(|\mathbf{E}_r|^2)}_{\text{order -1}} + \underbrace{FT(\mathbf{E}_s^* \mathbf{E}_r)}_{\text{order +1}} + \underbrace{FT(\mathbf{E}_s \mathbf{E}_r^*)}_{\text{order +1}}. \quad (5.8)$$

The 2-D Fourier transform of an interferogram recorded on a CCD has three components, the first two terms are the DC component (or auto-correlation terms and contains no phase information) and they are located in the center of the Fourier domain as can be seen in Fig. 5.1(b), which depicts the principle scheme of off-axis digital holography. The Fourier transform of the plane wave is a single bright spot in the center and on top of this is the Fourier transform of the intensity of the signal beam. This central region is not required for our purpose as it does not contain any phase information. In Fig. 5.1(b), it can be observed that the off-axis higher order terms (or cross-correlation terms of order +1 and -1) are located spatially at different position in the Fourier domain. The Fourier transform of the term $\mathbf{E}_s \mathbf{E}_r^*$ (signal times the conjugated reference) can also be written as the convolution of Fourier transform of signal and reference beams i.e. $FT(\mathbf{E}_s) * FT(\mathbf{E}_r^*)$. As mentioned earlier the $FT(\mathbf{E}_r^*)$ is just a single point in Fourier space thus this term just represents the Fourier transform of the signal wave shifted in space corresponding to the tilt angle of the reference wave. Here it is important to mention that the tilt angle of the reference beam should be reasonable to have well resolved interference fringes but enough to separate the high order terms (cross-correlations terms) from the DC component (auto-correlation term). Thus the spatial separation between the higher order components allows to filter the order +1 ($FT(\mathbf{E}_s \mathbf{E}_r^*)$) by cropping this component and then moving it to the center of the Fourier domain for removing the tilt of the reference wave³. Finally, an inverse 2-D Fourier transform allows to go back to the image plane to retrieve the complex wavefront of the signal beam (see right panel in Fig. 5.1(b)).

Quantitative measurement of the fractional orbital angular momentum

Here a quantitative method for determining the fractional OAM via a cylindrical lens is presented. Before discussing the experimental setup and presentation of results, a brief discussion is presented on how a cylindrical lens is utilized for determining the OAM of a beam. This experimental method is presented in detail in Ref. [191]. From classical mechanics, a single photon angular momentum with respect to the beam center is defined as

$$L_z = (\mathbf{r} \times \mathbf{p}) \cdot \hat{z} = xp_y - yp_x = \hbar(xk_y - yk_x) \quad (5.9)$$

Here \hat{z} is considered as the direction of propagation of the beam, (x, y) represent the Cartesian coordinates, (p_x, p_y) represent the photon momentum in the transverse plane and

³The tilt of the reference can be removed as a linear phase ramp becomes a shift in the Fourier space. An alternative way to accomplish this is as follows. One selects the desired higher order component in Fourier space and inverse Fourier transform this region to go back to the image plane, where one can multiply the field with the reference wave to remove the tilt. Both the methods are equally effective in removing the tilt of the reference wave.

(k_x, k_y) are the wavevector transverse components giving the local propagation direction with respect to the z -direction. By using the formalism of geometrical optics in order to relate the wavevectors transverse components with the spatial positions in the focal plane of a cylindrical lens, the average OAM for a collection of photons can be defined as [191]

$$\langle L_z \rangle = \frac{2\pi\hbar}{f\lambda} [\langle xy' \rangle - \langle yx' \rangle]. \quad (5.10)$$

A cylindrical lens transforms an incident photon linear momentum to a corresponding spatial position in its focal plane (see inset in Fig. 5.1(c)). Which implies that the two terms in the parenthesis on the right side of Eq. (5.10) can be determined by orienting the axis of cylindrical lens horizontally and vertically. By the lens horizontal orientation, the distribution of photons momentum along the y -axis is obtained and vice versa for the vertically orientation. A cylindrical lens provides a one-dimensional Fourier transform of a mode in its focal plane, this allows to calculate the average OAM by calculating the covariance terms according to

$$V_{x'y} = \langle yx' \rangle = \frac{\iint_{-\infty}^{\infty} I(x', y) x' y dx' dy}{\iint_{-\infty}^{\infty} I(x', y) dx' dy}, \quad (5.11)$$

and, analogously

$$V_{xy'} = \langle xy' \rangle = \frac{\iint_{-\infty}^{\infty} I(x, y') x y' dx dy'}{\iint_{-\infty}^{\infty} I(x, y') dx dy'}. \quad (5.12)$$

The term $V_{x'y}$ is the covariance term that calculates the distribution of photons momentum along the x -axis by orienting the cylindrical lens axis along the y -axis. Analogously, $V_{xy'}$ calculates the photon momentum along y -axis for an x -axis oriented cylindrical lens. The intensities $I(x', y)$ and $I(x, y')$ in Eqs. (5.11) and (5.12) represent the spatially resolved intensities at the cylindrical lens focal plane. Finally, the measured OAM is related to the above covariance as

$$l_{measured} = \frac{2\pi}{f\lambda} (V_{x'y} - V_{xy'}) \quad (5.13)$$

The experimental setup is shown in Fig. 5.1(c). The generation part of the non-circular patterns from a conjugate cascade is exactly the same as discussed earlier on in chapter 4. For quantitative OAM measurements, the generated non-circular patterns are collimated by a spherical lens and are then focused by the cylindrical lens onto a CCD. Importantly, the CCD is placed at the focal plane of the cylindrical lens. Thus by orienting the cylindrical lens axis horizontally and vertically, both covariance terms $V_{x'y}$ and $V_{xy'}$ can be measured from the recorded CCD images. Each recorded CCD image is a two-dimensional array of intensity values, with $x' = y = 0$ as a centroid of the reference Gaussian beam traversing the whole optical system.

5.2 Examples of OAM determination

In this section, few illustrative examples on how to determine the OAM of hypergeometric-Gaussian beams (HyGG) and of conical diffraction beams are discussed. The HyGG modes are modelled based on Ref. [57]. They have azimuthally varying phase profile and also possess an on-axis vortex (the field amplitude vanishes at the center where there is an on-axis

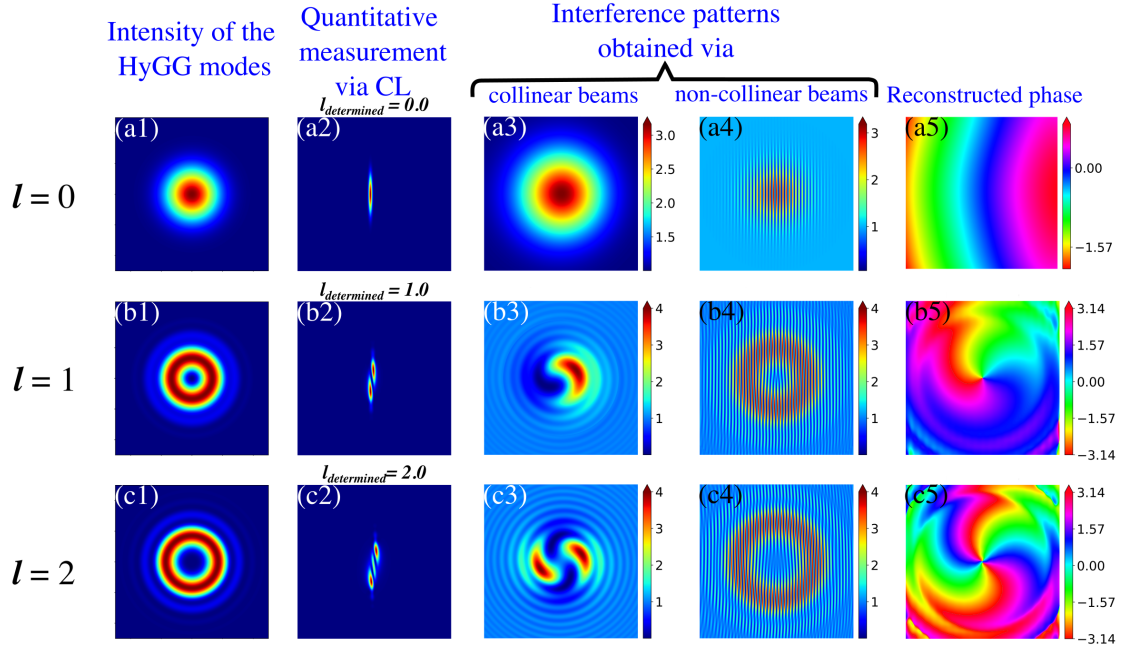


Figure 5.2 – Principle of OAM determination of the HyGG beams via different techniques. First column (a1)-(c1): intensity distributions of the various modes; Second column (a2)-(c2): intensity distribution for the modes after focusing by a cylindrical lens (oriented vertically) for quantitative measurement of OAM; Third (a3)-(c3): and fourth (a4)-(c4) column: collinear and non-collinear interference patterns of the modes with a plane wave, respectively. Fifth column (a5)-(c5): extracted phase distribution of each mode via the off-axis digital holography technique described in Sect. 5.1.

singularity) with topological charge equal to l . Their intensity profile consists of a single ring (for modes with $l > 0$). In order to verify the techniques, several modes of HyGG modes are numerically generated with a known OAM value (l value), we then verify this value by the techniques described above. Figure 5.2 shows the determination of OAM for Hypergeometric-Gaussian (HYGG) fundamental mode ($l = 0$) and two other modes with $l = 1, 2$. As mentioned earlier, their intensity distribution is characterized by a single ring (see Fig. 5.2(a1)-(c1)). The quantitative determination of the OAM value of these modes via the cylindrical lens method is performed and the results showed that this technique aided in retrieving the exact OAM value for each of the mode (see Fig. 5.2(a2)-(c2)). Similarly, a collinear and non-collinear plane wave interference with the modes $l = 1$ and $l = 2$ revealed the presence of spirals (see Fig. 5.2(b3)-(c3)) and forks (see Fig. 5.2(b4)-(c4)) at the center of the beam, respectively. The number of spirals and forks correspond to the l value of the modes. While for the mode with $l = 0$, neither spiral nor forks are observed for the collinear and non-collinear plane wave interference, verifying the topological charge $l = 0$ for this fundamental mode (see Fig. 5.2(a3)-(a4)). By utilizing the interference pattern obtained via non-collinear interference of these modes with the plane wave, the azimuthal phase of these modes is obtained using the off-axis digital holography technique. It is observed that, as expected, the azimuthal phase changes by 2π (one turn) around the center for the $l = 1$ mode (Fig. 5.2(b5)) and by 4π (two turns) around the center for $l = 2$ mode (Fig. 5.2(c5)). Also, again there is no variation or turning of azimuthal phase around the center for the HyGG fundamental mode, thus verifying its zero OAM value.

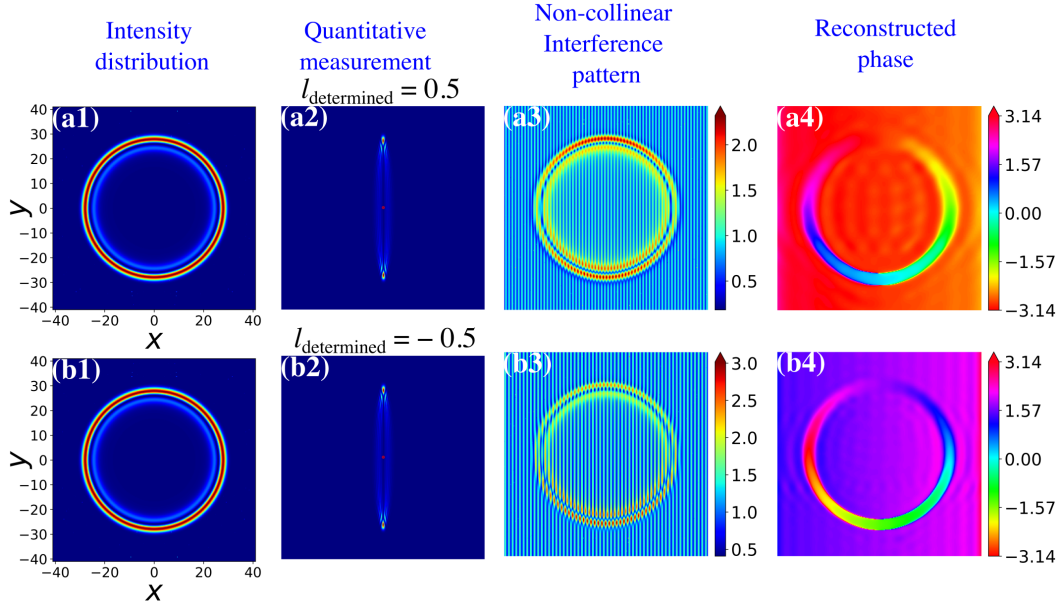


Figure 5.3 – OAM measurement of the conical diffraction beam via various techniques. The first and second row corresponds to a simple CD patterns obtained via left handed and right handed incident circular polarization respectively. (a1) and (b1) shows CD patterns intensity distribution, (a2)-(b2) shows the intensity distribution for each CD pattern after focusing by a cylindrical lens (oriented vertically) for the quantitative measurement of OAM, (a3) and (b3) shows interference patterns obtained via interfering of CD beams with an off-axis plane wave, (a4) and (b4) shows the phase of the CD beams obtained via off-axis digital holography from the corresponding interference patterns.

The OAM of the simple conical diffraction beam is also investigated for a further illustration of the three techniques described in the last section. It has already been shown that a CD beam possess fractional OAM of exactly $\pm\hbar/2$ with $+$ charge for left and $-$ charge for right circularly polarized incident beam [25]. Figure 5.3 shows the determined OAM values via different techniques for a CD beam obtained by focusing a circularly polarized beam along the optic axis of a single biaxial crystal. The intensity distributions for CD beam obtained via left and right circular incident beam are identical (see Fig. 5.3(a1) - left and (b1) - right). A quantitative determination of the OAM value of the CD beam showed that indeed a CD beam obtained from left(right) circularly polarized incident beam has fractional OAM of $+(-)\hbar/2$ (see Fig. 5.3(a2)-(b2)). Similarly, an interference pattern obtained via interfering non-collinearly CD beam and a plane wave is shown in Fig. 5.3(a3)-(b3). Since the interference patterns can only give qualitative measurement of OAM, the fractional nature of the CD beams makes it impossible to guess any value of OAM in this case. Nonetheless the interference patterns reveals slight shifting of the fringes at particular spatial positions thus indicating the presence of phase discontinuity lines. However an off-axis digital holography measurement obtained from these interference patterns reveals that indeed there is an azimuthal phase change of 2π along the CD ring circumference. This azimuthal phase changes is clockwise (anti-clockwise) for CD beam obtained from left (right) circularly polarized incident beam (see Fig. 5.3(a4)-(b4)).

It is pertinent to mention few important things about the three techniques that have

been discussed in the earlier section and illustrated in this section for the OAM of HyGG and CD beams. CD beams have two intrinsic features that make them unique from other conventional OAM beams, firstly they are vectorial in nature, i.e they have a spatially varying linear polarization, while most of the beam carrying OAM are scalar (like HyGG beams). Secondly, they possess fractional OAM values. Now, the plane wave interference experiments that give a qualitative sense of OAM are most helpful when the two beams are linearly polarized. So it is obvious that CD interference patterns can not give a complete picture about the fractional OAM value or phase information. On the same line of arguments, off-axis digital holography which utilizes non-collinear interference patterns also requires that two beams have same polarization. It is in principle possible to record two interferograms with orthogonal polarizations and then process them to retrieve phase information. However, this would still not solve the problem as CD beams possess all linear polarizations. On the other hand, the quantitative measurement of OAM via cylindrical lens is the only method that can work efficiently. It is independent of the polarization nature of the beam and it is equally effective in determining the fractional (non-integer) OAM [191]. Thus, this is the preferred method in our investigations on the OAM of non-circular CD beams described in the next section.

5.3 OAM of non-circular CD beams

Here, the investigation of the OAM nature of our non-circular CD beams are reported by the techniques discussed and illustrated with examples earlier on. It is shown that the fractional charge OAM of the non-circular CD beams can be scaled with the magnification values of the cylindrical lenses utilized in the conjugate cascade. For the purpose of clarity only two non-circular patterns are being discussed. The results on the investigations of these two cases via plane wave interference, off-axis digital holography and quantitative measurement are shown below.

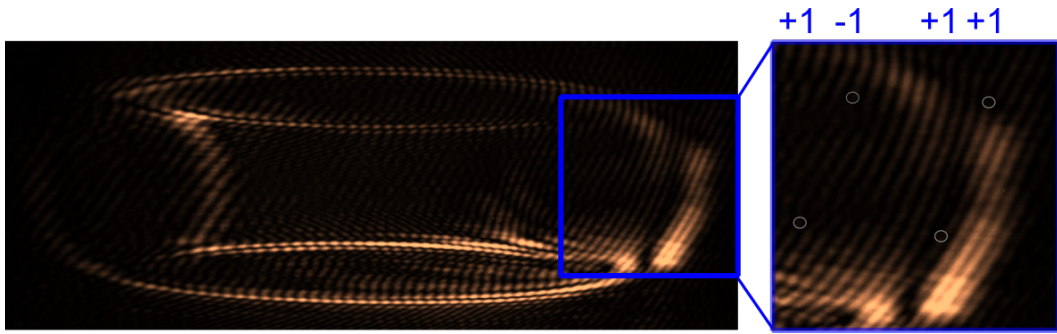


Figure 5.4 – Intensity distribution for an interference pattern between a non-circular CD wave and a plane wave. The non-circular CD beam is experimentally generated from an asymmetric cascade of two biaxial crystals with parameters: $M_x = 2.50$ and $M_y = 0.233$ and $\rho_1 = 17.9$, $\rho_2 = 13.9$.

Figure 5.4 shows the experimental interferogram for a plane wave interference with one of the non-circular pattern generated by a two-BC conjugate cascade. The zoomed figure on the right shows the positions of single charged vortices, two of the vortices are connected via a single fringe line and possess opposite charges. It is clearly observed that these non-

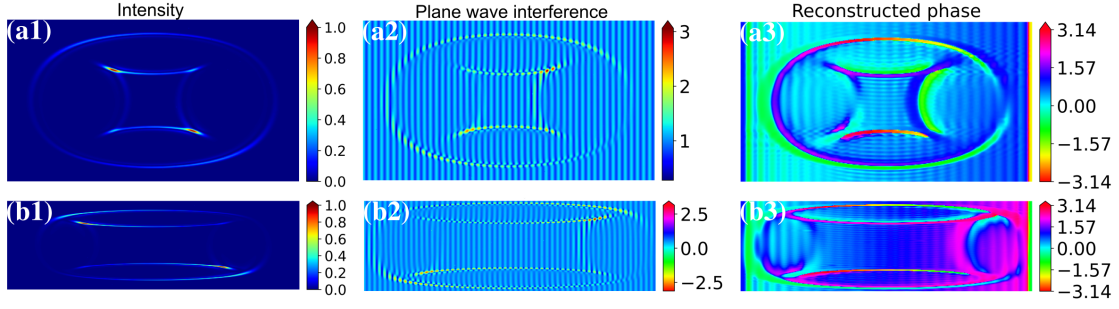


Figure 5.5 – Theoretically obtained interference patterns and reconstructed phase for two of the non-circular CD patterns obtained from the two BCs conjugate cascade with parameters: for $\rho_1 = 17.9$, $\rho_2 = 13.9$ and crystal orientation angles $\gamma_1 = 0, \gamma_2 = \pi/2$. In (a1)-(a3) $M_x = 1.25$, $M_y = 0.325$ and in (b1)-(b3) $M_x = 2.50$ and $M_y = 0.233$.

M_x	M_y	Intensity	CL axis - Horizontal	CL axis - Vertical	OAM
1.25	0.325	Theory (a1)	(a2)	(a3)	$l_{det} = 0.99$
		Experiment (b1)	(b2)	(b3)	$l_{meas} = 1$
2.50	0.233	Theory (c1)	(c2)	(c3)	$l_{det} = 2.56$
		Experiment (d1)	(d2)	(d3)	$l_{meas} = 2.7$

Figure 5.6 – Quantitative measurement of OAM for the same two non-circular patterns as in Fig. 5.5. Both patterns are for $\rho_1 = 17.9 = \rho_2 = 13.9$ and crystal orientation angles $\gamma_1 = 0, \gamma_2 = \pi/2$. while the magnification values are $M_x = 1.25$ and $M_y = 0.325$ [theory (a1)-(a3) and experiment (b1)-(b3)] and $M_x = 2.50$ and $M_y = 0.233$ [theory (c1)-(c3) and experiment (d1)-(d3)].

circular patterns possess single charge vortices that are distributed in the cross-section of the beam, which makes it difficult to reliably determine qualitatively the fractional OAM per photon. However another interesting feature observed from this interference pattern is that there are phase discontinuity lines along the four nearly horizontal lines in the pattern. As already mentioned, it has been observed in various investigations that such phase discontinuity lines possess alternating single charge vortices along them [91].

Theoretically determined non-collinear interference pattern and associated phase on the two non-circular CD patterns examples are shown in Fig. 5.5. The calculated interference patterns also show indications of the presence of phase discontinuity lines or lines

where the fringes are slightly shifted and appear broken (see the four nearly horizontal lines in Fig. 5.5(a2),(b2)). As mentioned earlier, whenever the fractional value of OAM is exactly half integer, an infinite number of alternating single charge vortices could appear along these lines. By extracting the phase information from these interference patterns via off-axis digital holography, it is observed that indeed there is an azimuthally varying phase on the structures near to these phase discontinuity lines (see Fig. 5.5(a3),(b3)). These two qualitative techniques for determining the OAM directly point out the presence of fractionally charged OAM vortices inside the cross-section of these two non-circular patterns.

Table 5.1 – Theoretical OAM values of non-circular CD patterns with varying magnification ratios of the cylindrical lenses along x and y axis. The OAM is determined by the technique of CL focusing described in Fig. 5.1(c). It can be observed that the fractional OAM value can scale continuously from less than half integer to around 8.

Sr. #	M _x	M _y	M _x /M _y ratio	OAM
1	0.150	0.103	1.46	0.42
2	0.250	0.161	1.55	0.45
3	0.400	0.232	1.72	0.49
4	0.500	0.268	1.87	0.52
5	0.606	0.295	2.05	0.64
6	0.778	0.323	2.41	0.65
7	0.800	0.326	2.45	0.67
8	1.000	0.333	3.00	0.76
9	1.250	0.325	3.85	0.99
10	1.538	0.303	5.08	1.30
11	2.000	0.268	7.46	1.89
12	2.500	0.233	10.73	2.56
13	3.333	0.189	17.63	4.31
14	4.000	0.162	24.69	5.90
15	5.000	0.134	37.31	8.78

Figure 5.6 shows the quantitative determination of OAM via both the experiment and theory with the method of Fig. 5.1(c) for the same two non-circular patterns. Since the intensity distribution in these two patterns does not possess a reflection symmetry, in order to quantitatively determine OAM, two measurements are needed, one by orienting the CL axis horizontally and the other by orienting it vertically. The theoretically and experimentally obtained intensity distribution in the focal plane of the CLs for the case with magnification values $M_x = 1.25$ and $M_y = 0.325$ are shown in Fig. 5.6[theory (a2)-(a3) and experiment (b2)-(b3)] and for the case with $M_x = 2.50$ and $M_y = 0.233$ in Fig. 5.6[theory (c2)-(c3) and experiment (d2)-(d3)]. The fractional OAM value is calculated by using Eq. (5.13) by considering both of the patterns of each case and the obtained fractional OAM values are listed in the last column of Fig. 5.6. A good match between experimentally (l_{meas}) and theoretically

obtained (l_{det}) fractional OAM values can be observed. Similarly, the fractional OAM is determined for other non-circular patterns and the obtained values are listed in table 5.1. It is observed that the fractional OAM value increases with the ratio of the magnification values (M_x/M_y) of the crossed cylindrical lenses. It is pertinent to mention here that the minimum OAM values observed in our investigations are for the cases, where the ratio of magnification value $M_x/M_y \approx 1$. For magnification ratio values less than one i.e. $M_y/M_x > 1$, the fractional OAM values starts to increase again. Hence, the fractional charge OAM of these non-circular beams increases with the ratio of the magnification values (i.e. either the increase of M_x/M_y or M_y/M_x ratio) of the two CLs utilized to generate them.

5.4 Conclusion

In this chapter, the spatial phase of the non-circular CD beams has been investigated with different techniques, showing their respective pros and cons. It was shown that there is an inherent difficulty owing to the vectorial nature of the beams, as well the fractional OAM character of the non-circular CD beams. Plane wave interference experiments revealed that these beams possess multiple phase discontinuity lines in the beam cross-section and there also exists spatially distributed single charge vortices in the beam cross-section. Off-axis digital holography measurements utilized to determine the phase of the non-circular CD beams showed that indeed the azimuthal phase evolves in a complex manner on different spatial regions of the CD pattern, this verifies the presence of single charged vortices at different spatial positions and also indirectly hints at the fractional nature of these beams. Finally in order to determine the definite value of the fractional OAM, a quantitative method based on single cylindrical lens is utilized. This method turned out to be very robust for determining the OAM value of these beams. The obtained values showed that the fractional OAM scales with the ratio of the magnifications (i.e. either increase of M_x/M_y or M_y/M_x values) of the cylindrical lens. These results may provide interesting perspectives for non-circular CD beams as there is a lot of interest in fractionally charged OAM beams for their utilization in atom optics [193], quantum communication [194–197], optical tweezing or manipulation of microscopic particles [198, 199], optical imaging [200, 201] and many others [187, 202–205].

IN-SITU HOLOGRAPHIC RECORDING AND TWO-WAVE MIXING OF CD BEAMS

6.1 Introduction

Conical diffraction is a manifestation of the linear optical properties of the crystal and most of the earlier investigations have all been performed in the linear regime with the BC acting as passive elements. Nevertheless, few studies have combined CD with nonlinear optics, where CD at the second-harmonic wave in frequency doubling [206–208] or at the sum-frequency generation frequency [209] have been studied. Properly doped BC of $\text{KGd}(\text{WO}_4)_2$ or $\text{KY}(\text{WO}_4)_2$ have also been employed as active elements within a cavity for realizing conical diffraction lasers with specific polarization properties [39, 210–213].

Some of the BC giving rise to CD also show another nonlinear optical effect, the photorefractive effect [142, 214]. This is an indirect effect leading to refractive index changes already upon low power light illumination. In this chapter we combine conical diffraction with photorefraction within the same medium to demonstrate conical diffraction holograms as well as the selective amplification of the CD wave via dynamic two-wave mixing. Section 6.2 describes briefly the experimental approach and the $\text{Sn}_2\text{P}_2\text{S}_6$ (SPS) BC used both as medium giving rise to CD and as nonlinear holographic recording material. Section 6.3 illustrates the major experimental results that show that propagation of the object wave along one of the optical axes of the BC is crucial and critical. Indeed it is shown that, provided that the object wave propagates along the optical axis and gives rise to CD, holographic recording and two-wave mixing amplification can be efficiently achieved with any combination of the polarizations of the object and reference waves, including mutually orthogonal ones. The underlying physical phenomenon is highly complex and involves the physics of the photorefractive effect in strongly anisotropic configurations as well as the constraints associated to the propagation of light in singular directions within the BC. While a complete theory would require the knowledge of several still unknown material parameters, it is possible to qualitatively catch the main experimental features with a simplified model which is presented and discussed in Section 6.4. Finally, Sect. 6.5 includes a

brief discussion and conclusion on the results.

6.2 Crystal sample and experimental approach

The BC used for the investigations is a nominally undoped ferroelectric SPS, which belongs to the monoclinic point group m at room temperature. SPS is an attractive nonlinear optical material owing to its transparency range extending from 530 to 8000 nm wavelength, its interesting electro-optical [215, 216] and nonlinear optical properties [217] and the high photorefractive sensitivity [218]. The anisotropic optical properties and their dispersion were studied in detail in [219] and optical activity near the ferroelectric-paraelectric phase transition was evidenced in [220]. A summary of some of the most relevant material parameters is given in Ref. [218]. A 11.2 mm-long SPS sample was cut from a crystal grown by the vapour transport method [221] and electrically polarized to insure a ferroelectric monodomain state. The sample was oriented with the parallel entrance and exit faces of the beams being nearly perpendicular to one of the two optic axes. These steps were performed by our collaborators at the Uzhhorod National University in the Ukraine.

A simplified scheme of the experimental arrangement for holographic recording and two-wave mixing is shown in Fig. 6.1. Figure 6.1(a) is for the holographic recording and read-out of the CD beam created in-situ by the object wave. A He-Ne laser beam at the wavelength of 632.8 nm is split into a reference and an object wave by taking care that the path lengths difference is within the coherence length of the laser. Their polarizations are initially left and right circular, respectively. Before each wave reaches the SPS BC, the polarizations can be individually modified by polarization controllers (Pol-contr) in each path being composed of linear polarizers, wave-plates or adjustable liquid crystal retarders. The Gaussian input waves have initially an equal diameter and are focused by the spherical lenses L_1 (focal length $f = 200$ mm) and L_2 ($f = 75$ mm) inside the SPS crystal, where they interfere. The different focal lengths insure that the reference wave has a larger diameter than the object wave inside the BC. The focal plane of lens L_2 corresponds to the focal image plane where the CD ring pattern formed by the object wave is the sharpest. The spherical lens L_3 images this plane onto a CCD camera to observe the transmitted, amplified or reconstructed CD object wave with the corresponding power being detected in parallel by a photodiode. For holographic recording (but not for two-wave mixing) the input powers of the two beams are adjusted in such a way that the reference and object waves have nearly the same average intensity inside the SPS crystal ($I \approx 30$ mW/cm²). For holographic recording (Fig. 6.1(a)) shutter S_1 on the object wave is kept open during 90 seconds. This allows to record a photorefractive grating composed of a fast primary grating nearly fully compensated by a slow secondary grating, this behavior is typical for type I nominally undoped SPS crystals [218]. When the shutter S_1 is being closed, the primary gratings disappears quickly revealing the secondary grating that results in the diffraction of the reference wave into the reconstructed object wave. For the examples presented in the next section this reconstructed wave is observed within 5 seconds after closing shutter S_1 .

The situation for two-wave mixing (Fig. 6.1(b)) is similar, however with different boundary conditions. Here the object wave is first attenuated by a neutral density filter (ND) to an intensity less than 1/100 (inside the BC) with respect to the one of the reference. In this case,

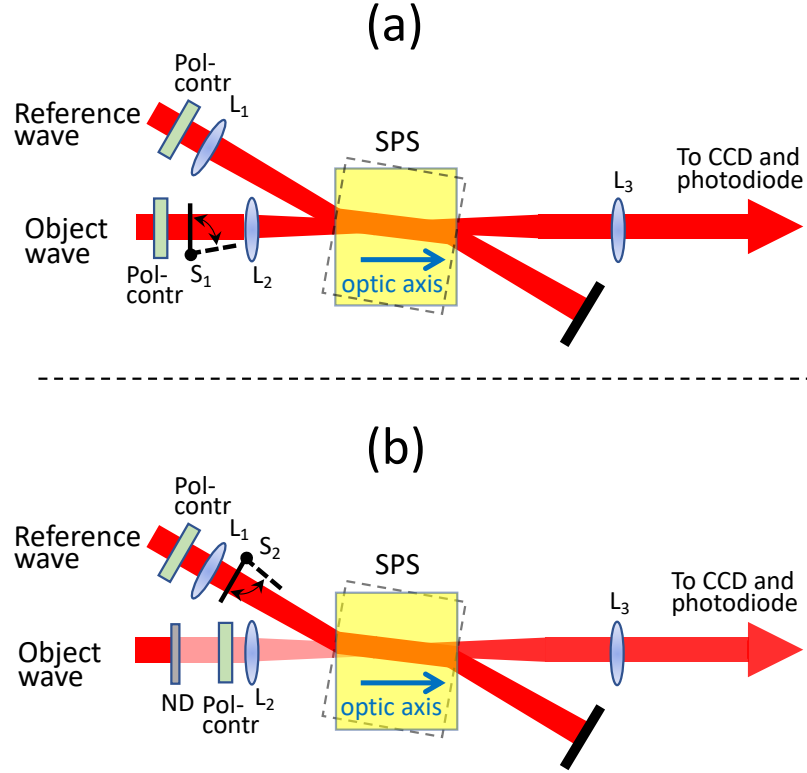


Figure 6.1 – Scheme of experimental arrangement for the holographic recording and read-out of the CD object wave (a) and for its amplification by two-wave mixing (b). SPS: $\text{Sn}_2\text{P}_2\text{S}_6$ biaxial crystal; S_1 , S_2 : shutters; L_1 , L_2 , L_3 : spherical lenses; Pol-contr.: polarization controller; ND: neutral density filter. The optic axis of the SPS crystal is aligned with the object wave (yellow shape). The dashed shape give an alternative (misaligned) crystal orientation. The polarization controllers in the reference and object beam paths can be adjusted to excite any polarization combination for the two waves. This includes the case where one or both waves correspond to pure eigenwaves inside the SPS crystal.

injection of the reference wave by opening shutter S_2 leads to an amplification (or eventual depletion) of the CD object wave. Importantly, we recall that the object wave produces the CD vector beams only if it propagates along the optic axis (yellow orientation of SPS in Fig. 6.1). By misaligning the crystal (dashed orientation) CD no longer occurs and the behavior differs strongly, as discussed in the next section. In our experiments, the horizontal laboratory plane is spanned by the optic axis of the crystal and by the x crystallo-physical axis of the orthogonal cartesian system used to describe the tensorial properties of SPS. The convention taken is the same one as in Ref. [219] (see Fig. 6.2), the x -axis is close to the crystallographic a -axis of the monoclinic SPS and to the direction of the spontaneous polarization (P_s). The examples given below are obtained for an external crossing angle of 31° between the two waves, what corresponds to a spatial grating period of $\Lambda \approx 1.2 \mu\text{m}$, however other crossing angles give qualitatively similar results.

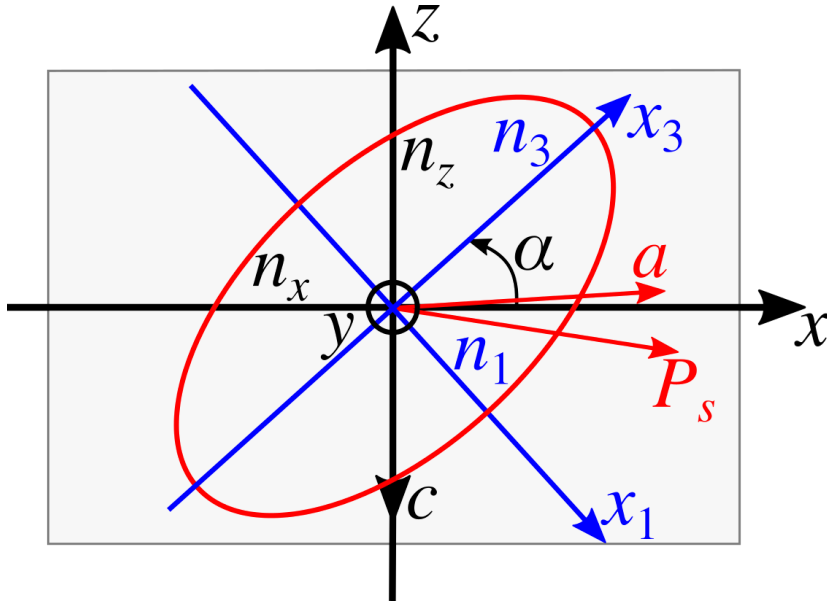


Figure 6.2 – Indicatrix position and the direction of spontaneous polarization P_s in the xz -plane. (a, b, c) represent crystallographic coordinates (non-orthogonal for monoclinic systems), (x, y, z) represent cartesian coordinates and (x_1, x_2, x_3) represent dielectric coordinate system (after Ref. [219]).

6.3 Experiments

As mentioned above, propagation along the optical axis leads to spreading of different linear polarizations across the CD ring pattern. If the input wave is circularly polarized, all the linear polarizations are equally important and the ring pattern is homogeneous in intensity. If, in contrast, the input polarization is already linear, the local polarizations on the ring are the same as for circularly polarized input. However, in this case the local intensity depends on the azimuthal position on the ring. This local intensity is proportional to the one obtained by transmitting a wave with a given (local) polarization through an analyzer oriented in direction of the input polarization, what leaves an intensity node at the position on the ring where the local polarization would be perpendicular to the input one (see for instance the Fig. 4.9). This remarkable property of the CD wave allows to record photorefractive holograms with any combinations of the input beam polarizations. It is indeed always possible to find ring sections of the object wave where the local polarization is such as to produce strong interference with the uniformly polarized reference wave.

We illustrate first this mutual polarization versatility in the case of dynamic two-wave mixing (TWM). This is shown in Fig. 6.3 which represents the temporal build-up of the spatially integrated object wave amplification $\bar{\gamma}_0$ for various polarizations of the reference wave acting as a pump and a unique polarization of the object wave. The quantity $\bar{\gamma}_0$ is defined as the transmitted object wave total power in presence of the reference pump wave divided by the transmitted object wave power without the reference wave. For Fig. 6.3, the incident object wave is aligned to the optic axis of the BC and is kept right circularly polarized (RCP) while the reference wave polarization is either left circular (LCP) or linear at

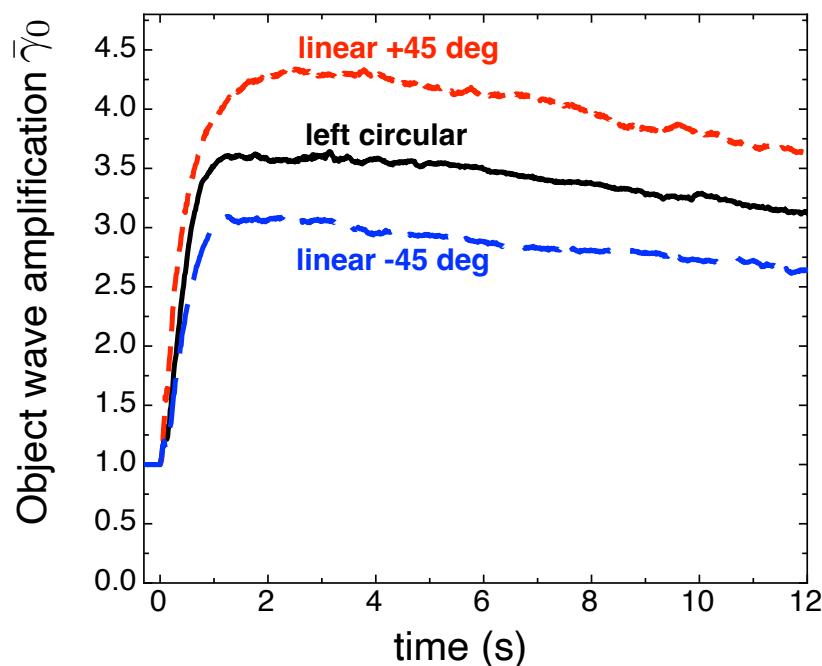


Figure 6.3 – Spatially averaged two-wave mixing amplification of the object wave as a function of time. The input object wave is aligned to the crystal optic axis and is right circularly polarized. Results for three different polarizations of the incident pumping reference wave are shown: left circular polarization (solid black curve), linear polarization (LP) at +45 deg (red dashed curve) and LP at -45 deg (blue dashed curve).

+45° or -45°. Clearly, upon injection of the reference wave at $t = 0$ (opening of shutter S_2 in Fig. 6.1(b)), a significant amplification is observed for all polarization combinations, including the case where the two incident waves are mutually orthogonal (RCP and LCP). The amount of amplification differs slightly for the three cases as the strength of the underlying photorefractive gratings and the electro-optic coupling is a function of the wave polarizations. The dynamics seen in Fig. 6.3 shows the rise of the primary photorefractive grating in a time of the order of one second. Here the maximum of $\bar{\gamma}_0$ does not correspond to a steady-state because, as mentioned above, for type I SPS crystals a secondary grating starts to compensate the primary one, resulting in the slight decrease of the amplification seen after the maximum. This compensation would be nearly complete after a time of ≈ 100 s. It is worth noting that the amplification $\bar{\gamma}_0$ shown in Fig. 6.3 is an average amplification over the CD ring as obtained by integrating all the power in the object wave using a photodiode. In reality the amplification differs for different sections of the ring, that correspond to different local linear polarizations of the CD wave. This point will be discussed below in connection with Fig. 6.4. Finally, we would like to point out that larger amplifications than those shown in Fig. 6.3 are possible for situations where the two input waves share a same polarization. This is the usual condition under which photorefractive holograms are normally recorded. By choosing a reference wave polarization corresponding to one of the two eigenwaves in SPS and the corresponding polarization for the input object wave, we have observed a maximum amplification $\bar{\gamma}_0 \approx 10.2$, as compared to a maximum of $\bar{\gamma}_0 \approx 4.3$ in Fig. 6.3.

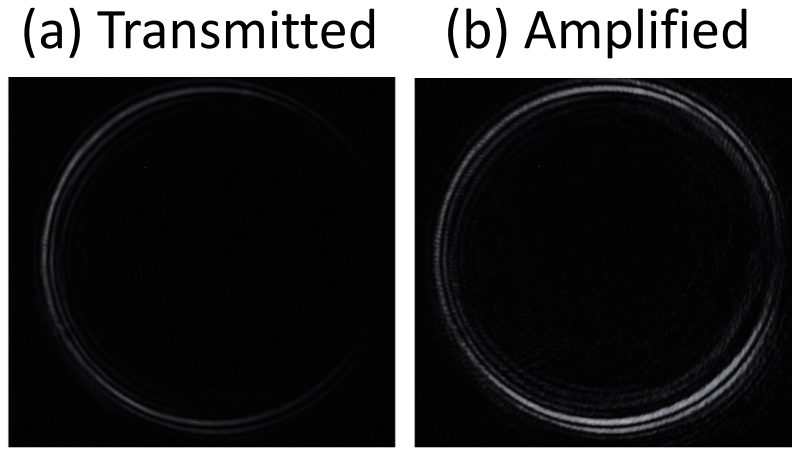


Figure 6.4 – Two-wave mixing amplification for interfering linearly polarized orthogonal eigenwaves. (a) Transmitted CD object wave in absence of the reference pump wave. (b) Amplified CD object wave.

As mentioned above, the TWM amplification differs locally, what can be easily seen in Fig. 6.4. Here the reference wave polarization is linear and corresponds to one of the eigenpolarizations in the SPS crystal. The polarization of the object wave is linear as well but is associated to the other (orthogonal) eigenpolarization when the crystal is slightly misaligned. Figure 6.4(a) shows the transmitted object wave for the aligned configuration in absence of the reference beam (shutter S_2 in Fig. 6.1(b) closed). As expected, the observed CD ring pattern is inhomogeneous in intensity as a result of the linear input polarization. After amplification (Fig. 6.4(b), three seconds after opening shutter S_2) one observes in this specific case a much stronger increase of intensity in the regions on the right side of the CD ring, that were initially weaker. The amplification for the left side of the ring is significantly less pronounced, what give rise to a kind of power equalization within the CD ring. Importantly, we have verified that the amplified CD conserves the same polarization distribution than the linearly transmitted one, meaning that the light amplified by the nonlinear process respects the constraints given by the linear properties of the medium. Note also that in the present example the spatially averaged amplification is $\bar{\gamma}_0 \approx 4.5$. It is interesting to compare this value with the one obtained under the same conditions except for the crystal being turned (misaligned) so that the the object wave no longer propagates along an optic axis. In this case the orthogonal eigenwaves prevent the creation of an efficient photorefractive grating. We have checked this case for an internal misalignment of $\approx 6.5^\circ$, finding that the object wave is essentially unaffected by the pumping with the reference beam, the amplification being less than 12% ($\bar{\gamma}_0 \approx 1.12$).

The same kind of behavior can be observed for grating diffraction at a photorefractive hologram recorded with orthogonal eigenwaves, as for the case of Fig. 6.4. Figure 6.5(a) shows the linear transmission of the object wave under CD conditions, while Fig. 6.5(b) shows the reconstructed CD wave after closing shutter S_1 in Fig. 6.1(a) at the end of the recording. Clearly, also here a reconstructed CD vector wave (with same local polarization as the transmitted object wave) is being observed despite for the orthogonal eigenwaves associated to the object and reference beams. As for TWM, also here one observes a locally stronger reconstruction on the right side of the ring, corresponding to region where the

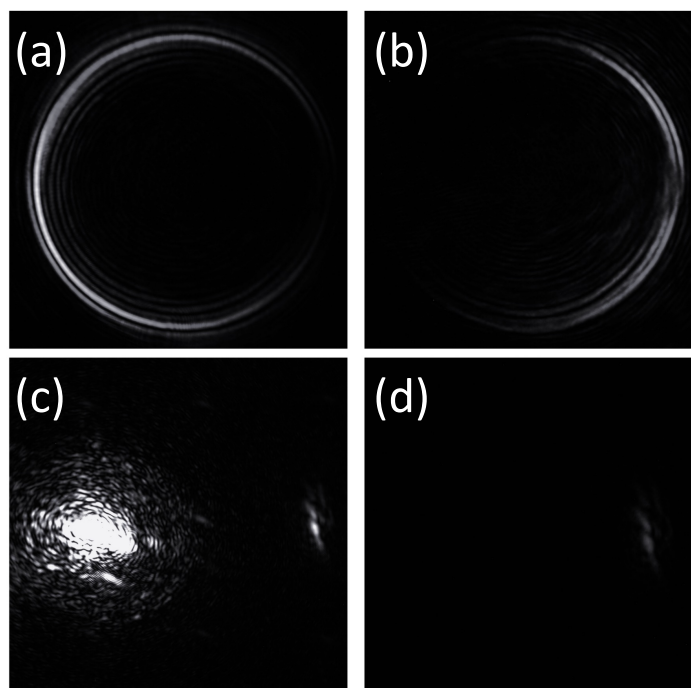


Figure 6.5 – Holographic recording with orthogonal eigenwaves. Left column: transmitted object wave prior to hologram recording for the aligned (a) and misaligned (6° misalignment) (c) configurations. Right column: object wave reconstruction at read-out after hologram recording, again for the aligned (b) and misaligned (d) configurations.

transmitted object wave is weaker. Figure 6.5(c) and (d) are for the case where the crystal is misaligned and the object wave makes an internal angle of about 6° with the optic axis. In this case the object wave experiences double refraction as seen in Fig. 6.5(c) that shows its transmission through the SPS crystal. Here the eigenwave corresponding to the saturated left spot is predominantly excited with only spurious power in the orthogonal eigenwave associated to the right spot. If a hologram is recorded with the reference wave of the orthogonal eigenwave (thus possessing a polarization nearly orthogonal to the one of the object wave), upon read-out one observes merely a weak diffraction at the position of the right spot (Fig. 6.5(d)). Under the same conditions used for the aligned configuration, the corresponding diffracted power in direction of the object wave is about 30 times weaker, which confirms the specific importance of propagating the object wave along the optic axis.

The section of the ring which is most strongly reconstructed depends on the input polarization of the reference wave. This is illustrated with the help of Fig. 6.6, that shows the results of hologram recording and read-out with linear horizontal or vertical polarization (in the laboratory frame) for the reference wave, together with a circular polarized object input wave at recording. Clearly the horizontal (H-pol) and vertical polarized (V-pol) reference lead to predominant enhancement of different sections of the CD ring at read-out, as seen in Fig. 6.6(b) and (c), respectively. The corresponding angular-dependent powers can be best visualized by integrating the intensity across a narrow radial section across the CD ring for different azimuthal angles along the ring, what gives the solid red curve (H-pol) and the dotted blue curve (V-pol) in Fig. 6.6(d). This behavior can be put in relation with

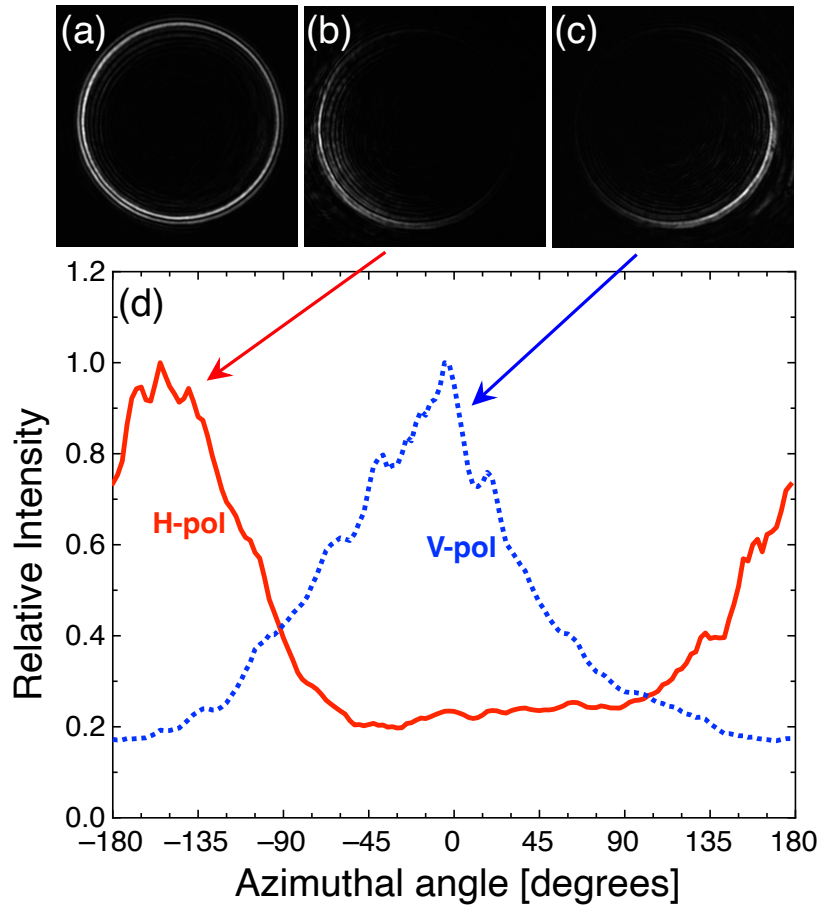


Figure 6.6 – CD holography with circularly polarized input object wave and linearly polarized (horizontal (H) or vertical (V) in laboratory frame) reference wave. (a) CD object wave transmission prior to hologram recording; (b) Object wave reconstruction for H-polarized reference; (c) Object wave reconstruction for V-polarized reference; (d) Normalized azimuthal dependence of local power on the reconstructed ring for cases (b) and (c).

the expectations of a simplified theory, as discussed in the next section.

6.4 Background theory

The detailed explanation of our above observations in connection with CD holography and TWM is a tedious task. It involves on one hand the physics related to the anisotropic optical properties leading to the CD effect and, on the other hand, the complex physics related to the photorefractive effect in such a low symmetry monoclinic crystal. The latter is concerned by the photoinduced charge transport leading to the formation of a space-charge hologram and by the conversion of this space-charge hologram into a refractive index modulation (phase hologram) by means of the material's electro-optic response. However, the space-charge electric field in the case of a photorefractive grating is periodically modulated in space and the electro-optic response gets an additional level of complexity as compared to the case where the field would be spatially homogeneous. A thorough quantitative descrip-

tion requires the knowledge of all clamped electro-optic coefficients, as well as of all the elastic, elasto-optic and piezo-electric properties of the crystal, a significant part of which is still unknown for SPS. More details on these aspects can be found in [150, 222] and references therein. For the above reasons the purpose of this section is not to find a quantitative agreement between experiments and theory, but rather to confirm the plausibility of the observation in the framework of a highly simplified theoretical approach.

As was discussed in Chapter 3 (see Fig. 3.4), the local polarization direction on the CD varies along the ring circumference and spans an angle θ of 180° over a full revolution of the polar angle φ by 360° , the variation in θ being always half the variation in φ . Considering different spatial positions on the ring is therefore equivalent to considering a given linear polarization component for the object wave among all the possible ones in the plane perpendicular to the object wave \mathbf{k} -vector. We recall that for a circularly polarized input object beam, the different linear polarizations are equally probable giving a complete ring. The easiest situation is the one where the reference wave is linearly polarized (as for instance in Fig. 6.6). In this case the problem of estimating the azimuthal dependence of the hologram diffraction efficiency and TWM gain reduces essentially to an evaluation of the coupling strengths between a plane reference wave with a fixed polarization and components of the object wave with all possible polarization directions taken as a variable parameter. This coupling strength depends on one hand on the modulation depth amplitude of photorefractive space-charge field created by the two considered wave components. On the other hand it depends on an effective scalar electro-optic coefficient r_{eff} specific to the pair of waves being considered. This coefficient is a function of the unit vector \hat{K} in the direction of the grating vector, of the anisotropic electro-optic properties expressed by a tensor r_{ijk}^{eff} , and of the two unit polarization vectors \hat{d}^{ref} and \hat{d}^{obj} for the reference wave and the local object wave, respectively. The expression for the scalar electro-optic coefficient determining the coupling is

$$r_{eff} = \hat{d}_i^{obj} \cdot (r_{ijk}^{eff} \hat{K}_k) \cdot \hat{d}_j^{ref}, \quad (6.1)$$

where the Einstein summation convention over equal indices is utilized. Importantly, all the vectors in the above equation have to be expressed in the orthogonal crystallo-physical reference frame (xyz) in which the electro-optic tensor and other tensorial physical properties of the crystal are usually expressed. This crystallo-physical system (xyz) is depicted in Fig. 6.2 and is oblique with respect to the laboratory frame as well as with respect to the frame defined by the principle dielectric axes $(x_1x_2x_3)$. As an example, the unit vector along the optic axis of propagation of the object wave is expressed in the xyz -system as $(0.4678, 0.7660, 0.4408)$. In the laboratory frame the same vector would possess only a unique unity component along the longitudinal coordinate perpendicular to the entrance surface plane of the crystal. Unfortunately, due to the lack of sufficient data on the elastic, piezoelectric and elasto-optic properties of SPS, we do not have access to the correct values to be used for the coefficients of the tensor r_{ijk}^{eff} (see discussion in Ref. [150]). Instead we take a rather rude approximations and we utilize the unclamped (free) electro-optic tensor elements r_{ijk}^T that were measured in [215] and [216] for what matters the first and third column of the tensor, respectively. The employed values (in units of pm/V) are: $r_{111}^T=174$, $r_{221}^T=92$, $r_{331}^T=140$, $r_{131}^T=-25$, $r_{113}^T=-67$, $r_{223}^T=-22$, $r_{333}^T=-25$ and $r_{133}^T=14$. The two still unknown coefficients r_{322}^T and r_{122}^T are expected to be rather small as they are associated to electric field directions perpendicular to the crystallographic mirror plane containing the crystal's

spontaneous polarization. Both these coefficients are set equal to 0 for the following evaluation. Note also that the third column (index $k = 3$) diagonal coefficients r_{113} , r_{223} and r_{333} are taken here with the opposite sign as in the original publication. The reason is the different convention for the positive direction of the z -crystallo-physical axis. Here we stick to the convention in Ref. [219] which is consistent with the IEEE Standard on Piezoelectricity [223], with positive x - and z -direction such that both piezoelectric coefficients d_{111} and d_{333} are positive, while in [216] a convention with d_{333} negative was taken. It is also worth mentioning that for our experimental configuration the photorefractive space-charge electric field has the largest projection on the x -axis and the elements of the first column ($k = 1$) of the electro-optic tensor largely determine the resulting scalar electro-optic coefficient of Eq. (6.1).

The expected local hologram diffraction efficiency η is proportional to the square of the product of r_{eff} with the amplitude E_{sc} of the photorefractive space-charge grating responsible for the coupling of the two waves, i.e. [224]

$$\eta \propto [r_{eff}(\theta)E_{sc}]^2 . \quad (6.2)$$

This relation is valid for moderate diffraction efficiencies of the phase hologram, what is the case for our gratings where the spatially averaged diffraction efficiency is typically of the order of 2-3 %. For what matters the space-charge field amplitude, we assume here that it is proportional to the light modulation index induced by the two local polarizations, i.e. to the scalar product $E_{sc} \propto (\hat{d}^{obj} \cdot \hat{d}^{ref})$. This is a rather rude approximation for various reasons, the principal one being associated to the fact that the space-charge field saturates at large modulation (for nearly parallel \hat{d}^{obj} and \hat{d}^{ref}), what leads to a sublinear dependence of E_{sc} on the modulation depth in this regime. Therefore, the use of this approximation may lead to a somehow larger contrast in the simulated curves for η as a function of the object wave polarization angle. Such a simulation is shown in Fig. 6.7 for the case of a circularly polarized input object wave and a linearly polarized reference (horizontal or vertical), as in Fig. 6.6. It can be easily recognized in Fig. 6.7 that the diffraction for the horizontal and vertical polarization of the reference beam are nearly (but not exactly) anti-phase, meaning that their maxima are separated by approximately 90° in the object wave polarization, what corresponds to 180° on the CD ring. Despite for the many simplifying assumptions, such a behavior agrees qualitatively with the experimental results shown in Fig. 6.6.

In the case of two-wave mixing with weak signal wave the local amplification $\gamma(\theta)$ is expected to depend exponentially on the exponential gain $\Gamma(\theta)$ as

$$\gamma(\theta) = e^{\Gamma(\theta)d} , \quad (6.3)$$

where d is the propagation distance in the crystal. In absence of an anisotropy of the photoexcitation process [222] the exponential gain can be expressed as

$$\Gamma \cong B(\hat{e}^{obj} \cdot \hat{e}^{ref})r_{eff}(\theta)\tilde{E}_{sc,im} , \quad (6.4)$$

where B is a constant that depends on the refractive indices associated to the two waves, on the light wavelength, and on the weak walk-off angle for the reference wave. Here $\tilde{E}_{sc,im}$ is the imaginary part of the space-charge field amplitude. This is the nonlocal component of the space-charge field (90° phase shifted with respect to the intensity modulation) and is

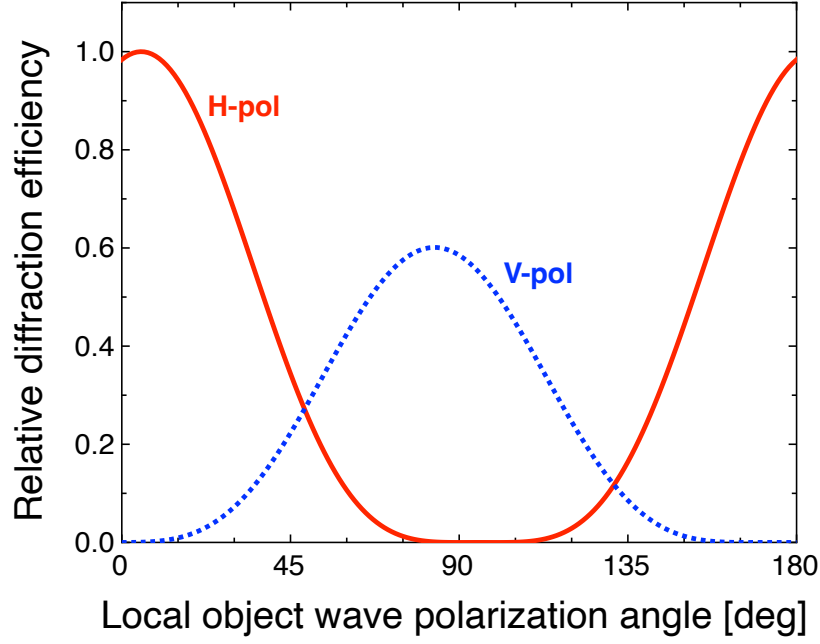


Figure 6.7 – Expected relative diffraction efficiency based on the simplified model described in Sect. 4. The object input wave is assumed circularly polarized and contain all linear polarization angles between 0° and 180° . The reference wave is assumed horizontally (red solid curve) or vertically polarized in the laboratory frame (blue dotted curve).

responsible for the TWM gain. In materials with diffusion dominated charge transport, as in SPS [218], this is the dominant component of the space-charge field. Importantly, this quantity depends on experimental and materials parameters such as the beams crossing angles, the trap density in the crystal or its static dielectric properties. However, $\tilde{E}_{sc,im}$ does not depend on the relative intensity of the two-waves and the corresponding light modulation depth, so that it can be considered as a constant for our purposes. In Eq. (6.4) the unit vectors \hat{e}^{obj} and \hat{e}^{ref} are along the electric fields of the object and reference waves, respectively. Due to the weak walk-off their scalar product can be safely approximated by the corresponding scalar product of the electric displacement unit vectors, so that

$$\Gamma \cong C(\hat{d}^{obj} \cdot \hat{d}^{ref})r_{eff}(\theta) , \quad (6.5)$$

where C is again a constant that depends on the specific experimental arrangement. In this equation the dependence on the local object wave polarization angle θ appears twice, in the effective scalar electro-optic coefficient $r_{eff}(\theta)$ and in the scalar product between the two \hat{d} vectors. Figure 6.8 shows the expected amplification of the object wave for the case where the input polarizations of the object and reference wave are linear and mutually orthogonal and the reference wave polarization is aligned to one of the eigenpolarizations. This situation corresponds to the one of Fig. 6.4. The evaluation follows from the simplifying approach of Eqs. (6.3), (6.5) and (6.1) where the constant C was adjusted to give an average amplification $\bar{\gamma}_0 \approx 4.5$. In Fig. 6.8 the angle θ is given relative to the input polarization angle $\theta_{0,obj}$ of the object wave ($\theta_{0,obj} = -63.2$ deg), so that the input wave intensity distribution (assumed proportional to $\cos^2(\theta - \theta_{0,obj})$) is centred on the graph (dashed red curve). It can be recognized that the central region where the object wave has a maximum in absence

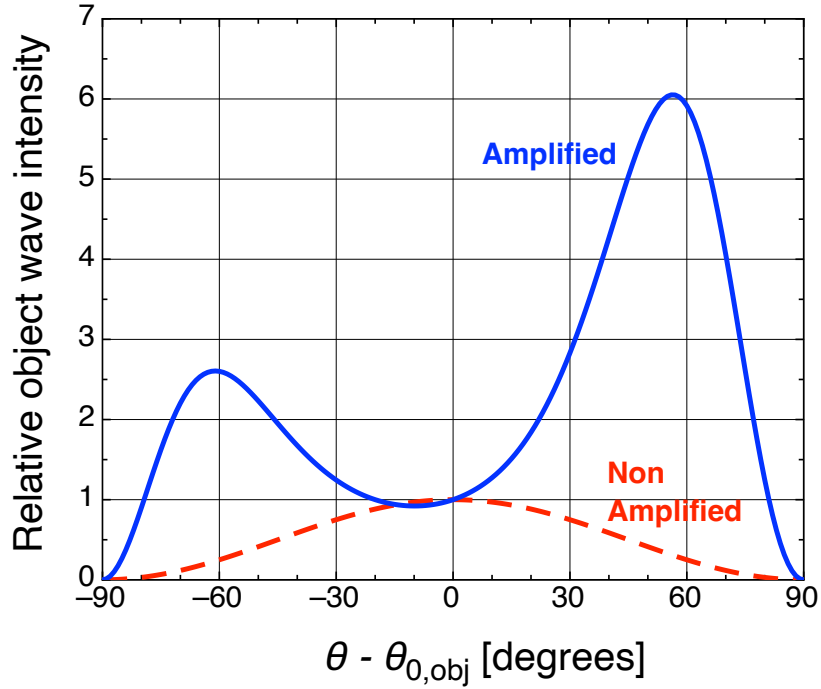


Figure 6.8 – Expected TWM amplification of the CD object wave as a function of the local angle of polarization θ for the case of orthogonal linearly polarized input waves with the reference wave as one of the eigenpolarizations. The angle $\theta_{0,obj}$ is the polarization angle of the input object wave, for which the non amplified CD wave is locally maximum. Red dashed curve: non amplified wave; Blue solid curve: amplified object wave with $\bar{\gamma}_0 \approx 4.5$.

of TWM interaction (corresponding to the left region in Fig. 6.4(a)) is not being amplified. This is due to the vanishing scalar product in (6.5) at this point. The maximum power in the amplified wave is predicted for two regions with a deviation of roughly $\pm 60^\circ$ in θ ($\pm 120^\circ$ along the ring) from this position. These maxima have different heights and are mainly a result of a combination of the effects of $r_{eff}(\theta)$ together with the initial θ -dependence of the unaffected CD wave. Even though the gain Γ tends to increase when the polarization direction θ gets closer to one of the reference (at the two borders of the graph in Fig. 6.8), from a certain point on the lack of input light possessing such polarization components becomes dominant, what gives the minimum at ± 90 deg in Fig. 6.8) that corresponds to the dark region on the right-hand side of the circle on Fig. 6.4(b). Again, despite the highly simplifying assumptions, one can conclude that our modeling gives a satisfactory qualitative agreement with the observations. It is also worth mentioning that, even though here the average amplification is only slightly more than a factor of 4, locally the light can be amplified much stronger with peaks exceeding a factor of 40.

6.5 Discussion and conclusion

We have considered conical diffraction vector waves in a nonlinear photorefractive and optically biaxial material and we have shown, for the first time to our knowledge, that it is possible to amplify locally or record in-situ holograms of such waves. The BC acts

both as a generator of the CD vector wave and as a recording material. Under aligned CD conditions of the crystal the recording is possible even for orthogonal polarizations of the two interacting input beams, owing to the polarization spreading resulting from the CD process. Under such conditions the effect possesses a kind of angular resonance for the object wave direction parallel to one of the optical axes. It was found that the pattern reconstruction depends on the combination of recording polarizations and on the read-out polarization. For two-wave mixing we obtain a varying local amplification across the CD ring, which can partially lead to a more homogeneous power around the circle. We have analyzed the situation with the help of a highly simplified theoretical approach based on the model of the photorefractive effect and general features of conical diffraction. Despite its simplicity and the number of assumptions, the model allows a surprisingly good qualitative description of the main experimental features. A more thorough modeling would require the determination of a number of still unknown anisotropic material parameters, as well as the consideration of details regarding CD under the conditions of optical activity [170, 225], which is little investigated to date and was neglected for the purpose of this work. The investigations in this chapter have dealt with CD in a single crystal without cascades. As discussed in Chapt. 4, 5 and Appendices A and B, more complex vector patterns can be obtained with CD cascades, specially with the conjugate cascades with intermediate crossed cylindrical lenses. Since the output patterns is obtained in the last focal image plane (near the last crystal in the cascade), recording and local amplifications of such complex patterns shall be possible if this last crystal is able to store a hologram. This may represent an interesting evolution of the studies described in the present chapter.

CONCLUSION AND PERSPECTIVES

In this thesis, conical diffraction (CD) has been studied fundamentally to tailor the shape, intensity, polarization and orbital angular momentum (OAM) of beams resulting from this complex phenomenon. Also, CD has been investigated within a photorefractive crystal allowing for a holographic recording and two wave mixing of the generated CD beams. Since partial conclusions have been presented at the end of each chapter, here our intention is to give a brief commentary and to present few perspectives.

The peculiar phenomena of conical diffraction happens as a tightly focused beam is incident on a biaxial crystal (BC) with its \mathbf{k} vector oriented along one of the optic axes, what leads to an infinite number of Poynting vectors lying on the surface of a cone. The beam propagates as a (diffracting) double ring cylinder, after exiting the BC. The rings in this cylinder are sharpest at the focal plane formed by the focusing lens before the crystal. Recently CD phenomenon has seen major developments via the exploration of cascaded configurations, whereby two or more crystals are placed in a cascade with their optical axes aligned. Such a cascade of N crystals leads to 2^{N-1} multiple concentric double rings in the focal image plane. In our investigations, it is shown that a conjugate cascade of two or N biaxial crystals (here $N = 2, 3, \dots$), which involves a wave-vector space manipulation performed via two crossed cylindrical lenses between any two adjacent BCs, results in the generation of highly structured vector beams with complex non-circular patterns. The generated CD patterns lacks the primary circular shape and is no longer characterized by concentric rings. Instead the pattern is composed of 2^{N-1} individual structures with non-homogeneous distribution of intensity and polarization around them. The key aspect in generating these highly structured non-circular CD patterns lies in the above-mentioned utilization of two crossed cylindrical lenses (with different focal lengths) for wave-vector space manipulation. These lenses placed between any two adjacent biaxial crystals, effectively split the 2D transverse \mathbf{k} -space into two orthogonal 1D \mathbf{k} -spaces. This allows the independent manipulation through the same pair of conjugated planes but independent magnification in the two transverse dimensions x and y . The experiments performed for a cascade of two biaxial crystals showed good agreements with the predictions of a corresponding paraxial diffraction model. The latter is an extension of Berry's paraxial diffraction theory for cascaded CD and takes properly into account the intermediate \mathbf{k} -space ma-

nipulations. It has also been shown that the extension of the conjugate cascade to more than two crystals leads to CD patterns with increased complexity. Theoretical and experimental analysis of our unusual non-circular patterns showed that each CD pattern is composed of individual structures, some of which can be convex as seen from the center of the pattern. This is in sharp contrast with the usual cascades where all the concentric circles are obviously concave. The intensity and polarization distribution on these concave or convex structures is successfully predicted by our model. By introducing structure parameters, one can express some simple rules of thumb which permit to predict qualitatively the shape of the individual structures without performing the rather heavy calculations required for the numerical solution of the model. As said, for a N -crystals cascade a total of 2^{N-1} structure parameters $X_{\pm\pm\pm}$ and $Y_{\pm\pm\pm}$ in each of the Cartesian directions are introduced. The structure parameters depend on the ρ values (CD strength parameter) of the individual crystals in the cascade and on the magnification values of the crossed cylindrical lenses placed between each of the adjacent conjugate planes. The structure parameters not only permit to qualitatively elucidate the structure general shape but also predict the existence of intersections between the individual structures. It is observed that the local polarization on the non-circular structures remains linear with the exception of the regions where structures cross each others or where a local overlap of different branches of a same structure occurs. These regions may be associated to elliptical or circular polarizations. It was also found that the polarization angle evolution is not a linear function of the polar angle on the structures. This is in contrast to CD patterns obtained from conventional cascade. The shapes and polarization distributions of non-circular CD patterns have been thoroughly discussed for a conjugate cascade of two biaxial crystals ($N = 2$). What has allowed to identify three distinct cases on the basis of their structure parameters combination. These three cases have been further investigated both theoretically and experimentally for polarization filtering at the input, output or at the intermediate position in the cascade. An excellent agreement between theory and experiments was observed. The results indicate that such polarization filtering can be used to deplete specific sections of a given structures and thus emphasizing other ones.

In addition, the investigation of the effect of the mutual rotation angles γ_i (around the common optic axis) of the individual BCs in the conjugate cascade was performed. This study has revealed that the local polarization angles and local intensities on the individual structures depend on these angles γ_i . The orientation of the last crystal determines the polarization distribution, while the relative orientation of all crystals determines the intensity distribution and the relative importance of individual structures. It was shown that it is possible to isolate anyone of the 2^{N-1} structures by specific choices of the orientation angles γ_i as combinations of the values of 0° and 180° (parallel and anti-parallel orientations). This has been specifically shown as an example in a conjugate cascade of three BCs (see chapter 4).

Most of our theoretical and experimental investigations are concerned with the last focal image plane of the conjugate cascade. However we already observed experimentally in a two BCs conjugate cascade that the non-circular CD beams evolve in a complex way both in terms of intensity and polarization. This evolution is already expected and besides the asymmetry associated to the diffraction in the two transverse dimensions, there is also an asymmetry in longitudinal direction, which has similar origins as the one discussed

recently in [226] for the case of a single crystal CD upon imaging by a spherical lens. A deeper investigation of such pseudo-astigmatic effects out of the focal image plane will be an interesting topic for future studies.

Biaxial crystals are inherently capable of spin-orbit coupling. CD vector beams have been shown in the past to possess half-integer OAM. The phase distribution for a non-integer OAM beam is generally very complex and intricate. It consists of single charged vortices round-off to the nearest integer values i.e. $\alpha = l + 1/2$ [91]. Here alpha is equal to the number of single charge vortices. This rule excludes the exactly half integer or multiples of half integer OAM values, as for them there exists an infinite number of alternating charge vortices along the direction of low intensity line which corresponds to the phase step discontinuity of the spatial phase plate utilized to generate them. Hence CD beams also present generally very interesting features in terms of the OAM of light. Cylindrical lenses are known to modify the OAM of beams and in chapter 5, we have studied the effects on the OAM of our special cascades. The OAM of the non-circular CD beams was investigated via different techniques. Due to the vector nature as well as the possession of fractional OAM values, the determination of the OAM of non-circular CD beams via conventional techniques is a tedious task. However by utilizing a quantitative technique introduced in [191], which utilizes an additional cylindrical lens just before the CCD, the determination of the fractional charge OAM is possible in a more simple way. The obtained fractional OAM values of the non-circular CD beams were showed to scale approximately with the ratio of the magnification values (i.e. M_x/M_y) of the cylindrical lens. Besides determining the fractional OAM charge, the position of the vortices inside these beams is also observed by plane wave interference and off-axis digital holography techniques. It is observed that vortices are spatially located at particular positions in the beam cross-sections. However these two techniques are unable to give a complete picture due to the vector nature of the CD beams. Nevertheless, our investigations permit to conclude that the fractional charge OAM is easily tunable in the complex non-circular CD beams.

Another interesting aspect of our investigations involved performing holographic recording and two-wave mixing (TWM) of CD beams inside a nonlinear photorefractive crystal. Conventional holograms record the intensity of an interference pattern and are therefore usually written using an object and a reference wave sharing a common light polarization, thus maximizing the fringe contrast. Exceptions to this rule exist in the framework of polarization holography[227], which permits to store the polarization state of a wave using polarization-sensitive media. This approach can be used for instance to generate vector beams [228] which have non-uniform polarization distribution. Our investigations have shown for the first time that the linear optical effect associated to CD can be combined with the nonlinear recording of dynamic holograms in a photorefractive material, with all processes taking place within the same medium. The experiments are performed using a nominally undoped $\text{Sn}_2\text{P}_2\text{S}_6$ (SPS) crystal sample cut with input and output faces nearly perpendicular to an optical axis. SPS possesses large electro-optic coefficients and interesting nonlinear optical and PR properties [142]. A unique scenario is considered in which the interfering object and reference waves are associated to orthogonal eigenwaves (perpendicular polarizations) of the SPS crystal. It is observed that when object beam propagates along the optic axis, it is possible to record and read-out holograms or amplify the CD ring even when the two interfering beams are orthogonal eigenwaves. Any slight rotation of

Conclusion and Perspectives

the crystal prior to recording, such that the object wave no longer leads to CD, results in the disappearance of the reconstructed wave for the hologram and negligible amplification of the object wave for TWM experiments.

Further detailed investigations of photorefractive holograms created by a circularly polarized input object wave and a linearly polarized input reference wave revealed that upon read-out the reconstructed conical diffraction wave shows an azimuthal dependence (crescent-like) that depends on the polarization of the reference wave. The reason for this kind of behavior lies in the complex structure of the electro-optic tensor of SPS in combination with the PR space-charge field orientation [215, 216]. The conclusive statement from these investigations is that even though the hologram recording is driven by the intensity distribution as in conventional holography, it is possible for CD beams to achieve efficient recording with any combination of the input polarizations of the object and reference waves, including the case of orthogonal linear or circular polarizations. This behavior can be qualitatively understood by a theoretical model combining the linear optical effect of conical diffraction with the optical nonlinearity associated to the photorefractive effect [142, 224]. Such a corresponding theoretical model verifies qualitatively the experimental observations. Finally, by temporally modulating the polarizations of reference and pump beams via a liquid crystal retarder (LCR), one can dynamically read-out or amplify particular polarization states on the CD ring. This aspect can lead to polarization multiplexing and appears promising for potential applications of such CD holography.

Perspectives for future work

We are convinced that our investigations are opening interesting prospects for further investigations of non-conventional CD beams. The non-circular CD beams generated via conjugate cascades could also be created inside a rectangular/ring cavity. Some preliminary investigations in this direction were performed and presented in appendix A. In these investigations, a single biaxial crystal and a retro-reflector element are utilized in the following way. A beam propagating along the optic axis of the biaxial crystal is sent back by a retro-reflector element placed behind the BC, thus there are two counter-propagating beams along the optic axis of the BC. Different types of retroreflector elements are employed such as prism, two flat mirrors at 45° and special optical elements for instance trihedral prism. The above CD double pass counterpropagating architecture can be thought as a virtual cascade two BCs. The analysis has to consider the wavevector-space transformations provided by the retroreflector element. It is useful in this context to unfold the situation by performing virtual mirroring of the crystal and the beam at the retroreflector mirror surfaces. This allows to determine the unfolded cascade (with the correct orientation angles γ_i) that corresponds to a given experimental situation. A combination of a retroreflector element with polarization scrambling elements or any other optical elements could also be used in such a configuration. Our investigations of such schemes clearly indicates the possibility to generate CD patterns which are easily tunable in intensity and polarization (see appendix A). The further extension of such schemes towards the integration of the BC within a ring cavity would be extremely appealing as it would permit a multiple pass through the same BC and a virtually nearly infinite cascade. Such a ring cavity may incorporate also cylindrical lenses to break the circular symmetry in a way similar to the

one investigated in this thesis.

Another promising area for future investigations involves generation of CD beams from Fibonacci and degenerate cascades. These are special type of cascades where the resulting CD patterns have superposed multiple rings at the same radius. Some preliminary investigation on such special type of cascades hints at the possibility to generate rings with circular polarization or rings, where the ellipticity of the polarization varies along the azimuth direction. In this situation the polarization content of the waves extends beyond the equator of the Poincaré sphere, what could be a path towards the establishment of an alternative technique to generate “Full Poincaré beams”. These special type of cascades such as Fibonacci and degenerate are discussed in Appendix B.

Investigations on the phase conjugation of CD beams is another interesting route yet to be explored. Our preliminary investigations show that one can construct a phase conjugate mirror that acts as a polarization filter.

In sect. 4.4.6 of chap. 4, the free space evolution outside the last focal image plane is observed experimentally. It is clearly observed that the non-circular CD beams evolves in a complex manner longitudinally. A future work in this direction could involve extending the theoretical model by explicitly taking into account the quadratic phase terms associated to the multiple conjugate imaging in those cascades. Generation of non-circular CD beams from conjugate cascade leads to an increased vector pattern richness and versatility as compared to the circular rings of conventional CD cascades. Also the rule of thumbs established from geometric parameters provide the knowledge and prediction power that could be extremely useful for the development of new CD applications and for the modification of existing ones. Also, it is possible to modify the conjugate cascades by the addition of intermediate polarization scrambling by electro-optic elements that can lead to a fast switching of the sub-structures in a way similar to the one proposed in [24], with speeds potentially of the order of GHz. The fast commutation of such highly complex structures is therefore feasible, which may be also used to address resonant phenomena, for instance in connection with optical trapping. Furthermore, the structured beams obtained by the technique described here may lead to multi-chamber and dynamically re-configurable bottle beams, as an extension to the single chamber bottle beams already demonstrated earlier with CD [18]. The ability to tune the fractional OAM charge of these beams as well as the position of single charge vortices could also open doors for interesting applications. It has been well understood and demonstrated that integer charged OAM beams could be used to rotate particles or manipulate them in certain fashion [229]. Similarly, half integer charged vortices are also capable to act as tweezers for trapping particles but in addition if there is a non-uniform distribution of vortices in the overall field of the beam, the particle in that field would experience kicks instead of a constant push. This could result in non-uniform acceleration or rotation around those vortices [41]. The holographic recording and two wave mixing effects also open nice perspectives, such as for instance in multichannel polarization multiplexing of vector beams. The above discussion clearly suggests that the richness and complexity of these naturally created vector beams and the versatility to tailor their properties by just a few parameters allows for a new platform for fundamental and applied studies of this kind of structured light.

CONICAL DIFFRACTION INSIDE A DOUBLE PASS SEMI-CAVITY

CD vector beams have already been investigated in a cavity to generate conical diffraction lasers [39, 230–232]. Such cavities were composed of a concave mirror and a flat mirror. As mentioned in the perspective section, in future it may be interesting to integrate the BC also in ring type cavities giving rise to a potentially almost infinite cascade. In the case of a ring cavity, the beam can be subjected to more than one reflection before entering again the BC. Remarkably, such a situation differs intrinsically from the one where the beam is simply retroreflected once. In this section, we elucidate this aspect with the help of few examples and explain the obtained results with the help of an unfolding technique. The type of semi-cavity that we consider is illustrated in Fig. A.1. The retroreflector produces a double pass through the same crystal. Various retroreflector elements are considered such as a flat mirror, two flat mirrors oriented at an angle of 90° between them thus constituting a double mirror retroreflector, and finally a trihedral prism¹ is also used to retroreflect the incident CD wave. In addition to the retroreflector element, a spherical lens and a linear polarizer are also placed inside the cavity in some of the experiments. This is used to switch k-vector components and/or for performing polarization filtering, respectively.

In Fig. A.1, a He-Ne laser beam (633 nm) is circularly polarized by a quarter wave plate (QWP) and focused by a spherical lens ($f = 200$ mm) to enter the KGW biaxial crystal along one of its optical axes. Our experiments are performed under the conditions of a normalized strength parameter $\rho_0 = 11.3$. The CD double ring obtained at the focal image plane (see inset in Fig. A.1) is made to counter-propagate along the optic axis via the retroreflector element placed at the end of the semi-cavity. A beam splitter placed before the KGW BC reflects the counter-propagating beam towards a CCD. A spherical lens is also placed before the CCD to image the correct plane onto the CCD.

¹This is a mounted TIR Retroreflector Prism commercially obtained from ThorLabs. Such retroreflectors are used to reflect a beam (or an image) back toward its original direction via three reflections, either total internal reflections (TIR) or specular reflections depending on whether the reflective faces are coated. The k-vectors of the corresponding beam will be inverted and reflected through 180° even for oblique incidence.

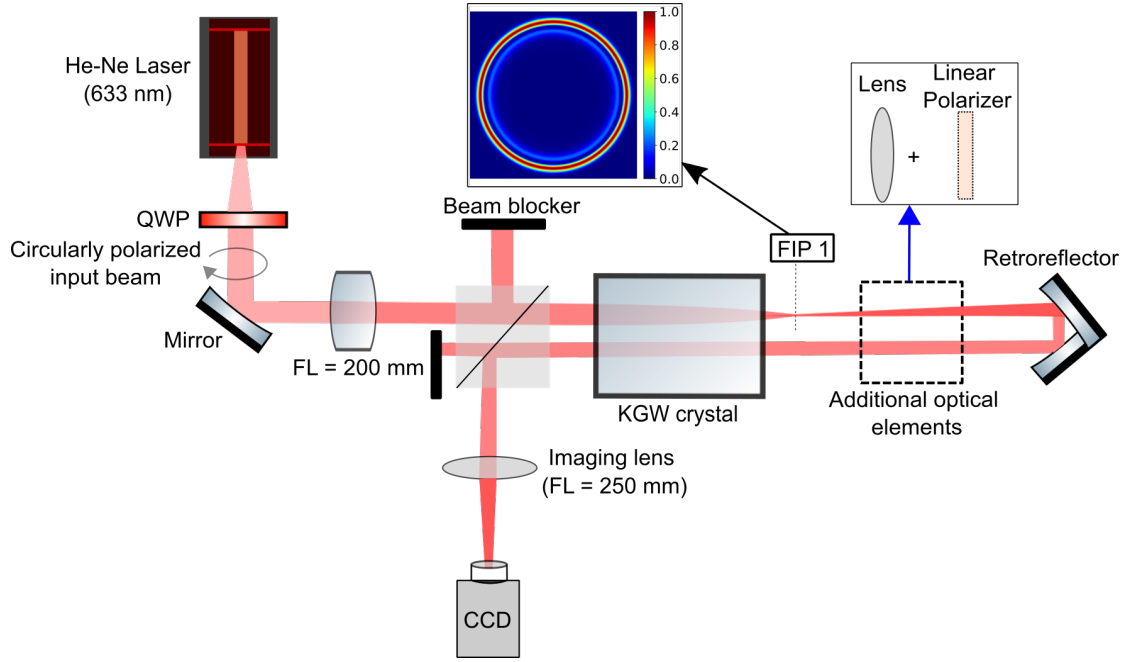


Figure A.1 – Optical setup for a double pass CD cavity utilizing various feedback architectures. The feedback architecture involves a retro-reflector element, which could be single flat mirror, two double mirrors with 90° angle between them, or special corner retroreflector prism. In addition to the retroreflector element, a spherical lens and a linear polarizer can also be used for switching k wavevector components and polarization filtering.

The obtained CD patterns for different retroreflectors are shown in Fig. A.2. By considering just a simple flat mirror, the second pass through the same crystal effectively undoes the effect of the first pass. This results in a single central spot identical to the incident (eventually Gaussian) one (see Fig. A.2(a)). As discussed earlier, the displacement vector γ_n (gives the cone displacement direction) is not uniquely a property of the crystal and its orientation depends on the propagation direction of light. A back reflection from a flat mirror transforms the right-handed system (x, y, z) into a left-handed one, thus in order to keep the dielectric coordinate system right-handed, one needs to flip the direction of the x -axis, which in turn leads to the switching of the γ vector. Thus the present case of flat mirror as retroreflector is equivalent to a CD cascade of two equal length BCs with anti-parallel γ vectors orientations. A theoretical calculation also verifies the experimental observation (see Fig. A.2(e)). This situation has been investigated earlier in the context of conical refraction laser [39]. An equally interesting situation is the one when one inserts a spherical lens between the BC and the flat mirror. In this case the degenerate situation is being lifted and one can expect a situation similar to a variable cascade configuration [23], whereby a spherical lens placed between a cascade of two BCs provides additional extensive versatility as the magnification associated to the lens can be modified. For a two BC variable cascade, a value of magnification can be chosen for which the inner rings would collapse to give a central spot (degeneracy). Since there is a double pass through the lens in the present case, one needs to calculate the effective focal length of the two lens combination in order to determine the magnification provided by this arrangement. By standard geometrical optics

the effective focal length f^* is given as

$$\frac{1}{f^*} = \frac{1}{f} + \frac{1}{f'} - \frac{2d}{ff'} \Rightarrow f^* = \frac{f^2}{2f - 2d}, \quad (\text{A.1})$$

here $d = 50$ mm represents the distance between the lens and flat mirror. Also, $f = f' = 100$ mm represents the lens focal length and its reflection. In this specific case the effective focal length f^* is equal to 100 mm and the effective lens is positioned exactly onto the mirror surface. By placing the spherical lens such that one gets a magnification $M = 1$ i.e. object distance is equal to image distance, one observes the outer ring with radius double as large as for a single pass. This radius corresponds to the one for a single pass through a double as long BC (see Fig. A.2(b)). The spherical lens has the effect of switching the transverse k components while as before the mirror has the effect of switching the γ vector orientation by 180° . Thus in this case, if one assumes that the $\gamma = 0^\circ$ for the first pass through the BC, then the second pass through the BC would have $\gamma = 180^\circ$ with the inverted transverse wavevectors components i.e. the transverse k components should have a negative sign for the second pass. This combined effect is equivalent to a cascade of two BC's with parallel orientation of the γ vector but whether this would result in a degenerate cascade (equal length BCs) or not depends on the magnification provided by the spherical lens. In the presented case $M = 1$, thus one observes a single CD ring with radius equals to the sum of the lengths of the two BCs (identical BCs considered). A theoretical calculation considering the effects of mirror (switching of γ vector orientation) and spherical lens (switching of transverse k components) verifies the experimental observation (see Fig. A.2(f)).

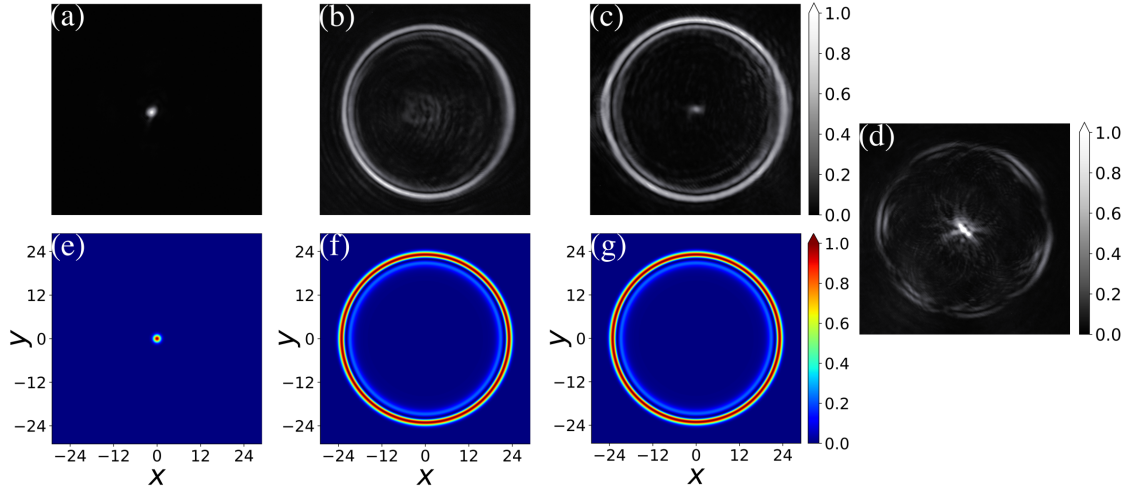


Figure A.2 – CD patterns obtained from a double pass CD cavity with different retroreflector optical elements. The latter are a flat mirror (experiment (a) and theory (e)), a flat mirror with a spherical lens of focal length 100 mm (experiment (b) and theory (f)), a double mirror retroreflector (experiment (c) and theory (g)) and a special trihedral prism (only experiment (d)).

Notably, if instead of a flat mirror one considers a double mirror retroreflector, constituted by two mutually orthogonal mirrors at $+45^\circ$ and -45° (see retroreflector element in Fig. A.1), the behaviour changes drastically. In absence of intermediate lens, such a double mirror retroreflector does not give a single central spot as in Fig. A.2(a), but results in a

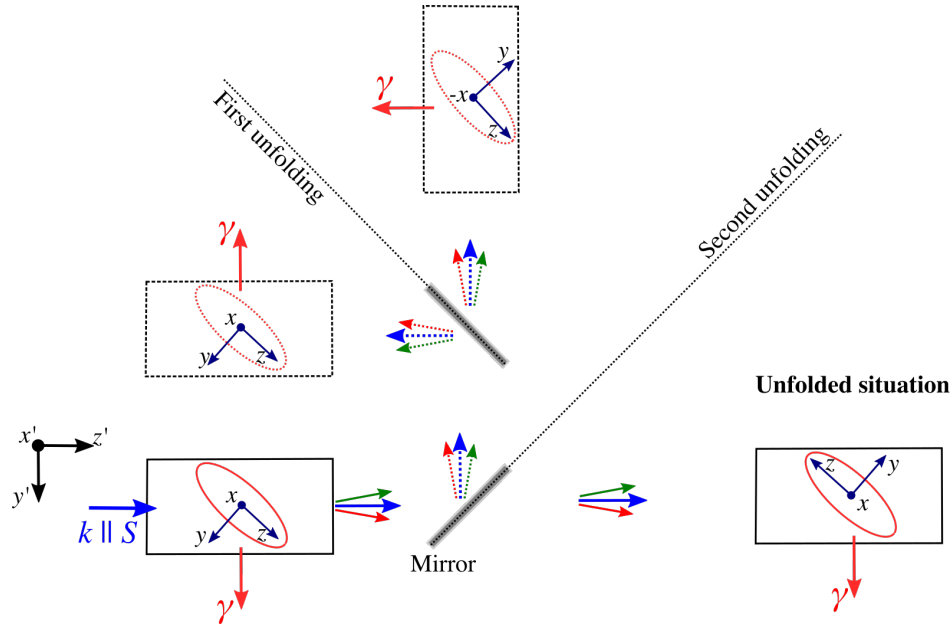


Figure A.3 – Geometrical arrangement corresponding to the case of a double mirror retroreflector and corresponding unfolding. It can be noted that to keep the dielectric coordinate system right-handed the direction of the x -axis is flipped each time along with the one of the γ vector. The thinner red and green arrow near the thick blue one denote k -vector components slightly to the right or to the left of the central one.

single CD ring with radius double as large to the one obtained for a single pass through the BC (see Fig. A.2(c)). Let's try to understand the effect of this double mirror retroreflector on the transverse components of the k wavevector by considering this situation geometrically. Firstly without any loss of generality, we choose the coordinate systems as shown in Fig. A.3, for the dielectric coordinates (x, y, z) and the laboratory coordinates (x', y', z') oriented along the crystal sample axes. The yz -plane (and the $y'z'$ -plane) is the plane containing the optical axes. Also the z -axis of the dielectric coordinate system is associated to the largest index n_g and z' corresponds to the direction of the optical axes parallel to the incident beam. For the considered convention, the axes z and z' make an angle of 42.6° (for KGW BC) between each other while the laboratory x' -axis and the dielectric x -axis are oriented in the same direction, i.e. $x = x'$. In order to ease the visualization, the k -vector components of the incident beam slightly to the right or to the left of the central one (blue) in the $y'z'$ -plane are depicted with red and green color, respectively (see Fig. A.3). It can be observed that double reflection by the two mirrors results in the switching of the sign of the transverse k wavevector components in the plane of incidence (red and green arrows have permutated) along with the switching of the γ . It should be carefully noted that only the transverse k in the plane of incidence is switched, the transverse k departing in vertical direction (the components along x and $-x$) do not switch. This comes from the fact that the plane of incidence (defined by the two mirrors) is the same as the plane of the optical axes (defined by how the crystal is placed on the holder). In order to simulate this situation, the unfolding procedure is illustrated in Fig. A.3. First the BC (as encountered after the retroreflection) is unfolded at the second mirror, then the obtained virtual image (on top in Fig. A.3) is unfolded again on the plane of the first mirror. The aim of this unfolding

is to represent the double pass through the unique crystal as a corresponding two-crystal cascade with the two BCs aligned on the same straight line. It is useful to perform a proper unfolding of the second pass through the BC. Upon each unfolding the dielectric axes and the BC are reflected, which also results in the switching of the γ (and of the x -axis to keep the dielectric coordinate system right handed). It can be observed that each unfolding also results in switching position of the transverse k vector components (red and green arrow). Thus the two unfolding shows that the present situation is equivalent to a cascade of two BCs of equal length and oriented parallel to each other. As already explained, such a situation results in a single CD ring with radius equal to the sum of the lengths of the two BCs and theoretical simulation verifies it (see Fig. A.2(g)). The appearance of a weak central intensity spot in the corresponding experimental CD pattern relates to the fact that the reflections at the two mirrors result in partial depolarization due to different reflectivities for the s and p polarizations. Note that the situation can become even more interesting, if either the crystal or the retroreflector are rotated around their axes by several degrees such that the transverse k components departing in vertical direction would also switch.

Finally, a trihedral prism is also utilized as a retroreflector element and the observed CD pattern when the incident ring hits the center of this prism is shown in Fig. A.2(d). The external ring has intensity distribution that resembles a petal structure. This trihedral prism has pyramid like shape with base formed by three orthogonal faces. Any beam that enters the trihedral prism undergoes three internal reflections (total internal reflection) before being sent out parallel to the incident beam but with lateral shift. One additional feature is that the output beam is modified in polarization as a linear polarization state is changed into elliptical polarization state owing to the polarization dependant phase shift upon total internal reflection. The (rather complex) theoretical modelling of the situation for this trihedral prism as retroreflector was not attempted yet. The acquired CD pattern shows quite interesting features and further experiments to completely understand the output light intensity and polarization are envisaged.

Polarization filtering performed by placing a linear polarizer between the BC and the different retroreflector elements are shown in Fig. A.4. The polarization filtering is performed at four different orientations of the linear polarizer i.e. at $\phi = 0^\circ, 45^\circ, 90^\circ, 135^\circ$. For the case of a flat mirror, as expected, the degenerate situation is lifted out and one can see the external ring with two intensity nodes at diametrically opposite positions on the external ring (see Fig. A.4(a1)-(a4)). A corresponding theoretical simulation verifies the experimental observation, by including additionally a Jones matrix of a polarizer with the corresponding transmission axis angle φ value of the linear polarizer for each situation (see Fig. A.4(b1)-(b4)). This situation is similar to the one analysed in Ref. [24] for a two-crystal cascade with intermediate polarizer. The observation of two nodes is obvious as the flat mirror changes the orientation of the gamma vector by making it anti-parallel to the original orientation. Thus the two nodes correspond to two orthogonal polarizations on the external ring, this is also the reason that one observes same intensity distributions for the polarizer transmission angles of 0° and 90° as well as at 45° and 135° .

By placing a linear polarizer in the situation of the flat mirror with spherical lens giving magnification of about 1.2 in order to avoid degenerate situation, one observes a single intensity node on the external ring but there are two intensity nodes on the internal ring

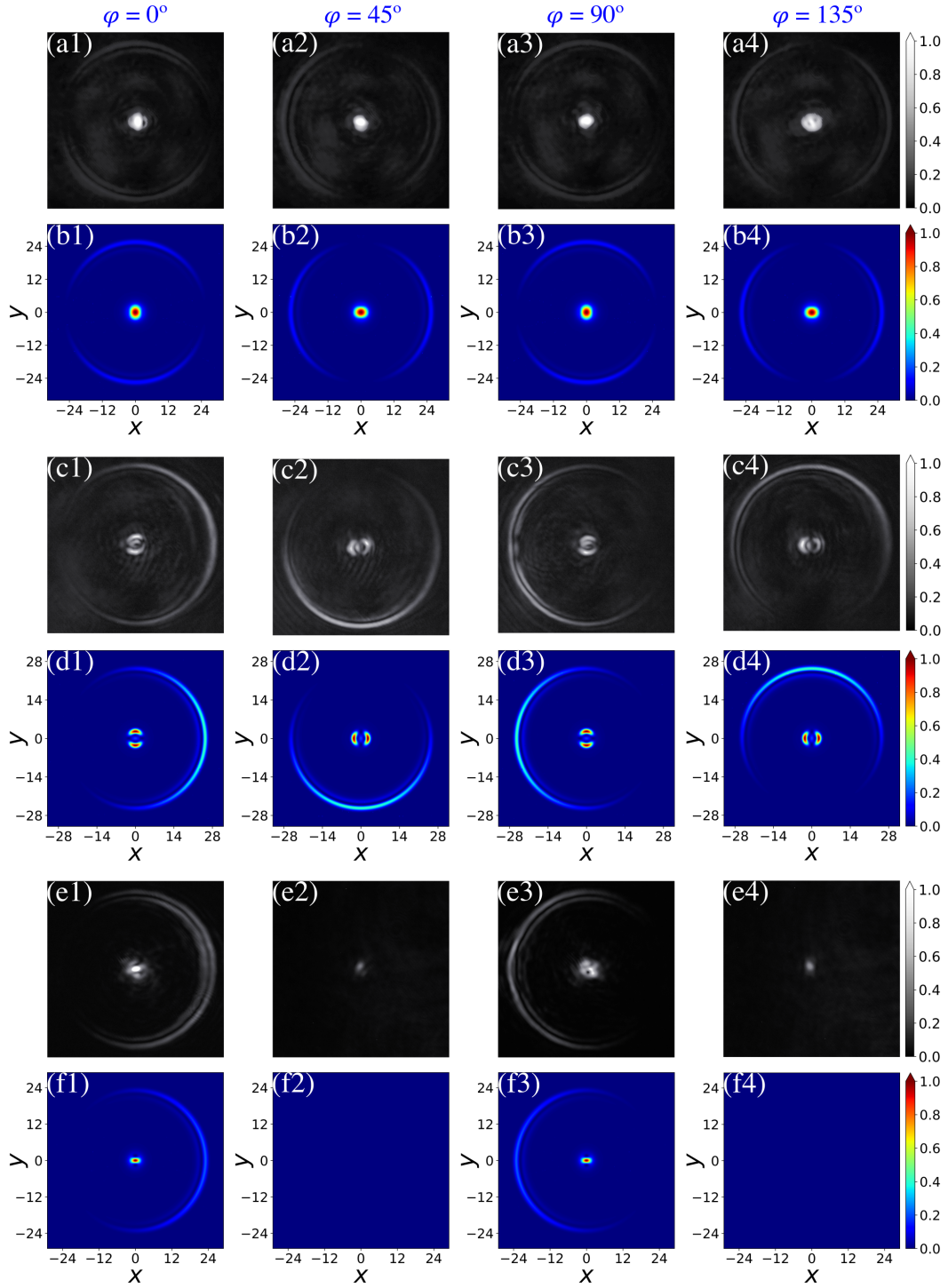


Figure A.4 – Polarization filtering via a linear polarizer placed between the crystal and the different retroreflector elements. The transmission angle φ of the linear polarizer is given on top of each column. Flat mirror + linear polarizer [experiment (a1)-(a4) and theory (b1)-(b4)] , flat mirror with a spherical lens (focal length 100 mm, magnification ≈ 1.2) + a linear polarizer [experiment (c1)-(c4) and theory (d1)-(d4)] and double mirror retroreflector + a linear polarizer [experiment (e1)-(e4) and theory (f1)-(f4)].

(see Fig. A.4(c1)-(c4)). Also it can be observed that the single node on the external ring and two nodes on the internal ring are along the same azimuthal angle and all nodes in the CD pattern rotate in phase as the orientation angle of the linear polarizer is changed. A modified theoretical model including additionally, the effect of the linear polarizer by adding a Jones matrix for the polarizer with the corresponding transmission axis angle φ of the linear polarizer for each situation verifies the experimental observation (see Fig. A.4(d1)-(d4)).

Finally, by placing the linear polarizer in the situation of the double mirror reflector, one observes that for the 0° and 90° orientation of the linear polarizer, a central intensity spot and a single node in the external ring corresponding to the orthogonal polarization being filtered out is observed in the intensity distribution (see Fig. A.4(e1),(e3)). But for the 45° and 135° orientation of the linear polarizer, one observes nothing at all, as all light is blocked out in these situations (see Fig. A.4(e2),(e4)). Again as mentioned before, the double mirror reflects the dielectric coordinates system two times in a way that this results in a cascade of two parallel crystals as in Fig. A.3. However here one needs to consider another important aspect. Indeed, a linearly polarized light oriented at 45° is converted to a 135° polarization after the two reflections from the double mirror retroreflector. In this case all the light would be blocked at the second pass through the 45° polarizer as seen theoretically in Fig. A.4(f2). A similar situation occurs for the polarizer at 135° (see Fig. A.4(f4)). Theoretically this is incorporated by adding two polarizer Jones matrices. For the two cases of linear polarizer transmission axis oriented at $\varphi = 0^\circ$ and 90° both the Jones matrix have the same value for the transmission axis (no rotation of polarization upon reflection) angle φ . In contrast, for the cases $\varphi = 45^\circ$ and 135° the first Jones matrix correspond to the initial transmission axis angle φ of the linear polarizer but the second has the orthogonal value to the first one i.e. if $\varphi_1 = 45^\circ$ then $\varphi_2 = 135^\circ$ and vice versa. Theoretical calculation including this incorporation verify the experimental observations (see Fig. A.4(f1)-(f4)). As before the appearance of a weak central intensity spot in the experimentally obtained patterns in Fig. A.4(e2) and (e4) is due to partial depolarization owing to different reflectivities by the two mirrors for the s and p polarizations.

In conclusion, we have shown that our two-pass investigations using various types of retroreflectors in a semi-cavity can be well modeled by taking advantage of a simple unfolding procedure. This relatively simple situations already shows an impressive richness. It is expected that this will be increased much further by implementing a full ring cavity including one or more BCs, several mirrors and some imaging lenses. Of particular interest will be the case where the cavity will contain one or more conjugate cascades based on cylindrical lenses that we have discussed extensively in this thesis.

FIBONACCI AND DEGENERATE CASCADES OF CONICAL DIFFRACTION

Here, we present preliminary investigations on special types of cascades, which exploit the fact that concentric 2^{N-1} double rings in an N crystal conventional cascade result from a superposition of ρ values of the individual biaxial crystals in that cascade. This is mathematically expressed as

$$\rho_{tot} = |\rho_1 \pm \rho_2 \pm \rho_3 \dots \pm \rho_{N-1} \pm \rho_N|, \quad (\text{B.1})$$

which in general leads to 2^{N-1} different values for ρ_{tot} . However, this equation hints at particular interesting situations, which can happen by choosing the ρ_i values for the individual BCs in a specific way. In some cases it is possible that two or more ρ_{tot} values are the same. In this case, the corresponding circular rings have the same radii and are coherently superposed. Two such special types of cascades are the Fibonacci and fully degenerate cascade, that we discuss briefly in this appendix. In a Fibonacci cascade, the ρ_i values follow a Fibonacci series, while in a degenerate cascade all the individual BCs in the cascade have the same CD strength, $\rho_i = \rho_0$.

As an example, a Fibonacci cascade of four and five BCs has been investigated with ρ values following a Fibonacci series starting from five (see Fig. B.1). The γ values are chosen such that each two adjacent BCs are in crossed configuration but this also implies that each concentric double ring possess same energy density in terms of intensity of light. By evaluating the radii of the concentric double rings via eq. (B.1) for a four BCs Fibonacci cascade, it turns out that there are two concentric double rings superposed at radius of $\rho = 5$ and two at radius of $\rho = 21$, so that there are only 6 instead of 8 double rings. One can observe that the intensity of these two double rings is enhanced in comparison to the other double rings (Fig. B.1(a1)). Here the relative phase $\Delta\phi$ between the y and x components of \mathbf{D} still remains either 0° or 180° on these two double rings, thus suggesting a varying linear polarization with the azimuth direction (see Fig. B.1(a2)). Another interesting observation consist in the fact that the exact position of either horizontal or vertical linear polarization on the double ring at $\rho = 21$ is not aligned with the one for the other double rings (see Fig. B.1(a3)). Again, it should be kept in mind that the exact spatial position of vertical and hor-

horizontal linear polarization states on the double rings depends primarily on the orientation of the last BC in the cascade.

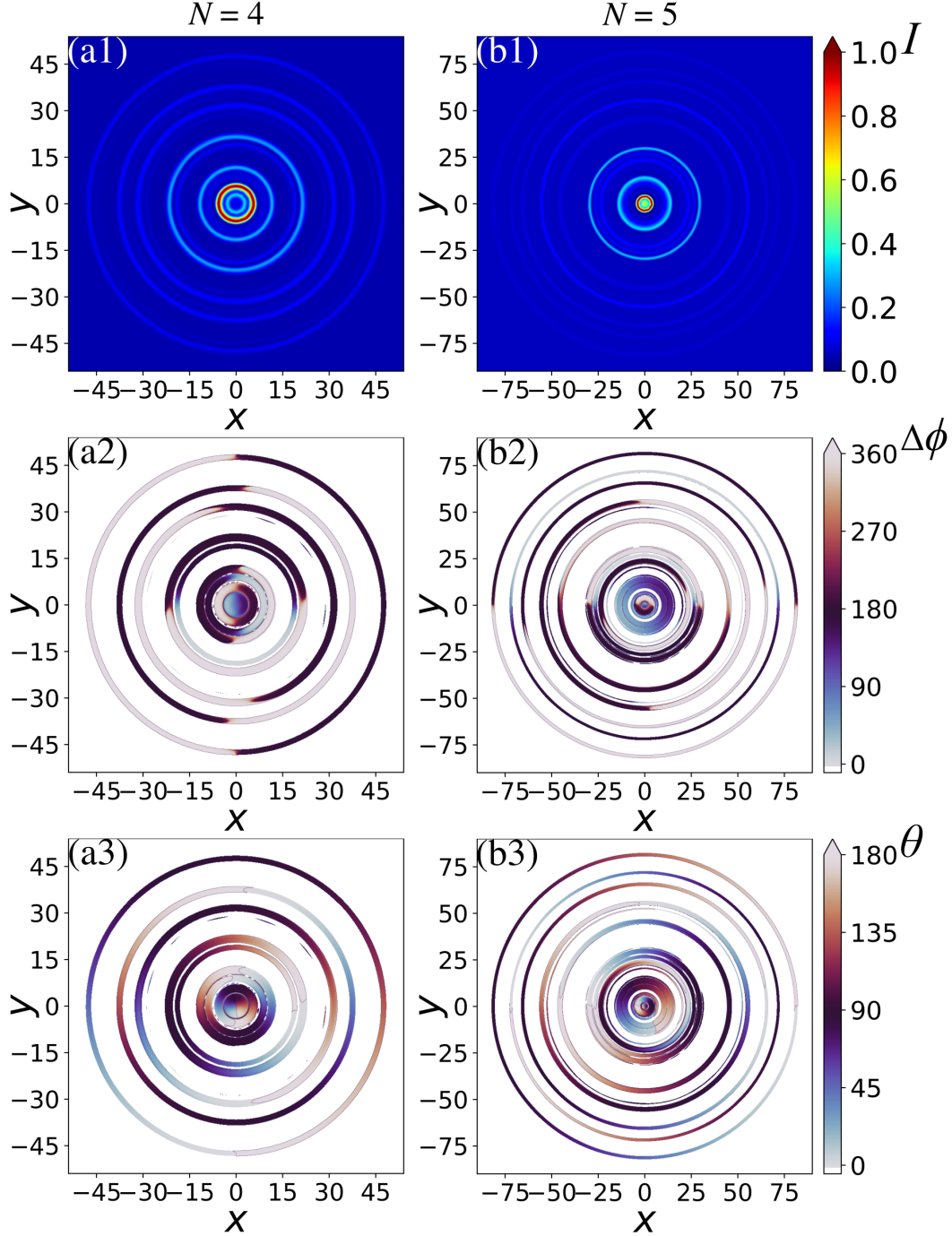


Figure B.1 – Intensity (first row: (a1),(b1)), relative phase $\Delta\phi$ (second row: (a2),(b2)) and polarization angle θ (third row: (a3),(b3)) distributions of a Fibonacci cascade of four (first column: (a1)-(a3)) and five (second column: (b1)-(b3)) biaxial crystals. The parameters are as follows: ρ_i values correspond to a Fibonacci series starting from 5, i.e. for four BCs cascade ρ values correspond to 5, 8, 13, 21 while for five BCs 5, 8, 13, 21, 34. The γ_i values follow the series $0^\circ, 90^\circ, 0^\circ, 90^\circ \dots$ and so on, depending on the number of crystals in the cascade.

Similarly by evaluating the double rings radii via eq. (B.1) in the case of five crystals Fibonacci cascade, it turns out that two double rings are superposed at each of the radial positions $\rho = 3, 29, 39, 55$ while there are three double rings superposed at the radial distance $\rho = 13$. Again as before the superposed double rings are brighter in comparison to other double rings (see Fig. B.1(b1)). However an interesting observation is that the superposition of three double rings at radius of $\rho = 13$ results in a double ring, which possess relative phase that vary linearly between 45° and 135° implying the presence of elliptical polarization with varying ellipticity along the azimuth direction (see Fig. B.1(b2)). As a consequence of this variation in the relative phase, there exists a spatial position on this double ring with a relative phase of 90° indicating the presence of circular polarization. The relative phase $\Delta\phi$ on all other rings takes only values of either 0° or 180° , thus implying linear polarization on them. The polarization distribution for all the rings is shown in Fig. B.1(b3). For the ring possessing elliptical polarization states (at radius $\rho = 13$), the angle θ represents the orientation of the polarization ellipse, i.e. the direction of a linear polarizer giving maximum local transmission of the light at the corresponding position on the pattern.

Although the Fibonacci cascade enables superposition of double rings, but the most interesting double rings with three or more superposed rings only happens for a cascade of more than five BCs. On the other hand, a degenerate cascade of three or more crystals always possesses at least two superposed rings at each of the ring radii except at the outermost ring, where there will always be just one double ring (addition of all the ρ_i values).

As an example, Fig. B.2 illustrates degenerate cascades of up to five BCs with $\rho_0 = 10$ starting from a two BCs degenerate cascade. It has been observed that a degenerate cascade of an even number of BCs always result in a central intensity spot (see Fig. B.2(a1),(c1)) with polarization matching the incident polarization state. As in our case a left circularly polarized incident beam is considered, it can be observed that the relative phase at this central spot is 90° corresponding to this circular polarization (see Fig. B.2(a2),(c2)). A degenerate cascade with odd number of crystals lacks such central intensity spot feature (see Fig. B.2(b1),(d1)). A degenerate cascade of two BCs has been investigated theoretically and experimentally earlier and it has been shown that the central intensity spot do possess polarization that matches with the incident polarization state [23, 184, 233].

For a three BCs degenerate cascade, one gets three superposed double rings at radius of $\rho = 10$ and no superposition on the outermost rings for the reason mentioned above (see Fig. B.2(b1)-(b3)). These three double rings superposition results in a relative phase $\Delta\phi$ that varies between 225° and 315° thus implying azimuthally varying elliptic polarization (see Fig. B.2(b2)). The orientation of the polarization ellipse for these elliptic polarization states on this double ring can be observed in Fig. B.2(b3). As before, there exists a spatial position on this ring where the relative phase $\Delta\phi = 270^\circ$ with the polarization ellipse orientation of 45° , thus indicating the presence of right circular polarization at this point. Similarly, an investigation into four and five BCs degenerate crystals results in similar interesting features observed on the internal superposed rings. For Four BCs degenerate cascade, one gets three double rings merged into a single spot at the center with left circular polarization state, four double rings superposed onto each other at $\rho = 20$ resulting into a double ring with varying elliptic polarization states along the azimuth direction and one outer-

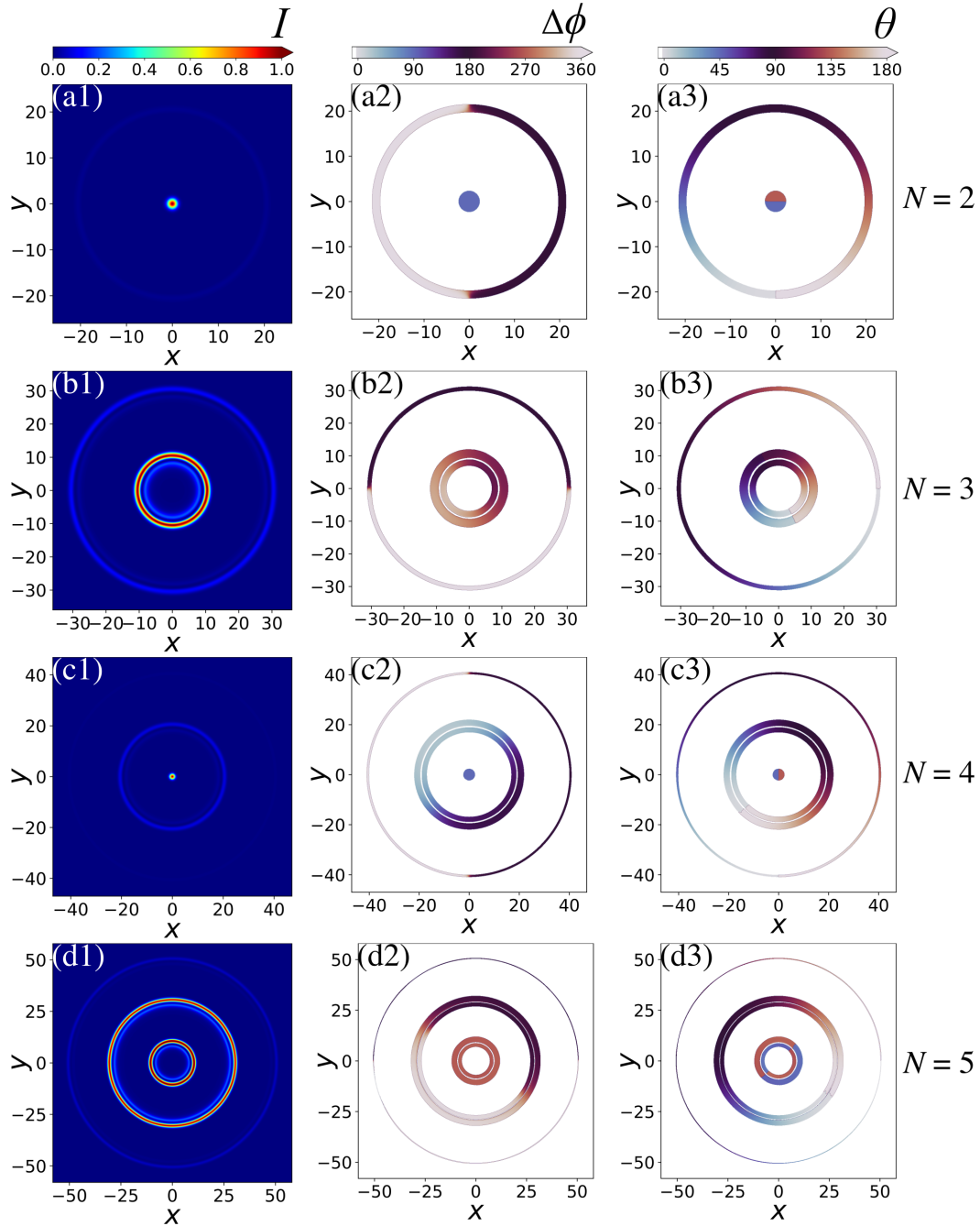


Figure B.2 – Intensity (first column), relative phase $\Delta\phi$ among \mathbf{D} components (second column) and polarization direction θ (third column) distributions for a degenerate cascade of two (first row), three (second row), four (third row) and five (fourth row) BCs. The parameters are: $\rho_0 = 10$ for all crystals in the cascade. The γ values follow a series of $0^\circ, 90^\circ, 0^\circ, 90^\circ \dots$, and are therefore in a mutually crossed configuration.

most double ring at $\rho = 40$ with conventional varying linear polarization states (see Fig. B.2(c1)-(c3)). Finally, for five BCs degenerate cascade one gets ten superposed double rings at $\rho = 10$ resulting in a double ring with a relative phase $\Delta\phi = 270^\circ$ implying that this is a double ring with circular polarization state, five double rings superposed at $\rho = 30$ and one

outermost ring at $\rho = 50$ both of which possess a relative phase $\Delta\phi$ values of either 0° or 180° , thus implying conventional varying linear polarization states (see Fig. B.2(d1)-(d3)).

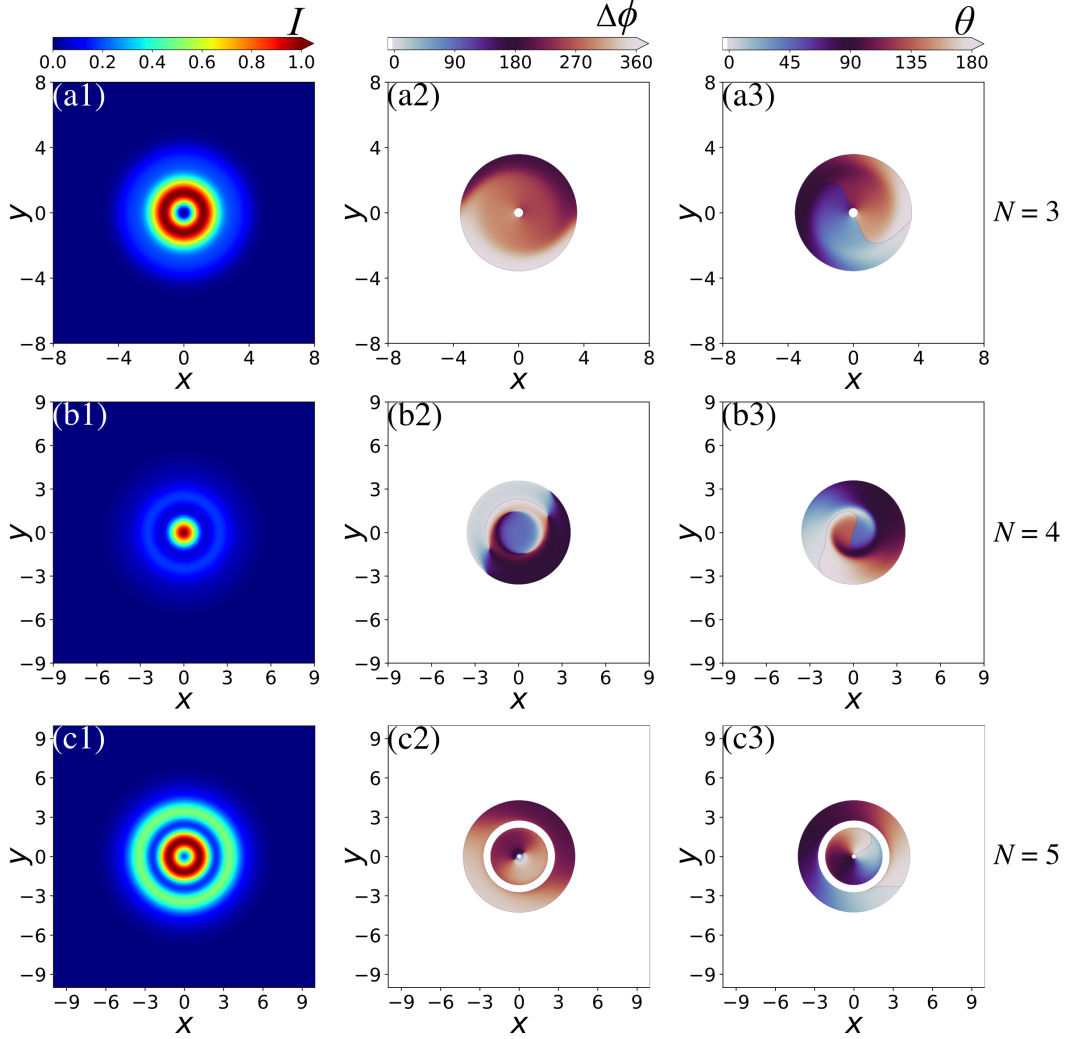


Figure B.3 – Intensity (first column), phase (second column) and polarization (third column) distributions for a degenerate cascade of three (first row), four (second row) and five (third row) BCs are presented. The parameters are as follows: $\rho = 1$ for each biaxial crystal in the cascade and the γ values follow a series of $0^\circ, 90^\circ, 0^\circ, 90^\circ \dots$ and so on, depending on the number of crystals in the cascade.

It has been shown with few illustrative examples of a degenerate cascade with $\rho_0 = 10$ that it is possible to generate CD rings with varying elliptic polarization or a CD ring with a circular polarization. Another interesting situation for a degenerate cascade is to choose $\rho_0 = 1$, that is a less strong focusing of the input wave. A single CD pattern with $\rho_0 = 1$ leads to a donut shaped beam instead of a conventional CD double ring as the Poggendorf ring is not observed. Degenerate cascades with $\rho_0 = 1$ for a three, four and five BCs are shown in Fig. B.3. It can be observed that the intensity distribution for such a three crystal cascade is still a donut (see Fig. B.3(a1)) with a relative phase that varies between 225° and 315° but in addition this variation happens not only along azimuth but also radially to some extent (see Fig. B.3(a2)). An extension of such a degenerate cascade of $\rho_0 = 1$ to four and

five crystals results in a central intensity spot with ring outside and donut inside an outer ring respectively (see Fig. B.3(b1) and (c1)). The relative phase ($\Delta\phi$) distributions on the inner donut and outer ring reveal the presence of varying elliptic polarizations along the azimuth direction and these elliptic polarization states are not same on the inner donut and outer ring along any azimuth angle (see Fig. B.3(c2)). The orientation of the polarization ellipse for these varying elliptic polarization states can be observed in the last column of Fig. B.3(a3)-(c3).

It is quite evident from these preliminary investigations that these special Fibonacci or degenerate cascades can lead to CD patterns which possess besides varying linear polarization states, double rings with varying elliptical polarization states or even a double ring with just circular polarization. Additionally these results also show an interesting potential towards “Full Poincare kind of beams” with spatially separated linear, circular and elliptical polarization states in the form of rings. Hence the Fibonacci or degenerate cascades proposed here could greatly improve the versatility of the tailoring of the polarization profile of CD vector beams.

SYNTHÈSE DE LA THÈSE

La mise en forme et la structuration de faisceaux lumineux en termes d'intensité, de phase et de distribution de polarisation attirent actuellement une grande attention avec des applications allant de la micromanipulation et de l'imagerie 3D à la communication classique et quantique [1, 12]. Parmi les structurations lumineuses possibles, on trouve les faisceaux vectoriels qui possèdent une polarisation variable distribuée spatialement sur la coupe transverse des faisceaux, ainsi que les faisceaux présentant des singularités de phase et un moment cinétique orbital (OAM), tels que les vortex optiques. Outre leur fort intérêt fondamental, de tels faisceaux dits non conventionnels émergent pour un nombre croissant d'applications. Il s'agit notamment de la manipulation optique ou "pince optique" [10, 11], de l'exploitation de l'OAM pour le multiplexage par répartition en modes dans la communication optique [13] ou pour l'information quantique [14, 15], l'imagerie super-résolution [16], ainsi que d'autres technologies clés dans des domaines tels que la métrologie, l'usinage optique, la biomédecine, la chimie... [1, 81].

La diffraction conique interne (CD, également appelée réfraction conique interne) est un phénomène naturel conduisant à des faisceaux vectoriels de forme circulaire possédant un OAM fractionnaire. Cet effet particulier a intrigué la communauté scientifique depuis sa prédiction par W. R. Hamilton il y a près de 200 ans et la première observation expérimentale par H. Lloyd peu après. Le phénomène de CD est observé lorsqu'un faisceau suffisamment focalisé est incident sur un cristal optiquement biaxial (BC) avec son vecteur d'onde \mathbf{k} parallèle à l'un des axes optiques du cristal [18]. Pour cette direction \mathbf{k} singulière, les directions du vecteur de Poynting sont dégénérées et se trouvent à la surface d'un cône incliné à base circulaire à l'intérieur du cristal. La section de ce cône peut être facilement visualisée dans un plan de focalisation particulier de l'onde incidente (plan focal image, FIP), où l'on observe deux anneaux lumineux rapprochés et séparés par un anneau sombre (appelé anneau de Poggendorff). Deux points diamétralement opposés possèdent toujours des polarisations linéaires orthogonales, conduisant au caractère vectoriel du faisceau [18–20]. Une explication géométrique élégante de la façon dont les directions des vecteurs de Poynting sur le cône dépendent des vecteurs électriques locaux (\mathbf{E}) et de déplacement électrique (\mathbf{D}) de l'onde est donnée dans le livre de Born et Wolf. [21]. Au cours des deux dernières décennies, la recherche sur le CD a été fortement relancée. Ceci est dû d'une part à une meilleure compréhension théorique du phénomène suite à la théorie de la diffraction paraxiale [19] et d'autre part à son potentiel pour plusieurs applications photoniques modernes dans le cadre de la lumière structurée [18] parmi lesquelles on peut citer le piégeage optique [35, 180], la mise en forme de faisceaux [24, 36], le multiplexage en espace libre pour la communication [37], la polarimétrie [38, 175, 181], l'imagerie super-résolution [40] ou le contrôle d' OAM [26, 27, 29].

Un développement récent majeur dans le domaine du CD consiste en l'étude de configurations dites "en cascade" dans lesquelles deux ou plusieurs cristaux sont mis en série avec leurs axes optiques alignés [22, 172–174]. Une telle CD en cascade conduit à une multiplication du nombre d'anneaux observés dans le FIP, pour N cristaux on obtient 2^{N-1} doubles anneaux [22]. La cascade a comme paramètres libres les angles de rotation relatifs γ_n (autour de l'axe optique commun) du $n^{\text{ème}}$ cristal par rapport au premier de la cascade.

Par exemple, pour $N = 2$ les intensités relatives dans les deux doubles anneaux dépendent de cet angle [174], pour $\gamma_2 = 0$ (cristaux parallèles) seul l'extérieur des deux doubles anneaux survit, tandis que pour $\gamma_2 = \pi$ (cristaux antiparallèles), seul celui interne survit. Pour un monocristal le rayon du double anneau correspond au produit $\mathcal{R} = \alpha L$ du demi-angle d'ouverture α du cône de CD (qui est fonction de la biréfringence du matériau) et de la longueur du cristal L . Surtout, pour deux BC en cascade du même genre (même α) et de longueurs L_1 et L_2 les doubles anneaux externe et interne ont un rayon $\mathcal{R}_{ext} \propto L_1 + L_2$ et $\mathcal{R}_{int} \propto |L_1 - L_2|$, respectivement [22, 174]. Évidemment, si les longueurs des deux cristaux sont identiques, le double anneau interne dégénérera en une tache centrale. Il existe cependant une manière élégante introduite récemment par Peet[23] de modifier ces rayons par une technique appelée cascade variable à deux cristaux. Une lentille sphérique est intercalée entre les deux cristaux en cascade de manière à imager le FIP proche du premier cristal dans un second FIP proche du second BC. Il a été montré que le facteur de grossissement M de cette imagerie modifie les valeurs relatives des rayons du double anneau observés selon $\mathcal{R}_{ext} \propto ML_1 + L_2$ et $\mathcal{R}_{int} \propto |ML_1 - L_2|$ [23]. Cela rend l'effet beaucoup plus polyvalent et permet le réglage continu des paramètres réels de la cascade malgré l'utilisation de cristaux de longueurs fixes.

En ce qui concerne la distribution d'intensité, si l'onde d'entrée a une polarisation circulaire, l'intensité le long des anneaux est homogène. Une distribution azimutale inhomogène peut être obtenue en polarisant linéairement la lumière à l'entrée ou à la sortie[18] ou, de manière plus drastique, en modifiant la polarisation entre deux ou plusieurs BC en cascade[24], auquel cas des motifs vectoriels d'une complexité accrue sont obtenus. Néanmoins, malgré tous les développements décrits ci-dessus, les motifs CD obtenus jusqu'à présent possèdent toujours intrinsèquement une forme circulaire. Cette forme est associée à la section du cône CD avec un plan perpendiculaire au vecteur d'onde central et à l'axe optique des BC.

Ce travail de recherche montre que la symétrie circulaire peut être considérablement brisée par une manipulation appropriée dans l'espace des vecteurs d'onde entre les BC dans une cascade. Cela conduit à des motifs CD d'une grande complexité, tant en termes de formes que de distribution de polarisation. L'aspect clé de cette approche est de diviser l'espace des vecteurs d'onde 2D (espace \mathbf{k}) entre deux BC en deux sous espaces 1D. Cette manipulation est réalisée en insérant deux lentilles cylindriques (CL) avec leurs axes perpendiculaires l'un à l'autre. Les deux CL sont disposées de manière à fournir un plan image commun du premier FIP (FIP1 correspondant au plan focal de l'onde incidente focalisée) dans un deuxième plan placé à proximité du deuxième BC (FIP2). Cette imagerie est cependant associée à différents facteurs de grossissement M_x et M_y selon les directions transversales x et y (voir Fig. 4.1 au chapitre 4). La transformation ci-dessus conduit à des modèles de CD en cascade (observés à FIP2) avec une symétrie circulaire fortement brisée possédant une distribution complexe d'intensité et de polarisation[152]. Un modèle théorique basé sur l'approche optique de Fourier prend en compte les manipulations asymétriques de l'espace des \mathbf{k} par des lentilles cylindriques croisées ainsi que l'effet de chaque BC sur la phase de l'onde vectorielle. Une fonction de transfert appropriée permet de calculer le champ \mathbf{D} de sortie au dernier plan focal image en effectuant une intégration numérique de l'intégrale complexe bidimensionnelle.

La figure 1 montre la distribution d'intensité et de polarisation ainsi que la composante S_3 des motifs CD non circulaires acquis à partir d'une cascade conjuguée de deux (Fig. 1(a1)-(b3)) et trois (Fig. 1(c1)-(c3)) BC. La première ligne représente la distribution d'intensité obtenue en calculant l'intensité locale en tout point du plan focal image (FIP) correspondant ($I \propto |\mathbf{D}|^2$). On peut observer que sur la figure 1, les trois modèles CD non circulaires possèdent une distribution d'intensité variable de manière non homogène le long de la direction de l'azimut. La deuxième ligne de la figure 1 donne les valeurs codées par couleur de la direction de polarisation locale θ sur le motif lumineux observable dans le plan focal image. L'angle θ est lié au rapport des composantes y et x du champ \mathbf{D} de sortie. Ces composantes sont en générale complexes, c'est-à-dire $D_x = R_x \exp(i\phi_x)$, $D_y = R_y \exp(i\phi_y)$ et θ est défini comme $\theta \equiv \arctan [(R_y/R_x)\text{sign}(\cos \Delta\phi)]$, avec $\Delta\phi \equiv (\phi_y - \phi_x)$. Aux positions où la polarisation est linéaire, θ donne simplement la direction de polarisation par rapport à l'axe x du laboratoire. Aux positions où une composante elliptique existe, l'angle θ donne l'orientation du grand axe de l'ellipse de polarisation, c'est-à-dire la direction d'un polariseur linéaire donnant une transmission locale maximale de la lumière à la position correspondante sur le motif. On observe que la polarisation locale sur les structures non circulaires générées est linéaire à l'exception des régions où les structures individuelles non circulaires se croisent ou se chevauchent localement avec différentes branches d'une même structure: ces régions possèdent alors des polarisations elliptiques ou circulaires. A noter que la structure interne du motif CD non circulaire sur la Fig. 1(b1) fusionne avec elle-même en raison de la dégénérescence le long de l'axe des x , de sorte que la région locale au centre possède une polarisation circulaire ou elliptique. De même, la distribution d'intensité du motif de la Fig. 1(c1) montre des croisements ou des chevauchements avec d'autres structures indiquant la présence d'une polarisation circulaire ou elliptique. Ces observations sont vérifiées en évaluant la composante elliptique S_3 du vecteur de polarisation de Stokes défini comme $S_3 \equiv I_R - I_L$, où I_R (I_L) sont les composantes polarisées circulairement droite (gauche) de l'intensité locale. Enfin, on peut observer dans les trois motifs CD non circulaires de la Fig. 1 que l'évolution de l'angle de polarisation n'est pas une fonction linéaire de l'angle polaire sur les structures. Ces observations contrastent fortement avec les modèles CD obtenus à partir d'une cascade conventionnelle, qui aboutissent à la génération de plusieurs anneaux concentriques avec une intensité uniforme et une polarisation variable de manière homogène.

Les cristaux biaxiaux sont intrinsèquement capables de couplages spin-orbite. Cela implique une propriété supplémentaire aux faisceaux vectoriels CD: ils possèdent un moment cinétique orbital (OAM) demi-entier. La distribution de phase pour un faisceau OAM non entier est extrêmement complexe. Il se compose de vortex chargés dont la charge topologique est arrondie aux valeurs entières les plus proches, c'est-à-dire $\alpha = \mathcal{L}_{mesur} + 1/2$ [91]. Ici, α est égal au nombre de vortex à charge unique. Il a été démontré que la position de ces vortex à charge unique peut également être contrôlée. De plus des faisceaux OAM chargés entiers peuvent être utilisés pour faire tourner des particules ou les manœuvrer d'une certaine manière [229]. Enfin, les faisceaux OAM demi-entiers ont des vortex capables de pincer ou de piéger des particules, ou bien encore s'il y a une distribution non uniforme des vortex dans le champ global du faisceau, la particule dans ce champ subirait des à-coups au lieu d'une poussée constante. Cela pourrait entraîner une accélération ou une rotation non uniforme autour de ces vortex à charges uniques [41].

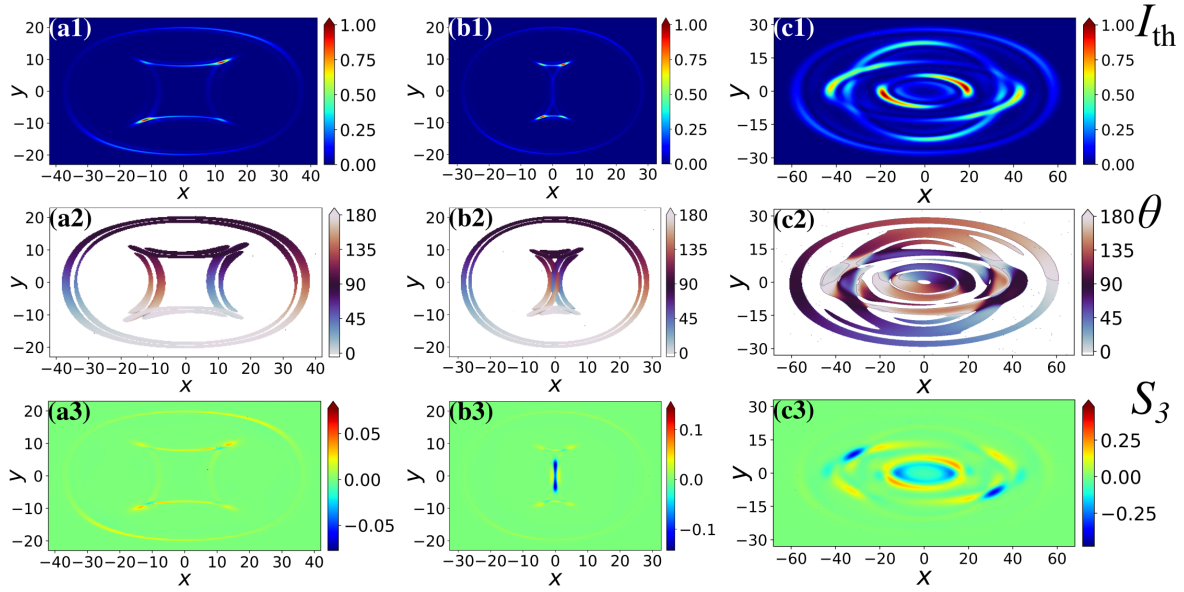


Figure 1 – La distribution d'intensité (première ligne), la distribution de polarisation (deuxième ligne) et la composante S_3 Stokes parameter (troisième ligne) sont présentées à titre d'exemple pour trois modèles de CD non circulaires obtenus via une cascade conjuguée de deux (les deux premières colonnes, c'est-à-dire (a1)-(b3)) et trois BC (dernière colonne, c'est-à-dire (c1)-(c3)). Ici, $\rho_1 = 17, 9$, $\rho_2 = 13, 9$; $\gamma_1 = 0^\circ$, $\gamma_2 = 90^\circ$ pour les deux premières colonnes représentant deux BC en cascade, tandis que $\rho_1 = 12$, $\rho_2 = 9, 3$, $\rho_3 = 7, 3$; $\gamma_1 = 0^\circ$, $\gamma_2 = 90^\circ$, $\gamma_3 = 180^\circ$ pour la dernière colonne représentant la cascade de trois BC. Les paramètres de cascade conjuguée sont les suivants: (a1)-(a3) $(M_{x,1}; M_{y,1}) = (1, 25; 0, 325)$, (b1)-(b3) $(M_{x,1}; M_{y,1}) = (0, 778; 0, 323)$ et (c1)-(c3) $(M_{x,1}; M_{y,1}) = (2, 50; 4, 30)$ et $(M_{x,2}; M_{y,2}) = (1, 25; 0, 325)$. Les paramètres ρ_i , γ_i et M_x , M_y donnent la force de diffraction conique de chaque cristal, leur orientation relative et les conditions d'imagerie de la cascade conjuguée avec lentilles cylindriques croisées respectivement (voir chapitre 4).

En raison de la nature vectorielle ainsi que de leurs OAM à valeurs fractionnaires, il s'avère difficile de déterminer l'OAM de faisceaux CD non circulaires via des techniques conventionnelles. Cependant, en utilisant une technique de mesure quantitative[191], à base d'une lentille cylindrique (CL) supplémentaire placée juste avant le CCD, on pourrait déterminer la charge fractionnaire OAM. La figure 2 montre la mesure quantitative de l'OAM pour deux des modèles de CD non circulaires obtenus via une cascade conjuguée. Étant donné que la distribution d'intensité dans ces deux modèles ne possède pas de symétrie de réflexion, afin de déterminer quantitativement l'OAM, deux mesures sont nécessaires, c'est-à-dire une avec l'axe horizontal de CL et l'autre avec l'axe vertical de CL. La distribution d'intensité obtenue théoriquement et expérimentalement dans le plan focal des CL pour le cas avec des valeurs de grossissement $M_x = 1.25$ et $M_y = 0.325$ est présentée sur la Fig. 2 [théorie (a2)-(a3) et expérience (b2)-(b3)] et pour le cas avec $M_x = 2.50$ et $M_y = 0.233$ sur la Fig. 2 [théorie (c2)-(c3) et expérience (d2)-(d3)]. La valeur OAM fractionnaire est calculée à l'aide de l'équation. (5.13) en considérant les deux modèles de chaque cas et les valeurs OAM fractionnaires obtenues sont répertoriées dans la dernière colonne de la figure. 2. Une bonne correspondance entre les valeurs OAM fractionnaires obtenues expérimentalement et théoriquement peut être observée. De même, l'OAM fractionnaire est mesuré pour d'autres motifs non circulaires et on observe que la charge fractionnaire

OAM de ces faisceaux non circulaires augmente avec le rapport des valeurs de grossissement (M_x/M_y ou M_y/M_x) des deux lentilles cylindriques utilisées pour les générer. Ces résultats offrent des perspectives intéressantes pour les faisceaux CD non circulaires, car des vortex à charge fractionnaire ont été utilisés en optique atomique [193], communication quantique [194–197], les pinces optiques ou la manipulation de particules microscopiques [198, 199] et bien d'autres [187, 202–205].

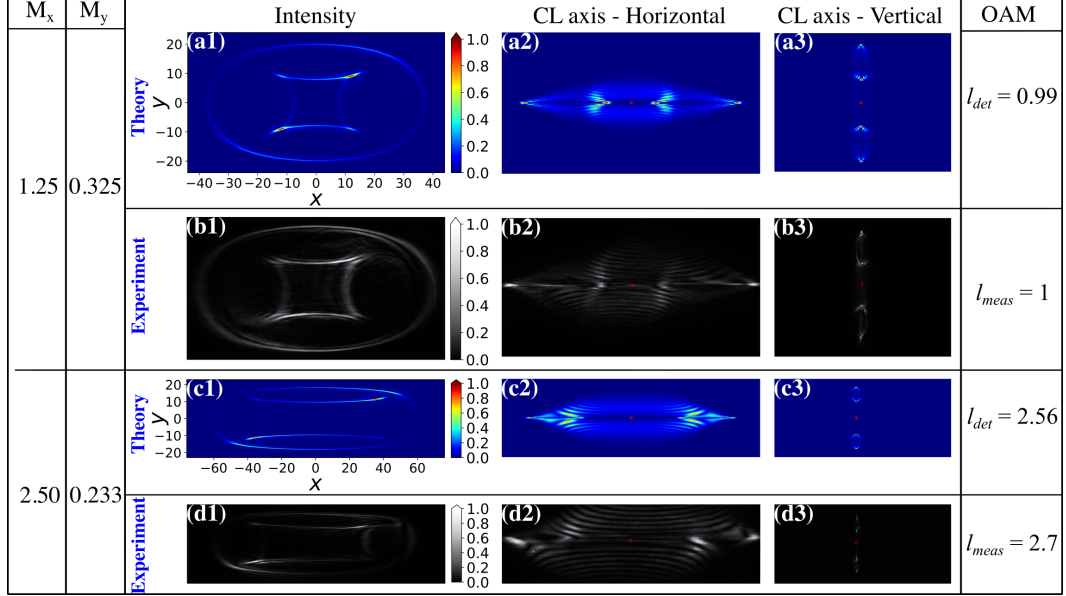


Figure 2 – OAM pour deux motifs non circulaires générés dans une cascade conjuguée de deux cristaux biaxiaux. Les deux modèles sont pour $\rho_1 = 17,9 = \rho_2 = 13,9$ et les angles d'orientation des cristaux $\gamma_1 = 0, \gamma_2 = \pi/2$. tandis que les valeurs de grossissement sont $M_x = 1,25$ et $M_y = 0,325$ [théorie (a1)-(a3) et expérience (b1)-(b3)] et $M_x = 2,50$ et $M_y = 0,233$ [théorie (c1)-(c3) et expérience (d1)-(d3)]. Les valeurs théoriquement déterminées (l_{det}) et mesurées expérimentalement (l_{meas}) de l'OAM sont écrites dans la dernière colonne.

Un autre aspect intéressant de nos recherches consiste à réaliser un enregistrement holographique d'un faisceau CD et une amplification locale par mélange à deux ondes d'un tel faisceau à l'intérieur d'un cristal photoréfractif non linéaire. Les hologrammes conventionnels enregistrent l'intensité d'un motif d'interférence et sont donc généralement écrits à l'aide d'une onde objet et d'une onde de référence partageant une polarisation lumineuse commune, maximisant ainsi le contraste des franges. Des exceptions à cette règle existent dans le cadre de l'holographie de polarisation[227], qui permet de stocker l'état de polarisation d'une onde à l'aide d'un support sensible à la polarisation. Cette approche peut être utilisée par exemple pour générer des faisceaux vectoriels [228] de distribution de polarisation non uniforme. Dans nos recherches, nous montrons pour la première fois que l'effet optique CD linéaire peut être combiné avec l'enregistrement non linéaire d'hologrammes dynamiques dans un matériau photoréfractif, tous les processus se déroulant dans le même milieu. Les expériences sont réalisées en utilisant un échantillon de cristal $\text{Sn}_2\text{P}_2\text{S}_6$ (SPS) nominale non dopé, coupé avec des faces d'entrée et de sortie perpendiculaires à un de deux axes optiques. Le cristal SPS possède de grands coefficients électro-optiques et des propriétés optiques et PR non linéaires intéressantes [142].

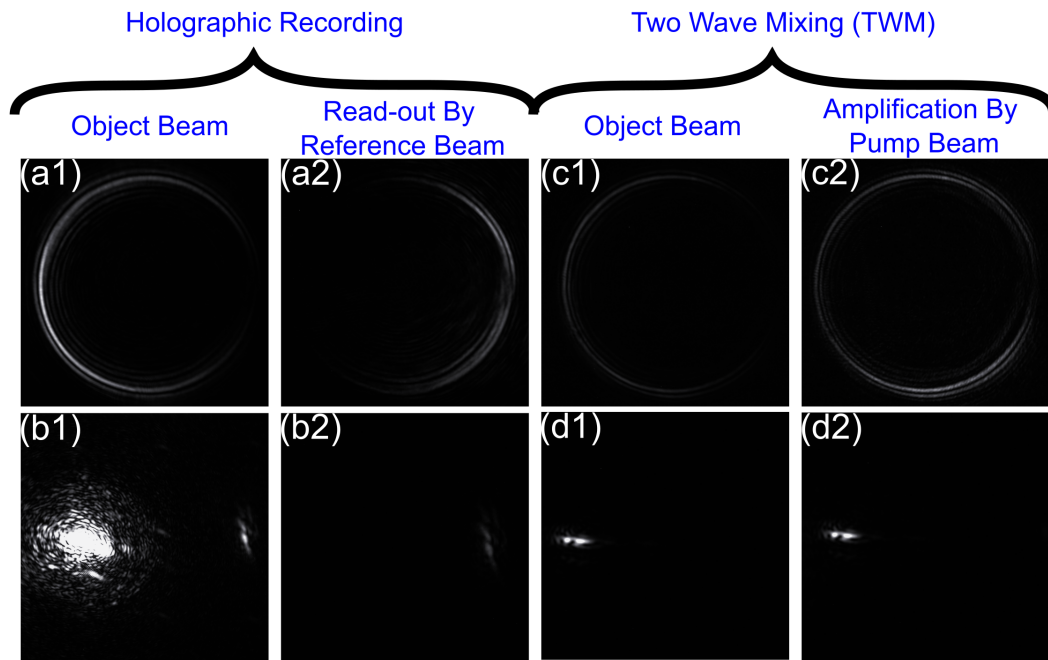


Figure 3 – Reconstruction holographique et images d’amplification par mélange à deux ondes pour le cas où l’onde objet d’entrée et l’onde de référence sont associés à des polarisations orthogonales (onde de référence correspond à une des deux ondes propres). Première ligne: onde objet alignée sur un axe optique. (a1) et (c1) : onde objet seule ; (a2) onde objet reconstruite après enregistrement d’hologramme ; (c2) onde objet amplifiée par mélange à deux ondes. Longueur d’onde = 633 nm. La deuxième ligne donne le cas correspondant pour le cristal désaligné de façon que l’onde objet ne donne pas lieu à une CD.

Un exemple illustrant la lecture d’un hologramme pré-enregistré ainsi que l’amplification dynamique par mélange à deux ondes est donné sur la Fig. 3. Il s’agit du pire des cas dans lequel l’onde objet et de référence sont associées à des ondes propres orthogonales (polarisations perpendiculaires). Les figures 3(a1) et (c1) montrent l’onde objet en régime aligné (menant à CD) et en absence de l’onde de référence. La figure 3(a2), montre l’onde objet reconstruite par l’onde de référence polarisée orthogonalement après l’enregistrement de l’hologramme à la longueur d’onde de 633 nm. Ici la reconstruction est plus forte sur la partie droite de l’anneau où l’onde objet est plus faible. Cependant, cette dépendance en intensité azimutale peut être modifiée en modifiant les orientations relatives des polarisations des deux ondes ou en utilisant une lumière polarisée circulairement. Il en va de même pour l’amplification par mélange à deux ondes (TWM) d’une onde d’objet initialement à faible intensité illustrée sur la figure 3(c2). Ici, on obtient une distribution d’intensité azimutale presque homogène malgré l’inhomogénéité du faisceau objet non amplifié sur la figure 3(c1). La raison de ce type de comportement réside dans la structure complexe du tenseur électro-optique du SPS [215, 216] en combinaison avec l’orientation du champ de charge d’espace associé à l’effet photorefractif (PR). Il est important de noter que l’alignement de l’onde objet sur l’axe optique est crucial. Toute légère rotation de l’échantillon avant l’enregistrement, de telle sorte que l’onde objet ne mène plus à une diffraction conique, offre une efficacité de diffraction insignifiante lors de la lecture (environ 30 fois plus faible, Fig. 3(b2)) et une amplification quasi-indétectable en TWM (Fig. 3(d2)), par rapport à une

amplification de 450 % pour le cas aligné. Cet effet ouvre de belles perspectives, par exemple pour le multiplexage multicanal en polarisation de faisceaux vectoriels.

Quelques investigations préliminaires réalisées au cours de cette thèse sont également présentées en annexe. L'annexe A présente les résultats sur les motifs CD obtenus à partir d'une demi-cavité, qui impliquent un monocristal avec diffraction conique à double passage dans une architecture à simple rétroaction optique. Ces investigations avec différents types de rétroreflecteurs dans une semi-cavité sont bien modélisées à l'aide d'une procédure de dépliage simple. Les recherches sur de telles configurations indiquent clairement la possibilité de générer des modèles CD facilement réglables en intensité et en polarisation. En outre, l'extension de tels schémas vers l'intégration du BC dans une cavité annulaire serait extrêmement attrayante car elle permettrait un passage multiple à travers le même BC et une cascade pratiquement infinie. Une telle cavité annulaire peut également incorporer des lentilles cylindriques pour briser la symétrie circulaire d'une manière similaire à celle étudiée dans cette thèse. L'annexe B décrit la génération de motifs CD circulaires via un arrangement des paramètres dits de Fibonacci ou des cascades dégénérées. Il est montré avec quelques exemples que ces types spéciaux de cascades peuvent aider à générer des doubles anneaux CD avec une polarisation elliptique dont l'ellipticité varie le long de la direction de l'azimut. Il ressort clairement de cette recherche que Fibonacci ou les cascades dégénérées pourraient grandement améliorer la polyvalence en permettant une adaptation plus poussée du profil de polarisation des faisceaux de vecteurs CD.

BIBLIOGRAPHY

1. Rubinsztein-Dunlop, H., Forbes, A., Berry, M. V., *et al.* Roadmap on structured light. *J. Opt.* **19**, 013001 (2016).
2. Forbes, A., de Oliveira, M. & Dennis, M. R. Structured light. *Nat. Photonics* **15**, 253–262 (2021).
3. Piccardo, M., Ginis, V., Forbes, A., *et al.* Roadmap on multimode light shaping. *J. Opt.* **24**, 013001 (Dec. 2021).
4. He, C., Shen, Y. & Forbes, A. Towards higher-dimensional structured light. *Light Sci. Appl.* **11**, 205 (2022).
5. Shen, Y., Zhan, Q., Wright, L. G., *et al.* Roadmap on spatiotemporal light fields. *J. Opt.* **25**, 093001 (2023).
6. Bliokh, K. Y., Karimi, E., Padgett, M. J., *et al.* Roadmap on structured waves. *J. Opt.* **25**, 103001 (2023).
7. Maurer, C., Jesacher, A., Fürhapter, S., Bernet, S. & Ritsch-Marte, M. Tailoring of arbitrary optical vector beams. *New J. Phys.* **9**, 78 (2007).
8. Cardano, F., Karimi, E., Marrucci, L., de Lisio, C. & Santamato, E. Generation and dynamics of optical beams with polarization singularities. *Opt. Express* **21**, 8815–8820 (2013).
9. Rosales-Guzmán, C., Ndagano, B. & Forbes, A. A review of complex vector light fields and their applications. *J. Opt.* **20**, 123001 (2018).
10. Taylor, M. A., Waleed, M., Stilgoe, A. B., Rubinsztein-Dunlop, H. & Bowen, W. P. Enhanced optical trapping via structured scattering. *Nat. Photonics* **9**, 669–673 (2015).
11. Dholakia, K. & Čížmár, T. Shaping the future of manipulation. *Nat. Photonics* **5**, 335–342 (2011).
12. Shen, Y., Yang, X., Naidoo, D., Fu, X. & Forbes, A. Structured ray-wave vector vortex beams in multiple degrees of freedom from a laser. *Optica* **7**, 820–831 (2020).
13. Bozinovic, N., Yue, Y., Ren, Y., Tur, M., Kristensen, P., Huang, H., Willner, A. E. & Ramachandran, S. Terabit-scale orbital angular momentum mode division multiplexing in fibers. *Science* **340**, 1545–1548 (2013).
14. Molina-Terriza, G., Torres, J. P. & Torner, L. Twisted photons. *Nat. Phys.* **3**, 305–310 (2007).
15. Mair, A., Vaziri, A., Weihs, G. & Zeilinger, A. Entanglement of the orbital angular momentum states of photons. *Nature* **412**, 313–316 (2001).
16. Maurer, P. C., Maze, J. R., Stanwix, P. L., *et al.* Far-field optical imaging and manipulation of individual spins with nanoscale resolution. *Nat. Phys.* **6**, 912–918 (2010).
17. Gbur, G. J. *Singular optics* (CRC press, 2016).

BIBLIOGRAPHY

18. Turpin, A., Loiko, Y. V., Kalkandjiev, T. K. & Mompart, J. Conical refraction: fundamentals and applications. *Laser Photonics Rev.* **10**, 750–771 (2016).
19. Berry, M. V. Conical diffraction asymptotics: fine structure of Poggendorff rings and axial spike. *J. Opt. A: Pure Appl. Opt.* **6**, 289–300 (2004).
20. Berry, M. V., Jeffrey, M. R. & Lunney, J. G. Conical diffraction: observations and theory. *Proc. R. Soc. A.* **462**, 1629–1642 (2006).
21. Born, M., Wolf, E., Bhatia, A. B., Clemmow, P. C., Gabor, D., Stokes, A. R., Taylor, A. M., Wayman, P. A. & Wilcock, W. L. *Principles of Optics: Electromagnetic Theory of Propagation, Interference and Diffraction of Light* 7th ed. (Cambridge University Press, 1999).
22. Berry, M. V. Conical diffraction from an N -crystal cascade. *J. Opt.* **12**, 075704 (2010).
23. Peet, V. Variable two-crystal cascade for conical refraction. *Opt. Lett.* **40**, 2405–2408 (2015).
24. Mohammadou, S., Mohammadou, B. & Montemezzani, G. Complex beam shaping by cascaded conical diffraction with intercalated polarization transforming elements. *Opt. Express* **25**, 25392–25406 (2017).
25. Berry, M. V., Jeffrey, M. R. & Mansuripur, M. Orbital and spin angular momentum in conical diffraction. *J. Opt. A: Pure Appl. Opt.* **7**, 685 (2005).
26. O'Dwyer, D. P., Phelan, C. F., Rakovich, Y. P., Eastham, P. R., Lunney, J. G. & Donegan, J. F. Generation of continuously tunable fractional optical orbital angular momentum using internal conical diffraction. *Opt. Express* **18**, 16480–16485 (2010).
27. Brenier, A. Evolution of vortices created by conical diffraction in biaxial crystals versus orbital angular momentum. *Opt. Mater.* **110**, 110504 (2020).
28. Brenier, A., Majchrowski, A. & Michalski, E. Light propagation properties of the $\text{Bi}_2\text{ZnOB}_2\text{O}_6$ acentric biaxial crystal: angular orbital momentum from conical diffraction. *Opt. Mater.* **91**, 286–291 (2019).
29. Turpin, A., Rego, L., Picón, A., San Román, J. & Hernández-García, C. Extreme ultra-violet fractional orbital angular momentum beams from high harmonic generation. *Sci. Rep.* **7**, 1–10 (2017).
30. O'Dwyer, D., Phelan, C., Rakovich, Y. P., Eastham, P., Lunney, J. & Donegan, J. F. The creation and annihilation of optical vortices using cascade conical diffraction. *Opt. Express* **19**, 2580–2588 (2011).
31. Brenier, A. Investigation of the sum of orbital angular momentum generated by conical diffraction. *J. Opt.* **22**, 045603 (2020).
32. Brenier, A. Measure by interferential conoscopy of the phase distribution acquired from conical diffraction. *Optik* **246**, 167798 (2021).
33. Brenier, A., Majchrowski, A. & Michalski, E. Some aspects of scaling the orbital angular momentum of light with conical diffraction. *Optik* **227**, 166020 (2021).

34. Turpin, A., Loiko, Y. V., Kalkandjiev, T. K., Trull, J., Cojocaru, C. & Mompарт, J. Type I and type II second harmonic generation of conically refracted beams. *Opt. Lett.* **38**, 2484–2486 (2013).
35. O'Dwyer, D., Ballantine, K., Phelan, C., Lunney, J. & Donegan, J. Optical trapping using cascade conical refraction of light. *Opt. Express* **20**, 21119–21125 (2012).
36. Peet, V. Biaxial crystal as a versatile mode converter. *J. Opt.* **12**, 095706 (2010).
37. Turpin, A., Loiko, Y., Kalkandjiev, T. K. & Mompарт, J. Free-space optical polarization demultiplexing and multiplexing by means of conical refraction. *Opt. Lett.* **37**, 4197–4199 (2012).
38. Novikova, T., De Martino, A., Bulkin, P., Nguyen, Q., Drévillon, B., Popov, V. & Chumakov, A. Metrology of replicated diffractive optics with Mueller polarimetry in conical diffraction. *Opt. Express* **15**, 2033–2046 (2007).
39. Abdolvand, A., Wilcox, K. G., Kalkandjiev, T. K. & Rafailov, E. U. Conical refraction Nd:KGd(WO₄)₂ laser. *Opt. Express* **18**, 2753–2759 (2010).
40. Caron, J., Fallet, C., Tinevez, J.-Y., Moisan, L., Braitbart, L. P., Sirat, G. Y. & Shorte, S. L. Conical diffraction illumination opens the way for low phototoxicity super-resolution imaging. *Cell Adhes. Migr.* **8**, 430–439 (2014).
41. Soskin, M. S. & Vasnetsov, M. V. in *Progress in Optics* 219–276 (Elsevier, 2001).
42. Thom, R. Topological models in biology. *Topology* **8**, 313–335 (1969).
43. Thom, R. Stabilité structurelle et morphogénèse. *Poetics* **3**, 7–19 (1974).
44. Thom, R. *Mathematical models of morphogenesis* (Ellis Horwood Chichester, 1983).
45. Arnol'd, V. I. Critical points of smooth functions and their normal forms. *Russ. Math. Surv.* **30**, 1 (1975).
46. Arnol'd, V. *Singularities of caustics and wave fronts* (Springer Science & Business Media, 2001).
47. Arnol'd, V. I. *Catastrophe theory* (Springer Science & Business Media, 2003).
48. Nye, J. F. & Berry, M. V. Dislocations in wave trains. *Proc. R. Soc. Lond. A* **336**, 165–190 (1974).
49. Nye, J. F. *Natural focusing and fine structure of light: caustics and wave dislocations* (Bristol, Institute of Physics Publishing, 1999).
50. Berry, M. V. & Upstill, C. in *Progress in Optics* 257–346 (Elsevier, 1980).
51. Nye, J. F. & Hajnal, J. The wave structure of monochromatic electromagnetic radiation. *Proc. R. Soc. Lond. A* **409**, 21–36 (1987).
52. Berry, M. Making waves in physics. *Nature* **403**, 21–21 (2000).
53. Berry, M. V. The singularities of light: intensity, phase, polarisation. *Light Sci. Appl.* **12**, 238 (2023).

BIBLIOGRAPHY

54. Durnin, J., Miceli Jr, J. & Eberly, J. H. Diffraction-free beams. *Phys. Rev. Lett.* **58**, 1499 (1987).
55. Gutiérrez-Vega, J. C., Iturbe-Castillo, M. & Chávez-Cerda, S. Alternative formulation for invariant optical fields: Mathieu beams. *Opt. Lett.* **25**, 1493–1495 (2000).
56. Yao, A. M. & Padgett, M. J. Orbital angular momentum: origins, behavior and applications. *Adv. Opt. Photon.* **3**, 161–204 (2011).
57. Karimi, E., Zito, G., Piccirillo, B., Marrucci, L. & Santamato, E. Hypergeometric-gaussian modes. *Opt. Lett.* **32**, 3053–3055 (2007).
58. Padgett, M. J. & Allen, L. The Poynting vector in Laguerre-Gaussian laser modes. *Opt. Commun.* **121**, 36–40 (1995).
59. Allen, L. & Padgett, M. The Poynting vector in Laguerre–Gaussian beams and the interpretation of their angular momentum density. *Opt. Commun.* **184**, 67–71 (2000).
60. Leach, J., Keen, S., Padgett, M. J., Saunter, C. & Love, G. D. Direct measurement of the skew angle of the Poynting vector in a helically phased beam. *Opt. Express* **14**, 11919–11924 (2006).
61. Allen, L., Beijersbergen, M. W., Spreeuw, R. & Woerdman, J. Orbital angular momentum of light and the transformation of Laguerre-Gaussian laser modes. *Phys. Rev. A* **45**, 8185 (1992).
62. Allen, L., Padgett, M. & Babiker, M. in *Progress in optics* 291–372 (Elsevier, 1999).
63. Barnett, S. M. Optical angular-momentum flux. *J. Opt. B: Quantum Semiclassical Opt.* **4**, S7 (2001).
64. Paterson, L., MacDonald, M. P., Arlt, J., Sibbett, W., Bryant, P. E. & Dholakia, K. Controlled rotation of optically trapped microscopic particles. *Science* **292**, 912–914 (2001).
65. MacDonald, M. P., Paterson, L., Volke-Sepulveda, K., Arlt, J., Sibbett, W. & Dholakia, K. Creation and manipulation of three-dimensional optically trapped structures. *Science* **296**, 1101–1103 (2002).
66. Grier, D. G. A revolution in optical manipulation. *Nature* **424**, 810–816 (2003).
67. Barreiro, J. T., Wei, T.-C. & Kwiat, P. G. Beating the channel capacity limit for linear photonic superdense coding. *Nat. Phys.* **4**, 282–286 (2008).
68. Wang, J., Yang, J.-Y., Fazal, I. M., *et al.* Terabit free-space data transmission employing orbital angular momentum multiplexing. *Nat. Photonics* **6**, 488–496 (2012).
69. Fickler, R., Campbell, G., Buchler, B., Lam, P. K. & Zeilinger, A. Quantum entanglement of angular momentum states with quantum numbers up to 10,010. *Proc. Natl. Acad. Sci. U.S.A.* **113**, 13642–13647 (2016).
70. Erhard, M., Fickler, R., Krenn, M. & Zeilinger, A. Twisted photons: new quantum perspectives in high dimensions. *Light Sci. Appl.* **7**, 17146–17146 (2018).

71. Kong, F., Zhang, C., Bouchard, F., *et al.* Controlling the orbital angular momentum of high harmonic vortices. *Nat. Commun.* **8**, 14970 (2017).
72. Gauthier, D., Ribič, P. R., Adhikary, G., *et al.* Tunable orbital angular momentum in high-harmonic generation. *Nat. Commun.* **8**, 14971 (Apr. 2017).
73. Huang, L., Chen, X., Muhlenbernd, H., Li, G., Bai, B., Tan, Q., Jin, G., Zentgraf, T. & Zhang, S. Dispersionless phase discontinuities for controlling light propagation. *Nano Lett.* **12**, 5750–5755 (2012).
74. Devlin, R. C., Ambrosio, A., Rubin, N. A., Mueller, J. B. & Capasso, F. Arbitrary spin-to-orbital angular momentum conversion of light. *Science* **358**, 896–901 (2017).
75. Stav, T., Faerman, A., Maguid, E., Oren, D., Kleiner, V., Hasman, E. & Segev, M. Quantum entanglement of the spin and orbital angular momentum of photons using metamaterials. *Science* **361**, 1101–1104 (2018).
76. Zhuang, X. Unraveling DNA condensation with optical tweezers. *Science* **305**, 188–190 (2004).
77. Lavery, M. P., Speirits, F. C., Barnett, S. M. & Padgett, M. J. Detection of a spinning object using light’s orbital angular momentum. *Science* **341**, 537–540 (2013).
78. Cvijetic, N., Milione, G., Ip, E. & Wang, T. Detecting lateral motion using light’s orbital angular momentum. *Sci. Rep.* **5**, 1–7 (2015).
79. Xie, G., Song, H., Zhao, Z., *et al.* Using a complex optical orbital-angular-momentum spectrum to measure object parameters. *Opt. Lett.* **42**, 4482–4485 (Nov. 2017).
80. Harwit, M. Photon orbital angular momentum in astrophysics. *Astrophys. J.* **597**, 1266 (2003).
81. Shen, Y., Wang, X., Xie, Z., Min, C., Fu, X., Liu, Q., Gong, M. & Yuan, X. Optical vortices 30 years on: OAM manipulation from topological charge to multiple singularities. *Light Sci. Appl.* **8**, 90 (2019).
82. Cristiani, I., Lacava, C., Rademacher, G., *et al.* Roadmap on multimode photonics. *J. Opt.* **24**, 083001 (2022).
83. Berry, M. V. *Paraxial beams of spinning light* in *International Conference on Singular Optics* (ed Soskin, M. S.) **3487** (SPIE, 1998), 6–11.
84. O’neil, A., MacVicar, I., Allen, L. & Padgett, M. Intrinsic and extrinsic nature of the orbital angular momentum of a light beam. *Phys. Rev. Lett.* **88**, 053601 (2002).
85. Couillet, P., Gil, L. & Rocca, F. Optical vortices. *Opt. Commun.* **73**, 403–408 (1989).
86. Couillet, P., Gil, L. & Lega, J. Defect-mediated turbulence. *Phys. Rev. Lett.* **62**, 1619 (1989).
87. Brambilla, M., Battipede, F., Lugiato, L., Penna, V., Prati, F., Tamm, C. & Weiss, C. Transverse laser patterns. I. Phase singularity crystals. *Phys. Rev. A* **43**, 5090 (1991).

BIBLIOGRAPHY

88. Brambilla, M., Lugiato, L., Penna, V., Prati, F., Tamm, C. & Weiss, C. Transverse laser patterns. II. Variational principle for pattern selection, spatial multistability, and laser hydrodynamics. *Phys. Rev. A* **43**, 5114 (1991).
89. Barland, S., Caboche, E., Genevet, P., Hachair, X., Giudici, M., Pedaci, F. & Tredicce, J. R. in *Nonlinear Photonics and Novel Optical Phenomena* (eds Chen, Z. & Morandotti, R.) 195–205 (Springer, 2012).
90. Bazhenov, V. Y., Soskin, M. & Vasnetsov, M. Screw dislocations in light wavefronts. *J. Mod. Opt.* **39**, 985–990 (1992).
91. Berry, M. V. Optical vortices evolving from helicoidal integer and fractional phase steps. *J. Opt. A: Pure Appl. Opt.* **6**, 259 (2004).
92. Leach, J., Yao, E. & Padgett, M. J. Observation of the vortex structure of a non-integer vortex beam. *New J. Phys.* **6**, 71 (2004).
93. Leach, J., Dennis, M. R., Courtial, J. & Padgett, M. J. Knotted threads of darkness. *Nature* **432**, 165–165 (2004).
94. Wright, A. J., Patterson, B. A., Poland, S. P., Girkin, J. M., Gibson, G. M. & Padgett, M. J. Dynamic closed-loop system for focus tracking using a spatial light modulator and a deformable membrane mirror. *Opt. Express* **14**, 222–228 (2006).
95. Leach, J. & Padgett, M. Observation of chromatic effects near a white-light vortex. *New J. Phys.* **5**, 154 (2003).
96. Berry, M. Coloured phase singularities. *New J. Phys.* **4**, 66 (2002).
97. Berry, M. Exploring the colours of dark light. *New J. Phys.* **4**, 74 (2002).
98. Mariyenko, I., Strohaber, J. & Uiterwaal, C. Creation of optical vortices in femtosecond pulses. *Opt. Express* **13**, 7599–7608 (2005).
99. Zeylikovich, I., Sztul, H., Kartazhev, V., Le, T. & Alfano, R. Ultrashort Laguerre-Gaussian pulses with angular and group velocity dispersion compensation. *Opt. Lett.* **32**, 2025–2027 (2007).
100. Bezuharov, K., Dreischuh, A., Paulus, G. G., Schätzel, M. G., Walther, H., Neshev, D., Królikowski, W. & Kivshar, Y. Spatial phase dislocations in femtosecond laser pulses. *J. Opt. Soc. Am. B* **23**, 26–35 (2006).
101. Wang, S., Zhao, Z., Ito, I. & Kobayashi, Y. Direct generation of femtosecond vortex beam from a Yb:KYW oscillator featuring a defect-spot mirror. *OSA Continuum* **2**, 523–530 (2019).
102. Stoyanov, L., Topuzoski, S., Paulus, G. G. & Dreischuh, A. Optical vortices in brief: introduction for experimentalists. *Eur. Phys. J. Plus* **138**, 702 (2023).
103. Courtial, J., Dholakia, K., Allen, L. & Padgett, M. Gaussian beams with very high orbital angular momentum. *Opt. Commun.* **144**, 210–213 (1997).
104. Andrews, D. L. *Structured light and its applications: An introduction to phase-structured beams and nanoscale optical forces* (Academic Press, 2011).

105. Andrews, D. L. & Babiker, M. *The angular momentum of light* (Cambridge University Press, 2012).
106. Dennis, M. R., O'holleran, K. & Padgett, M. J. in *Progress in optics* 293–363 (Elsevier, 2009).
107. Peatross, J. & Ware, M. *Physics of light and optics* (Brigham Young University, Department of Physics, 2011).
108. Collett, E. *Polarized light in fiber optics* (SPIE Press, 2003).
109. Chipman, R., Lam, W. S. T. & Young, G. *Polarized light and optical systems* (CRC press, 2018).
110. Nye, J. F. Lines of circular polarization in electromagnetic wave fields. *Proc. R. Soc. Lond. A* **389**, 279–290 (1983).
111. Hajnal, J. Singularities in the transverse fields of electromagnetic waves. I. Theory. *Proc. R. Soc. Lond. A* **414**, 433–446 (1987).
112. Hajnal, J. Singularities in the transverse fields of electromagnetic waves. II. Observations on the electric field. *Proc. R. Soc. Lond. A* **414**, 447–468 (1987).
113. Delmarcelle, T. & Hesselink, L. *The topology of symmetric, second-order tensor fields in Proceedings Visualization'94* (1994), 140–147.
114. Zhan, Q. Cylindrical vector beams: from mathematical concepts to applications. *Adv. Opt. Photon.* **1**, 1–57 (2009).
115. Zhan, Q. *Vectorial optical fields: Fundamentals and applications* (World Scientific, 2013).
116. Milione, G., Nguyen, T. A., Leach, J., Nolan, D. A. & Alfano, R. R. Using the nonseparability of vector beams to encode information for optical communication. *Opt. Lett.* **40**, 4887–4890 (2015).
117. Lerman, G. M. & Levy, U. Effect of radial polarization and apodization on spot size under tight focusing conditions. *Opt. Express* **16**, 4567–4581 (2008).
118. Chen, R., Agarwal, K., Sheppard, C. J. R. & Chen, X. Imaging using cylindrical vector beams in a high-numerical-aperture microscopy system. *Opt. Lett.* **38**, 3111–3114 (2013).
119. Segawa, S., Kozawa, Y. & Sato, S. Resolution enhancement of confocal microscopy by subtraction method with vector beams. *Opt. Lett.* **39**, 3118–3121 (2014).
120. Neugebauer, M., WoÅ°niak, P., Bag, A., Leuchs, G. & Banzer, P. Polarization-controlled directional scattering for nanoscopic position sensing. *Nat. Commun.* **7**, 11286 (2016).
121. Meier, M., Romano, V. & Feurer, T. Material processing with pulsed radially and azimuthally polarized laser radiation. *Appl. Phys. A* **86**, 329–334 (2007).
122. Padgett, M., Arlt, J., Simpson, N. & Allen, L. An experiment to observe the intensity and phase structure of Laguerre–Gaussian laser modes. *Am. J. Phys.* **64**, 77–82 (1996).

BIBLIOGRAPHY

123. Courtial, J. & Padgett, M. Performance of a cylindrical lens mode converter for producing Laguerre–Gaussian laser modes. *Opt. Commun.* **159**, 13–18 (1999).
124. Liang, G. & Wang, Q. Controllable conversion between Hermite Gaussian and Laguerre Gaussian modes due to cross phase. *Opt. Express* **27**, 10684–10691 (2019).
125. Quabis, S., Dorn, R., Eberler, M., Glöckl, O. & Leuchs, G. Focusing light to a tighter spot. *Opt. Commun.* **179**, 1–7 (2000).
126. Dorn, R., Quabis, S. & Leuchs, G. Sharper focus for a radially polarized light beam. *Phys. Rev. Lett.* **91**, 233901 (2003).
127. Youngworth, K. S. & Brown, T. G. Focusing of high numerical aperture cylindrical-vector beams. *Opt. Express* **7**, 77–87 (2000).
128. Fontana, J. & Pantell, R. A high-energy, laser accelerator for electrons using the inverse Cherenkov effect. *J. Appl. Phys.* **54**, 4285–4288 (1983).
129. Galvez, E. J., Khadka, S., Schubert, W. H. & Nomoto, S. Poincaré-beam patterns produced by nonseparable superpositions of Laguerre–Gauss and polarization modes of light. *Appl. Opt.* **51**, 2925–2934 (2012).
130. Beckley, A. M., Brown, T. G. & Alonso, M. A. Full Poincaré beams. *Opt. Express* **18**, 10777–10785 (2010).
131. Mao, D., Zheng, Y., Zeng, C., Lu, H., Wang, C., Zhang, H., Zhang, W., Mei, T. & Zhao, J. Generation of polarization and phase singular beams in fibers and fiber lasers. *Adv. Photon.* **3**, 014002–014002 (2021).
132. Phelan, C. F., Donegan, J. F. & Lunney, J. G. Generation of a radially polarized light beam using internal conical diffraction. *Opt. Express* **19**, 21793–21802 (2011).
133. Fadeyeva, T. A., Shvedov, V. G., Izdebskaya, Y. V., Volyar, A. V., Brasselet, E., Neshev, D. N., Desyatnikov, A. S., Krolikowski, W. & Kivshar, Y. S. Spatially engineered polarization states and optical vortices in uniaxial crystals. *Opt. Express* **18**, 10848–10863 (2010).
134. Milione, G., Sztul, H., Nolan, D. & Alfano, R. Higher-order Poincaré sphere, Stokes parameters, and the angular momentum of light. *Phys. Rev. Lett.* **107**, 053601 (2011).
135. Forbes, A. Structured Light from Lasers. *Laser Photonics Rev.* **13**, 1900140 (2019).
136. Wang, J. & Liang, Y. Generation and Detection of Structured Light: A Review. *Front. Phys.* **9**, 688284 (2021).
137. Hell, S. W. & Wichmann, J. Breaking the diffraction resolution limit by stimulated emission: stimulated-emission-depletion fluorescence microscopy. *Opt. Lett.* **19**, 780–782 (1994).
138. Griffiths, D. J. *Introduction to Electrodynamics* (Cambridge University Press, 2017).
139. Jackson, J. D. *Classical electrodynamics* (John Wiley & Sons, 1999).
140. Boyd, R. W. *Nonlinear Optics* 3rd ed. (Academic Press, 2008).

141. Newell, A. *Nonlinear optics* (CRC Press, 2018).
142. Günter, P. & Huignard, J.-P. *Photorefractive Materials and Their Applications, Vol. 1: Basic Effects* (Springer, 2006).
143. Yariv, A. & Yeh, P. *Optical waves in crystal propagation and control of laser radiation* (John Wiley & Sons, Inc., 1983).
144. Guha, S. & Gonzalez, L. P. *Laser Beam Propagation in Nonlinear Optical Media* (CRC Press Boca Raton, FL, USA, 2014).
145. Saleh, B. E. & Teich, M. C. *Fundamentals of photonics* (John Wiley & Sons, 2019).
146. Frejlich, J. *Photorefractive materials: fundamental concepts, holographic recording and materials characterization* (John Wiley & Sons, 2007).
147. Petrov, M. P., Stepanov, S. I. & Khomenko, A. V. *Photorefractive crystals in coherent optical systems* (Springer, 2013).
148. Montemezzani, G., Rogin, P., Zgonik, M. & Günter, P. Interband photorefractive effects: Theory and experiments in KNbO_3 . *Phys. Rev. B* **49**, 2484–2502 (1994).
149. Nye, J. F. *Physical properties of crystals: their representation by tensors and matrices* (Oxford University Press, 1985).
150. Montemezzani, G. & Zgonik, M. in *Photorefractive Materials and Their Applications 1: Basic Effects* (eds Günter, P. & Huignard, J.-P.) 83–118 (Springer, 2006).
151. Kogelnik, H. Coupled wave theory for thick hologram gratings. *Bell System Technical Journal* **48**, 2909–2947 (1969).
152. Iqbal, M. W., Marsal, N. & Montemezzani, G. Non-circularly shaped conical diffraction. *Sci. Rep.* **12**, 7317 (2022).
153. Berry, M. V. & Jeffrey, M. R. Chiral conical diffraction. *J. Opt. A: Pure Appl. Opt.* **8**, 363 (2006).
154. Berry, M. V. & Jeffrey, M. R. in *Progress in Optics* (ed Wolf, E.) 13–50 (Elsevier, 2007).
155. Phelan, C., O'dwyer, D., Rakovich, Y., Donegan, J. & Lunney, J. Conical diffraction and Bessel beam formation with a high optical quality biaxial crystal. *Opt. Express* **17**, 12891–12899 (2009).
156. Hamilton, W. R. Third Supplement to an Essay on the Theory of Systems of Rays. *Trans. Roy. Irish Acad.* **17**, 1–144 (1831).
157. Lloyd, H. On the phenomena presented by light in its passage along the axes of biaxial crystals. *Trans. Roy. Irish Acad.*, 145–157 (1831).
158. Llyold, H. Further Experiments on the Phenomena presented by Light in its Passage along the axes of Biaxial Crystals. *Lond. Edinb. Phil. Mag.* **ii**, 207–210 (1833).
159. Poggendorff, J. Ueber die konische Refraction. *Pogg. Ann* **48**, 461–462 (1839).
160. Voigt, W. Theoretisches und Experimentelles zur Aufklärung des optischen Verhaltens aktiver Kristalle. *Ann. Phys.* **323**, 645–694 (1905).

BIBLIOGRAPHY

161. Raman, C. V. Conical refraction in biaxial crystals. *Nature* **107**, 747–747 (1921).
162. Raman, C. V. The phenomena of conical refraction. *Current Science* **11**, 44–46 (1942).
163. Lalor, É. An analytical approach to the theory of internal conical refraction. *J. Math. Phys.* **13**, 449–454 (1972).
164. Lalor, É. The angular spectrum representation of electromagnetic fields in crystals. I. uniaxial crystals. *J. Math. Phys.* **13**, 437–443 (1972).
165. Lalor, É. The angular spectrum representation of electromagnetic fields in crystals. II. Biaxial crystals. *J. Math. Phys.* **13**, 443–449 (1972).
166. Schell, A. & Bloembergen, N. Laser studies of internal conical diffraction. I. Quantitative comparison of experimental and theoretical conical intensity distribution in aragonite. *J. Opt. Soc. Am.* **68**, 1093–1098 (1978).
167. Schell, A. & Bloembergen, N. Laser studies of internal conical diffraction. II. Intensity patterns in an optically active crystal, α -iodic acid. *J. Opt. Soc. Am.* **68**, 1098–1106 (1978).
168. Belskii, A. & Khapalyuk, A. Propagation of confined light beams along the beam axes (axes of single ray velocity) of biaxial crystals. *Opt. Spectrosc.* **44**, 312–315 (1978).
169. Belsky, A. M. & Stepanov, M. A. Internal conical refraction of coherent light beams. *Opt. Commun.* **167**, 1–5 (1999).
170. Belsky, A. & Stepanov, M. Internal conical refraction of light beams in biaxial gyrotropic crystals. *Opt. Commun.* **204**, 1–6 (2002).
171. Warnick, K. F. & Arnold, D. V. Secondary dark rings of internal conical refraction. *Phys. Rev. E* **55**, 6092 (1997).
172. Phelan, C. F., Ballantine, K. E., Eastham, P. R., Donegan, J. F. & Lunney, J. G. Conical diffraction of a Gaussian beam with a two crystal cascade. *Opt. Express* **20**, 13201–13207 (2012).
173. Grant, S. D. & Abdolvand, A. Left- and right-circularly polarized light in cascade conical diffraction. *Opt. Lett.* **37**, 5226–5228 (2012).
174. Turpin, A., Loiko, Y. V., Kalkandjiev, T. K. & Mompart, J. Multiple rings formation in cascaded conical refraction. *Opt. Lett.* **38**, 1455–1457 (2013).
175. Sun, X., Geng, Y., Zhu, Q., Huang, W., Zhang, Y., Wang, W. & Liu, L. Unitary transformation for Poincaré beams on different parts of Poincaré sphere. *Sci. Rep.* **10**, 1–10 (2020).
176. O'Dwyer, D., Phelan, C., Ballantine, K., Rakovich, Y., Lunney, J. G. & Donegan, J. Conical diffraction of linearly polarised light controls the angular position of a microscopic object. *Opt. Express* **18**, 27319–27326 (2010).
177. McDonald, C., McDougall, C., Rafailov, E. & McGloin, D. Characterizing conical refraction optical tweezers. *Opt. Lett.* **39**, 6691–6694 (2014).

178. Fallet, C., Caron, J., Oddos, S., Tinevez, J.-Y., Moisan, L., Sirat, G. Y., Braitbart, P. O. & Shorte, S. L. *Conical diffraction as a versatile building block to implement new imaging modalities for superresolution in fluorescence microscopy in Nanoimaging and Nanospectroscopy II* **9169** (2014), 9–14.
179. Grant, S. D., Reynolds, S. & Abdolvand, A. Optical sensing of polarization using conical diffraction phenomenon. *J. Opt.* **18**, 025609 (2016).
180. Turpin, A., Polo, J., Loiko, Y. V., Küber, J., Schmaltz, F., Kalkandjiev, T. K., Ahufinger, V., Birkel, G. & Mompart, J. Blue-detuned optical ring trap for Bose-Einstein condensates based on conical refraction. *Opt. Express* **23**, 1638–1650 (2015).
181. Peinado, A., Lizana, A., Turpín, A., Iemmi, C., Kalkandjiev, T. K., Mompart, J. & Campos, J. Optimization, tolerance analysis and implementation of a Stokes polarimeter based on the conical refraction phenomenon. *Opt. Express* **23**, 5636–5652 (2015).
182. Iqbal, M. W., Marsal, N. & Montemezzani, G. Shape and polarization distribution of non-circular conical diffraction beams from conjugate cascades. *Opt. Express* **31**, 29859–29876 (2023).
183. Jensen, A. S. Impact of quadratic phase factors on optical Fourier transforms and imaging. *Opt. Lett.* **16**, 886–888 (1991).
184. Jalviste, E. & Peet, V. Interplay of vortex and non-vortex beam components in a variable two-crystal cascade conical refraction. *Opt. Lett.* **43**, 4566–4569 (2018).
185. Khonina, S. N., Kharitonov, S. I., Volotovskiy, S. G. & Soifer, V. A. Caustics of Non-Paraxial Perfect Optical Vortices Generated by Toroidal Vortex Lenses. *Photonics* **8** (2021).
186. Zannotti, A., Denz, C., Alonso, M. A. & Dennis, M. R. Shaping caustics into propagation-invariant light. *Nat. Commun.* **11**, 3597 (2020).
187. Götte, J. B., O’Holleran, K., Preece, D., Flossmann, F., Franke-Arnold, S., Barnett, S. M. & Padgett, M. J. Light beams with fractional orbital angular momentum and their vortex structure. *Opt. Express* **16**, 993–1006 (2008).
188. Lee, W., Yuan, X.-C. & Dholakia, K. Experimental observation of optical vortex evolution in a Gaussian beam with an embedded fractional phase step. *Opt. Commun.* **239**, 129–135 (2004).
189. Garcia-Gracia, H. & Gutiérrez-Vega, J. C. Diffraction of plane waves by finite-radius spiral phase plates of integer and fractional topological charge. *J. Opt. Soc. Am. A* **26**, 794–803 (2009).
190. De la Rosa, P., Pereiro-García, J., Caño-García, M., Oton, J. M., Quintana, X. & Geday, M. Generation of integer and fractional vortex beams based on liquid crystal electronically reconfigurable spiral phase plates. *Opt. Express* **31**, 31212–31220 (2023).
191. Alperin, S. N., Niederriter, R. D., Gopinath, J. T. & Siemens, M. E. Quantitative measurement of the orbital angular momentum of light with a single, stationary lens. *Opt. Lett.* **41**, 5019–5022 (2016).

BIBLIOGRAPHY

192. Cuche, E., Marquet, P. & Depeursinge, C. Spatial filtering for zero-order and twin-image elimination in digital off-axis holography. *Appl. Opt.* **39**, 4070–4075 (2000).
193. Chattrapiban, N., Rogers, E. A., Arakelyan, I. V., Roy, R. & Hill III, W. T. Laser beams with embedded vortices: tools for atom optics. *J. Opt. Soc. Am. B* **23**, 94–103 (2006).
194. Oemrawsingh, S. S. R., de Jong, J. A., Ma, X., Aiello, A., Eliel, E. R., 't Hooft, G. W. & Woerdman, J. P. High-dimensional mode analyzers for spatial quantum entanglement. *Phys. Rev. A* **73**, 032339 (2006).
195. Oemrawsingh, S. S. R., Ma, X., Voigt, D., Aiello, A., Eliel, E. R., 't Hooft, G. W. & Woerdman, J. P. Experimental Demonstration of Fractional Orbital Angular Momentum Entanglement of Two Photons. *Phys. Rev. Lett.* **95**, 240501 (2005).
196. Franke-Arnold, S., Barnett, S. M., Padgett, M. J. & Allen, L. Two-photon entanglement of orbital angular momentum states. *Phys. Rev. A* **65**, 033823 (2002).
197. Oemrawsingh, S., Aiello, A., Eliel, E., Nienhuis, G. & Woerdman, J. How to observe high-dimensional two-photon entanglement with only two detectors. *Phys. Rev. Lett.* **92**, 217901 (2004).
198. Tao, S., Lee, W. & Yuan, X.-C. Dynamic optical manipulation with a higher-order fractional Bessel beam generated from a spatial light modulator. *Opt. Lett.* **28**, 1867–1869 (2003).
199. Tao, S., Yuan, X., Lin, J., Peng, X. & Niu, H. Fractional optical vortex beam induced rotation of particles. *Opt. Express* **13**, 7726–7731 (2005).
200. Wang, J., Zhang, W., Qi, Q., Zheng, S. & Chen, L. Gradual edge enhancement in spiral phase contrast imaging with fractional vortex filters. *Sci. Rep.* **5**, 15826 (2015).
201. Sharma, M. K., Joseph, J. & Senthilkumaran, P. Fractional vortex dipole phase filter. *Appl. Phys. B* **117**, 325–332 (2014).
202. Götte, J. B., Franke-Arnold, S., Zambrini, R. & Barnett, S. M. Quantum formulation of fractional orbital angular momentum. *J. Mod. Opt.* **54**, 1723–1738 (2007).
203. Xu, Z., Gui, C., Li, S., Zhou, J. & Wang, J. *Fractional Orbital Angular Momentum (OAM) Free-Space Optical Communications with Atmospheric Turbulence Assisted by MIMO Equalization in Advanced Photonics for Communications* (Optica Publishing Group, 2014), JT3A.1.
204. Zeng, J., Liu, X., Wang, F., Zhao, C. & Cai, Y. Partially coherent fractional vortex beam. *Opt. Express* **26**, 26830–26844 (2018).
205. Zhang, H., Zeng, J., Lu, X., Wang, Z., Zhao, C. & Cai, Y. Review on fractional vortex beam. *Nanophotonics* **11**, 241–273 (2021).
206. Kroupa, J. Second-harmonic conical refraction in GUHP. *J. Opt.* **12**, 045706 (2010).
207. Peet, V. & Shchemelyov, S. Frequency doubling with laser beams transformed by conical refraction in a biaxial crystal. *J. Opt.* **13**, 055205 (2011).

208. Grant, S. D., Zolotovskaya, S. A., Kalkandjiev, T. K., Gillespie, W. A. & Abdolvand, A. On the frequency-doubled conically-refracted Gaussian beam. *Opt. Express* **22**, 21347–21353 (2014).
209. Ma, J., Yuan, P., Wang, J., Xie, G., Zhu, H. & Qian, L. Sum-frequency generation with femtosecond conical refraction pulses. *Opt. Lett.* **43**, 3670–3673 (2018).
210. Hellström, J., Henricsson, H., Pasiskevicius, V., Bunting, U. & Haussmann, D. Polarization tunable Yb:KGW laser based on internal conical refraction. *Opt. Lett.* **32**, 2783–2785 (2007).
211. Wilcox, K., Abdolvand, A., Kalkandjiev, T. & Rafailov, E. Laser with simultaneous Gaussian and conical refraction outputs. *Appl. Phys. B* **99**, 619–622 (2010).
212. Cattoor, R., Manek-Hönninger, I., Rytz, D., Canioni, L. & Eichhorn, M. Laser action along and near the optic axis of a Holmium-doped KY(WO₄)₂ crystal. *Opt. Lett.* **39**, 6407–6410 (2014).
213. Brenier, A. Lasing with conical diffraction feature in the KGd(WO₄)₂:Nd biaxial crystal. *Appl. Phys. B* **122**, 237 (2016).
214. Günter, P. & Huignard, J. P. *Photorefractive materials and their applications, Vol. 3: Applications* (Springer, 2007).
215. Haertle, D., Caimi, G., Haldi, A., Montemezzani, G., Günter, P., Grabar, A. A., Stoika, I. & Vysochanskii, Y. M. Electro-optical properties of Sn₂P₂S₆. *Opt. Commun.* **215**, 333–343 (2003).
216. Montemezzani, G., Aillerie, M., Zheng, X., Remmach, H. & Grabar, A. A. Third column electro-optical coefficients of monoclinic Sn₂P₂S₆. *Opt. Mater. Express* **2**, 920–928 (2012).
217. Haertle, D., Jazbinšek, M., Montemezzani, G. & Günter, P. Nonlinear optical coefficients and phase-matching conditions in Sn₂P₂S₆. *Opt. Express* **13**, 3765–3776 (2005).
218. Grabar, A. A., Jazbinšek, M., Shumelyuk, A. N., Vysochanskii, Y. M., Montemezzani, G. & Günter, P. in *Photorefractive Materials and Their Applications 2: Materials* (eds Günter, P. & Huignard, J.-P.) 327–362 (Springer, 2007).
219. Haertle, D., Guarino, A., Hajfler, J., Montemezzani, G. & Günter, P. Refractive indices of Sn₂P₂S₆ at visible and infrared wavelengths. *Opt. Express* **13**, 2047–2057 (2005).
220. Vlokh, R., Mys, O., Grabar, A. & Vysochanskii, Y. Optical activity of Sn₂P₂S₆ crystals at the phase transition. *Ukr. J. Phys. Opt* **9**, 1–9 (2008).
221. Carpentier, C. & Nitsche, R. Vapour growth and crystal data of the thio(seleno)-hypodiphosphates Sn₂P₂S₆, Sn₂P₂Se₆, Pb₂P₂Se₆ and their mixed crystals. *Mater. Res. Bull.* **9**, 401–410 (1974).
222. Montemezzani, G. Optimization of photorefractive two-wave mixing by accounting for material anisotropies: KNbO₃ and BaTiO₃. *Phys. Rev. A* **62**, 053803 (2000).
223. IEEE Standard on Piezoelectricity. *ANSI/IEEE Std 176-1987*, 242 (1988).

BIBLIOGRAPHY

- 224. Montemezzani, G. & Zgonik, M. Light diffraction at mixed phase and absorption gratings in anisotropic media for arbitrary geometries. *Phys. Rev. E* **55**, 1035 (1997).
- 225. Brenier, A., Majchrowski, A. & Michalski, E. Phase distributions accompanying the conical diffraction through a Pasteur acentric biaxial crystal, displayed with $\text{Bi}_2\text{ZnOB}_2\text{O}_6$. *Opt. Mater.* **128**, 112353 (2022).
- 226. Jalviste, E., Palm, V. & Peet, V. Conically refracted Gaussian beam transformed by a lens. *J. Mod. Opt.* **67**, 252–260 (2020).
- 227. Wang, J., Tan, X., Qi, P., *et al.* Linear polarization holography. *Opto-Electron Sci.* **1**, 210009-1-210009–20 (2022).
- 228. Huang, L., Zhang, Y., Zhang, Q., Chen, Y., Chen, X., Huang, Z., Lin, X. & Tan, X. Generation of a vector light field based on polarization holography. *Opt. Lett.* **46**, 4542–4545 (2021).
- 229. Padgett, M., Courtial, J. & Allen, L. Light's orbital angular momentum. *Phys. Today* **57**, 35–40 (2004).
- 230. Brenier, A. Revealing modes from controlling an off-optical axis conical diffraction laser. *Laser Phys.* **27**, 105001 (2017).
- 231. Akbari, R., Howlader, C., Fedorova, K. A., Sokolovskii, G. S., Rafailov, E. U. & Major, A. Conical refraction output from a Nd:YVO₄ laser with an intracavity conerefringent element. *Opt. Lett.* **44**, 642–645 (2019).
- 232. Loiko, Y. V., Turpin, A., Sokolovskii, G. S. & Rafailov, E. U. Conical refraction mode of an optical resonator. *Opt. Lett.* **45**, 1317–1320 (2020).
- 233. Jalviste, E., Palm, V. & Peet, V. Vortex light beams in a degenerate two-crystal cascade conical refraction. *J. Opt.* **20**, 015601 (2017).

List of Publications

1. M. W. Iqbal, N. Marsal, & G. Montemezzani, “Non-circularly shaped conical diffraction”, *Sci Rep* **12**, 7317 (2022).
2. M. W. Iqbal, N. Marsal, and G. Montemezzani, “Shape and polarization distribution of non-circular conical diffraction beams from conjugate cascades”, *Opt. Express* **31**, 29859-29876 (2023).
3. M. W. Iqbal, N. Marsal, and G. Montemezzani, “In-situ holographic recording and two-wave mixing of conical diffraction beams”, *Submitted in JOSA-B*.
4. M. W. Iqbal, N. Marsal, and G. Montemezzani, “Fractional charged OAM beams via conjugate CD cascades”, *in preparation*.

Conferences

1. M. W. Iqbal, N. Marsal, and G. Montemezzani, “Complexly Shaped Vector Beams via Conical Diffraction Cascade”, in **CLEO/Europe-EQEC 2021**, (21st – 25th June), Munich Germany.
2. M. W. Iqbal, N. Marsal, and G. Montemezzani, “Faisceaux Vectoriels de Formes Complexes par Diffraction Conique en Cascade”, in **OPTIQUE Dijon 2021** (05th – 09th July), Dijon France.
3. M. W. Iqbal, N. Marsal, and G. Montemezzani, “Non-Circular Conical Diffraction with Fractional Optical Angular Momentum”, in **ICOAM 2022** (12th – 17th June), Tampere Finland.
4. M. W. Iqbal, N. Marsal, and G. Montemezzani, “Shaping of Non-circular Beams with Extended Conical Diffraction Cascade”, in **OPTIQUE Nice 2022** (04th – 08th July), Nice France.
5. M. W. Iqbal, Y. Shiposh, A. Kohutych, N. Marsal, A. Grabar and G. Montemezzani, “Conical diffraction cascades and interplay with linear and nonlinear material properties”, in **Photorefractive Photonics and Beyond 2022** (05th – 09th September), Treviso Italy.
6. M. W. Iqbal, N. Marsal, and G. Montemezzani, “Structured Vector Beams via Conical Diffraction Cascade”, in **Workshop on Structured light and its applications 2022** (07th – 08th November), Jena, Germany.
7. M. W. Iqbal, Y. Shiposh, A. Kohutych, N. Marsal, A. Grabar and G. Montemezzani, “Conical Diffraction Holography and Two-Wave Mixing”, in **CLEO/Europe-EQEC 2023** (26th – 30th June), Munich Germany.

8. G. Montemezzani, M. W. Iqbal , S. Mohammadou and N. Marsal, “Tailoring of Conical Diffraction Vector Beams by Manipulating Biaxial Crystal Cascades”, in **NOMA 2022** (22nd – 28th May), Cetraro Italy.
9. G. Montemezzani, M. W. Iqbal, Y. Shiposh, A. Kohutych, N. Marsal, and A. A. Grabar, “In-situ Holographic Recording of Conical Diffraction Vector Beams”, in **PIERS 2023** (3rd – 6th July), Prague Czech Republic.